

A COST-EFFECTIVE APPROACH TO
PREDICT AND ENHANCE SURFACE
INTEGRITY AND FATIGUE LIFE OF
PRECISION MILLED FORMING AND
FORGING DIES

by

ANDREAS REIMER

A thesis presented in fulfilment of the requirements for the
Degree of Engineering Doctorate

Department of Design, Manufacture & Engineering Management

Advanced Forming Research Centre

University of Strathclyde

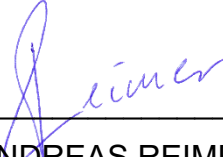
Glasgow, Scotland, UK

March 2019

Declaration

This thesis is the result of the author's original research. It has been composed by the author and has not been previously submitted for examination which has led to the award of a degree.

The copyright of this thesis belongs to the author under the terms of the United Kingdom Copyright Acts as qualified by University of Strathclyde Regulation 3.50. Due acknowledgement must always be made of the use of any material contained in, or derived from, this thesis.

Signed: 

(ANDREAS REIMER)

Date: _____12/03/2019_____

Acknowledgements

First of all, I would like to express my sincere gratitude and acknowledge the support of my supervisor Prof. Xichun Luo at University of Strathclyde, UK, who has given me tremendous and valuable advice, guidance and feedback during my EngD research. His knowledge, expertise insight in my study and spirit of scientific research are highly appreciated. I would like to extend my thanks to my industrial supervisor Mr Stephen Fitzpatrick and my colleagues Mr Jim Foster, Mr Michael Canavan and Mr Crawford Cullen for their support and motivation throughout my EngD period. I also would like to thank all the technicians and colleagues, who helped me to carry out my experiments. Thanks to the Advanced Forming Research Centre and Dr Dorothy Evans to give me the opportunity and funding for this research.

Thanks also to all my friends in Glasgow and Germany, for some of them I have known and been good friends for many years. It has been a great pleasure to share the most excellent time and experiences in my life with extraordinary friends. Additionally Fraser Kay for his very helpful proofreading.

I also would like to thank my parents Frank & Petra Reimer for their advice and motivation throughout a very long and tough period. I like to thank my Grandparents Wolfgang & Ingrid Gaefke as well as my brother Christian Reimer for their support.

Finally, I would like to special thank my wife Dr Jie Zhao and my daughter Emily for their unrestricted support and love throughout the time motivating and helping me through challenging times.

Additionally, I thank everyone else who helped me throughout this time.

Abstract

The machining process determines the overall quality of produced forming and forging dies, including surface integrity. Previous research found that surface integrity has a significant influence on the fatigue life of the dies. This thesis aims to establish a cost-effective approach for precision milling to obtain AISI H13 forming and forging dies with good surface integrity and long fatigue life. It combined experimental study accompanied by Finite Element Modelling and Artificial Intelligence soft modelling to predict and enhance forming and forging die life.

Four machining parameters, namely Surface Speed, Depth of cut, Feed Rate and Tool Lead Angle, each with five levels, were investigated experimentally using Design of Experiment. An ANOVA analysis was carried out to identify the key factor for every Surface Integrity (SI) parameter and the interaction of every factor. It was found that the cutting force was mostly influenced by the tool lead angle. The residual stress and microhardness were both significantly influenced by the surface speed. However, on the surface roughness it was found that the feed rate had the most influence.

After the machining experiments, four-point bending fatigue tests were carried out to evaluate the fatigue life of precision milled parts at an elevated temperature in a low cycle fatigue set-up imitated for the forming and forging production. It was found that surface roughness and hardness were the most influential factors for fatigue life. A 3D-FE-Modelling framework including a new material model subroutine was developed; this led to a more comprehensive material model. A fractional factorial simulation with over 180 simulations was carried out and validated with the machining experiment.

Based on the experimental and simulation results, a soft prediction model for surface integrity was established by using Artificial Neural Networks (ANN) approach. These predictions for SI were then used in a Genetic Algorithm model to optimise the SI. The confirmation tests showed that the machining strategy was successfully optimised and the average fatigue duration was increased by at least a factor of two. It was found that a surface speed of 270

m/min, a feed rate of 0.0589 mm/tooth, a depth of cut of 0.39 mm and a tool lead angle of 16.045° provided the good surface integrity and increased fatigue performance. Overall, these findings conclude that the fundamentals and methodology utilised have developed a further understanding between machining and forming/forging process, resulting in a good foundation for a framework to generate FE and soft prediction models which can be used to in optimisation of precision milling strategy for different materials.

List of Publications

1. Reimer, Andreas, Stephen Fitzpatrick, Xichun Luo and Jie Zhao, "Numerical Investigation of Mechanical Induced Stress during Precision End Milling Hardened Tool Steel", *Solid State Phenomena*, Vol. 261, pp. 362-369, **2017**, Trans Tech Publ.
2. Reimer, Andreas and X. Luo, Prediction of residual stress in precision milling of AISI H13 steel in *Procedia CIRP*, Vol. 71, Page 329 – 334, **2018**, Elsevier
3. Reimer, Andreas, X. Luo, J. Foster, S. Fitzpatrick, "Surface Integrity and its influence on fatigue performance of hard materials", *International Journal of Advanced Manufacturing Technology*, **2019** (*in preparation, to be submitted to International Journal of Advanced Manufacturing Technology*)
4. Reimer, Andreas, S. Fitzpatrick, and X. Luo, A full factorial numerical investigation and validation of precision end milling process for hardened tool steel in Euspen's 17th International Conference & Exhibition. **2017**, Euspen: Hannover, Germany. (*Peer Reviewed*)

Table of Contents

Declaration.....	I
Acknowledgements.....	II
Abstract.....	III
List of Publications.....	V
Table of Contents.....	VI
List of Figures.....	XI
List of Tables.....	XVI
List of Symbols and Abbreviations.....	XVIII
Chapter 1 Introduction.....	1
1.1 Background.....	1
1.2 Aim and Objectives.....	4
1.3 Methodology.....	5
1.4 Structure of the thesis.....	6
Chapter 2 Literature Review.....	9
2.1 Introduction.....	9
2.2 Surface Integrity.....	10
2.2.1 Residual stress.....	11
2.2.1.1 X-Ray Diffraction Method.....	17
2.2.2 Micro- & Macrostructure.....	19
2.2.3 Surface Roughness.....	21
2.2.4 (Micro) Hardness.....	25
2.2.5 Summary.....	27
2.3 Fatigue Life.....	28
2.3.1 Mechanical Fatigue.....	28

2.3.1.1	Thermal Fatigue.....	35
2.3.1.2	Thermomechanical Fatigue	36
2.3.2	Summary.....	38
2.4	Influence of Machining Process on Surface Integrity & Fatigue Life	38
2.4.1	Influence Machining Process on Surface Integrity.....	38
2.4.1.1	Influence of Tool Geometry and Forces.....	40
2.4.1.2	Machining of Hard Materials	45
2.4.2	Influence of Surface Integrity on Fatigue Life	46
2.4.3	Summary.....	47
2.5	Prediction Models	48
2.5.1	Descriptive Surface Integrity and Fatigue Life Model	48
2.5.2	Finite Element Modelling	50
2.5.2.1	Material Model of FEA	51
2.5.3	Soft Prediction Model	54
2.5.3.1	Artificial Neural Network	54
2.5.3.2	Genetic Algorithm	59
2.5.4	Summary.....	62
2.6	Chapter Summary.....	63
Chapter 3	Precision Milling Experiment	64
3.1	Introduction	64
3.2	Methodology of Experiments	65
3.2.1	Design of Experiment Methodology.....	68
3.3	Experimental Setup and procedure	74
3.3.1	Workpiece	76
3.3.2	Experimental Procedure.....	77
3.3.3	Measurements	79

3.3.3.1	Cutting Forces	79
3.3.3.2	Microstructure	81
3.3.3.3	Residual Stress.....	82
3.3.3.4	Microhardness	83
3.3.3.5	Surface Roughness	84
3.4	Experimental results and discussion.....	86
3.4.1	Cutting Forces	86
3.4.2	Residual Stress	91
3.4.3	(Micro)hardness	97
3.4.4	Surface Roughness.....	102
3.4.5	Macro- & Microstructure	107
3.5	Summary	110
Chapter 4	Experimental Evaluation of Fatigue Life	111
4.1	Introduction	111
4.2	Experimental set-up and procedure.....	112
4.2.1	Equipment and Tools	113
4.2.1	Experimental procedure	119
4.3	Analysis of the Influence of Surface Integrity on Fatigue Life	122
4.3.1	Fractography	130
4.4	Summary	134
Chapter 5	Modelling & Simulation of 3D-Milling Process	135
5.1	Introduction	135
5.2	Description of the 3D FE model for End-Milling	136
5.2.1	Material parameters	138
5.2.2	Scripting Model (Python).....	140
5.2.3	Validation Strategy	141

5.3	Finite Element Material Model	143
5.3.1	Subroutine (VUHARD)	145
5.4	Modelling of Surface Integrity	147
5.4.1	Temperature.....	147
5.4.2	Cutting Forces	149
5.4.3	Residual Stress	153
5.4.4	Surface Roughness.....	157
5.5	Summary	161
Chapter 6	Modelling & Optimisation of Fatigue Life.....	162
6.1	Developing Soft Prediction Model.....	162
6.1.1	Creating an Artificial Neural Network.....	163
6.1.2	Optimisation with Genetic Algorithm.....	166
6.1.3	Validation Strategy of Soft Prediction Model	168
6.2	Experimental studies for optimised process.....	169
6.2.1	The Parameter for Optimised Process	170
6.2.2	Experimental Results and Discussion of Optimised Process .	175
6.2.2.1	Machining Experiment	175
6.2.2.2	Fatigue Experiment.....	177
6.2.3	FEA results of the optimised process.....	177
6.3	Summary	179
Chapter 7	Conclusions and future work	180
7.1	Conclusions	180
7.2	Contribution to Knowledge.....	183
7.3	Limitations and Future Work.....	186
	List of References	188
	Appendices	i

Appendix I Framework.....	i
Appendix II Kistler Datasheet	iii
Appendix III Surface Topology.....	x
Appendix IV Underpinning Cutting Force Data	xviii
Appendix V Underpinning Residual Stress Data	xxviii
Appendix VI Underpinning Microstructure Data	xxxix
Appendix VII Subroutine	lvii
Appendix VII Script	lxii
Appendix IIX Matlab Codes	lxxxviii
Appendix IX Script Framework	xciii
Appendix X Workpiece Fixture Drawing	xciv
Appendix XI Fatigue Testing Setup Drawings	xcvii
Appendix XII Certificates of Conformance	cviii

List of Figures

Figure 1.1: Typical precision machining industries and applications for forming and forging dies [1-3]	1
Figure 1.2: Research methodology of the thesis	5
Figure 1.3: Thesis structure	6
Figure 2.1: Residual stress interaction plot [16]	12
Figure 2.2: Influence of RS in machining a) mechanical load b) thermal load [21].....	14
Figure 2.3: Comparison of RS measurement techniques by penetration & spatial resolution [15].	16
Figure 2.4: X-Ray diffraction at a single crystal lattice	17
Figure 2.5: Schematic XRD setup and $\sin^2\psi$ analyse [30]	19
Figure 2.6: White layer formation under a microscope of AISI H13 [35, 36]	20
Figure 2.7: Components and parameter of surface roughness profile	21
Figure 2.8: Vickers Indenter	25
Figure 2.9: Cross-Section of Spheroconical Diamond	27
Figure 2.10: Stress Cycle of fatigue testing	30
Figure 2.11: Wöhler curve / log-S-N Curve	31
Figure 2.12: Stress-Strain hysteresis loop	32
Figure 2.13: Influence of Hardness to the cycle performance [65]	34
Figure 2.14: Thermo-mechanical loads in forging and forming die	37
Figure 2.15: Geometry and tool coordinates for a ball end mill cutter	40
Figure 2.16: Effective tool radius.....	43
Figure 2.17: Selection of cutting tool material for machining purpose [21]... ..	44
Figure 2.18: Descriptive Surface Integrity Model	49
Figure 2.19: Artificial Neural Network - Feed Forward Network schematic.. ..	55
Figure 2.20: Artificial Neural Network - Radial Basis Function schematic....	57

Figure 2.21: Genetic Algorithm by natural mutation	60
Figure 2.22: Genetic Algorithm optimisation principle	61
Figure 3.1: Experimental procedure	65
Figure 3.2: Root cause diagram (Ishikawa-Diagram) on Surface Integrity ...	67
Figure 3.3: Visualisation of Central Composite Design Method	70
Figure 3.4: Experimental setup	74
Figure 3.5: Workpiece fixture and dynamometer illustration	75
Figure 3.6: Experimental process procedure	78
Figure 3.7: Workpiece cutting sequence	78
Figure 3.8: (a) Kistler Dynamometer 9129AA, (b) Kistler Multichannel Charge Amplifier 5070 [144]	79
Figure 3.9: FEI Quanta 250 FEG SEM	81
Figure 3.10: XRD test setup	82
Figure 3.11: Struers Hardness tester	84
Figure 3.12: Alicona Infinite focus	85
Figure 3.13: Example of cutting force readings	86
Figure 3.14: Main effects of machining parameter for Cutting force	88
Figure 3.15: Machining parameter interaction plot for cutting force	90
Figure 3.16: SRM for Cutting Force on Feed Rate and Lead Angle	91
Figure 3.17: Main effects of machining parameter for Plane-Residual Stress	95
Figure 3.18: Machining parameter interaction plot for residual stress	96
Figure 3.19: SRM on Residual Stress for Surface Speed and Feed Rate ...	97
Figure 3.20: Workpiece hardness before and after machining experiments	98
Figure 3.21: Main effects of machining parameter for hardness	100
Figure 3.22: Machining parameter interaction plot for microhardness	101

Figure 3.23: Surface Response Model for Depth of Cut and Tool lead Angle of Microhardness	102
Figure 3.24: Main effects of machining parameter for Surface Roughness (S_a)	105
Figure 3.25: Machining parameter interaction plot for hardness	105
Figure 3.26: SRM for Depth of Cut and Lead Angle of Surface Roughness (S_a)	106
Figure 3.27: Surface topology of machined surfaces	108
Figure 3.28: Surface Microstructure of Fatigue Workpiece 24	108
Figure 3.29: Workpiece microstructure of raw material.....	109
Figure 3.30: Microstructure of fatigue workpiece after machining.....	110
Figure 4.1: Force flow in four-point bending test.....	113
Figure 4.2: Fatigue Testing Set-up.....	114
Figure 4.3: Heat treatment temperature-time-table	115
Figure 4.4: Tempering Curve [146]	116
Figure 4.5: Four-point bend test rig – first die design.....	117
Figure 4.6: Breakage of the 1 st design of the four-point bending die.....	118
Figure 4.7: Second design iteration of the four-point bending die.....	119
Figure 4.8: Geometrical measurements of fatigue workpieces before fatigue testing	120
Figure 4.9: Force incline rate to start of the experiment.....	121
Figure 4.10: First five cycles of fatigue experiment.....	122
Figure 4.11: Interaction of Surface Roughness S_a [μm] and Fatigue Cycles [-]	125
Figure 4.12: Interaction of Micro-Hardness [HRC] and Fatigue Cycles [-] .	126
Figure 4.13: Hardness Cross-section original and deformed comparison..	127
Figure 4.14: Microstructure of workpieces with high (left) and lower (right) Martensite content	128

Figure 4.15: Workpiece surface drag microstructure deformation.....	129
Figure 4.16: Interaction of Residual Stress (VM) [MPa] and Fatigue Cycles [-]	130
Figure 4.17: Fracture Model (based on [57]).....	131
Figure 4.18: Exemplary fracture surface	132
Figure 4.19: Crack propagation from dimple of the fractured surface	133
Figure 4.20: Fractured surface showing beach marks and ductile fracture	133
Figure 5.1: General FEM Setup	137
Figure 5.2: FEM Validation strategy	142
Figure 5.3: Flow in Abaqus / Standard (based on [152]).....	145
Figure 5.4: UTS deletion criteria principle	146
Figure 5.5: FE Temperature and residual stress development	148
Figure 5.6: Effect and interaction plots for Temperature on machining.....	149
Figure 5.7: Cutting Force - Experiment vs. Simulation Comparison.....	150
Figure 5.8: Effect and interaction plots on cutting forces during machining	153
Figure 5.9: Residual stress comparison between experiments and FEM ..	154
Figure 5.10: Residual stress development in the cutting process [107]	155
Figure 5.11: Effect and interaction plots on Residual Stress during machining	157
Figure 5.12: Comparison of surface roughness obtained by FEM and Experiment.....	158
Figure 5.13: Effect and interaction plots for surface roughness on machining	160
Figure 6.1: Soft prediction model - the optimisation process	163
Figure 6.2: FF Network structure	164
Figure 6.3: RBF Network structure.....	165
Figure 6.4: Soft prediction validation model	169

Figure 6.5: Correlation regression of target values and predicted values ..	170
Figure 6.6: Optimisation evolution of soft prediction model.....	171
Figure 6.7: Optimisation regression model	172
Figure 6.8: Surface response optimisation.....	174
Figure 6.9: Element boundaries in validation simulation	178
Figure 7.1: Implementation to Industry 4.0 - Basic Schematic	187
Figure 7.2: NX implementation.....	187

List of Tables

Table 2.1: Levels of Datasets to characterise and evaluate Surface Integrity [14].....	11
Table 2.2: Categorising residual stress measuring methods	16
Table 2.3: Physical & functional significance of surface textures [46]	24
Table 2.4: Description of the conventional parameter based on ISO 13565-2	24
Table 3.1: Design of Experiment types with regards to the experimental objectives [141].....	68
Table 3.2: Comparison between CCD and D-Optimal (based on [141])	69
Table 3.3: Level and design for machining experiment.....	71
Table 3.4: Machining experiment plan and parameters, sort by run order...	72
Table 3.5: End-mill ball nose cutter specifications [143]	76
Table 3.6: Workpiece Material properties AISI H13	77
Table 3.7: Kistler Sensitivity Calibration.....	80
Table 3.8: XRD-Settings	83
Table 3.9: Alicona specification.....	85
Table 3.10: Cutting force results	87
Table 3.11: ANOVA for machining parameter on cutting force	88
Table 3.12: Measured Surface Residual Stress.....	92
Table 3.13: Measured results as Von-Mises Stress.....	93
Table 3.14: Results of ANOVA for plane residual stress (Von-Mises) by Experiments	94
Table 3.15: Result of ANOVA for Microhardness.....	99
Table 3.16: Surface Roughness after Machining	103
Table 3.17: Result of ANOVA for Surface Roughness S_a	104
Table 4.1: Fatigue performance setup parameter	112

Table 4.2: AISI D2 - Material composition - as received material.....	115
Table 4.3: Fatigue die hardness [HRC] before and after heat treatment....	117
Table 4.4: The Central Composite Design of the experiment for fatigue tests	123
Table 4.5: Regression Analysis of Cyclic Fatigue	124
Table 5.1: Material composition as an average.....	138
Table 5.2: Johnson-Cook Parameter for selected materials	139
Table 5.3: Mechanical material properties	139
Table 5.4: FEM material parameters.....	144
Table 5.5: ANOVA for FEM machining parameter on Cutting force	152
Table 5.6: ANOVA for FEM machining parameter on Von-Mises residual stress	156
Table 5.7 ANOVA for FEM machining parameter on surface roughness (R_a)	159
Table 6.1: Bounds for Genetic Algorithm	168
Table 6.2: Outcome of the optimisation process	173
Table 6.3: Optimised cutting parameters and tool lead angle values.....	174
Table 6.4: Optimised validation results for Residual stress [MPa]	175
Table 6.5: Optimised validation results for Microhardness [HRC].....	176
Table 6.6: Optimised validation results for surface roughness S_a [μm]	176
Table 6.7: Optimisation validation results for fatigue performance.....	177
Table 6.8: Simulation results of optimised validation runs	178

List of Symbols and Abbreviations

Symbols

Symbol	Description
A	Surface area
A, B, C, m, n, T0, Tm	Johnson-Cook material parameter
b	Fatigue strength component
c0	Number of replication in centre point
C1	Material specific constant of elongation at break point
c_i	Centre of neuron I
C_{J,K}	Connection C from J to K
d	The lattice spacing of the component
D₁ ... D₅	Johnson-cook failure parameter
d_{1,2}	Diagonal Length of the indentation
d_{axial}	Axial depth of cut
D_{K,L}	Connection D from K to L
F_x	Cutting force in X direction
F_y	Cutting force in Y direction
F_z	Cutting force in Z direction
i	Cutting edge / flute
j	Position of the discrete element
M	Sampling number in X direction (Surface Roughness)
n	Order of the X-rays
N	Sampling number in Y direction (Surface Roughness)
n_c	Number of central points
N_f	Number of cycles (Fatigue Cycles)
P	Force
R	Stress ratio
r₀	Nominal tool radius

R_a	Arithmetic average roughness
R_{DelA}	The average slope of the profile
r_{eff}	Effective tool radius
r_{ji}	Vector of the cutting position of the discrete element <i>j</i> on cutting edge <i>i</i>
R_{ku}	Kurtosis of the profile height distribution
R_p	Maximum profile peak height (surface roughness) / yield strength (proof stress)
R_q	Root Mean Square roughness
R_{sk}	Skewness of the profile height distribution
R_{sm}	Mean spacing of the profile
R_t	Maximum peak-to-valley height
R_z	Ten-Points height
s	Friction coefficient
S_a	The average surface roughness profile
s_k	Weighted input to the specific hidden layer element
S_q	The root mean square surface roughness
S_z	Ten-points height
T	Temperature
t_k	Target value at point k
UT	Ultimate tensile strength in material model
UT1 ... UT4	Ultimate tensile factors based on empirical models
UTTemp	Temporary calculation temperature
W_a	The average depth of waviness motifs
x_i	Weighted input vector for the specific element/neuron <i>i</i>
x_j	Input <i>x</i> of <i>j</i> -th input variable
y_i	Measured surface height in position <i>i</i>
y_k	Output of neural network at point <i>k</i>
α	Learning rate
α₀	Positioning angle of the main cutting edge of each cutting edge element
α_k	Notch shape factor
α_{k max}	Maximum notch stress

$\Delta\varepsilon$	Total strain amplitude
$\Delta\sigma$	Stress range
ε	Strain component / current strain
$\bar{\varepsilon}$	Proportional strain
$\dot{\bar{\varepsilon}}$	Proportional strain rate
ε^f	Strain equivalent to fracture
$\varepsilon_{a,t}^{mech}$	Mechanical strain at location a and time t
$\varepsilon_{a,t}^{therm}$	Thermal strain at location a and time t
$\bar{\varepsilon}_0$	Reference strain rate
ε_a	Strain amplitude
ε_B	True strain at break point
ε_{el}	Elastic strain
ε_{pl}	Plastic strain
θ	The angle of diffraction
λ	The wavelength in XRD
μ	Coulomb friction
μ_k	Gaussian Centre of hidden layer element/neuron K
σ	Stress component
$\bar{\sigma}$	Flow stress (Von-Mises)
$\bar{\sigma}_f$	Reference flow stress
σ'_f	Fatigue strength coefficient
σ_a	Stress amplitude
σ_k	Standard deviation of element/neuron width K
σ_m	Mean stress
σ_{max}	Maximum stress
σ_{min}	Minimum stress
σ_n	Reference stress
τ	Equivalent shear stress
τ_{max}	Maximum equivalent shear stress
φ	XRD relative measurement direction
φ_i	Positioning angle of the i cutting edge
φ_{ri}	Positioning angle of the i cutting edge to radial reference plane

Φ_k	Hidden layer element/neuron k
Ψ_L	Output layer element/neuron L
ψ_{i1}	Initial lag angle
ψ_{i2}	Final lag angle
ω	Rotational speed (rev. Per min)
ω_i	Width of element/neuron i
$\vec{i}, \vec{j}, \vec{k}$	Vectors in a cylindrical coordinate system

Abbreviations

Abbreviation	Description
AFRC	Advanced Forming Research Centre
AISI	American Iron and Steel Institute
ANN	Artificial Neural Network
ANOVA	Analysis of Variance
ANSI	American National Standard
ASTM	American Society for Testing and Materials
BAC	Bearing Area Curve
BS	British Standards
CAM	Computer-Aided Manufacturing
CBN	Cubic Boron Nitride
CCD	Central Composite Design (Method)
CERN	The European Organization for Nuclear Research
CNC	Computer Numerical Control
DAQ	Data Acquisition
DIN	German National Organization for Standardization
DoC	Depth of Cut
DoE	Design of Experiments
EDM	Electro Discharge Machining
EN	European Standard
FEA	Finite Element Analysis
FEM	Finite Element Model / Method
FF	Feed Forward (Network)
FFBP	Feedforward Backpropagation
FR	Feed Rate
GA	Genetic Algorithm
HCF	High-Cycle Fatigue
HM	Hard Machining
HRC	Hardness in the Unit Of Rockwell Type C
HSS	High-Speed Steel
HV	Vickers Hardness

IP	In-Phase
ISO	International Organization for Standardization
kgf	Kilo Gram Force
LA	Lead Angle
LCF	Low-Cycle Fatigue
MLP	Multilayer Preceptron Network
MPa	Mega Pascal
MSE	Mean Squared Error
OEM	Original Equipment Manufacturer
OP	Out of Phase
PCBN	Polycrystalline Cubic Boron Nitride
PCD	Polycrystalline Diamonds
PI	Performance Index
RBF	Radial Basis Function
RMSE	Root Mean Squared Error
RPM	Revolution (Rounds) per Minute [on a Machine Tool Spindle]
RS	Residual Stress
SEM	Scanning Electron Microscope
SI	Surface Integrity
SRM	Surface Response Model
SS	Surface Speed
TEM	Transmission Electron Microscopy
TMF	Thermo-Mechanical Fatigue
TRL	Technology Readiness Level
UTS	Ultimate Tensile Stress
VM	Von-Mises Stress
VUHARD	Abaqus Explicit Subroutine Interface
XRD	X-Ray Diffraction Method

Chapter 1 Introduction

This chapter will present the overall background and motivation for researching the topic, followed by the specific aim, objectives, methodology and structure of this work.

1.1 Background

Forming and forging are fundamental manufacturing processes and typically involve shaping metal by plastic deformation under localised compressive forces applied by various tools and dies. They are becoming increasingly important core competencies in aerospace, automotive, oil and gas, and many other sectors since they help produce high-performance components with high efficiency and repeatability - these include compressor blades, aircraft fuselage, car bodies, transmission gears or camshafts, as shown in Figure 1.1.

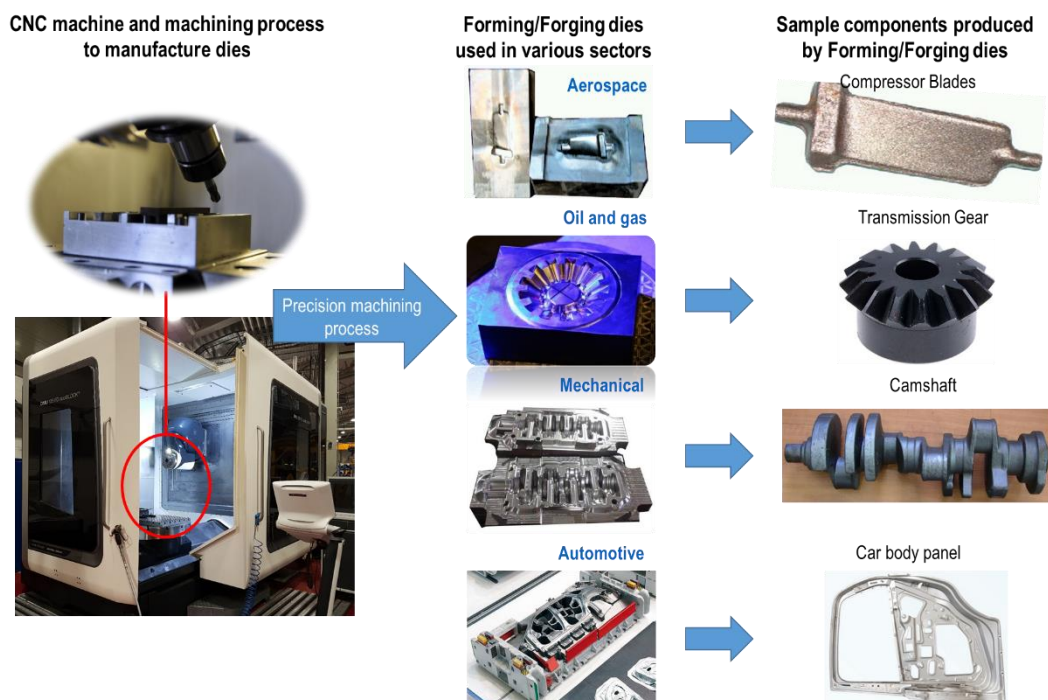


Figure 1.1: Typical precision machining industries and applications for forming and forging dies [1-3]

The forming and forging dies are usually manufactured using various machining operations like milling, turning, grinding or electro-discharge machining (EDM). Generally, the cost of these forging and forming dies is around 10-15% of the entire manufacturing process. The cost includes die material, machining and heat treatment, coating - if applicable - and set-up time. Set-up time for dies in a production environment can often take several hours depending on its complexity, which is also correlated with the costs of wages, downtime, material, scrap parts and other indirect costs [4]. Therefore, die life has a significant impact on the overall cost of forming and forging processes.

The machining process influences the overall quality and performance of the produced dies, including the surface integrity and fatigue life. During the machining process, residual stresses are inducted to the machined component. The residual stresses have a direct influence on the die life. Previous research has shown that both types of residual stress (tensile and compressive) influence the tool life [5, 6]. Furthermore, research has proved that the surface roughness and hardness also affects the fatigue life of the forming and forging die life [7-9].

Additionally, in some forming and forging operations such as the forging of compressor blades, the forging die cannot be treated or coated as it will affect the final accuracy of the forging die and consequently the forged component. It is crucial to optimise the machining process in a controlled environment to improve fatigue life as well as the surface integrity of dies for better in-service performance.

The development of machining technologies for making the forging dies, such as reducing machining time, tool wear, cutter deflection and improving surface integrity and fatigue life has become a crucial factor and has a high impact on the economy in the forging or forming process industry. Global competition has increased the pressure on tool manufacturers to improve the die life for forming or forging dies as it has a significant impact on the economy of a process. Improvements such as increased productivity, material utilisation and complex

geometries enhanced the developmental process in creating the final forming and forging die. [10]

Machining hardened components are often a challenge for the material removal process. Therefore, an appropriate setup of machining parameters is essential since an incorrect set-up can increase undesired tensile stresses and thus lead to a significantly reduced die life-cycle. On the other hand, an optimised machining process can control the induced heat, stresses and surface roughness, thus improving surface integrity.

The aim of this body of work is to investigate in a scientific manner the connection between the surface integrity of die produced by machining, and its fatigue life. Whilst the coherent relationship between fatigue life and surface integrity in combination with multi-axis machining will not be investigated in great depth it is still a valuable topic due to the significant impact on related costs. This research aims to help fill gaps in knowledge, understand and optimise the machining process for tool steel, and develop a framework flexible enough to cover a variety of components as well as material and cutter. Once the bridge between the surface integrity and fatigue life is built, the machining process can be conducted to optimise the relationship between those components and therefore increase the die life and productivity significantly.

1.2 Aim and Objectives

This thesis aims to establish a cost-effective approach to predict and enhance AISI H13 forming and forging die performance (improved fatigue life and surface integrity) obtained by precision milling. This research will consist of a systematic experimental study accompanied by Finite Element (FE) simulation and optimisation of the precision milling process.

The key objectives identified for this project are as follows:

1. To develop prediction models for surface integrity and fatigue life at elevated temperature of bulk-forming dies obtained by precision milling by conducting machining and fatigue life experiments on AISI H13 material workpieces
2. To develop a FE-model for the precision milling to understand in-process parameters behaviour and validate the model by using machining experiments.
3. To develop a soft-prediction model for optimisation of the machining strategy for enhanced die-life and validate by conducting additional validation experiments.
4. To establish a generic framework to generate FE and soft prediction models which can be used to optimise precision machining process for different materials.

1.3 Methodology

A systematic approach, as illustrated in Figure 1.2, is employed to fulfil the aim and objectives of the project. A more comprehensive methodology of this work can be found in Appendix I Framework.

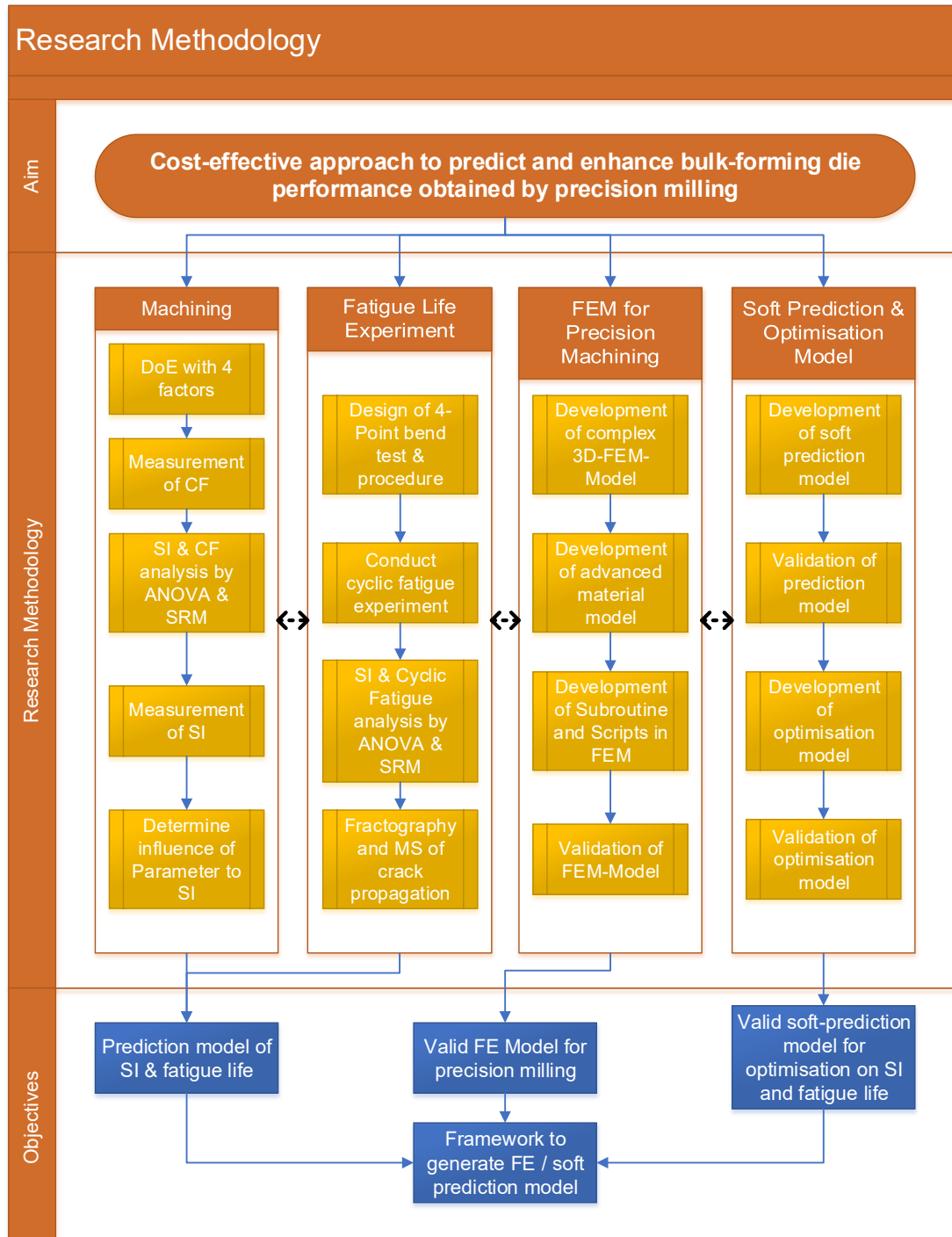


Figure 1.2: Research methodology of the thesis

The machining experiment with four parameters (Surface Speed, Depth of Cut, Feed Rate, Tool Lead Angle) is prepared and carried out. Additionally, the process is accompanied by FE-simulation. Once the machining trials are completed, the results (surface integrity and cutting force) are analysed, compared and validated in FEM.

In the next stage, a fatigue life performance experiment will be carried out by using a four-point bend test.

Finally, the results from the machining and fatigue performance experiment, as well as FEA, are used to develop a soft prediction model and an optimisation algorithm. Validation trials will be carried out to verify the process optimisation and draw conclusions from all results.

1.4 Structure of the thesis

The thesis is structured as shown in Figure 1.3.

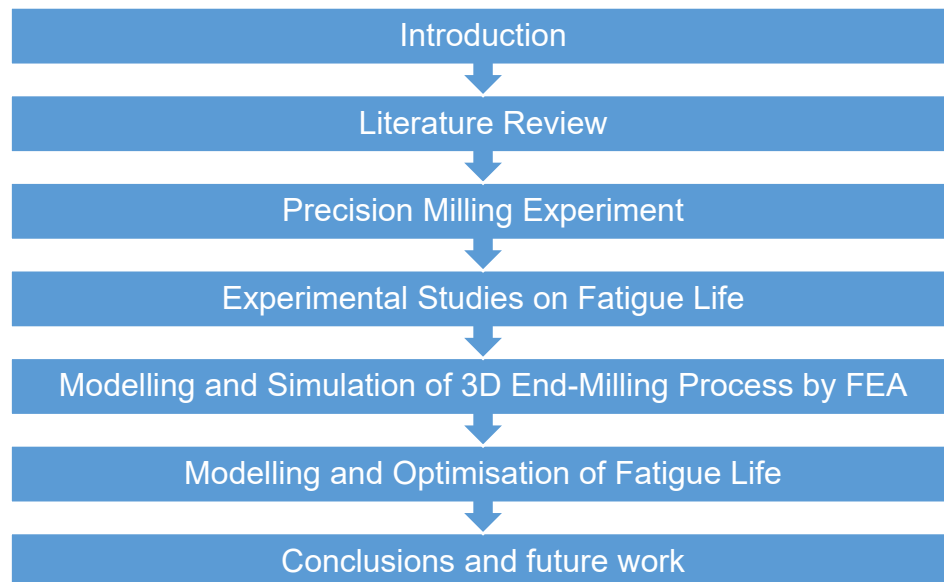


Figure 1.3: Thesis structure

A short outline of the structure of the thesis is given as follows:

In Chapter 1 an introduction to the topic is given, including background information, motivation, aims and objectives, the conducted methodology and the structure of this thesis.

Chapter 2 gives an overview of literature on the topic. The main focus is on surface integrity and its influence on the fatigue performance. It also contains modelling approaches, including neural networks, genetic algorithms and finite element for the prediction of surface integrity and fatigue life. This chapter will also include a brief review of the measurement approach to be used in the research.

Machining experiments are developed and discussed in Chapter 3, beginning with an introduction of experimental methodology which minimises the number of experiments required whilst maintaining the quality of analysis. The experimental set-up and procedure are explained in detail before all of the results are presented. The experimental results (surface integrity and cutting force) are analysed in more detail by using ANOVA (Analysis of Variance) and SRM (Surface Response Modelling) to determine the influence of the machining parameter to the surface integrity.

Chapter 4 concerns the fatigue life performance of the machined workpieces. Firstly, the experimental set-up of the fatigue life test is shown and discussed; this includes the development of tooling and the testing procedure. The focus in this chapter is the analysis of results gained from the fatigue performance experiments. The surface integrity results are analysed using ANOVA and regression method. Additionally, the Fractography and Microstructure of broken workpieces are analysed to identify the typical crack propagation.

Chapter 5 presents a 3D-FEA model of the milling process. It shows the advantage of revealing multiple cutting-edge engagements on the workpiece. The material parameter, scripts and validation strategy are discussed. The focus of this chapter is the newly developed material model which was

implemented in a subroutine. The outcome of the developed subroutine will be discussed and validated.

Chapter 6 discusses the optimisation of the machining process using data and information obtained from previous chapters. Initially, the soft prediction model using artificial neural networks and a genetic algorithm are described and developed. The focus of this chapter is to identify parameters for the optimised process using the results from previous chapters. At the end of Chapter 6 validation trials are presented to prove the concept of the developed model.

Chapter 7 concludes the thesis with a summary of the key findings of this research, contribution to knowledge, limitations and future work.

Chapter 2 Literature Review

This chapter reviews research fundamentals on the surface integrity, fatigue life and machining as well as FEM (Finite Element Modelling). The review assesses the interaction of these research fundamentals and discuss soft prediction models. This review also discusses the current research to provide a state-of-the-art overview. At the end of this section a summary including the identified knowledge gaps is presented and discussed.

2.1 Introduction

Surface requirements are increasingly significant in achieving goals set by industries. The manufactured components can be exposed to very harsh environments where the temperature can fluctuate widely within a couple of milliseconds to seconds. These fluctuations are exhibited in applications like aircraft, car engines, oil and gas, or tooling, and dominate these environments. New lightweight structures are usually complex in their design and require high accuracy on the formed part, i.e. in aircraft compressor blades or car engine parts. Therefore, high standards for forging and forming dies are required and this often includes the surface quality of the dies to ensure the final part is geometrically accurate and has as fewer non-conforming parts as possible. Forming and forging dies must be able to produce a high volume of parts at a consistently high standard. The significant temperature variation within seconds as well as applied forces during the forming and forging process can potentially damage dies. These factors often lead to reduced forming die life performance. The prediction of die life performance needs to consider multiple factors such as temperatures, forming velocity and force, the size of the component, surface integrity of all components, and contact behaviour - especially friction. Surface integrity is a crucial component as it is the direct contact area between the component and the forming die. To determine the die life and increase the fatigue life performance, it is necessary to improve the surface integrity for these forming / forging dies.

2.2 Surface Integrity

Machined parts must withstand both mechanical and thermal dynamic loads. The manufacturing industry must meet this challenge using new materials, methods and processes. A critical component of measuring the success of a component is fatigue life, while surface integrity is regarded as one of the most influential factors. Field and Kahles [11] split the surface quality into two components. In the first component geometric texture and topography are both defined by measuring the surface roughness and topography. The second part involves the metallurgy which defines the parameter “under” the surface / “surface integrity” where micro-cracks, phase transformation, hardness and residual stress are measured and defined [11]. Field and Kahles were the first to introduce the concept of Surface Integrity (SI) and defined it as “*the inherent or enhanced condition of a surface produced in machining or other surface generation operation*” [12]. Field and Kahles concluded that the geometrical surface, as well as the physical properties, interact and influence fatigue life [13, 14].

The surface integrity was later then split into three types of datasets and also recognised and adopted by the ANSI (American National Standard Institution). The dataset table is shown in Table 2.1.

Based on Table 2.1, the following chapters discuss the components of the standard dataset in more detail.

Table 2.1: Levels of Datasets to characterise and evaluate Surface Integrity [14]

Minimum SI dataset	Standard SI dataset	Extended SI dataset
Surface finish	Minimum SI data set	Standard SI data set
Macrostructure ($\leq 10\times$)	Fatigue test (screening)	Fatigue test (extended to obtain design data)
Microcracks	Stress corrosion test	Additional mechanical tests
Macrocrack indications	Residual stress and distortion	Tensile
Microhardness		Stress rapture
Microstructure		Creep
Plastic deformation		Other specific tests (e.g., bearing performance, sliding, friction evaluation, sealing, properties of the surface)
Phase transformation		
Intergranular attack		
Pits, tears, laps, protrusions		
Built-up edge		
Melted and re-deposited layers		
Selective etching		

2.2.1 Residual stress

Residual Stress (RS) is defined as the stresses that remain in a component after a process, when no heat and/or force influence are occurring on the workpiece [15]. The RS occurs in all components, and these stresses are critical values. The presence of RS within the component increases the chance of failure.

In Figure 2.1 the interaction between the three main characteristics of RS is illustrated by Brinksmeier et al. [16]. These characteristics can be placed in three categories: metallurgical, thermal and mechanical. Figure 2.1 clarifies the change of a process parameter and its effect on residual stress.

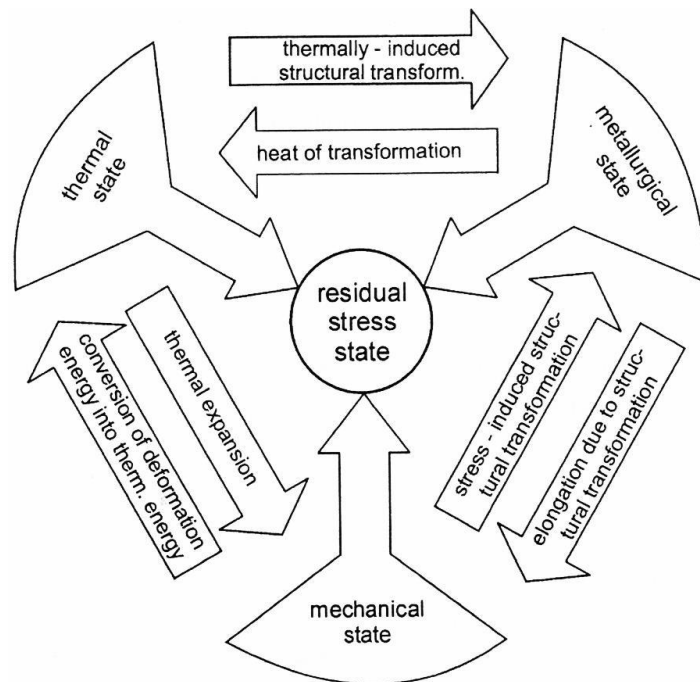


Figure 2.1: Residual stress interaction plot [16]

The model can be explained as follows:

- The thermal influence of the machining process increases - this causes thermal expansion in the mechanical state.
- The thermally-induced stress structurally transforms the metallurgical state.
- Lastly, the thermal impact causes an increase in tensile stress and an interaction between both mechanical and metallurgical states.

Residual stress can be categorised in three different types:

1. Order: Macro RS, stress developed on large grain size and is nearly homogeneous (σ^I)
2. Order: Micro RS, stress is depending and varying on the grain size and is nearly homogenous along small grains (σ^{II})
3. Order: Micro RS, stress is within the grain and results from dislocations and other crystalline defects and varies along atomic distances. (σ^{III})

Condition on the pre-processes the workpiece has been subjected to, it may contain higher or lower RS before machining. However, during the machining

process, residual stresses can be added or removed from the component. The amount and distribution of RS is depending on numerous factors, as listed below [17]:

1. Clamping technique
2. Machining condition
3. Tool properties
4. Environment
5. Induction direction and period of mechanical and thermal impacts

From this list:

- Factor 1 influences the distribution of the stress.
- Factors 2 to 4 influences the amount of RS.
- Factor 5 influences the formation of residual stress.

The machining-induced stress to the surface and sub-surface can result in tensile or compressive residual stresses which have different effects on the part – i.e. its functionality and fatigue life - as research in this area currently shows [18-20].

Residual stress can also be classified into two types as mentioned, namely tensile and compressive stress. Tensile stress is caused mostly by thermal impacts which are critical to workpiece performance. However compressive stresses are often induced by mechanical loads and are preferred on the surface. Compressive stresses are preferred as they strengthen the tensile resistance as well as increase the life-cycle performance. Nevertheless, both RS types usually occur in combination, and therefore RS depends on the dominating stress [17]. Figure 2.2 shows the residual stress influenced by a) theoretically purely mechanical load, and b) theoretically a purely thermal load.

As shown in Figure 2.2a (section 0-A-B) only mechanical load compression stresses are applied to the chip formation. In section C-D-E we see tensile stresses developing behind the cutting tool. When the cutting tool has been removed from the workpiece, the workpiece unloads the residual stress which

shifts from section E to F; the remaining part of compressive stress remains in the surface of the workpiece.

When considering only the thermal load, the most influential factor is thermal expansion. For most alloys thermal expansion is a positive value coefficient. In the chip formation area is it a consequently compressive stress (Figure 2.2 b) section 0-A-B). The surface area on and behind the tool is cooling down and causes additional compressive stresses (section B-C-D). Once the workpiece has completely cooled to room temperature only the tensile stresses persist on the surface, with compressive stresses occur mostly in the sub-surface. [21]

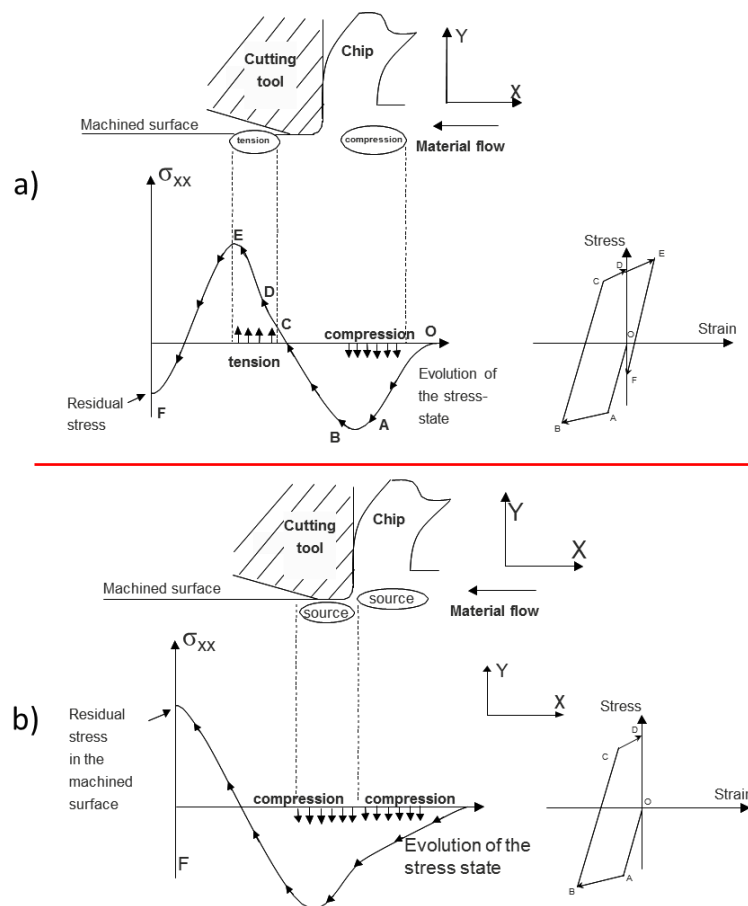


Figure 2.2: Influence of RS in machining a) mechanical load b) thermal load [21]

Batalha et al. [22] analysed the influencing parameter for the cutting forces and residual stresses on the EN 100CrMn6 (DIN 1.3520) Steel with a hardness of 62 HRC and a CBN tool. They found that the cutting force was the most influencing parameter generating residual stresses and these were influenced by the feed rate and depth of cut.

In the review paper using FEM to analyse RS by Maranhão et al. [23], researchers concluded that compressive stress improves the life cycle of the component and its overall performance. It was concluded that the most influencing factors were the feed rate, rake angle and tool nose radius; moreover, increasing the feed rate increases the compressive RS.

Takacs et al. [24] conducted experiments to see the effect of the cutting parameters of tool steel AISI D2; CBN tools and workpiece material hardness between 45 – 68 HRC and were analysed in their study. Their results were modelled in FEM for future process improvement. They found that passive force was the most dominant force component. Similar observations were also reported by Klocke et al. [25]. However, no correlation was found between the cutting speed and the cutting force. The FEM identified that cutting force increased with an increase in cutting speed.

The latest research also records the same behaviour on the residual stress, regardless of the material. Furthermore, this research topic is significant since the residual stress defines how the material will behave [26-29].

To determine the RS several techniques/methods can be applied. These measurement techniques are categorised as destructive, semi-destructive and non-destructive measurement. A selection of methods can be identified in their appropriate category in Table 2.2.

Table 2.2: Categorising residual stress measuring methods

Non-Destructive	Semi-Destructive	Destructive
X-Ray diffraction method	Hole-drilling method	Sectioning method
Electronic speckle pattern interferometry	Ring-core method	Contour method
Neutron diffraction method	Deep-hole method	Sach's boring
Ultrasonic method		
Barkhausen noise method		

Each technique has a different spatial resolution as well as a different penetration depth on the workpiece. A suitable measurement technique can then be selected based on this information and the advantages and disadvantages of each technique. Figure 2.3 [15] compares the selection of measurement techniques by spatial resolution and the penetration accessibility; the semi/destructive methods (grey) and the non-destructive methods (white) can then be compared comprehensively.

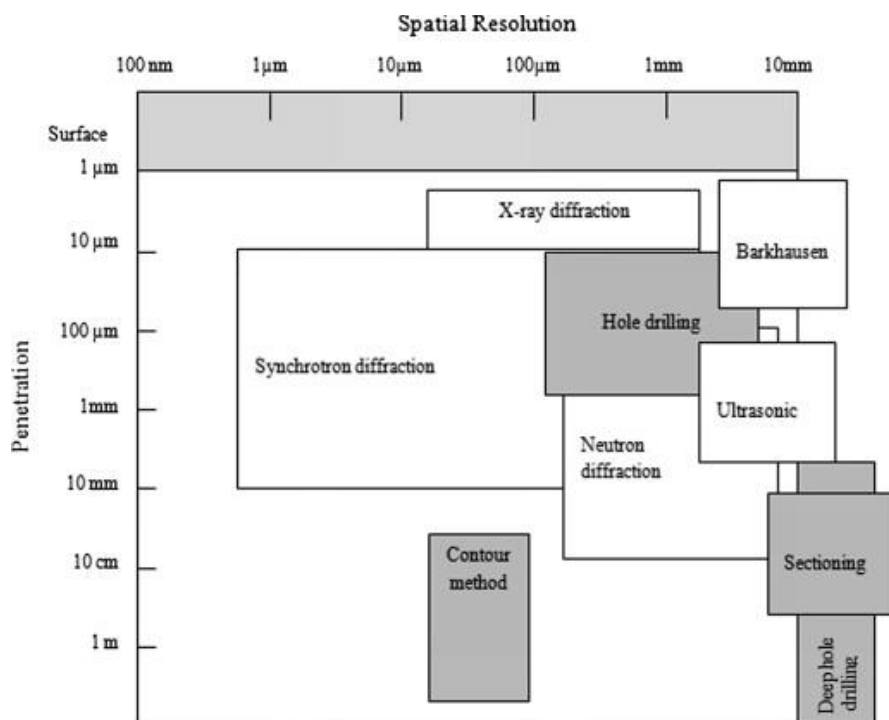


Figure 2.3: Comparison of RS measurement techniques by penetration & spatial resolution [15].

Based on the different methods and depths of penetration of the different methods, the XRD (X-Ray Diffraction) Method was selected for this work since this is a non-destructive method and workpieces can be analysed without influencing them. The XRD method explained in more detail below in chapter 2.2.1.1.

2.2.1.1 X-Ray Diffraction Method

The X-Ray Diffraction (XRD) technique is a non-destructive method to measure residual stress. This method measures the inter-planar atomic spacing which is caused by elastic strains of the atomic planes in the crystal structure of the observed metal [15, 17]. XRD-technology is based on the Bragg's law, as described in equation (2.1), whereby the change of distance on the wavelength and change of diffraction angle can be measured while using the interference effect.

$$n \lambda = 2 d \sin \theta \quad (2.1)$$

where λ represents the wavelength and n is the order of the X-Rays. θ is the angle of diffraction and d is the lattice spacing of the component.

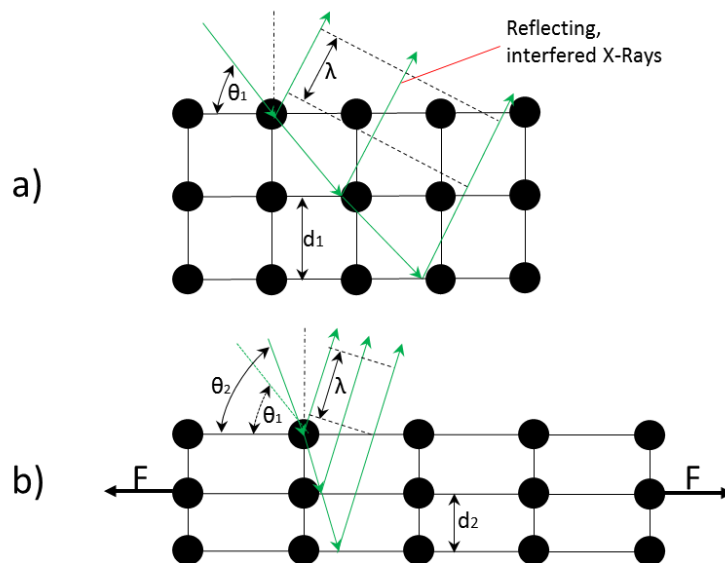


Figure 2.4: X-Ray diffraction at a single crystal lattice

Figure 2.4 shows the diffraction of the X-Rays on a single crystal lattice. Figure 2.4 a) shows an unstressed lattice with the diffraction angle θ_1 and a lattice plane spacing d_1 . The outgoing reflection angle of the X-Rays is characteristic for the specific material. This reflection results from the individual lattice structure in the crystal for this specific material. If the measured object is distorted - Figure 2.4 b) shows the diffraction angle θ_2 is significantly larger and the lattice plane spacing d_2 is smaller than normal – then the diffraction will be different from the unstressed material.

One disadvantages of this method is that the material must be discovered and recorded in a database for further analysis. This database contains structural information of the material. The XRD-System compares its measurement results with the database to calculate the residual stresses in the component. Furthermore, it is a Lab-based system which is only suitable for small components and supports only basic measurements (bigger machines are available but not feasible for most of the studies as they are placed in CERN for more fundamental research).

The advantages of the XRD include: reliability, accuracy, availability, a wide range of suitable materials, portability (it is a handheld system), and its ability to identify macro and micro residual stresses.

In the following Figure 2.5, a schematic setup for the XRD can be seen; this figure also shows *sin² ψ – Method* to analyse the stress and strain within an angle.

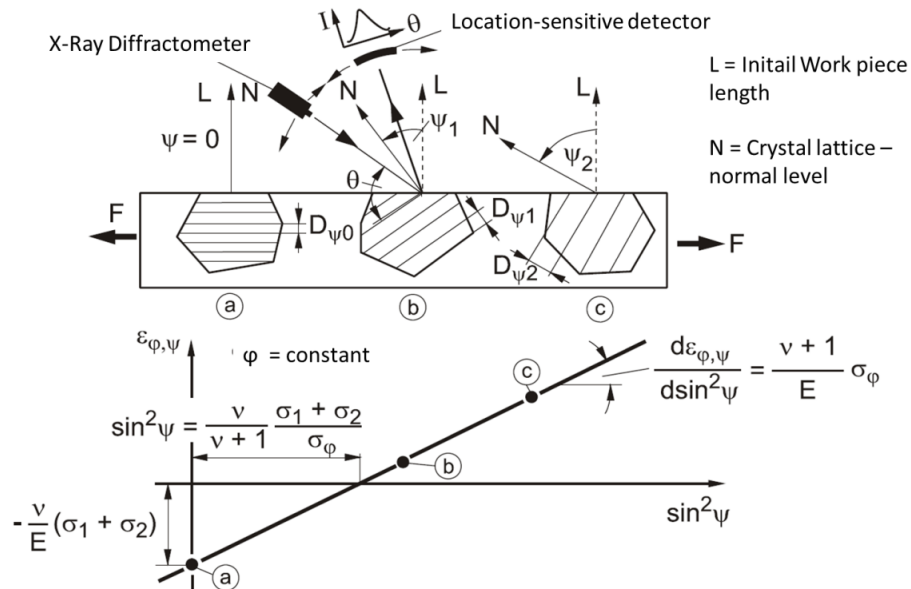


Figure 2.5: Schematic XRD setup and $\sin^2\psi$ analyse [30]

2.2.2 Micro- & Macrostructure

High thermo-mechanical stresses in the workpiece can lead to a change of the microstructure and therefore the mechanical properties of the workpiece. This change of structure can also lead to a build-up of a so-called “white layer”. The white layer can be observed under the SEM. This surface structural change is often characterised with a very high hardness but also high brittleness which can easily lead to failure of the workpiece performance and accuracy. The white layer has a major impact on surface integrity, and this research area is still being investigated [31-34].

In Figure 2.6 the white layer is shown in the work of Zhang et al. [35]. They investigated the effect of tool wear and lubricant on the white layer formation when machining AISI H13. Not only is the white layer clearly visible, it also varies in thickness, in this example from less than 10 μm and around 42 μm .

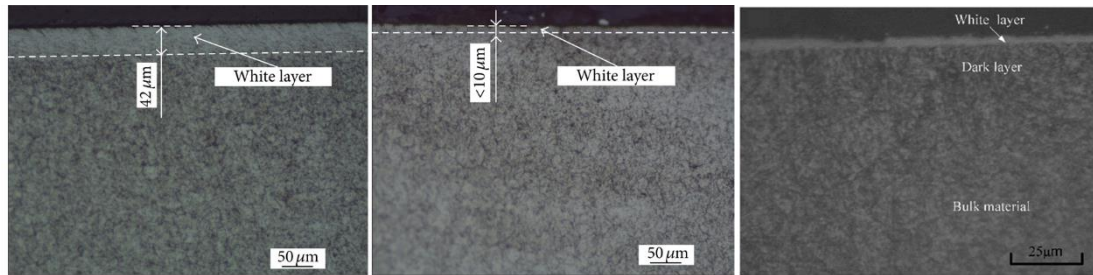


Figure 2.6: White layer formation under a microscope of AISI H13 [35, 36]

Further characteristics to qualify the microstructure are the microcracks, plastic deformation, phase transformation, pits/tears/laps/protrusions, melted and re-deposited layers, built-up edges and material altered layers such as the white layer. The microstructure is influenced by the heat induction during the machining process. This is connected with the phase-transformation, and the grain growth by strain, strain rate and temperature [33]. However, if the adiabatic heating is not significant enough to transform the material, only little/no change can be noticed in the bulk material, nevertheless the plastic deformation can be noticeable on the surface and bulk material.

The microstructure gives a further analysis of the functional behaviour as the material hardness is determined by the microstructure. Materials such as AISI H13 can contain a higher percentage of Martensite which increases the hardness but also the brittleness, and these can be identified through their larger grain formation in the microstructural analysis [37-39].

The macrostructure changes vary with feeds, speeds and step over. The macrostructure is also often referred to as the topology of the workpiece, and it can influence the functional performance [40, 41]. The macrostructure topology is often combined with the surface roughness.

2.2.3 Surface Roughness

Any manufactured workpiece will have marks on its surface from the material removal (or addition) process, and therefore the surface is not entirely flat. These irregularities are essentially microscopic peaks and valleys on the surface. In Figure 2.7, an example of a surface roughness profile is shown with its main components, surface roughness, waviness and form error.

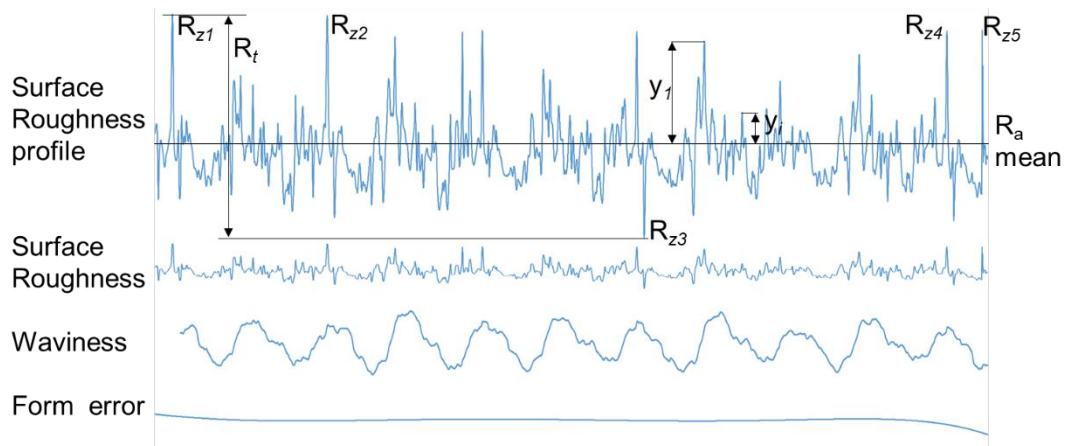


Figure 2.7: Components and parameter of surface roughness profile

The surface topology varies significantly by changing the cutting strategy. Usually, the topology can achieve very complex structures for machined parts. This complexity requires analysis of the effect of the surface by statistical functions and arithmetic parameters. Arithmetic measured parameters like R_a or R_q are used to describe the surface roughness in two dimensions. The parameter R_a is defined as the Arithmetic average roughness and can be calculated as shown in Equation (2.2):

$$R_a = \frac{1}{n} \sum_{i=1}^n |y_i| \quad (2.2)$$

where n is the total number of measurements and y is the measured distance from the mean of surface profile at position i . The Root Mean Square roughness (R_q) is also referred to as a general averaged roughness parameter

and is the root squared over the average surface roughness as expressed in Equation (2.3):

$$R_q = \sqrt{\frac{1}{n} \sum_{i=1}^n |y_i|} \quad (2.3)$$

Even though the surface roughness is often used in research and industry to understand the impact of parameters, the surface roughness factor is easy to obtain. However, surfaces can have significantly different topologies while having the same surface roughness parameter. Therefore, other surface roughness parameter such as R_t or R_z are often used to describe the surface roughness while taking the topology into account to a certain degree. R_t is defined as the Maximum peak-to-valley height and is expressed in Equation (2.4):

$$R_t = |y_{i_max} - y_{j_min}| \quad (2.4)$$

The Ten-Points height is shown as R_z and can be defined as follows in Equation (2.5):

$$R_z = \frac{1}{5} \left[\sum_{i=1}^5 y_{i_max} + \sum_{j=1}^5 |y_{j_min}| \right] \quad (2.5)$$

As previously discussed, the surface roughness R-series components are only 2-Dimensional measurements. However, newer technologies allow the measurement of 3-Dimensional surface roughness using primarily optical measurements. This has the advantage of covering one further dimension which allows it to describe the surface roughness further compared to the 2D measurement.

In the early 1990s [42] the first characterisations of 3-Dimensional surfaces were proposed. Later, the surface characterisation was refined and defined in an ISO Standard (ISO 25178), including the naming convention [43, 44]. The root mean square surface roughness (S_q) in the 3D-profile can be expressed as followed in equation (2.6):

$$S_q = \sqrt{\frac{1}{MN} \sum_{j=1}^N \sum_{i=1}^M [z(x_i, y_j)]^2} \quad (2.6)$$

The average surface roughness profile S_a can be described as follows in equation (2.7):

$$S_a = \frac{1}{MN} \sum_{j=1}^N \sum_{i=1}^M [z(x_i, y_j)] \quad (2.7)$$

Where M and N represent the sampling number in x and y -direction, respectively, furthermore, $z(x_i, y_j)$ is defined as the difference between the reference datum and original surface. The reference datum is defined by the least mean squares plane method [43].

Similar to 2D surface roughness, the ten-point height (S_z) can also be defined – see equation (2.8) below – wherein selection of the five highest and five lowest points of the measured surface are taken.

$$S_z = \frac{1}{5} \left[\sum_{i=1}^5 z_{pi_max} + \sum_{j=1}^5 |z_{vj_min}| \right] \quad (2.8)$$

A point to consider is the bearing area curve (BAC) or Abbott curve. The BAC is a cumulative probability of the profile heights and is directly related to the tribological behaviour of the workpiece and the real contact area which influences the wear on the workpiece [45]. However in this work, the BAC is

not being analysed, since the focus will be on the average (S_a) and ten-point height (S_z).

As indicated above, the different surface roughness parameters are aiming to characterise the surface in different ways. Therefore, the different characteristics also have a different impact on the function depending on the surface texture. See the following Table 2.3 [46], in which two asterisks denote a clear influence.

Table 2.3: Physical & functional significance of surface textures [46]

Functional properties	R_a, R_q	R_p	R_t, R_z	R_{sk}	R_{ku}	R_{sm}	R_{DelA}	W_a
<i>Contact / Contact stiffness</i>	*		**	*	*	**	*	*
<i>Fatigue strength</i>	*	*	**		*		**	
<i>Thermal conductivity</i>	*	**				**	*	*
<i>Electrical conductivity</i>	*					*	*	*
<i>Reflexivity</i>			**				**	
<i>Friction and Wear</i>	*		**	**	**	*	**	*
<i>Lubrication</i>	*	*	**	**	*		*	**
<i>Mechanical sealing</i>	*		**	**			**	**
<i>Fatigue corrosion</i>	*	*		*		*	*	
<i>Assembly tolerances</i>	*		**				*	**

The parameter convention in Table 2.3 is based on the ISO-Standard 13565-2:1997 and is described in Table 2.4 below.

Table 2.4: Description of the conventional parameter based on ISO 13565-2

Parameter	Description
R_a	Profile average height
R_t	Maximum profile height
R_q	The standard deviation of the profile height distribution
R_p	Maximum profile peak height
R_{DelA}	The average slope of the profile
R_{sk}	Skewness of the profile height distribution
R_{ku}	Kurtosis of the profile height distribution
R_{sm}	Mean spacing of the profile
R_z	The average maximum height of the profile
W_a	The average depth of waviness motifs

2.2.4 (Micro) Hardness

As described in section 2.2.2 the hardness of a material is strongly influenced by its Microstructure. In this section, a brief overview of the hardness calculation and its background is given.

Hardness is also included in the surface integrity as it is significant for the functional performance of a workpiece. In the last decade, researchers have regularly investigated the influence of this hardness in their research [20, 47-51].

The hardness measurement is standardised in all available standards of measurement, including but not limited to the ASTM, ISO, EN, DIN and BS. In this work the hardness will be measured based on the ASTM standard E384-16 [52].

Hardness can be measured using different methods such as Brinell, Vickers, Rockwell, Superficial, Knoop, Scleroscope, or Leeb Hardness. Each hardness value can be easily converted to other units based on the ASTM Standard E140- 12b [53]. In the following, Vickers and Rockwell hardness will be described in more detail since the following experiments will be measured in Vickers and converted to Rockwell Hardness.

Vickers Hardness (HV) is measured using a defined squared pyramidal shaped diamond to indent the surface. The face angle is defined at 136° , as shown in Figure 2.8.

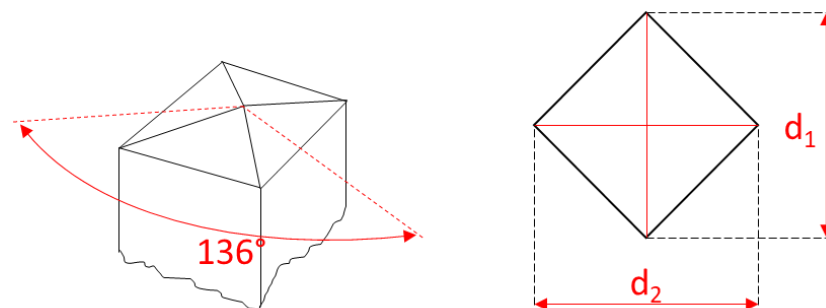


Figure 2.8: Vickers Indenter

The hardness can be calculated as shown in equation (2.9).

$$HV = 10^3 \cdot \frac{P}{A} = 2 \cdot 10^3 \cdot \frac{P \cdot \sin\left(\frac{\alpha}{2}\right)}{d^2} = 1854.4 \cdot \frac{P}{d^2} \quad (2.9)$$

Where P is the force in gf (gram force), the surface area A in μm^2 and the mean diagonal length of the indentation $d_{1,2}$ in μm (as indicated in Figure 2.8) and the face angle $\alpha = 136^\circ$.

The force P can also be changed to kgf (kilogram-force) or N and the diagonal length d to mm , whereby the formula changes as follows respectively in equation (2.10).

$$HV = 1.8544 \cdot \frac{P_{kgf}}{d_{mm}^2} \quad (2.10)$$

$$HV = 0.0018544 \cdot \frac{P_N}{d_{mm}^2}$$

It is widely accepted that the definition of microhardness refers to measurements below 1 kgf and loads above 1 kgf are defined as (macro) hardness [52, 54, 55].

Rockwell hardness type C [HRC] (for metallic components), is similar in principle to Vickers hardness. However, the indenter is a sphere-cone with an angle of 120° and a round peak of 0.2mm [56], as indicated in Figure 2.9. The challenge in using this method is the indentation time, as the dimension of the penetration changes over time and depends on the methods selected (selection of penetrator).

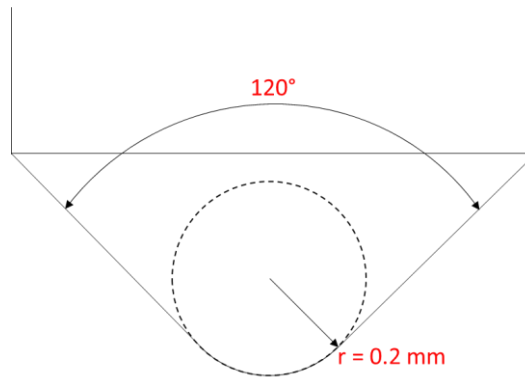


Figure 2.9: Cross-Section of Spheroconical Diamond

The conversion of Vickers Hardness and the Rockwell Hardness can be carried out by using tables or empirical formulas which are standardised by ASTM [53].

2.2.5 Summary

From the review of the previous studies on the surface integrity in precision machining, the main focus of recent research has been residual stress and surface roughness. This is to be expected since these components significantly influence the surface integrity and fatigue performance. The micro-/macrostructure of the components has also been partially investigated. However, in this work, the purpose of reviewing the microstructure is to investigate the white layer formation, but not to link the general microstructure to the fatigue life, in this work. As a result, more research is needed to investigate the influence of machining and fatigue performance throughout the complete standard data-set of surface integrity.

2.3 Fatigue Life

A good definition of fracture was given by González-Velázquez et al. [57] as follows: “*Fracture is the process of separation or fragmentation of a solid body under the action of loads or stresses, thus creating new surfaces, which are referred to as the ‘fractured surface’.*” Based on this, it can be concluded that two surfaces are always involved when analysing the fracture. Additionally, it can be stated that fractures occur from the direct action of loads or another kind of stresses (i.e. corrosion). During the fracture, three components are occurring at the same time.

- Stress state – the geometrical influence of the stress in the component
- The relationship between the microstructure and the fracture
- The interaction between the environment and the fracture [57]

Fatigue failure starts in a local stressed area in the material when inclusions, micro-cracks, impurities or crystal dislocations are present. When a cyclic or increasing load is applied and the local yield is exceeded, this leads to a gradual failure of the component with increased micro-pitting. The size of these micro pits can vary, but they are usually in the magnitude of order of microns to tens of microns [58]. The failure progresses in three different stages. It starts with the crack nucleation, develops through stress propagation, and ends with the final fracture of the component/material [57, 59].

2.3.1 Mechanical Fatigue

One of the most common causes to failure in hot forging and cold forging is fatigue. Fatigue can be categorised in various ways; however, often fatigue is categorised by its thermal state, as follows: (isothermal) mechanical fatigue, thermomechanical fatigue, thermal fatigue, tribological fatigue and creep-fatigue. According to Radaj and Vormwald [60], fatigue is defined to mean that material fatigue is the damage or failure of the material and the component under time-changing and often repeated stresses. Faults in the lattice structure

of the material favour the formation of cracks on notches and cross-sectional transitions, depending on the smaller or larger number of vibrations. The resulting cracks increase with each cycle until a final break occurs. Fine micro cracks in the forming and forging die increase the possibility that quality standards for the final product to be shaped will not be achieved.

The cycles presented in the results are based on a sinus curve where the stress cycles between its maximum (σ_{max}) and minimum (σ_{min}) using an amplitude (σ_a). The stress cycle principle is illustrated in Figure 2.10. The different relationships are defined [61] in equations (2.11) and (2.12). The subsequent equation (2.11) expresses the average stress applied to the component whereby the is stress amplitude is σ_a , and the mean stress σ_m , σ_{max} and σ_{min} are the maximum and minimum stress component respectively.

$$\begin{aligned}\sigma_a &= \frac{\Delta\sigma}{2} = \frac{\sigma_{max} - \sigma_{min}}{2} \\ \sigma_m &= \frac{\sigma_{max} + \sigma_{min}}{2} \\ \sigma_{max} &= \sigma_m + \sigma_a \\ \sigma_{min} &= \sigma_m - \sigma_a\end{aligned}\tag{2.11}$$

The stress ratio can be calculated as shown in equation (2.12):

$$R = \frac{\sigma_{min}}{\sigma_{max}}\tag{2.12}$$

The ratio gives a nominalised value to compare the stress cycle applied to the workpiece. Further conclusions from the ratio can be drawn [61, 62],

- If $R = 1$ the set-up is in a static loading;
- If $0 < R < 1$ the set-up is loading in tensile stress;
- If $R = 0$ the test rig is in a zero-to-tension fatigue loading
- If $-1 < R < 0$ the test rig partially in reversed fatigue loading
- If $R = -1$ the set-up is in a fully reversed fatigue set-up

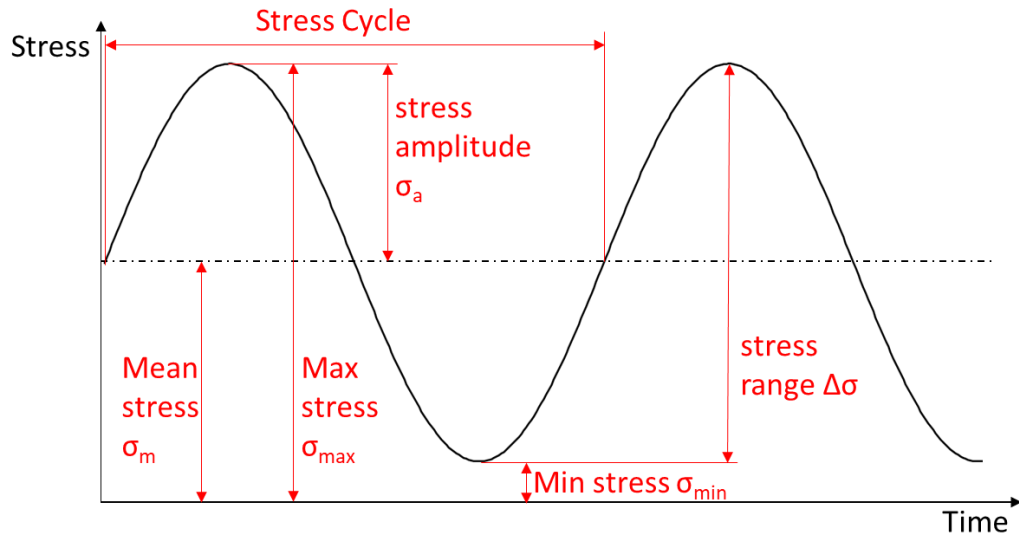


Figure 2.10: Stress Cycle of fatigue testing

In mechanical fatigue failure a distinction is made between long-term fatigue and short-term fatigue. The fatigue failure in the short-term fatigue range is often referred to as "low-cycle fatigue" (LCF). Fatigue in a high-load cycle is defined by stresses above the yield strength R_P and usually fractures in less than 10^4 cycles. High-cycle fatigue (HCF) differs from LCF in that the fatigue occurs at stresses below the yield strength R_P and usually fractures in more than 10^4 cycles [63].

The German standard association defined a standard (DIN 50100), and this denotes the fatigue resistance for steels with a minimum of 10×10^6 Cycles and light metals for more than 100×10^6 Cycles.

Low cycle fatigue is more crucial due to its short performance of the component. Therefore, this work will focus on the LCF range.

There are various ways to investigate how mechanical fatigue occurs in forming tools. One method uses a computational determination under given conditions which allows the development of a soft prediction model to determine the expected fatigue performance of a component. An additional method uses a numerical determination which combines the soft prediction method with a numerical simulation. In this case, the location, as well as the

magnitude of the occurring loads, can be calculated and the potential location of the fatigue propagation. Also, an approximation cycle can be given using a soft prediction model.

Nevertheless, physical determination needs to be carried out by using oscillation fatigue tests. These oscillatory tests can be transferred from general cases to the specific components, but it is desirable to carry out the analysis separately for the respective components [64]. Oscillation fatigue tests are standardised according to DIN 50100 or ASTM E466, C1161, E606, etc. The cyclic fatigue experiments are carried out according to the “Wöhler method” which measures the stresses applied to the workpiece and plots them against the number of fatigue cycles. These curves are also called S/N-Curves. The applied stress is a plot of the ratio to the number of oscillations as shown in Figure 2.11.

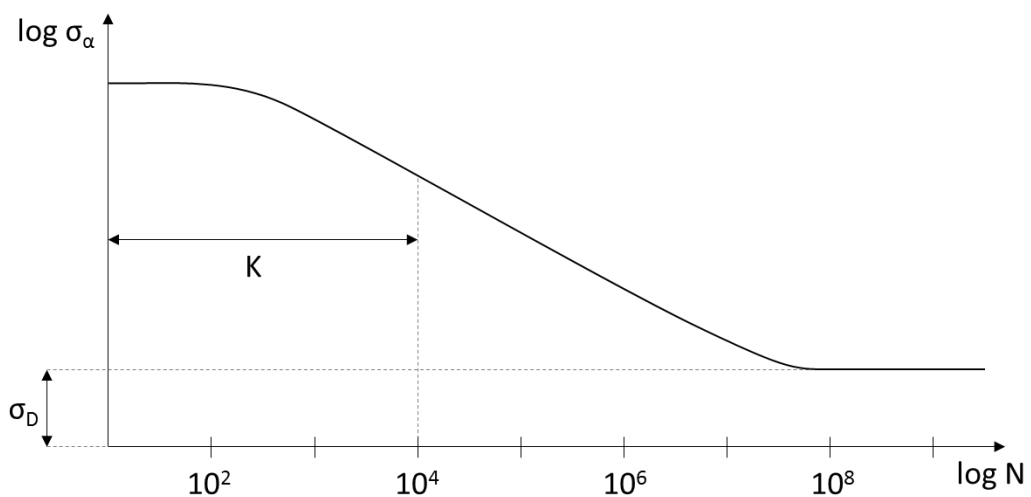


Figure 2.11: Wöhler curve / log-S-N Curve

As a result of applied stress during the cycles, the material strength decreases until the material fails. Figure 2.11 shows the low cycle fatigue (LCF) in the range of K . In order to simplify the graph, both axes are logarithmic, and the graph is presented as a double logarithmic function. On the abscissa, the number of oscillation amplitudes N is plotted logarithmically, and the logarithmic stress amplitude σ_a is mapped on the ordinate. The fatigue limit is

defined by σ_D , which indicates the lower stress limit to let the component perform “without” failing; this limit typically set for more than 10^7 cycles.

The relationship between stress and fatigue life is linked with the correlation of cycles, and this relationship can be described as follows in equation (2.13) [61, 62]:

$$\sigma_a = \sigma_f'(2N_f)^b \quad (2.13)$$

where σ_f' denotes fatigue strength coefficient, b fatigue strength component, and N_f the number of fatigue cycles.

When considering the strain on the component, the failure points can be mapped out using a stress-strain diagram. A characteristic of the hysteresis loop is developed from the results of the applied stress and resulting strain. This is, shown in Figure 2.12, where ϵ_{pl} describes the plastic strain and ϵ_{el} the elastic strain component. Figure 2.12 shows on the abscissa the strain ϵ and on the ordinate the stress σ . The plastic flow behaviour part of the strain amplitude ϵ_a is described through the total strain amplitude $\Delta\epsilon$, by $\Delta\epsilon/2$.

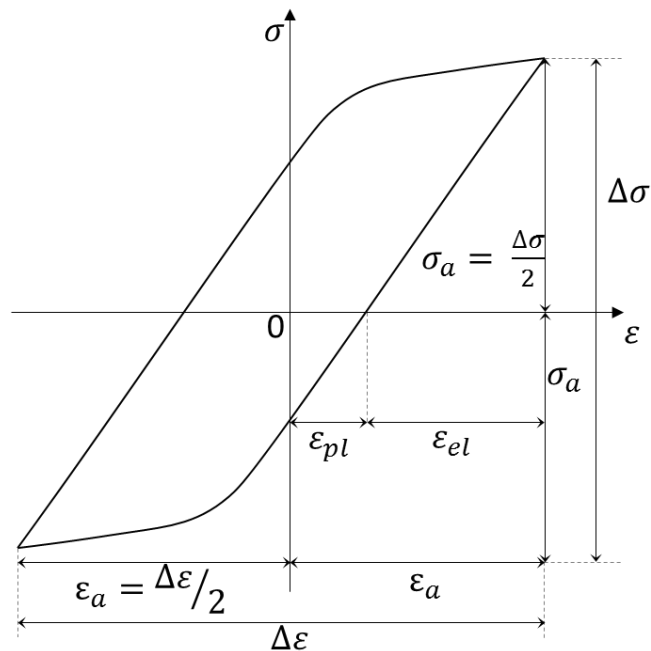


Figure 2.12: Stress-Strain hysteresis loop

For the calculation of the problem specific to this work, the Manson-Coffin relationship is used. This relationship is valid for the LCF range between $10 \leq N \leq 10^4$ cycles. The constant α , in this respect a material-specific exponent, assumes a value between 0.4 and 0.75 for steels, and aluminium alloys the value between 0.65 and 0.73 [64]. The Manson-Coffin relationship is described as follows in equation (2.14):

$$\varepsilon_a \cdot N^\alpha = C_1 \quad (2.14)$$

In this formula C_1 represents the material-specific constant of the elongation at break point, ε_a is the strain amplitude and N the number of cycles. This material-specific constant includes, among other things, the notch shape factor α_k which is explained below. The constant C_1 with the true strain ε_B at break can be described as follows in equation (2.15):

$$C_1 = \varepsilon_B / \alpha_k \quad (2.15)$$

In the case of forming tools, the notch effect due to a local increase in stress is of great importance for fatigue strength [60]. The notch shape number α_k is defined in equation (2.16):

$$\alpha_k = \alpha_{k \max} / \sigma_n \quad (2.16)$$

Where $\alpha_{k \max}$ is the maximum notch stress and σ_n the stress reference at that point. The notch stress is therefore dependent on geometry and material and can be enforced into a geometrically unfavourable shape; this involves a higher number on notch stress as the notch shape number increases the probability of micro-crack initiation and the risk of tool fatigue.

For the calculation of the number of cycles, equation (2.14) transforms to the number of cycles, and is shown in equation (2.17):

$$N = \left(C_1 / \varepsilon_a \right)^{\frac{1}{\alpha}} \quad (2.17)$$

Using this estimation before the tool is manufactured it can be determined whether it complies with the quantity requirements.

As previously mentioned before, among other things, hardness is also a factor that affects the life of a forming and forging die or component. Coatings, tempering and nitriding can sometimes influence the hardness.

Lange [65] showed that with increasing hardness the die wear decreases as long as the operating temperature remained under the tempering temperature of the die. It was also illustrated that when combined stress occurs a smaller hardness value may prove to be optimal. This suggests that a tool should not have a maximum hardness, but depending on the case, a specific hardness. Figure 2.13 shows this case, illustrated by Lange et al. [65]

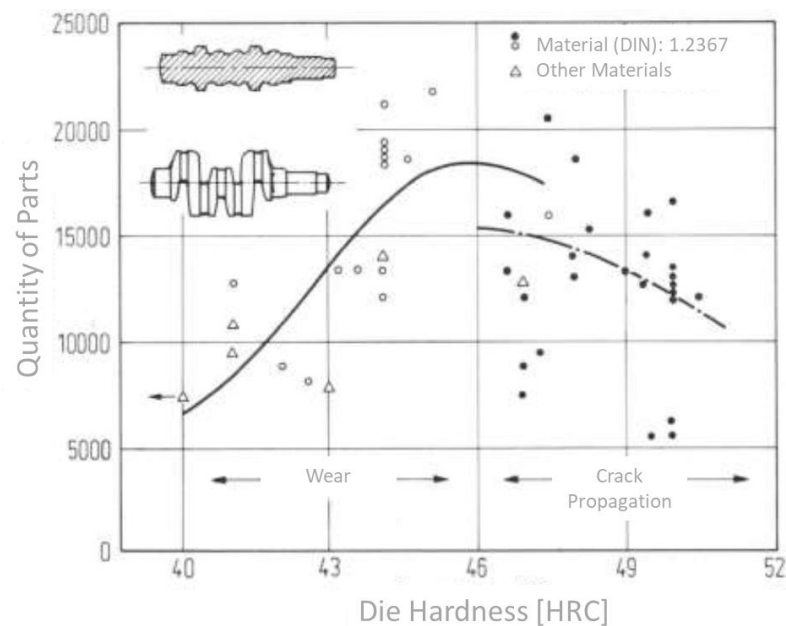


Figure 2.13: Influence of Hardness to the cycle performance [65]

Furthermore in this example using DIN 1.2367 (AISI H11), a lower hardness causes an increase in wear, which results in lower quantity of parts, but if the hardness is too high the component propagates more likely cracks, which would lead to failure. Therefore, an optimum in die hardness can be found for this example which is around 46 HRC.

2.3.1.1 Thermal Fatigue

In addition to mechanical influence on the tool failures, thermal influence must also be considered. It is different from mechanical fatigue but is frequently combined with it for the analytical purposes. The correlation between the thermal and mechanical effect are discussed in thermo-mechanical fatigue in section 2.3.1.2.

Thermal fatigue is considered for all changes of the real structure under any cyclic thermal loads. It is dependent on the predefined stress and properties of the material and, in most cases of failure, several thermal load changes are necessary until cracking or breakage occurs. [64]

In forging and forming, especially during hot forming, the die is affected by the thermal variations during the forming process. The temperature difference between the dies and the workpiece plays a decisive role. Contact time is therefore another critical predictor component for thermal fatigue. The established baseline temperature in the die expresses the temperature compensation of the energy introduced in each cycle and the cooling between the cycles. [66]

Thermal stresses occur due to the inhomogeneous temperature distribution. The value of these stresses can be calculated as a function of the temperature change, the coefficient of thermal expansion, Young's modulus, yield stress, geometrical parameters and the degree of deformation hindrance [60]. Changing temperature stresses can ultimately lead to thermal fatigue.

Therefore, the thermal cycle range can also be subdivided into the LCF and HCF.

A stress-strain relationship in the thermal range can also be mapped using the hysteresis loop. Using the Coffin-Manson relationship a steady state estimate can be calculated on a thermal basis.

The rate of solely thermal cracking (no mechanical influence) for of the all major types of hot forging tools is 2 %, which is the lowest percentage compared to wear (70%), mechanical cracking (25%) and plastic deformation (3%) [66, 67].

2.3.1.2 Thermomechanical Fatigue

The third major component of fatigue failure is composed of mechanical and thermal fatigue. The expiration of the multiple forming cycles and the change in operating point results in a thermally induced stress-strain cycle, which can lead to failure of the component. This is referred to as Thermo-Mechanical Fatigue (TMF). Due to a disadvantageous combination of local temperatures and local expansion inhibition, the location of the highest temperature does not necessarily lead to the failure of the tool [68]. The existing stresses and the strains are composed of the thermal stress/strain and the mechanical stress/strain, and result in the following equations (2.18) & (2.19):

$$\varepsilon_{total} = \varepsilon_{a,t}^{mech} + \varepsilon_{a,t}^{therm} \quad (2.18)$$

$$\sigma_{total} = \sigma^{mech} + \sigma^{therm} \quad (2.19)$$

Equation (2.18) gives the total strain with ε_{total} and Equation (2.19) the total stress with σ_{total} . From the article by Luig and Bobke [66] it can be seen that the thermal and mechanical stresses compensate each other to a certain extent, as illustrated in Figure 2.14.

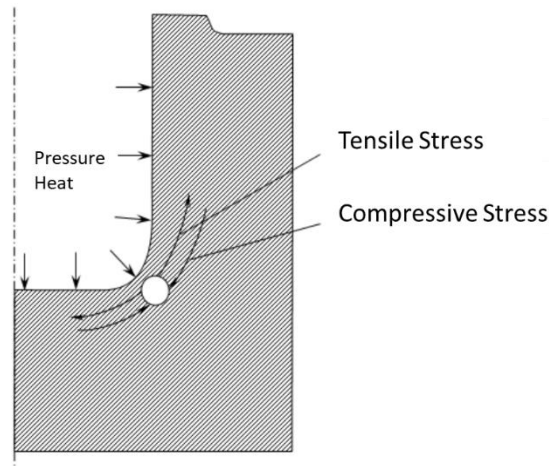


Figure 2.14: Thermo-mechanical loads in forging and forming die

The tensile stress arises from thermal expansion (volume increase) and the compressive stress at the applied bending moment. This can be described by Norton Law, using the factor K_{MT} as the relationship of these components [69]

$$K_{MT} = \frac{\varepsilon_{a,t}^{mech}}{\varepsilon_{a,t}^{therm}} \quad (2.20)$$

The mechanical strain at location "a" at time "t" is described by $\varepsilon_{a,t}^{mech}$, the thermal strain is adequately represented by $\varepsilon_{a,t}^{therm}$.

As explained above, the stresses can counteract, and therefore it must be divided into two different types of phases. If the mechanical stress runs in antiphase to the thermal load it is called "Out of Phase" (OP). If it runs in phase, it is called "in-phase" (IP). For example, this situation can occur when external forces impact compressor blades within gas turbines. During such TMF cycles, elastic-viscoplastic deformation, ageing and fatigue cracking, and propagation all interact in a complex manner [70].

2.3.2 Summary

From the review of fatigue life behaviour it was found that substantial work on the prediction as well as on the descriptions of all high and low cycle and thermal and thermo-mechanical cycles have been undertaken. However, it became evident that the thermo-mechanical cycle is the most challenging for the material and component. Furthermore, it was found that most research conducted is focused on high cycle fatigue as it is assumed that the part and material does not reach closely the yield point. A combination of these two categories still needs to be investigated further.

2.4 Influence of Machining Process on Surface Integrity & Fatigue Life

As mentioned in previous sections, surface integrity is a crucial part of the fatigue life of a component. The machining process used determines the surface integrity achieved. Depending on the choice of machining process variables, the surface roughness, residual stress, hardness and microstructure can be significantly influenced by the manufacturing process [32, 33, 71-75]. However, there is no direct link between the machining process and fatigue life. The fatigue life is influenced by the surface integrity and material [20].

2.4.1 Influence Machining Process on Surface Integrity

Machining is a material removal process and can be divided into several subcategories including milling, drilling, turning and grinding (according to DIN 8589-0 [76]). Milling (DIN 8589-3 [77]) enables a broad variety of different geometries to be manufactured, where CNC machines cut vertical, horizontal, inclined and other complex surface geometries [78]. Nowadays, multi-axis machines have often five to seven axes which allow to machine complex parts with advanced surfaces. These processes are often multi-cutting-edge

processes, whereby each cutting edge engages with new material to be removed and form a specific chip formation. Section 2.4.1.1 discusses in more detail the cutting tool for milling.

Depending on the machine configuration (multi-axial), the spindle and table have a relative movement contrary to each other to remove the material from the workpiece.

Milling has the following advantages:

- + Compatibility, milling can be used for a vast range of materials
- + Flexibility, a large variety of complex part geometry are achievable
- + Variety of modern milling machines can hold up to several hundreds of different milling tools to reduce tool changing time
- + Reduced lead times, with flexibility and variety of tools
- + The machining process with Computer Numerical Control (CNC) has a short process and tool changing time.

However, the milling process suffers from several disadvantages. These are:

- Control surface integrity of the machined component is challenging, and conditional on process parameter.
- Tool wear – the cutting tool can show signs of abrasion and wear after a short time, especially if the material is difficult-to-machine (i.e. die material, super alloys, etc.).
- Inaccuracy – the vibration of the machine often causes inaccuracy on the final part.
- Distortion – in some current applications high accuracy is demanded which causes stress relaxation of the workpiece.

Milling has a broad variety of subsections such as end-milling, face-milling, circular-milling, and form-milling. Each milling processes has its own application as well as its strength and weakness. Avallone et al. [79] gave recommendations based on the selection of workpiece material for tool material, feed per tooth and cutting speed.

Current research is still investigating the relationship between machining/manufacturing process and its resulting surface integrity. Many works in this in this area of research have been published recently, i.e. [23, 45, 80-82].

2.4.1.1 Influence of Tool Geometry and Forces

The cutting tool is one of the most critical parts of the manufacturing process, as it influences the chip formation, heat induction and surface integrity.

A three-dimensional force component must be applied to calculate the cutting force on a ball-nose end mill cutter. Lee and Altintas [83] developed a force prediction model for a ball-nose finishing process. Figure 2.15 shows the geometry cutting force geometries. The elemental radial and axial cutting forces are indicated by df_r and df_a , respectively.

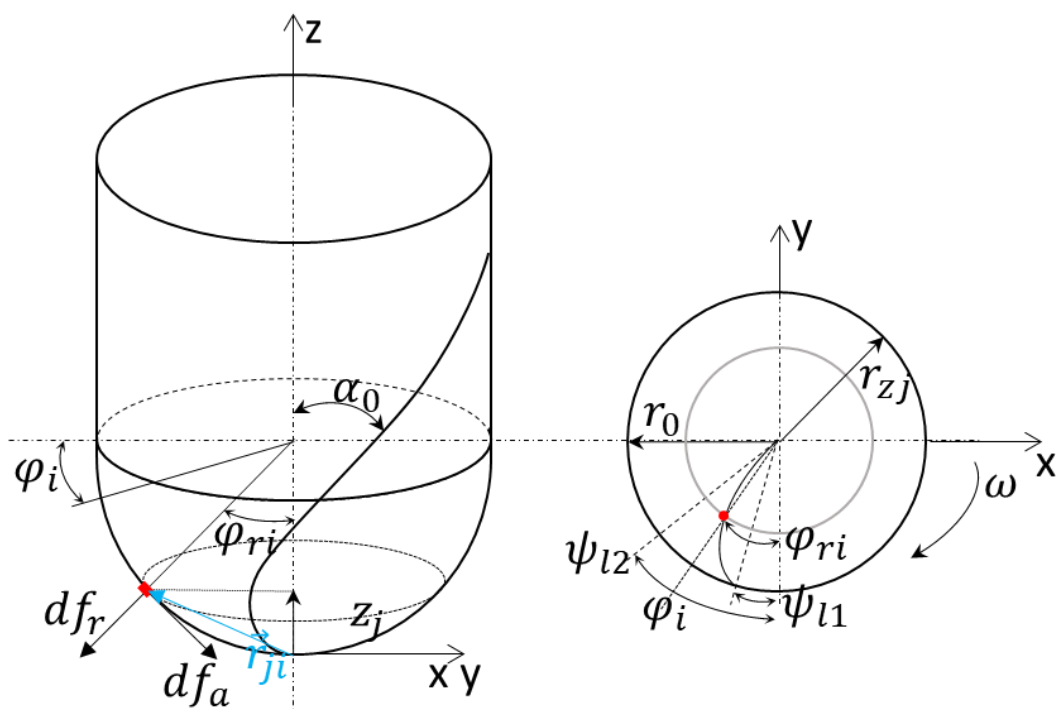


Figure 2.15: Geometry and tool coordinates for a ball end mill cutter

Firstly, the effective radius from the cutter will be calculated, where the geometrical locations of x, y and z of the effective radius can be expressed as follows:

$$\begin{aligned}x_{ji} &= r_z \sin(\varphi_{ri}) \\y_{ji} &= r_z \cos(\varphi_{ri}) \\z_{ji} &= \frac{r_0 \Psi_{l1}}{\tan(\omega)}\end{aligned}\tag{2.21}$$

Where, j is the position of the discrete element on cutting edge i . The discrete elements are placed around the tool radius with the angles φ_{ri} and α_0 , which provide the position of the cutting-edge element as a function of the rotation of the tool. The position angles (φ_i and φ_{ri}) of the flute i can be calculated as follows:

$$\varphi_{ri} = \frac{\varphi_{r1} + \varphi_{r2}}{2}\tag{2.22}$$

$$\varphi_i = \frac{\omega \cdot \pi \cdot t}{30} - \frac{\psi_{l1} + \psi_{l2}}{2} - (i - 1) \cdot \left(\frac{2\pi}{i_z}\right) - 2\pi(\omega_1 - 1)\tag{2.23}$$

The starting and final positioning angles in the reference plane φ_{r1} and φ_{r2} are measured in radians, as are the initial and final lag angles ψ_{l1} and ψ_{l2} , respectively. The rotational speed (ω) is defined as the unit revolution per minute, ω_1 expresses in equation (2.23) the number of tool rotations and time t in seconds. The number of flutes was expressed by i_z . [84]

Equations (2.21) show the coordinates of the cutting edge, which can be transformed to a vector of the cutting position of the discrete element j on cutting edge i . The transformed vector is shown in equation (2.24) [85].

$$\vec{r}_{ji} = x_{ji}\vec{i} + y_{ji}\vec{j} + z_{ji}\vec{k}\tag{2.24}$$

where $\vec{i}, \vec{j}, \vec{k}$ are describing vectors in a cylindrical coordinate system, to define the position of the discrete element of each cutting edge. Substituting the parameters from equation (2.21) into equation (2.24), the following statement can be drawn and be expressed as the following equation (2.25):

$$\vec{r}_{ji}(\varphi_{ri}) = r_{zi} \sin(\varphi_{ri}) \vec{i} + r_{zi} \cos(\varphi_{ri}) \vec{j} + z \vec{k} \quad (2.25)$$

where r_{ji} differentiates with respect to z and take the modulus of a differential edge length of cutting.

Based on the model shown in Figure 2.15, the cutting forces can be calculated, and expressed by [83, 84]. The cutting force in the X, Y, Z-direction is F_x , F_y and F_z , respectively.

$$F_x = \sum_{i=1}^N F_{Ti} \cdot \sin \varphi_i - F_{Ri} \cdot \sin \varphi_{ri} \cdot \cos \varphi_i - F_{Ai} \cdot \cos \varphi_{ri} \cdot \cos \varphi_i \quad (2.26)$$

$$F_y = \sum_{i=1}^N -F_{Ti} \cdot \cos \varphi_i - F_{Ri} \cdot \sin \varphi_{ri} \cdot \sin \varphi_i - F_{Ai} \cdot \cos \varphi_{ri} \cdot \sin \varphi_i \quad (2.27)$$

$$F_z = \sum_{i=1}^N F_{Ri} \cdot \cos \varphi_{ri} - F_{Ai} \cdot \sin \varphi_{ri} \quad (2.28)$$

The cutting forces in X and Y direction contain a tangential force component at the flute i (F_{Ti}), a radial force component at flute i (F_{Ri}) and an axial force component at flute i (F_{Ai}). The cutting force in z-direction only contains the radial and axial force component.

A simplified method to calculate the effective radius on the tool is shown in Figure 2.16 and equation (2.30).

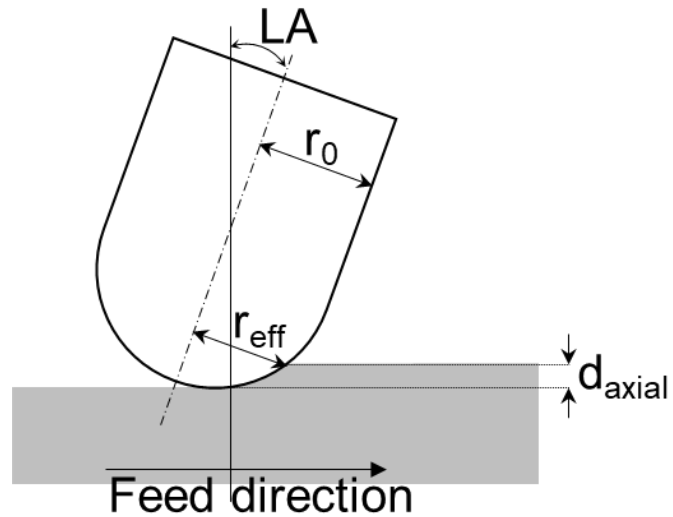


Figure 2.16: Effective tool radius

$$r_{eff} = r_0 \cdot \sin \left(LA + \arccos \left(\frac{r_0 - d_{axial}}{r_0} \right) \right) \quad (2.29)$$

Where the nominal tool radius is r_0 [mm], the Lead Angle LA [deg] and d_{axial} the (axial) depth of cut [mm], the effective radius determines (r_{eff}) the actual engaging radius of the cutter during the machining process.

The cutting tool is defined by the tool material. Choosing the right cutting tool material is essential. Next to its dimensions (size and shape), the mechanical properties such as high hardness and toughness and additionally good thermal shock resistance are critical parameters [86]. There is a variety of machining tool materials. Figure 2.17 shows a selection of tool material which is used for machining.

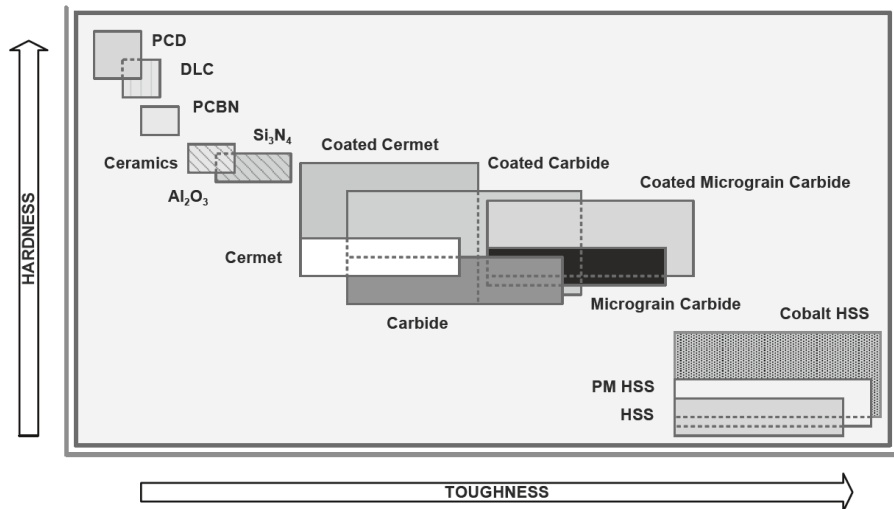


Figure 2.17: Selection of cutting tool material for machining purpose [21]

Figure 2.17 lists the materials regarding toughness and hardness. The graph shows that an increase of toughness usually causes a decrease in hardness. Very hard materials such as PCD (Polycrystalline Diamonds) are brittle; whereas HSS (High-Speed Steel) is very tough (ductile) but not as hard as diamond. Currently, an ideal tool material does not exist; if it did it would sit in the top-right corner of Figure 2.17 with high toughness and high hardness.

The most common machining tool material is PCBN (Polycrystalline Cubic Boron Nitride) or CBN (Cubic Boron Nitride). PCBN / CBN is known as the second hardest material in the world after diamond. PCBN is a sintered product with a metallic binder and tungsten carbide substrate. Using PCBN as a cutting material, high cutting speeds, high feed rates and extended tool life can be achieved. Productivity is increased by up to 4 times compared to grinding. Additionally, abrasion is up to 10 times less when compared to carbides. PCBN is also very commonly used in industry for machining hard materials. [21]

Suresh et al. [87] concluded in their state of the art report that selecting a suitable material for hard machining is one of the major challenges as it influences the tool life and the precision of the machining process. Furthermore, it was concluded that it is especially hard machining a negative rake angle, lower feed rate and cutting depth and still have a positive impact on the tool as well as the surface integrity of the workpiece. Additionally, it was

concluded that new cutting tools apply more residual stresses below the surface of the workpiece, whereby tensile stresses and the formation of the white layer are caused by worn tools. Often Tungsten carbide is used for hard machining processes required by lower tool costs.

The manufacturers of cutting inserts and cutters are currently developing their own mixture of coatings which are often based on the materials mentioned above. However, as this is a relatively new area of development it falls outside the scope of this paper.

2.4.1.2 Machining of Hard Materials

Newly developed products require a functional and good surface finish. Achieving these conditions for a hard material requires an adjusted machine set-up with defined process parameters for the hard material.

A widely accepted hard machining (HM) process is when the machined part has a hardness above 45 HRC. Often these materials are superalloys, tool steels or nitride irons (FeN) [88]. The characterisation of a hard machining process is cutting tools, usually made from a hard material such as tungsten or PCBN as discussed in the previous section 2.4.1.1. Characteristically for hard machining, high cutting speed and high spindle speed are used.

The chip formation when milling hard material varies with the cutting speed. Recent research has shown that for tool steel AISI H13, a cutting speed between 1,000 and 1,400 m/min for face milling is optimal to achieve a good surface finish and chip condition [72]. Furthermore, it was found that surpassing the cutting speed of 1,400 m/min, shortens the chips and the colour turns yellow.

In end-milling processes, the cutting parameter varies depending on tool material, tool diameter, the number of flutes and the lead angle. Therefore, the literature suggests different cutting parameters to achieve various results [27, 28, 48, 88-92].

The benefits of hard machining are the high flexibility and capability to manufacture complex geometries. Hard machining is often compared with grinding as a surface finishing process implemented in the process chain – both technologies have their own strength and capability [93-95].

In Byrne [86] it was shown that residual stress is mostly influenced by friction between the workpiece and tooltip. The wear on the cutting tool causes an increase in temperature during the cutting process. Tool wear increases the thermal influence of hard machining and causes tensile residual stress and the appearance of the white layer on the surface.

2.4.2 Influence of Surface Integrity on Fatigue Life

As mentioned in previous sections, surface integrity has a significant influence on fatigue life, and in this chapter the influence of the different components of surface integrity are discussed. Surface integrity (SI) has been studied since it was first considered in 1964, and with increased attention it has become more significant over time since SI influences the workpiece functions such as fatigue performance, accuracy and wear resistance. [20]. Different research has established different aspects / focus on fatigue life influenced by SI since all components of SI are interacting.

Firstly, residual stress should be considered and its influence on the performance. Studies have found that residual stress has a significant influence on fatigue performance. Generally, it was found that tensile residual stress has a fatigue performance life-shortening effect on the component. However, compressive stress on the surface and subsurface can prolong the fatigue performance of the component. [7, 20, 48, 96]

Secondly, surface roughness must be considered. Research has shown that with an increased surface roughness the fatigue performance of the workpiece decreases. There are multiple reasons for this because with an increased surface roughness the irregularity of the profile also increases, which can lead

to an increased probability of surface defects, which in turn will develop micro cracks and lead ultimately to the failure of the component. In a different application the increased surface roughness generates a greater friction factor with other components. Increased friction leads to increased forces and heat induction, which will cause an increased possibility of damaging the surface and therefore ultimately leading to a failure of the workpiece. [18, 47, 48, 97, 98]

In addition to residual stress and surface roughness, the fatigue performance is also influenced by the hardness and microstructure. The hardness often does not have a significant influence on the high cycle fatigue performance as Eichlseder et al. stated [99]. However, the hardness becomes more critical when conducting low cycle experiments [100]. It also has to be acknowledged that the (static) fatigue strength (not cycle fatigue) of a component increases with increasing hardness [101]. Similarly, it was found that as far as the microstructure and topography of the components go, it is not been reported that the microstructure has an influence on the fatigue performance.

2.4.3 Summary

It became evident in this chapter that significant work has been carried out on high cycle fatigue. However, little research has been carried out on low cycle fatigue under the influence of surface integrity. Furthermore, no work was found where the behaviour on the fatigue life of the components were studied under an elevated temperature. Nevertheless, tool geometry and the associated result of cutting forces during the cutting process have been well researched.

2.5 Prediction Models

Over the last twenty years research has helped greatly improved prediction models, resulting in better predict outcomes for adjusting parameters. Models have become more comprehensive and complex than they were a few decades ago. A significant contribution has also been made by the increased performance of computing which enables us to calculate complex algorithms in a faster timeframe.

In this chapter, an overview of the soft prediction model of surface integrity is presented. This is followed by a numerical prediction model in finite element modelling and as well as soft prediction modelling.

2.5.1 Descriptive Surface Integrity and Fatigue Life Model

Surface integrity (SI) has gained more significance in the few last years as SI can be directly linked to a workpiece performance. The surface integrity can be defined by several parameters as described in chapter 2.2. These parameters can be measured by technologies such as SEM, 2D/3D surface measurements, etc.

As discussed in Section 2.2, the surface roughness has a major influence on functional performance as the roughness can induce crack initiation points. The Micro- and Macro-structure of the surface and subsurface shows the effect of machining, as the parts grain size changes and indicates possible deformation or phase transformations (incl. white layer). The hardness gives an indication of the robustness of a part when the surface and subsurface are measured. Different hardness will influence ductility and wear resistance. Furthermore, the micro-hardness will give a complete evaluation of surface integrity. Residual stress (RS) has a significant influence on the fatigue performance on high-cycle fatigue as the surface and subsurface can consist of tensile or compressive (more favourable) stresses. The results of these factors form a descriptive surface integrity model, as shown in Figure 2.18.

The descriptive model is needed to develop prediction models as results from each element of the surface integrity will contribute to the development of an optimum outcome in the prediction model. The elements of the surface integrity model and their calculation were discussed in section 2.2.

The fatigue performance model is measured by its cycles as described in section 2.3. The degradation of the component caused by cycles can also be explained by a hysteresis loop. This work focusses on the overall cycle performance in a workpiece.

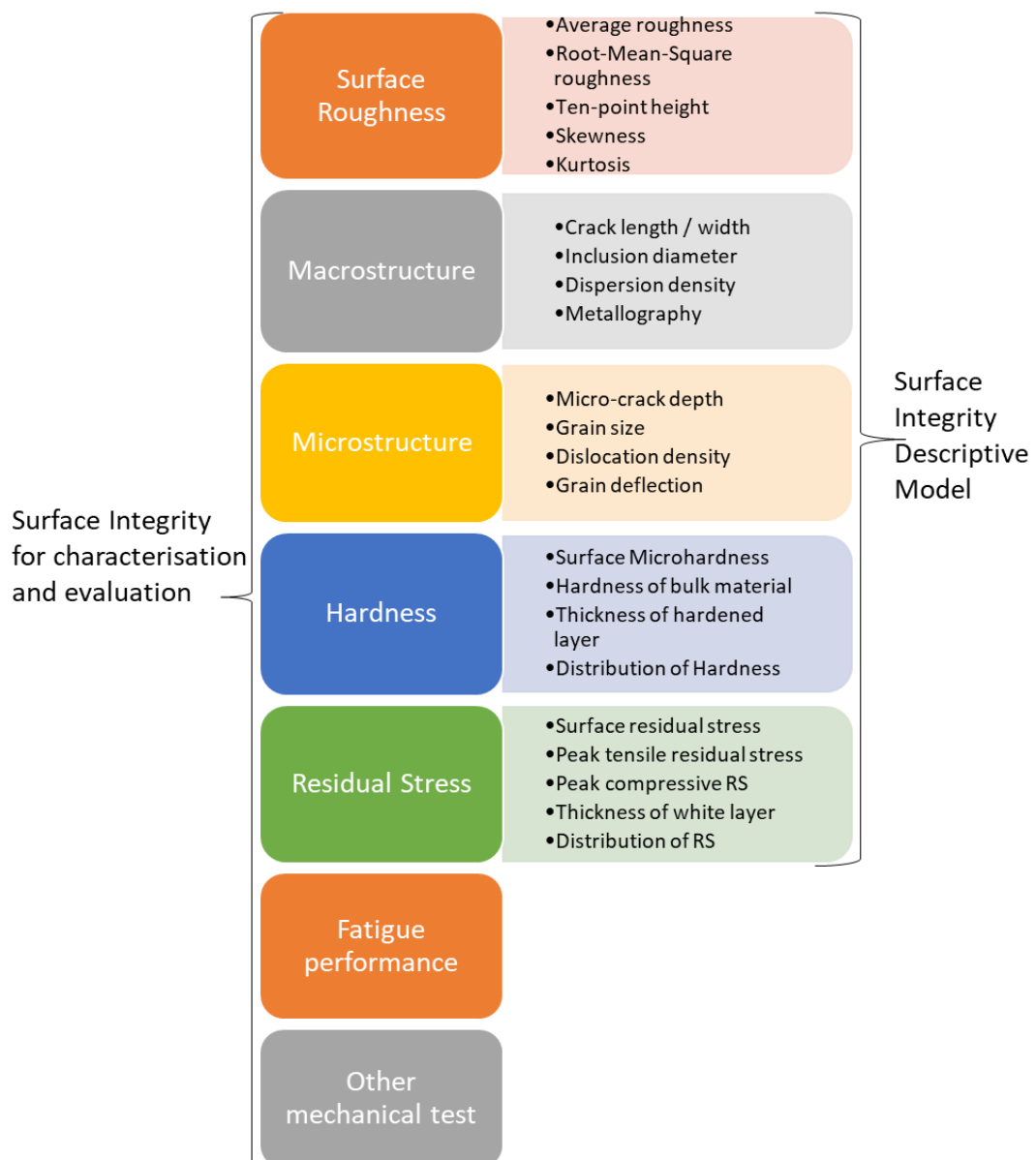


Figure 2.18: Descriptive Surface Integrity Model

2.5.2 Finite Element Modelling

Finite Element Modelling (FEM, also referred to Finite Element Method), is one of the most established methods for numerical simulations. The interpretation of results and validation of the FE-Model is called Finite Element Analysis (FEA). Clough [102] first coined the term “FEM” in 1960 and linked it with the visualisation of a model as a continuum of a portion (finite elements). The Finite Element Model aims to transform the descriptive differential equation problem into a linear equation system [103]. Nowadays the computing power and calculation method have been vastly improved compared to decades ago. It is now possible to simulate very complex problems. The FEM allows engineers to simulate any industrial processes resulting in time and cost savings by eliminating nearly every physical trial and error process. FE modelling has been applied and studied for a large variety of processes and used for research in processes such as forging, forming, machining and heat treatments. [82, 92, 104-108].

This numerical simulation finds application in a broad range of stages in the manufacturing process. It can be used to characterise different parameters such as heat exchange, friction, material removal, chip formation, stresses and the degree of deformation. These parameters can be provided through input in the boundary conditions to the FEM. The simulation accuracy increases as more precise boundary conditions are provided, such as stress, strain, temperature and damage evolution.

In order to model the stress and strain in the simulation, the equations of Johnson-Cook in ABAQUS are used by implementing a subroutine. This equation is usually used for dynamic problems with high strain rates and temperature effects [109]. The Johnson-Cook approach achieves a good macroscopic material description compared to the standard stress-strain descriptive model as these values are usually obtained with low strain rates. However, to represent a more precise material behaviour at the microscopic level this equation needs expanding using additional parameters. The material model used will be discussed in the following section 2.5.2.1.

2.5.2.1 Material Model of FEA

The flow stress $\bar{\sigma}$ can be combined by the Von-Mises yield criterion and describes an isotropic hardening developed by Johnson & Cook [110] as follows:

$$\bar{\sigma}(\bar{\varepsilon}, \dot{\bar{\varepsilon}}, T) = (A + B(\bar{\varepsilon})^n) \cdot \left(1 + C \ln \frac{\dot{\bar{\varepsilon}}}{\dot{\bar{\varepsilon}}_0}\right) \cdot \left[1 - \left(\frac{T - T_0}{T_m - T_0}\right)^m\right] \quad (2.30)$$

where $\bar{\varepsilon}$ is the proportional strain, $\dot{\bar{\varepsilon}}$ is the proportional strain rate, and T is the temperature. A , B , C , m , n , T_0 , T_m are material parameters in the Johnson-Cook equation, $\dot{\bar{\varepsilon}}_0$ is the reference strain rate and ε the current strain; these parameters can be found in [51, 78, 109-113]. One method to obtain parameters is to conduct the Split-Hopkinson-Pressure-Bar experiment. However, in this work this experiment cannot be conducted and therefore those parameters will be mainly taken from sufficient literature [51, 109-115].

The material behaviour varies with the hardness and therefore the hardness will be considered and applied to the flow stress model as follows in equation (2.31):

$$\bar{\sigma}(\bar{\varepsilon}, \dot{\bar{\varepsilon}}, T, HRC = const) = f\left(\bar{\sigma}_f(\bar{\varepsilon}, \dot{\bar{\varepsilon}}, T), \Delta\sigma_H(HRC = const)\right) \quad (2.31)$$

where the hardness is expressed as HRC in the unit of Rockwell type C, $\bar{\sigma}_f$ represents the reference flow stress and $\Delta\sigma_H(HRC = constant)$ an additional influence of the initial hardness of the workpiece [111].

This hardness influencing model can be described as followed in equation (2.32):

$$\Delta\sigma_H(HRC = const) = D \ln(\varepsilon_0 + \varepsilon) + E \quad (2.32)$$

Equation (2.33) results from equation (2.30) and (2.32) where the workpiece hardness is taken into account:

$$\bar{\sigma}(\bar{\varepsilon}, \dot{\bar{\varepsilon}}, T) = (A + B(\bar{\varepsilon})^n + D \ln(\varepsilon_0 + \varepsilon) + E) \cdot \left(1 + C \ln \frac{\dot{\bar{\varepsilon}}}{\dot{\bar{\varepsilon}}_0}\right) \cdot \left[1 - \left(\frac{T - T_0}{T_m - T_0}\right)^m\right] \quad (2.33)$$

The parameters D and E can be defined through a 2nd and 3rd-grade polynomial regression, respectively. The first step for this is to counterpart the hardness, flow stress and tensile strength. After nominating a reference hardness, the variety of the different forces (in MPa) can be listed in a table under consideration of different hardness; a regression function can then be determined. This newly determined function can be used to determine parameters in relation to the hardness. In the following sections of this work, the extended model of equation (2.33) is referred to as the Johnson-Cook model.

The “damage behaviour and evolution model” can also be described in Abaqus, which is a critical component for machining simulations. The damage model will influence chip formation, heat induction, forces etc. Abaqus has a variety of pre-implemented damage models. For this work the Johnson-Cook Damage model [110] was used as it has been proven to deliver acceptable results [116]. The Johnson-Cook Damage model is stated in equation (2.34):

$$\varepsilon^f = \left[D_1 + D_2 \exp D_3 \left(\frac{\sigma_m}{\bar{\sigma}}\right)\right] \left[1 + D_4 \ln \frac{\dot{\bar{\varepsilon}}}{\dot{\bar{\varepsilon}}_0}\right] \left[1 + D_5 \left(\frac{T - T_0}{T_m - T_0}\right)\right] \quad (2.34)$$

where, ε^f states the strain equivalent to the fracture, $D_1 \dots D_5$ are the failure parameters and σ_m as the average of three normal stress. The formula was developed using three parts (indicated by the square brackets). The first included the principle from Hancock and Mackenzie [117], the second the influence of the fracture by strain and the third by the influence of temperature.

Márton et al. [118] analysed tool steel AISI H13 in a machining FEM with varying feed rate and cutting speed. The focus of that research was to compare the cutting forces in the experiment along with FEM. The finding was that the cutting forces are 10 – 20% higher in the FEM compared to the experimental data. Takacs et al. [24] found in their work that the theoretical cutting forces from the FEM are 45 -120 % higher using tool steel AISI D2.

Tang et al., [119] simulated the machining of hardened D2 tool steel with a CBN cutting tool. For the simulation, the Johnson-Cook equation was applied and validation experiments carried out. An error on cutting forces of 8% between the experiment and simulation was achieved. It was concluded that residual stress relates directly to the cutting temperature. Furthermore, an optimal parameter for cutting speed and cutting depth was calculated.

The limitation of FE-simulations is strongly dependent upon the user. The development engineer must confirm a plausibility check and therefore critically analyse the results of the FEM. It has been shown that most of the authors have differences between the simulation and their experiments [24, 118-120]. To a certain degree knowing this difference validates the simulation for this specific process within the process parameters and the involved materials. However, a validation strategy for FE simulations is the knowledge that simulation and experiments.

In recent years FEM simulation has become a necessary research tool for understanding the mechanics and effects of the machining process in greater detail. Both the Johnson-Cook yield criterion and the Johnson-Cook damage evolution model are commonly used - sometimes with modification - in the latest research [20, 108, 121].

2.5.3 Soft Prediction Model

Recent research has shown that predictive models are used to optimise processes. In this research soft prediction methods such as artificial neural networks and genetic algorithm are presented and discussed to predict and optimise the machining process.

2.5.3.1 Artificial Neural Network

In the recent years, machine learning or artificial intelligence has gained more attention than ever in research on mathematical and computer science sites, but also for a more accurate prediction models in machining [107, 121-126]. Prediction results can be highly accurate and predict even more complex problems compared to other prediction methods, i.e. empirical models suffer necessary constraints, e.g. residual stress prediction is only valid for this particular process setup [122]. However, Machine Learning or Artificial Intelligence uses different tools to solve complex mathematical problems. The most common tool in process optimisation is an artificial neural network (ANN) including deep Feed Forward (FF) Neural Networks and Deep Recurrent Neural Networks, K-nearest Neighbour and Fuzzy Logic, etc. In the last decade this research field and approach has become increasingly more interesting as more literature has been published due to the increasing computing power [121-128].

This work will focus on artificial neural networks. The method is based on the human brain structure in that it consists of an input layer, followed by a hidden layer of neurons and an output layer. The ANN can be further divided into different types of networks such as FF networks, Radial Basis Function (RBF), Recurrent Neural Network and Dynamic Neural Networks [125, 128]. The Feedforward Network can be again further categorised using a backpropagation algorithm.

Firstly, the FF network is discussed. The general structure of the network consists of an input, some hidden layers and an output layer as indicated in Figure 2.19, wherein each layer contains at least one neuron/element. The neural network can consist of any number of hidden layers and any number of neurons (≥ 1) in each layer of the hidden layers. Each neuron is constructed with a bias Φ_K in the hidden layer and Ψ_L in the output layer. Furthermore, every neuron is connected from one layer to the other as indicated in Figure 2.19. Each connection carries different weights expressed by $C_{J,K}$ and $D_{K,L}$. This type of neural network needs to be trained as a human brain. With each training cycle the network gains more knowledge and accuracy of the learned process since the weights and biases are re-adjusting according to the target and output values in the backpropagation algorithm.

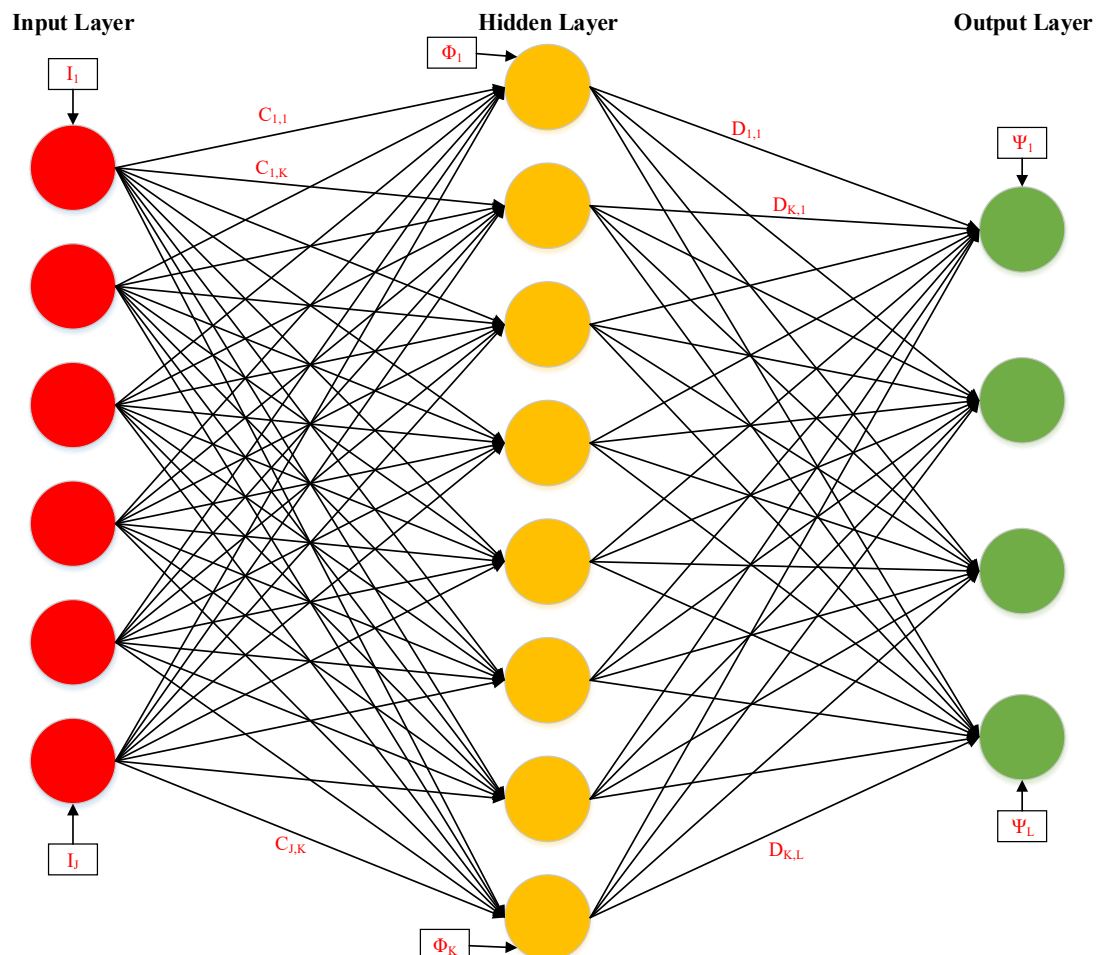


Figure 2.19: Artificial Neural Network - Feed Forward Network schematic

The neural network determines a performance index (PI) which calculates the difference between output values and target values. Subsequently, it generates a total error value of all outputs and this PI calculation can be expressed as followed in equation (2.33):

$$PI = \sum_{L=1}^L (\Psi_L^{target} - \Psi_L^{output}) \quad (2.35)$$

Based on this performance index, the backpropagation algorithm adjusts the calculation in the network, wherein the sensitivity of the adjusted weights results from the previously calculated output layer and is respectively implemented into the newly calculated values. The hidden layers can be expressed in the following equation (2.36):

$$\Delta C_{J,K} = -\alpha \frac{\partial PI}{\partial C_{J,K}}, \Delta \Phi_K = -\alpha \frac{\partial PI}{\partial \Phi_K} \quad (2.36)$$

Accordingly, the expression for the output layer can be stated as follows in equation (2.37):

$$\Delta D_{K,L} = -\alpha \frac{\partial PI}{\partial D_{K,L}}, \Delta \Psi_K = -\alpha \frac{\partial PI}{\partial \Psi_K} \quad (2.37)$$

The learning rate in the above-stated formulas is expressed as α . It is common to use different methods rather than minimisation in order to find the optimum in the neural network. But because the data set is limited, to physical experiments, methods such as early stopping or Bayesian regularisation are used [122, 129].

The Radial Basis Function has a similar structure to the feed forward network. However, this network type consists of one hidden layer and has therefore, in most cases, a simpler structure and faster approach than the 'traditional' FF network or multiplayer perceptron network (MLP). The RBF classifies data by

hyperspheres – this is the most significant difference from the FF network. Usually, MLP networks use arbitrarily shaped hypersurfaces to separate data [127]. As mentioned before, the structure of the RBF-network is like the FF network type as illustrated in Figure 2.20. However, the perception, calculation and functionality within the network are different from the feed forward network.

Based on the previously introduced structure, the RBF-elements can be mathematically expressed as follows. Initially, the input layer towards the hidden layer can be calculated as equation (2.38):

$$s_K = [x_1 C_{1,1}, x_2 C_{1,K} \dots x_J C_{J,K}] \quad (2.38)$$

where s_K expresses the weighted input to the specific hidden layer element, x_J expresses the j -th input and $C_{J,K}$ the weighted input J of hidden unit K . Using the above stated weighted input unit (equation (2.38)) the hidden layer based on a Gaussian algorithm can be expressed as follows in (2.39).

$$\Phi_K(s_K) = \exp\left(-\frac{\|s_K - \mu_K\|}{\sigma_K}\right) \quad (2.39)$$

where μ_K is the Gaussian centre of the hidden layer element K and the standard deviation σ_K uses the width of the hidden element K .

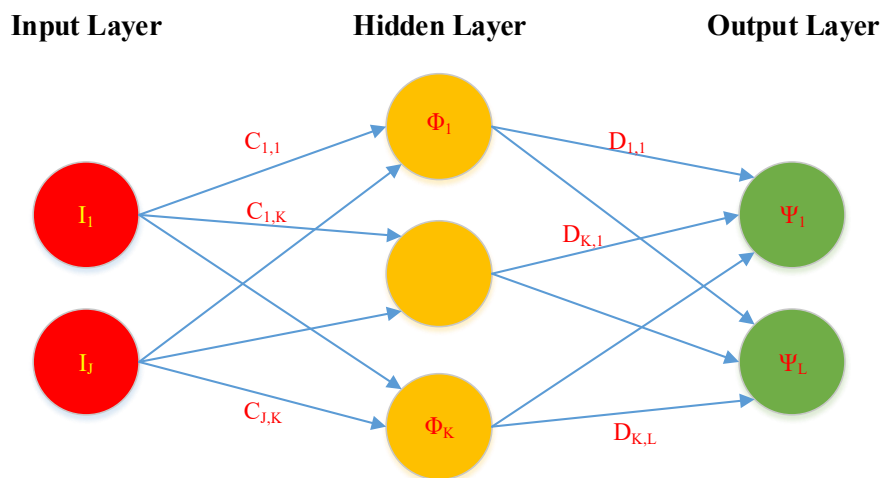


Figure 2.20: Artificial Neural Network - Radial Basis Function schematic

As mentioned previously, networks perform differently in the given environments. Therefore, a benchmark for the specific problems is recommended as different research sources come to different conclusions about these kinds of networks [107, 124, 127].

Recent research has increasingly used this method to optimise and predict results in machining and manufacturing applications. The developed neural network models are now more accurate than traditional models such as the linear regression model.

Kant [130] developed a neural network to predict and optimise the surface roughness of a machining process. The input values came from literature using the FF neural network with four input elements and one hidden layer of nine elements. The result was a relative error of just 4.11%.

Beatrice et al. [75] also used the artificial neural network to predict the surface roughness in a turning application of AISI H13 tool steel. In that paper, the FF network with backpropagation and one hidden layer was used. Furthermore, a combination trial of elements in the hidden layer was conducted to determine the most suitable network combination. It was found that the neural network was able to predict the surface roughness with an error of less than 7%.

An [121] used the ANN to predict the residual stress in a turning application. The research was conducted using a combination of the FEM and ANN using the FEM as a theoretical reference and predicting results using the ANN. In this research an FF network with back propagation was used, with one hidden layer. The difference between the two methods varied between 5 % and 10%.

2.5.3.2 Genetic Algorithm

Genetic Algorithms are based on the behaviour of natural genetics as well as the natural selection of the fittest. Applying this method has the advantage in that it is more likely to locate the global optimum of the investigated parameters [131]. The Genetic Algorithm (GA) calculates the fitness of settings and evolves with the fittest setting until the desired fitness target is reached or a number of evolutions are concluded. This method is very effective for optimisation as it discards weak combinations of settings. However, the evolution of optimum settings is not repetitive as the algorithm can evolve differently every time because the algorithm does not start from a single point, but a random group of points.

The initial settings and condition are encoded to *genes* which are read in binary encoding. See Figure 2.21 (left). A set of encoded genes are combined with other settings to build a *chromosome*. The resulting chromosome contains all of the information of one group of setting (called *population*) and is used in the next stage – the crossover and mutation [132] – in which a mechanism called ‘crossover’ will exchange parts of the chromosome with another set of chromosomes to produce offspring. The mechanism requires a crossover over point before the offspring can be generated. The mutation is taken into account after the crossover to allow randomness of the newly formed chromosome [133]. Figure 2.21 (right) illustrates the mutation process of a pair of chromosomes.

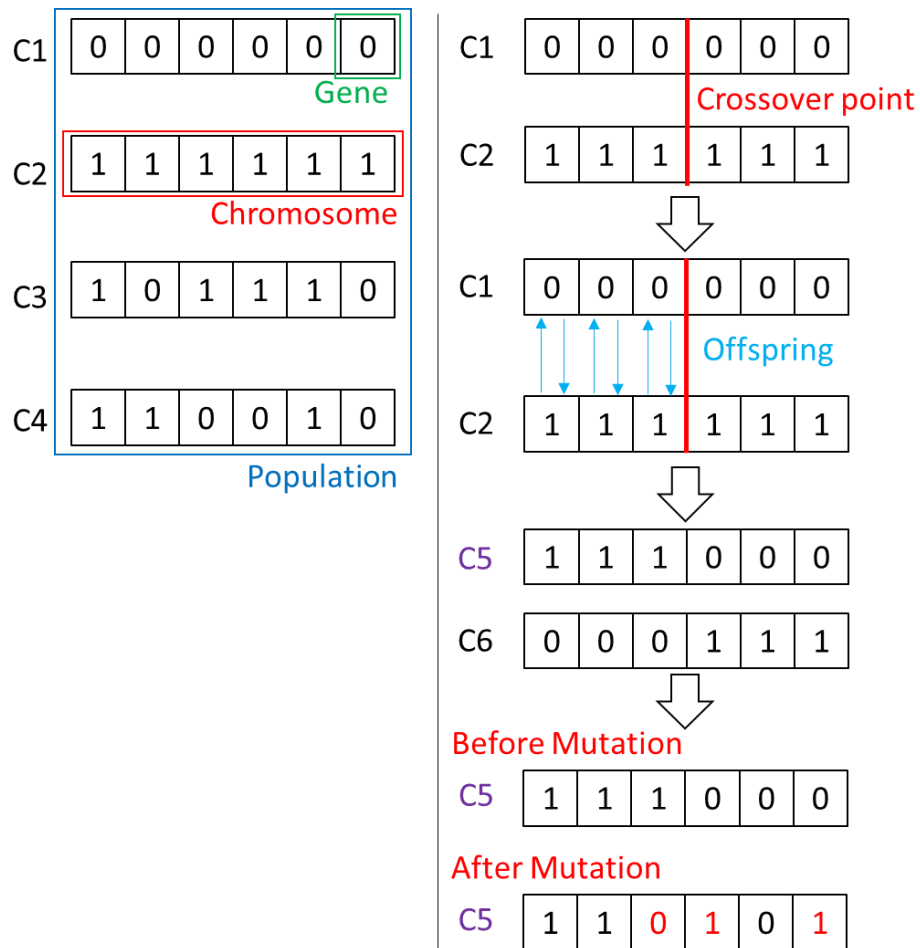


Figure 2.21: Genetic Algorithm by natural mutation

The fitness function is required to feed the optimisation process and natural selection process of the next generation chromosomes in the algorithm. After a few generations there is a great improvement in fitness compared to the beginning. In Figure 2.22 the general principle of the genetic algorithm optimisation is illustrated.

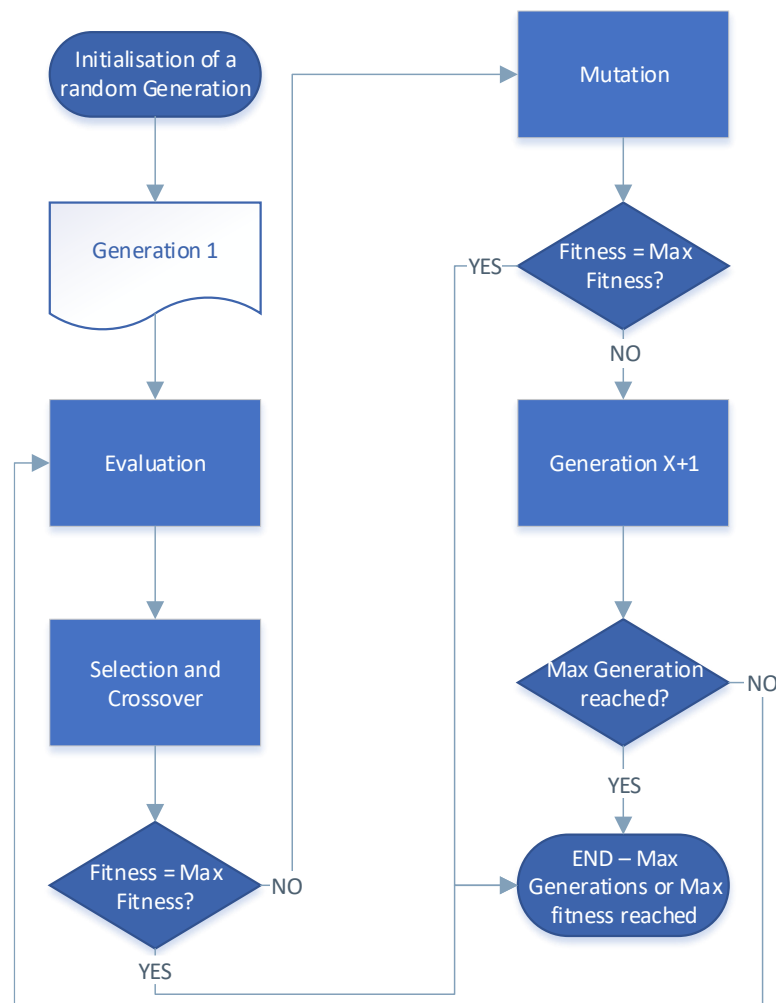


Figure 2.22: Genetic Algorithm optimisation principle

Every GA requires an initial algorithm which contains the function to be optimised and describes the overall objective. In addition to the initial function, the GA also requires a function which describes the fitness and optimisation criteria such as minimisation, maximisation or targeting. Furthermore, a boundary condition for the algorithm should be given to keep the optimum value realistic.

The advantages of the genetic algorithm have been used by various researchers in the field of machining with great success. As computing power has increased so have improvements in the calculation time for GA algorithms [132, 134-139]; the number of research studies in this field have proliferated over the last twenty years.

Jameel et al. [135] conducted a short review of a genetic algorithm for machining optimisation and found that GA is one of the most effective solutions for population search and optimisation. They discovered that many studies focused on the optimisation of the surface roughness, machining costs and the material removal rate but only a few on cutting temperature, torque, geometrical accuracy and heat affected zones.

Doriana et al. [136] optimised some machining parameters in a turning process and concluded that the advantage of the GA lies in its ability to take a multi-objective optimisation approach. This minimises the machining time whilst considering the technological and material constraints.

A similar finding was reported by Jawahir et al. [132]. They found that the strength of the GA lies in its optimisation of multiple objectives, in that example optimising the trade-off between the multi turning passes and the optimum of the cutting condition in the passes. It was concluded that this methodology could balance the cutting condition between the passes and determine the optimum cutting condition for tool and workpiece.

2.5.4 Summary

It was found that methods such as the neural network and genetic algorithms have been used more and more in the past decade as computing power has been increasing. The combination of soft prediction models and FEM has been tried out but not researched in great depth. Furthermore, it was found that the applied material model from Johnson-Cook for FEM simulation is often used. However, specific and new models are continuously being developed to describe material behaviour during manufacturing operations with ever greater accuracy. Additionally, it was found that no research has been undertaken on the combination of ANN and GA to predict and optimise the machining process in order to optimise resulting fatigue life.

2.6 Chapter Summary

This literature review has shown that surface integrity and fatigue performance is still a cutting-edge field in manufacturing research, and is still attracting much attention worldwide. Research findings on these topics have generally increased technology readiness levels (TRL) and so industries like tooling, automotive and aerospace are trying to implement these findings to their processes.

It was found that recent research has mainly been focused on residual stress and surface roughness, as these components significantly influence the surface integrity. The macro-/microstructure and hardness were partially investigated. Therefore, an investigation into the complete standard dataset of the surface integrity with its effects to the fatigue performance is needed.

Fatigue performance is most often used in high-cycle fatigues at an ambient temperature. However, the low cycle fatigue on any component is more critical as the workpiece will fatigue after only a few hundred to thousands of cycles. The criticality increases further, when the low-cycle condition is performed under elevated temperature and no reported baseline on this fatigue test condition on AISI H13 has been performed. The effect of geometry and its resulting machining strategies under the above mentioned fatigue performance condition was not reported to be investigated.

The review also highlighted that there is little research published which investigated the machining optimisation on fatigue life of tool steel using optimisation methods such as neural networks and genetic algorithms. However, it was identified that more publications will soon be released.

The review also revealed that there was no extensive amount of FEM simulation carried out on 3D-FEM machining models to investigate the surface integrity and so ultimately predict it. Furthermore, it was also found that a material model with high accuracy subroutine could significantly contribute to the precision of the FEM.

Chapter 3 Precision Milling Experiment

In order to optimise the process, precision milling experiments were conducted to understand the cutting process and its effects on surface integrity and fatigue life. Furthermore, the experiments were used to validate the simulation. In this chapter the methodology of experiments will be explained after an introduction to this topic, followed by an experimental setup. In the fourth section the results of the experiment of the machining process will be presented. In the last section a summary will be given.

3.1 Introduction

The challenges of machining have become more evident in recent times due to tighter tolerances on parts and more complex shapes and surfaces. Therefore, research on machining has risen significantly in the last decade in areas covering surface integrity and fatigue performance: it's a hot topic. The finishing process stage of a component is one of the most critical processes since the surface is often exposed to the functional environment after machining if no post-treatment is applied.

In order to achieve the first aim of this research - develop a prediction model on surface integrity - a physical understanding of the influence of machining parameter on the surface integrity needed advancing. With data obtained from the experiment, the prediction model can be developed. Furthermore, the experiments were used to validate the prediction models and prove theories to understand the machining process more fully and apply optimisation processes more rigorously. Notably, the surface integrity is process-specific, and changes on any machining parameter can vary. Since a minimum amount of experimental data is required to reach conclusions costs are greatly reduced - fewer experiments were needed. In the following section these approaches will be presented, conducted and discussed.

3.2 Methodology of Experiments

Before conducting experiments, a methodology was established to ensure the experiments would deliver the desired research results. This would also ensure that no data or factors would get lost or be made redundant during the process. The experimental methodology (which is part of the overall methodology introduced in section Chapter 1) can be seen in the following Figure 3.1.

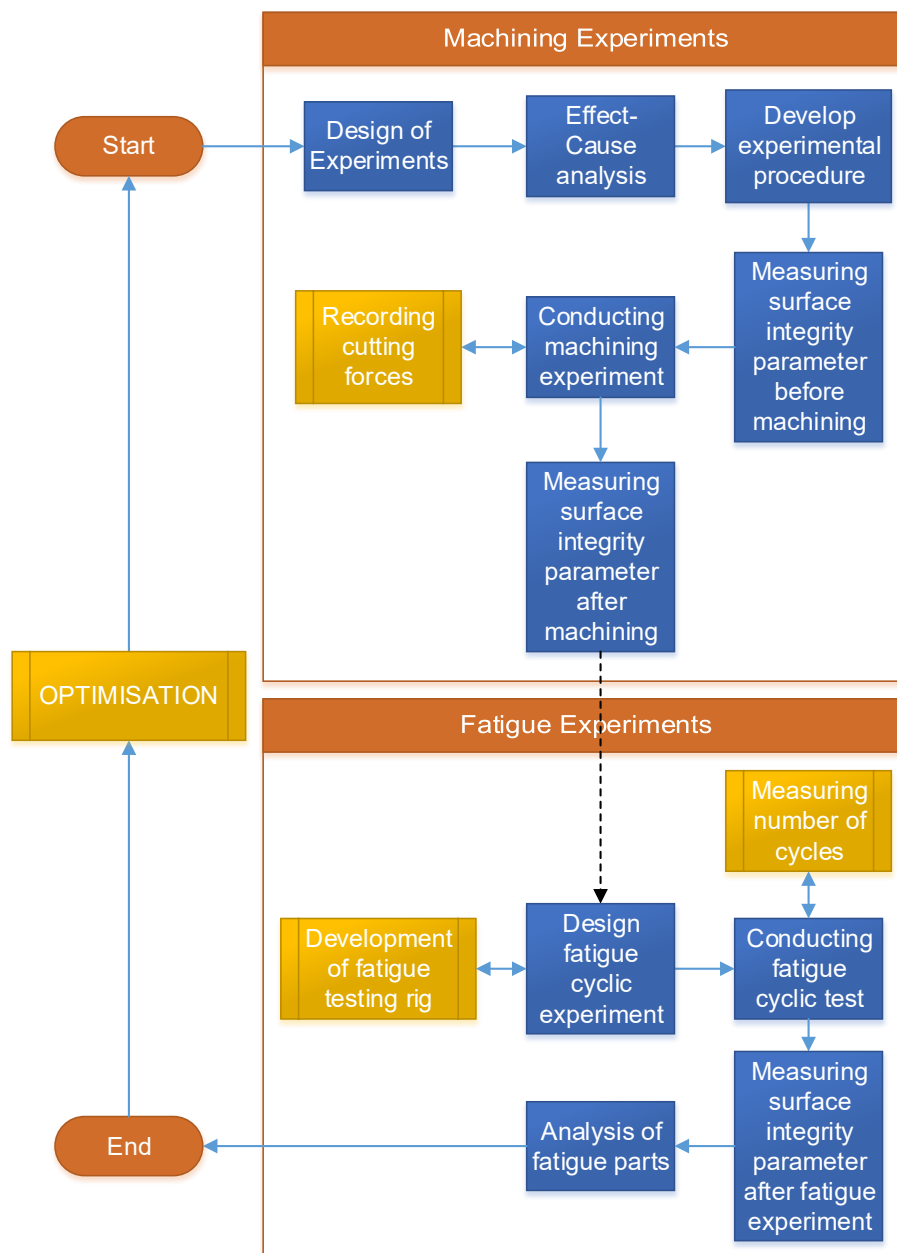


Figure 3.1: Experimental procedure

Initially, a root-cause-effect diagram, also called an Ishikawa-diagram, was created to determine possible variations and influence during the machining experiment. Those factors were considered during the experiments and kept under control to ensure comparable results. In Figure 3.2, the Ishikawa-Diagram can be seen. Based on this Ishikawa-diagram and literature review from Chapter 2, the following four machining parameters were chosen for investigation: Surface Speed, Depth of cut, Feed Rate and Lead Angle. The chosen factors are directly related to the machining strategy, are controllable, and have been identified as significant in previous studies. [8, 18, 20, 47, 48, 105-107, 140]

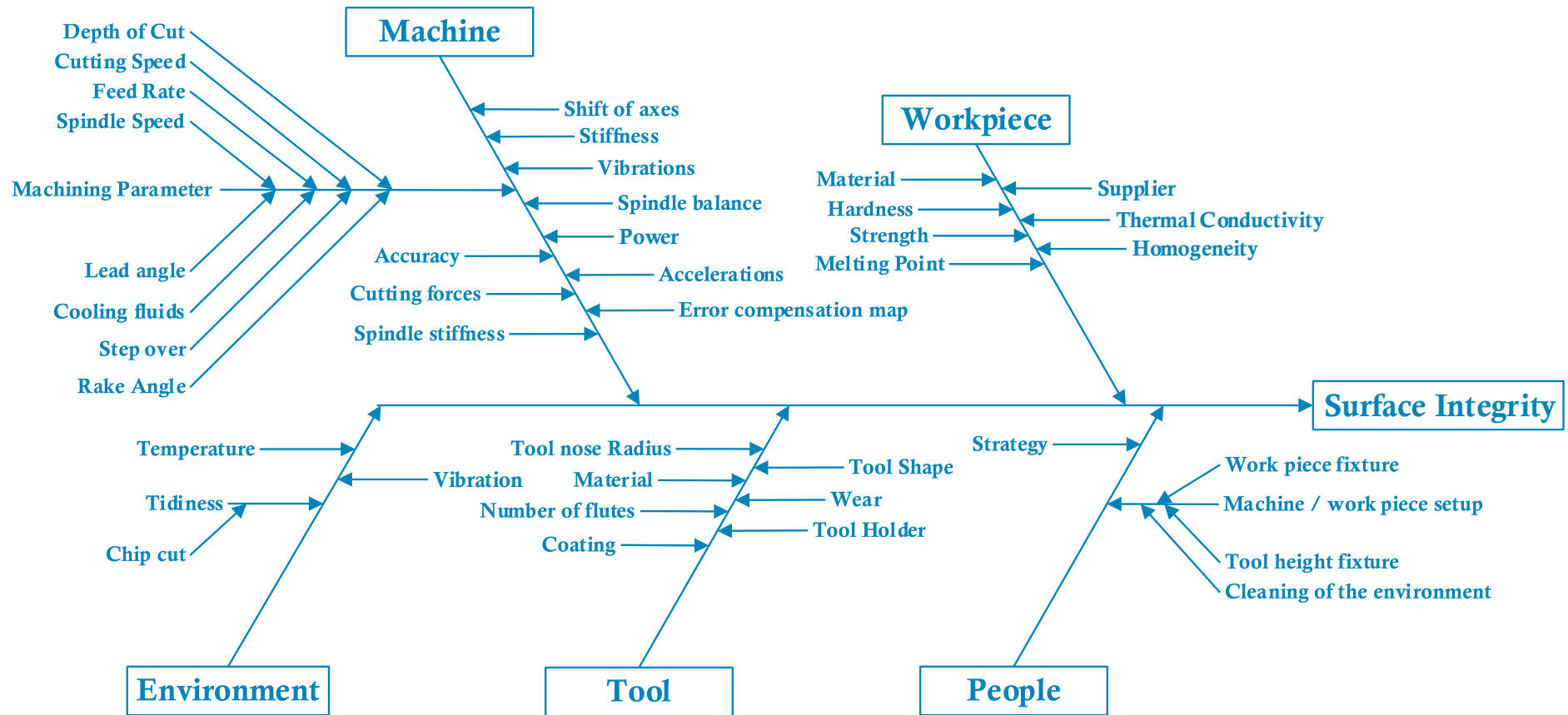


Figure 3.2: Root cause diagram (Ishikawa-Diagram) on Surface Integrity

3.2.1 Design of Experiment Methodology

Generally, there are several design methods with different objectives. In Table 3.1, an overview of a few selected design methods can be found.

Table 3.1: Design of Experiment types with regards to the experimental objectives [141]

Levels of Factors	Objective			
	Troubleshooting	Screening	Modelling	Robust design
2	Hadamard D-Optimal Taguchi	Hadamard/Foldover Plackett-Burman D-Optimal Taguchi	D-Optimal	Plackett-Burman D-Optimal Taguchi
3	D-Optimal Taguchi	D-Optimal Taguchi	Central Composite Box-Behnken D-Optimal	Fractional factorial Box-Behnken D-Optimal Taguchi
More than 3 levels	D-Optimal Taguchi	D-Optimal Taguchi	Central Composite D-Optimal	Central Composite D-Optimal Taguchi

Based on this Table 3.1 and the objective of this project, the selection of the design of experiments is reduced to the central composite design (CCD) method and D-Optimal. As this work focuses on more than three levels per factor the aim is to model & optimise the machining process. Therefore, these two design methods were compared in the following Table 3.2.

Table 3.2: Comparison between CCD and D-Optimal (based on [141])

Design	Objective	Capabilities	Disadvantages
Central Composite Design	Modelling Robust design	It estimates all linear, quadratic effects. It estimates all some or no interactions orthogonality and rotatability.	Best suited to quantitative factors
D-Optimal	Screening Troubleshooting Modelling Robust design	Able to be used for any number of factors and levels. Can use qualitative and quantitative factors. Designs accept any arrangement of interactions. Require fewer runs than an orthogonal design for the same situation.	No simple tables designs are available. Specialist computer software is required to generate designs. Regression is required to resolve to confounding in the designs. Designs are not generally orthogonal. The resultant confounding structure further complicates the subsequent analysis.

From Table 3.2, it can be concluded that the Central Composite Design method is the best design method for this research project. The experiment will only have quantitative factors, and this method is orthogonal with rotatability over the D-Optimal method. Consequently, all experiments are designed and based on the Central Composite Design (CCD) method. A visualisation for three factors of the CCD can be seen in Figure 3.3. The factorial levels are indicated by the red dots, in this case, eight. Each axis also has a minimum extreme and maximum extreme indicated by the black dots ($\pm\alpha$). The distance of α is determined by the type of design and number of factors, in this case 4 factors, and centred the distance of α is 2. The number of central points can vary depending on the number of runs; it is calculated as follows in equation (3.1):

$$n_c = \sqrt[4]{n_f + 1} - 2k \quad (3.1)$$

where n_c indicates the number of centre points, n_f the number of runs in the factorial 2-Level block and k the number of factors. In this case it has six central points.

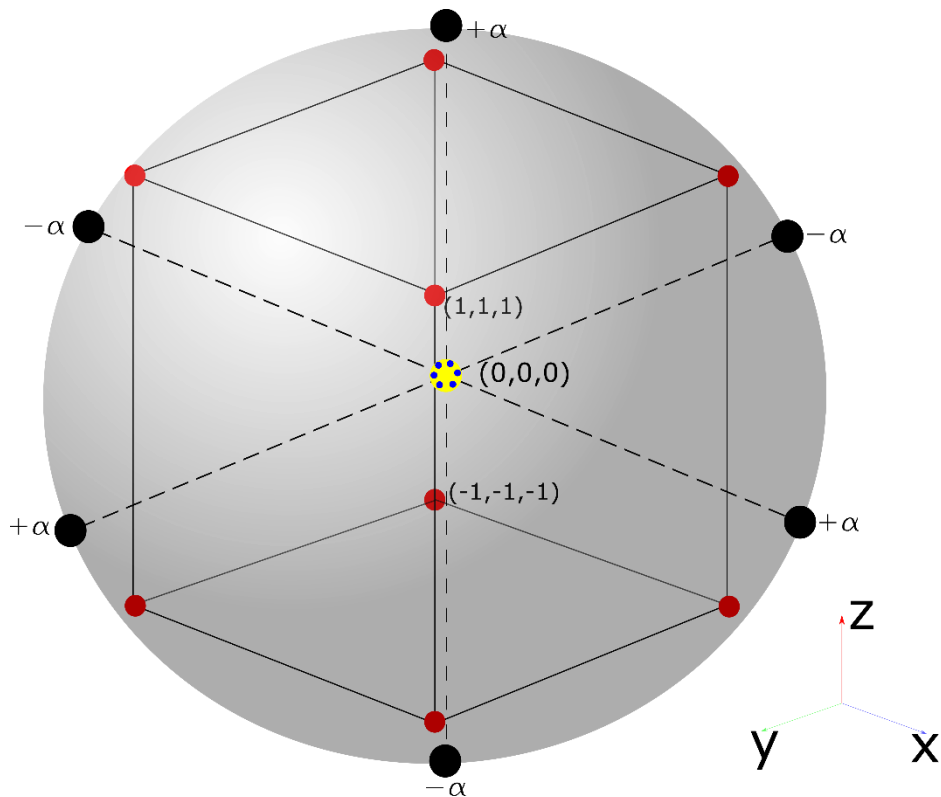


Figure 3.3: Visualisation of Central Composite Design Method

This method incorporated the four quantitative factors which were, as previously stated, the surface speed, depth of cut, feed rate and lead angle.

The total number of experiments needed can be calculated as shown in equation (6.1):

$$N = 2^K + 2K + C_0 \quad (3.2)$$

where K is the number of factors and C_0 the replications in the centre point [142], from this equation (6.1) it follows that the CCD requires 30 runs ($= 2^4 + 2 \times 4 + 6$).

The levels of the design method can be found. In this case in Table 3.3, Levels $+ or - 1$ indicates the factorial experiments, Level 0 is the central point and Level $\pm \alpha$ are the extremities of each factor. The central point indicates the typically used parameter for this kind of material and process.

Table 3.3: Level and design for machining experiment

Parameter	Unit	Level -α	Level -1	Level 0	Level +1	Level +α
Surface Speed	m/min	200	250	300	350	400
Depth of Cut	mm	0.1	0.3	0.4	0.5	0.6
Feed Rate	mm/tooth	0.02	0.08	0.12	0.16	0.2
Lead Angle	deg	0	7.5	15	22.5	45

Table 3.4 shows the experimental plan with all parameters and their levels. The increase in CCD is due to the repeated central points which validate the runs. However, to ensure that all runs - especially the extremities- are reliable, and to ensure contingency, a few points were repeated after the CCD experiment was completed. All runs were randomised to reduce the repeatability effect.

The table shows also additional trials for contingencies and validation of this experiment, whereby “Run Order” 1 – 30 indicates the CCD experimental runs and 31 to 37 the additional/contingency runs.

Table 3.4: Machining experiment plan and parameters, sort by run order.

Run Order	Standard Order	Surface Speed [Level]	Depth of cut [Level]	Feed Rate [Level]	Lead Angle [Level]	Surface Speed [m/min]	Depth of cut [mm]	Feed Rate [mm/tooth]	Lead Angle [deg]
1	2	-1	1	-1	-1	250	0.5	0.08	7.5
2	10	0	0	0	0	300	0.4	0.12	15.0
3	4	1	1	1	-1	350	0.5	0.16	7.5
4	7	1	-1	1	1	350	0.3	0.16	22.5
5	6	1	1	-1	1	350	0.5	0.08	22.5
6	1	1	-1	-1	-1	350	0.3	0.08	7.5
7	8	-1	1	1	1	250	0.5	0.16	22.5
8	9	0	0	0	0	300	0.4	0.12	15.0
9	5	-1	-1	-1	1	250	0.3	0.08	22.5
10	3	-1	-1	1	-1	250	0.3	0.16	7.5
11	12	1	1	-1	-1	350	0.5	0.08	7.5
12	20	0	0	0	0	300	0.4	0.12	15.0
13	18	1	1	1	1	350	0.5	0.16	22.5
14	14	-1	1	1	-1	250	0.5	0.16	7.5
15	16	-1	1	-1	1	250	0.5	0.08	22.5
16	17	-1	-1	1	1	250	0.3	0.16	22.5
17	13	1	-1	1	-1	350	0.3	0.16	7.5
18	19	0	0	0	0	300	0.4	0.12	15.0
19	11	-1	-1	-1	-1	250	0.3	0.08	7.5
20	15	1	-1	-1	1	350	0.3	0.08	22.5

Table 3.4 cont.

Run Order	Standard Order	Surface Speed [Level]	Depth of cut [Level]	Feed Rate [Level]	Lead Angle [Level]	Surface Speed [m/min]	Depth of cut [mm]	Feed Rate [mm/tooth]	Lead Angle [deg]
21	28	0	0	0	2	300	0.4	0.12	45.0
22	21	-2	0	0	0	200	0.4	0.12	15.0
23	29	0	0	0	0	300	0.4	0.12	15.0
24	25	0	0	-2	0	300	0.4	0.02	15.0
25	24	0	2	0	0	300	0.6	0.12	15.0
26	22	2	0	0	0	400	0.4	0.12	15.0
27	23	0	-2	0	0	300	0.1	0.12	15.0
28	30	0	0	0	0	300	0.4	0.12	15.0
29	27	0	0	0	-2	300	0.4	0.12	0.0
30	26	0	0	2	0	300	0.4	0.20	15.0
31	31	1	1	1	-1	350	0.5	0.16	7.5
32	32	-1	-1	1	1	250	0.3	0.16	22.5
33	33	0	0	-2	0	300	0.4	0.02	15.0
34	34	0	0	0	-2	300	0.4	0.12	0.0
35	35	0	0	0	2	300	0.4	0.12	45.0
36	36	2	0	0	0	400	0.4	0.12	15.0
37	37	-2	0	0	0	200	0.4	0.12	15.0

3.3 Experimental Setup and procedure

In this section, the machining experiment setup and procedure will be discussed.

General machining experiment setup is illustrated in Figure 3.4. Figure 3.4 (a), shows a general overview including the DMG Mori-Seiki HSC 75 with a Kistler dynamometer and data acquisition (DAQ) equipment. The top right Figure 3.4 (b) shows the dynamometer from Kistler (9129AA) with a specially designed workpiece fixture. In the bottom right Figure 3.4 (c) the DAQ equipment is illustrated and consists of an amplifier from the dynamometer, a logger from National Instruments, and a laptop running a customised MATLAB script to record measured data from the dynamometer. Furthermore, this machining experiment will be carried out in a dry condition, as nowadays the HSM applications are carried in dry condition and cutting tools are designed to cut in dry condition.

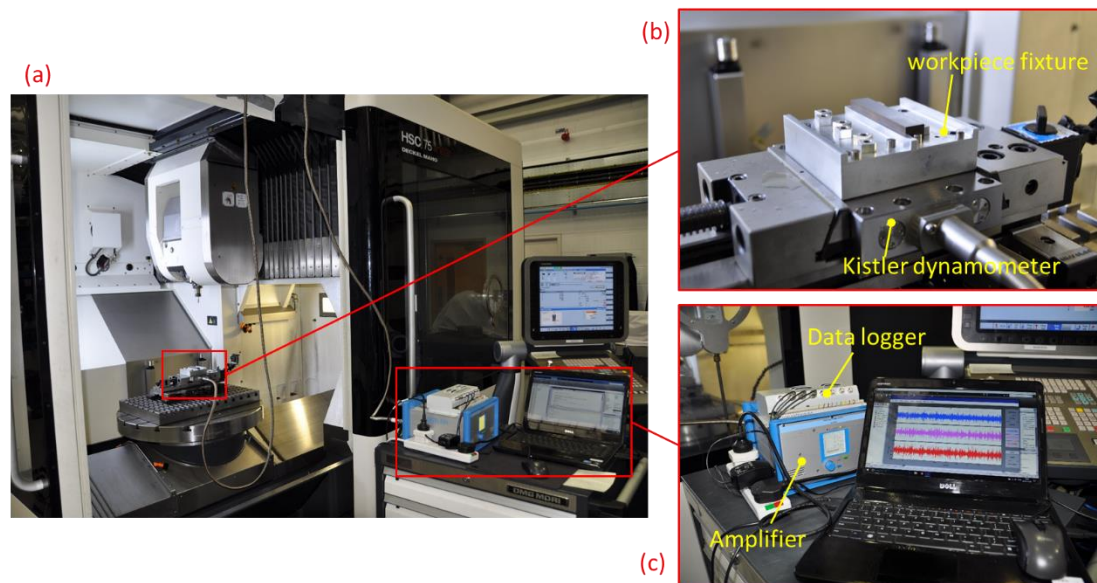


Figure 3.4: Experimental setup

Figure 3.5 illustrates the workpiece fixture assembly with the dynamometer.

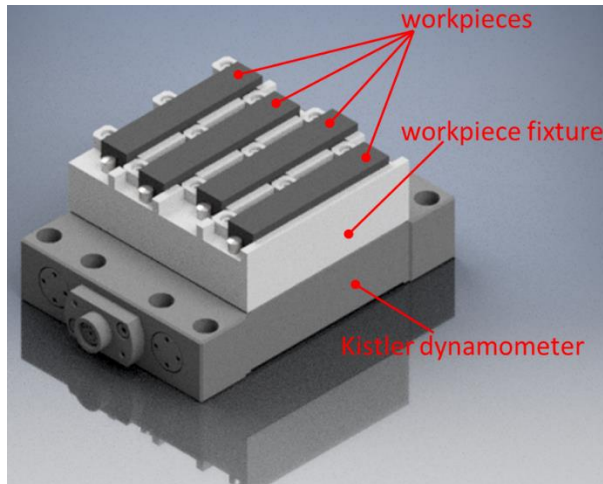


Figure 3.5: Workpiece fixture and dynamometer illustration

The workpiece fixture was specially designed for this project. The fixture is to hold the workpieces in place during the cutting trials. Additionally, it places the workpieces precisely over the piezoelectric area for measuring the cutting forces to achieve accurate cutting force recordings. The workpieces were mounted to reduce tool and workpiece deflection during the cutting trials. This fixture was used in the later stage of analysing the surface integrity to ensure that all workpieces were analysed in the same area, reduce errors and make the surfaces comparable. A technical drawing of the workpiece fixture is attached in Appendix X Workpiece Fixture Drawing, the fixture itself was made from aluminium, as this material was easy to source and cost effective for its purpose.

A four-flute end-mill ball nose cutter was used. A short description of the specifications of the ball nose end-milling cutter is given in Table 3.5. This cutter is currently used as a standard cutting tool for this kind of Material AISI H13. The experiment was divided into 8 new ball nose cutters, to avoid any kind of wear on the cutting tool. The cutter was also regularly inspected to record any possible wear, but no wear was detected on any cutter during and after the experiment.

Table 3.5: End-mill ball nose cutter specifications [143]

Item	Property	Item	Property
Manufacturer	Mitsubishi	Number of Flutes	4
Tool Material	Tungsten-Carbide	Manufacturer Model number	VF-4MB
Radius	4 mm	Hardness	3700HV
Mill Diameter	8 mm	Friction Coefficient [Coulomb]	0.48

3.3.1 Workpiece

The workpiece was designed as a homogenous brick to ensure that no other factors, such as different feeds and speeds caused by curves or inclinations, occur during the cutting process. This design enables a more consistent force recording during the cutting process as well as a more consistent measurement of surface integrity and comparability. The workpiece was designed to have final dimensions of 80 x 15 x 8 mm (L x W x H).

All workpieces were planned to have the same final height to ensure comparability when executing the fatigue testing; the thickness of the workpiece would therefore significantly influence the fatigue life using the same force. The workpieces were initially cut by Electro-Discharge Machining (EDM) to the dimension of 80 x 15 x 15 mm (L x W x H). The cut sequence and exact procedure are explained in the following section 3.3.2. The part was then analysed on its initial state on surface integrity in the following chapters from 3.3.3 onwards. A material certificate of conformance is attached to Appendix XII Certificates of Conformance

As the workpiece material AISI H13 was used. The workpiece material AISI H13 was used, which is a hot-work tool steel, being frequently used for forging die applications. Its properties are shown in Table 3.6.

Table 3.6: Workpiece Material properties AISI H13

Material	Density [kg/m ³]	Young's Modulus [GPa]	UTS (Rm) [MPa]	Hardness [HRC]	Yield strength (R _{p0.2}) [MPa]
AISI H13	7,800	210	1990	45 - 58	1660

3.3.2 Experimental Procedure

The actual experimental process on the cutting trials can be described in a few steps and are shown in Figure 3.6. Additionally, the measurements during and after the cutting trials required a comprehensive approach - the framework for this was illustrated in the start of Chapter 1 and also Chapter 3.

In the first step, the workpieces were cut to their specific heights depending on the experimental depth of cut, i.e. if a DoC of 0.4 mm is required, the workpiece was roughed in the beginning to 10.4 mm, and the finishing cut to 10 mm. In the 2nd step, the uncut side of the workpiece was roughed and finished accordingly to achieve a final height of 8 mm, a schematic diagram being representing the process in Figure 3.7.

After the workpieces were machined to their final heights, initial measurements were conducted on the workpieces. An initial analysis of the workpieces was carried out before the machining trial to identify the as Electric Discharge Machining (EDM) condition.

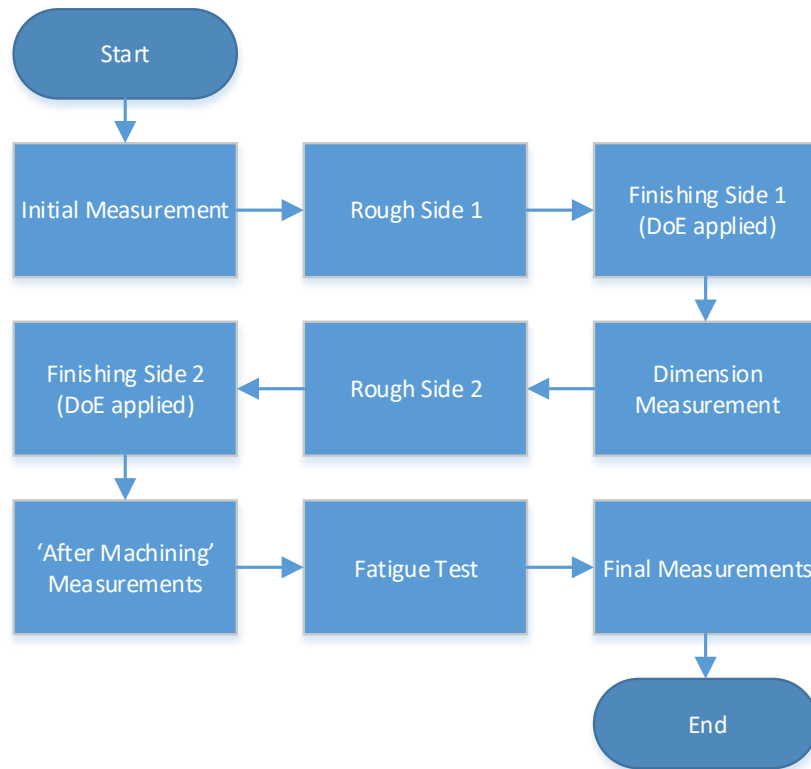


Figure 3.6: Experimental process procedure

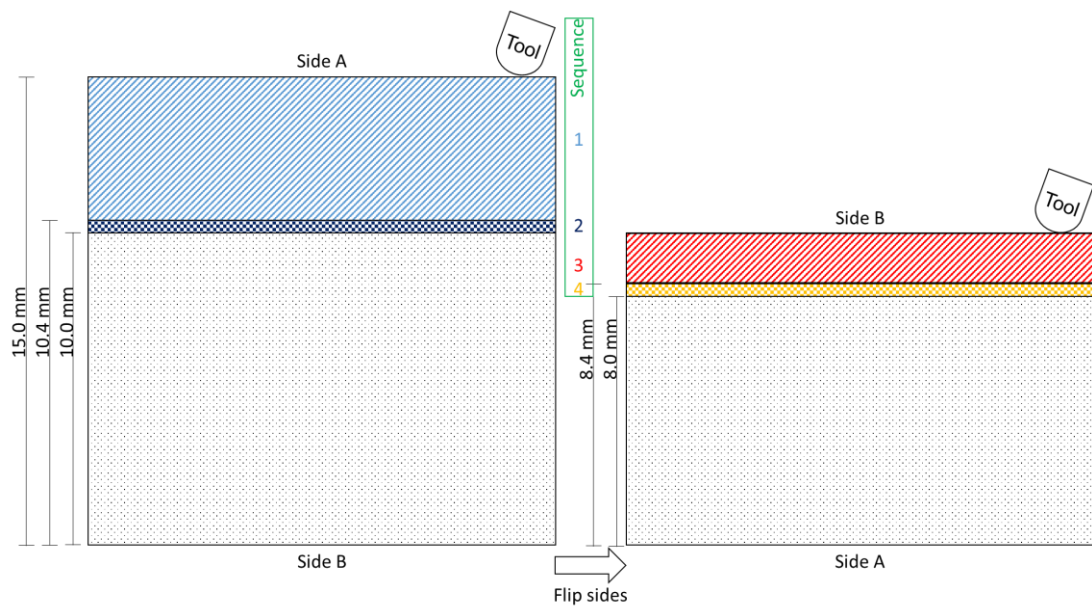


Figure 3.7: Workpiece cutting sequence

3.3.3 Measurements

The surface integrity includes the microstructure, residual stress, microhardness and surface roughness which all need to be determined. This requires a variety of metrology equipment. The equipment used and outlined below is regularly maintained, calibrated and certified to conform to a high-quality standard. Furthermore, the cutting force was obtained using a dynamometer and its use is also explained in the following section in more detail.

3.3.3.1 Cutting Forces

The cutting force is essential in scientifically analysing a material removal process. The measured forces are therefore used to verify numerical simulations and models, such as FEM.

In this work, the cutting forces in X, Y and Z direction were obtained. A dynamometer from Kistler (9129AA) was used to measure the cutting forces and an illustration of the dynamometer can be found in Figure 3.8 (a).

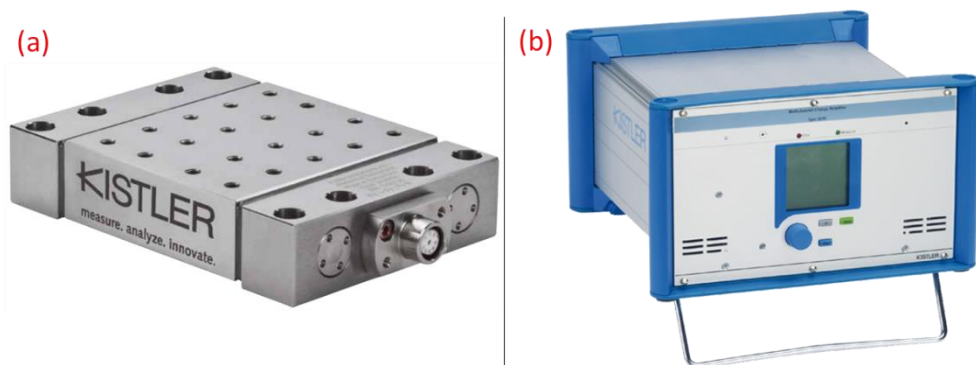


Figure 3.8: (a) Kistler Dynamometer 9129AA, (b) Kistler Multichannel Charge Amplifier 5070 [144]

The sensitivity of the dynamometer is shown in Table 3.7. From the sensitivity the error of the dynamometer can be calculated. Additional specifications and calibration results of the dynamometer can be found in the Appendix II Kistler Datasheet.

Table 3.7: Kistler Sensitivity Calibration

Calibrated Range [kN]		Sensitivity [pC/N]	Linearity [$\leq \pm\%$FSO]
<i>F_x</i>	0 ... 10	-8.118	0.03
<i>F_x</i>	0 ... 1	-8.111	0.05
<i>F_x</i>	0 ... 0.1	-8.102	0.09
<i>F_y</i>	0 ... 10	-4.165	0.09
<i>F_y</i>	0 ... 1	-4.157	0.13
<i>F_y</i>	0 ... 0.1	-4.142	0.11
<i>F_z</i>	0 ... 10	-8.133	0.03
<i>F_z</i>	0 ... 1	-8.123	0.06
<i>F_z</i>	0 ... 0.1	-8.133	0.14

The dynamometer has built-in piezoelectric sensors that measure the cutting forces in each direction. The quartz bars with the built-in sensors do the charging. These sensors are orientated and manufactured to minimise crossover reading. This has the advantage of ensuring that no wear will occur on the sensor itself, which helps produce consistent results. Forces in every bar can be measured in the Longitudinal and Transverse direction, as well as in shear direction.

The signal is amplified using an amplifier (Kistler Multichannel Charge Amplifier Type 5070) shown in Figure 3.8 (b), as the raw signals have a small voltage as well as an high signal-noise. The amplifier improves the Voltage signal strength and clears out the noise, splitting the signals into the different components X, Y, Z. A MATLAB script was used to record and process the signals and thus obtain and process the force; measurements were taken in Newton. In the signal a post-processing drift compensation was applied since the sensor capacitance increases over the time.

3.3.3.2 Microstructure

As mentioned in Section 2.2.2, the microstructure has a significant bearing on the workpiece performance as the microstructure defines the hardness, structural toughness, porosity and irregularities within the workpiece. In order to obtain the microstructure the workpiece needs to be prepared to be analysed in an SEM (Scanning Electron Microscope). For this work, an FEI/Oxford Instruments Quanta 250 FEG SEM and optical microscope were used to analyse the Microstructure and fractured surface after the fatigue test. The equipment is shown in Figure 3.9. This machine is regularly calibrated.



Figure 3.9: FEI Quanta 250 FEG SEM

The SEM vacuum chamber is relatively small and so the samples needed to be cut to a reasonable size. Furthermore, the analysed side needed to be polished to a mirror-like finish to identify the microstructure of the components. Since the workpiece needs to be cut to size, moulded and polished, only a few samples were selected to be analysed before the fatigue testing.

Analysing the Fractography does not require any preparation and the workpiece's fracture was analysed. The Fractography analysis will be discussed in more detail in section 4.3.1.

The outcome from the microstructure analysis is a qualitative picture analysis of the microstructure.

Additionally, the macro-structure of the workpiece was also analysed and compared to see if the qualitative structure had any influence on the workpiece performance. Those macro-structure results were obtained by using the Alicona infinite focus (see section 3.3.3.5).

3.3.3.3 Residual Stress

Residual stress, as shown in section 2.2.1 and 2.3, has a significant influence on the fatigue performance of the component. Due to the significance of the surface integrity and fatigue performance, the surface residual stress was measured before and after the machining process. It is important to identify the stress concentration on the surface as it influences the workpiece performance afterwards. Figure 3.10 shows the XRD machine utilised (Proto LXR).

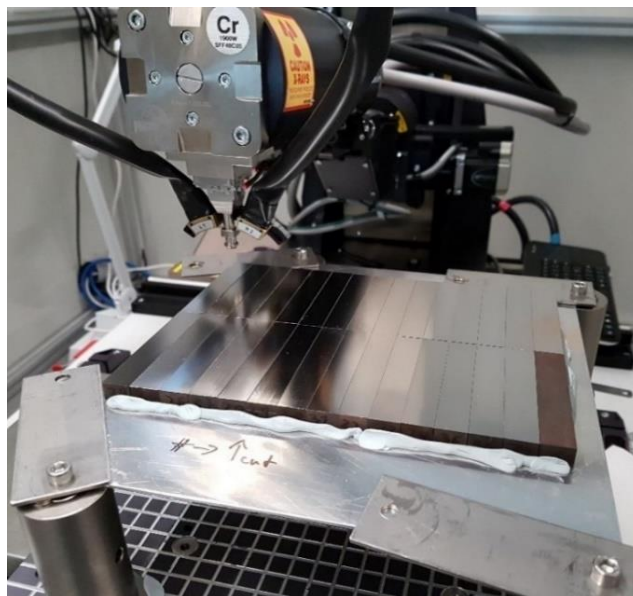


Figure 3.10: XRD test setup

All of the workpieces were lined up and laid out in the required cutting direction in order to compare them directly. Every workpiece was measured five times in $\varphi = 0$ and $\varphi = 90$ direction across the surface to build an average of the measured points. The working principle and theory behind the X-Ray diffraction method can be found in section 2.2.1. Initially the XRD-Machine was calibrated to a zero-stress sample. This calibration sample has a Stress of 0 ± 14 MPa. The LXRD measured on this calibration sample 12.04 ± 1.70 MPa which is well in the range of the calibration sample. For the setup the parameters shown in Table 3.8 were used.

Table 3.8: XRD-Settings

Item	Property	Item	Property
Material	AISI H13	Young's Modulus	210 GPa
Poisson Ratio	0.29	Radiation tube	Cr-K α
Bragg Angle	156.33° (2 Θ)	Number of Ψ -Angle	13
Ψ -Tilt	5°		

This analysis shows the stress vectors in Mega Pascal (MPa) for the cutting direction and perpendicular to it. Furthermore, the shear stresses of both stress vectors were obtained.

3.3.3.4 Microhardness

The hardness was measured on ten workpieces to validate an initial average hardness of the workpieces before they were machined. After the machining, all workpiece hardness was analysed.

The hardness was acquired based on Vickers Hardness on a Struers DuraScan 70 G5 Hardness Tester (see Figure 3.11). Every workpiece was measured with ten measurements and a distance of 0.5 mm between each measurement. The DuraScan is regularly calibrated to ensure a consistent and valid result.



Figure 3.11: Struers Hardness tester

A load of 0.5 kgf was used to obtain the Microhardness since higher loads are considered as “normal” / macro hardness. After measuring the Vickers hardness it was converted to Rockwell hardness Type C (HRC). The HRC is more commonly used to describe die-material as it allows a clearer comparison between the results obtained and other research work.

The workpiece was mounted and clamped to the designed fixture (shown in section 3.3) to ensure no lifting or movement of the workpiece during the measurement. This is shown in Figure 3.11.

3.3.3.5 Surface Roughness

In chapter 2.2.3 the theory of surface roughness was introduced and discussed. As mentioned before surface roughness (3D) is a modern approach and is now the subject of much research and many publications. Therefore, the surface roughness S_a , S_q , S_z was determined in this work.

Figure 3.12 shows an Alicona Infinite Focus microscope used to measure the surface roughness and topology. This optical measurement instrument has a

vertical resolution of a minimum of 10 nm and lateral resolution of a minimum to 400 nm. The cut-off length λ (L_c) was set to 800 μm .

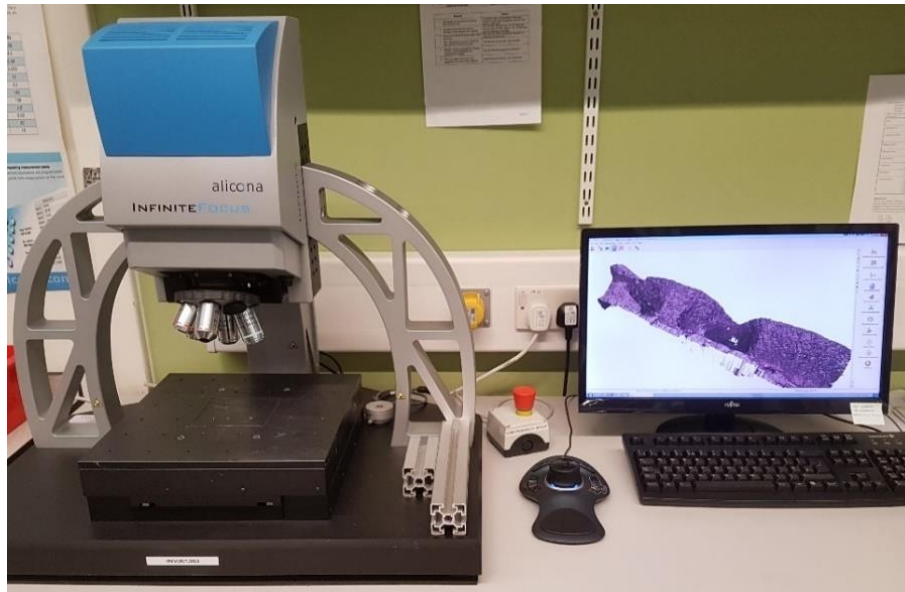


Figure 3.12: Alicona Infinite focus

Analysing the surface roughness will produce a calculated value of 2D and 3D series of surface roughness as well as the topology of the surface. It will also calculate a standard deviation for each measurement. The measurement was repeated three times to ensure the repeatability of the machine. The machine has the following tolerances as listed in Table 3.9.

Table 3.9: Alicona specification

<i>Roughness Range R_a</i>	50 – 200 nm	200 – 700 nm	700 – 3000 nm
<i>Repeatability</i>	5 nm	5 nm	15 nm
<i>Uncertainty</i>	25 nm	50 nm	300 nm

3.4 Experimental results and discussion

In this chapter all the experimental results from the machining experiments are presented. The results will be compared to their as-received condition in order to determine the changes in the surface integrity.

3.4.1 Cutting Forces

As mentioned before in section 3.3.3.1, the cutting force is often used to validate in-process conditions of numerical predictions. Furthermore, the cutting force can also be used as an indicator of residual stress and machined surface finish.

The cutting force was recorded during the cutting process, as described in section 3.3.3.1 with the given tolerance. A typical output of the measured cutting force is illustrated in Figure 3.13. An average value of the cutting forces were taken from the peaks and are indicated below by green and red spots.

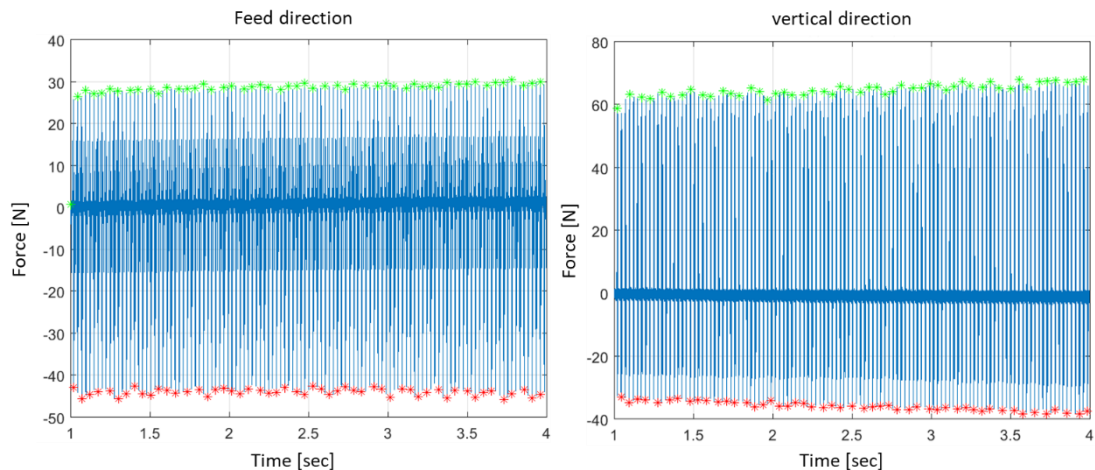


Figure 3.13: Example of cutting force readings

The cutting force measurements from the entire experiment can be found in the tangential Table 3.10. In this table, all three measured components can be found. The feed direction has a negative value due to the baseplate orientation. The tolerances of the measured values are marginal, so on the second digit of

the recorded forces the tolerances were not shown in the tables and graphs, but they were considered in the calculation. The measuring tolerance can be calculated applying the values of Table 3.7 to the measured value, i.e. the tolerance for experiment 1 (in standard order) can be calculated as followed, feed force -35.5 ± 0.01 N, tangential force 2.95 ± 0.0009 N and Vertical force 46.8 ± 0.01 N.

Table 3.10: Cutting force results

Standard Order	Feed force	Tangential force	Vertical force	Standard Order	Feed force	Tangential force	Vertical force
1	-35.5	2.9	46.8	20	-31.1	13.0	81.1
2	-25.5	12.6	41.2	21	-39.0	18.0	85.4
3	-33.1	3.6	75.7	22	-43.0	12.0	96.3
4	-98.7	52.3	150.8	23	-16.2	7.5	32.1
5	-16.1	3.4	34.8	24	-51.0	21.2	102.0
6	-38.2	29.0	91.7	25	-25.2	18.3	56.0
7	-34.9	16.2	71.7	26	-36.5	22.1	116.0
8	-18.9	2.8	34.8	27	-72.6	15.3	167.0
9	-22.4	4.7	75.4	28	-26.6	27.3	55.3
10	-37.4	21.9	92.4	29	-40.0	24.3	103.0
11	-41.4	11.1	74.0	30	-28.8	16.2	88.6
12	-53.1	17.6	157.0	31	-80.3	26.1	210.0
13	-44.0	12.7	64.8	32	-24.7	18.4	47.0
14	-55.2	7.6	96.8	33	-18.2	13.7	55.7
15	-34.3	17.5	69.2	34	-79.9	18.6	141.0
16	-20.6	7.9	41.3	35	-28.4	24.4	42.6
17	-17.3	13.8	37.8	36	-58.2	19.0	109.0
18	-36.9	19.7	93.2	37	-38.5	18.0	82.7
19	-33.9	18.2	84.2				

Figure 3.14 shows the variation of cutting forces under different cutting parameters and tool lead angle condition. It can be seen that the surface speed and the lead angle are the most factors influencing the cutting forces.

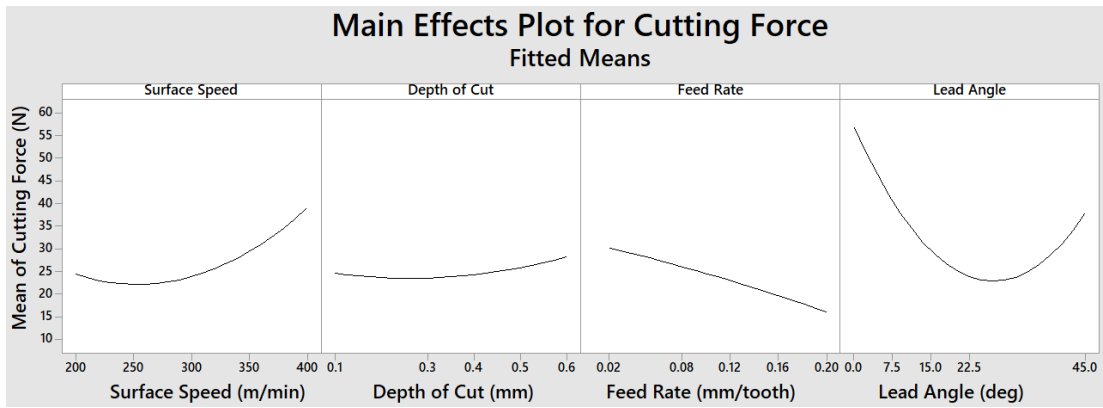


Figure 3.14: Main effects of machining parameter for Cutting force

The analysis of this data shows that the surface speed and the lead angle have the most influence on the cutting force. An ANOVA (Analysis of Variance) analysis confirms this observation as shown in Table 3.11. Furthermore, none of the factors count as significantly important, only the quadratic analysis reveals that the lead angle can be identified as significant.

Table 3.11: ANOVA for machining parameter on cutting force

Source	Adjusted Sums of Squares	Adjusted mean squares	F-Value	P-Value
Linear				
Surface Speed	105.84	105.84	1.12	0.306
Depth of Cut	4.78	4.78	0.05	0.825
Feed Rate	82.9	82.9	0.88	0.363
Lead Angle	203.58	203.58	2.16	0.162
Square				
Surface Speed * Surface Speed	99.06	99.06	1.05	0.322
Depth of Cut * Depth of Cut	11.47	11.47	0.12	0.732
Feed Rate * Feed Rate	0.77	0.77	0.01	0.929
Lead Angle * Lead Angle	1012.66	1012.66	10.75	0.005

2-Way				
<i>Surface Speed * Depth of Cut</i>	271.43	271.43	2.88	0.110
<i>Surface Speed * Feed Rate</i>	66.02	66.02	0.70	0.416
<i>Surface Speed * Lead Angle</i>	1.38	1.38	0.01	0.905
<i>Depth of Cut * Feed Rate</i>	308.88	308.88	3.28	0.090
<i>Depth of Cut * Lead Angle</i>	276.39	276.39	2.93	0.107
<i>Feed Rate * Lead Angle</i>	367.68	367.68	3.9	0.067
Error				
<i>Lack-of-Fit</i>	1214.05	121.40	3.04	0.116
<i>Pure</i>	199.55	39.91		

In this research the interaction between the different machining parameters was also analysed. Figure 3.14 illustrates most of the parameters having an interaction. However, there is no apparent interaction when considering surface speed and lead angle. An interaction between parameters can reflect the mutual influences among those parameters. For example, Surface Speed and Depth of Cut are working contractionary to each other as they interact at some point (visually, the lines are crossing). However, there is a balance between these two factors to optimise their outcomes. If there is no interaction between those factors, the lines would not be crossing each other, and both parameters would behave in the same way.

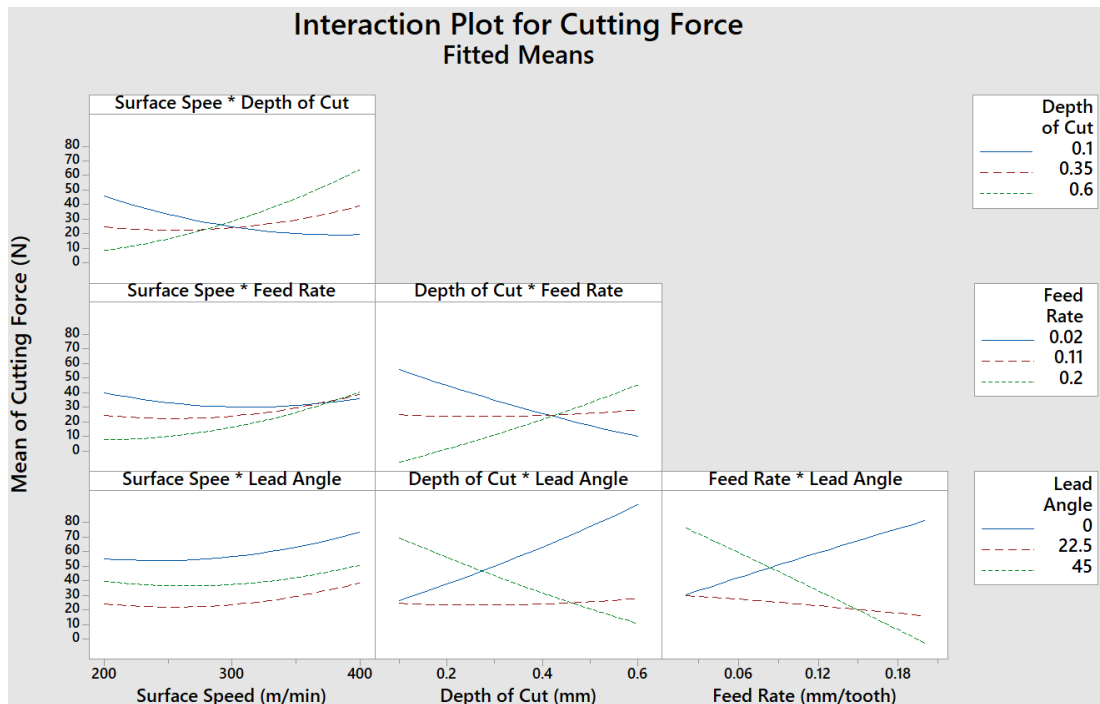


Figure 3.15: Machining parameter interaction plot for cutting force

As mentioned in section 3.2.1 the experiment was carried out as central composite design. Therefore, an analysis of the surface response is possible. Figure 3.16 shows an example of the interactions of parameters. It shows that with an increased feed rate and lead angle the cutting force will reduce since the heat induction during the cut is increased. Additionally, the force component changes due to the angular contact between the cutter and the workpiece. This is described in section 2.4.1.1. However, a large lead angle and small feed rate will cause the cutting force increasing to its maximum value; this is due to the increased contact area of the cutting tool and the reduced spindle speed as well as translational movement of the workpiece. The combination increases the mechanical deformation and consequently a reduced thermal impact on the part, which causes relatively higher cutting forces.

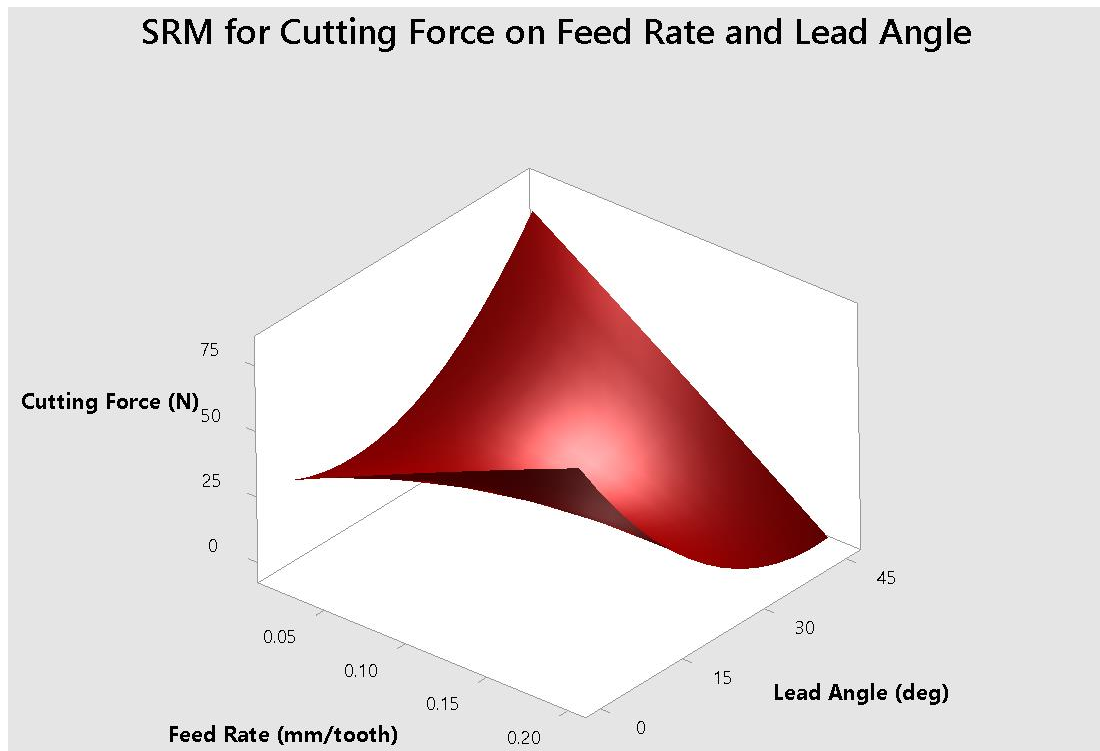


Figure 3.16: SRM for Cutting Force on Feed Rate and Lead Angle

3.4.2 Residual Stress

In this section residual stress results will be presented and discussed under corresponding machining parameters. Table 3.12 lists the results from the surface residual stress measurement after machining. An initial residual stress measurement was also carried out before the machining state. This measurement showed that the workpiece was highly stressed with tensile stresses; an average of 502.36 ± 7.0 MPa in $\varphi = 0^\circ$ and 508.56 ± 8.8 MPa in $\varphi = 90^\circ$ direction was discovered. This in turn led to an average von-Mises value of 505.55 MPa.

Table 3.12: Measured Surface Residual Stress

Std. Order	$\varphi=0$	$\varphi=0$ error	$\varphi=90$	$\varphi=90$ error	Std. Order	$\varphi=0$	$\varphi=0$ error	$\varphi=90$	$\varphi=90$ error
1	44.38	10.22	-110.4	5.92	20	51.55	12.35	33.77	5.52
2	-22.65	11.30	-34.45	5.80	21	41.18	16.90	6.87	6.20
3	15.33	11.88	25.37	6.30	22	33.23	12.62	116.33	7.45
4	25.52	10.08	59.22	7.67	23	19.83	12.90	85.55	6.23
5	84.65	15.32	-32.57	6.25	24	54.92	10.53	99.83	6.87
6	112.70	11.78	53.08	5.95	25	24.52	15.62	-87.75	6.42
7	107.05	13.20	102.67	7.02	26	77.13	13.95	206.52	7.88
8	40.77	8.45	16.97	6.10	27	-221.3	8.00	-65.13	13.20
9	64.43	13.17	-9.75	5.75	28	11.40	12.90	119.80	7.13
10	30.67	11.70	46.00	5.90	29	39.98	13.50	39.98	7.05
11	44.03	14.82	-36.63	6.77	30	39.65	13.83	125.85	7.40
12	41.30	8.78	-15.58	5.92	31	35.88	12.50	18.50	5.58
13	25.72	10.02	-23.43	5.75	32	72.67	13.03	143.13	7.20
14	-19.60	14.03	-64.60	5.18	33	-62.20	11.18	-157.8	5.33
15	119.80	16.83	96.65	7.42	34	-185.0	6.40	-39.83	11.63
16	143.23	17.28	131.88	6.87	35	8.17	14.40	74.72	6.42
17	66.83	10.83	80.75	6.88	36	110.12	14.53	81.50	6.75
18	113.02	15.35	119.33	10.12	37	19.62	14.15	0.25	5.85
19	95.47	14.33	168.13	6.53					

Table 3.12 lists the measured surface residual stress. It can be seen that the residual stress vectors in cutting direction are mostly tensile stresses. Most stresses also vary around a nearly stress-free surface state i.e. experiment with Standard Order 3 is around 15 MPa, these low residual stresses are often considered as nearly stress free. On the perpendicular orientated stress vector, more compressive stresses can be found. The tensile residual stress is likely to result from adiabatic heating during the machining process. The induced heat during the cutting process is an indication that the material shears more than the mechanical deformation which would introduce more compressive stress.

From Table 3.12 and the shear stress (see raw data in the Appendix V Underpinning Residual Stress Data) the Von-Mises plane stress can be calculated. The results of the calculated plane stress can be found in Table 3.13. The plane stresses were used to assess the correlation between the FEM simulation and XRD measurement. The results shown in Table 3.13 are calculated for DoE and therefore reduced to 30 results.

Table 3.13: Measured results as Von-Mises Stress

Standard Order	Von-Mises (MPa)	Standard Order	Von-Mises (MPa)	Standard Order	Von-Mises (MPa)
1	165.74	11	130.71	21	121.45
2	113.74	12	113.21	22	145.88
3	103.04	13	108.16	23	133.67
4	115.29	14	125.96	24	146.97
5	158.42	15	159.22	25	173.96
6	147.96	16	181.52	26	208.02
7	150.58	17	119.37	27	198.11
8	109.34	18	159.77	28	161.02
9	130.19	19	181.39	29	120.46
10	114.23	20	113.02	30	153.30

In the following section the residual stresses are presented in von-Mises plane stress, as it describes the residual stress plane of the surface. Furthermore, a detailed comparison between simulation and experiment is also presented.

Table 3.14 shows that the surface speed is most influential factor on the plane residual stress followed by the feed rate, depth of cut and lead angle respectively.

Table 3.14: Results of ANOVA for plane residual stress (Von-Mises) by Experiments

Source	Adjusted Sums of Squares	Adjusted mean squares	F-Value	P-Value
Linear				
<i>Surface Speed</i>	516.2	516.20	0.51	0.482
<i>Depth of Cut</i>	22.9	22.92	0.02	0.882
<i>Feed Rate</i>	259.6	259.58	0.26	0.617
<i>Lead Angle</i>	1.9	1.89	0.00	0.966
Square				
<i>Surface Speed * Surface Speed</i>	570.3	570.25	0.57	0.460
<i>Depth of Cut * Depth of Cut</i>	479.9	479.92	0.48	0.498
<i>Feed Rate * Feed Rate</i>	1740.2	1740.16	1.73	0.203
<i>Lead Angle * Lead Angle</i>	6.9	6.92	0.01	0.935
2-Way				
<i>Surface Speed * Depth of Cut</i>	252.8	252.78	0.25	0.622
<i>Surface Speed * Feed Rate</i>	13.0	13.01	0.01	0.911
<i>Surface Speed * Lead Angle</i>	14.0	14.02	0.01	0.907
<i>Depth of Cut * Feed Rate</i>	47.2	47.15	0.05	0.831
<i>Depth of Cut * Lead Angle</i>	137.1	137.07	0.14	0.716
<i>Feed Rate * Lead Angle</i>	37.1	37.11	0.04	0.850
Error				
<i>Lack-of-Fit</i>	16094.9	1609.49	3.17	0.031
<i>Pure</i>	6096.9	508.08		

Figure 3.17 illustrates that the surface speed and feed rate are the most influential factors. Furthermore, all functions are nearly quadratic functions, which indicate that the optimum is not in the extremum of a factor.

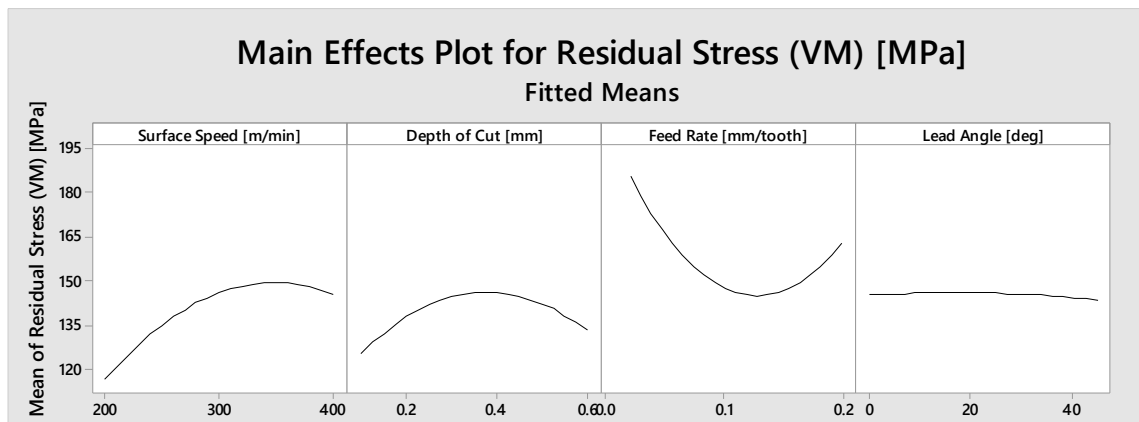


Figure 3.17: Main effects of machining parameter for Plane-Residual Stress

The quadratic function shows that an increase from 0.02 to 0.125 mm/tooth increases the induced heat during the machining process, which still allows the heat to distribute into the workpiece surface and softens the material locally. As a result, material resistance decreases and less stresses remain in the workpiece. However, when the feed rate is increased to over 0.125 mm/tooth the tool's relative transversal movement is too high, and consequently the material cannot be removed from the workpiece completely. The result is a heavily deformed surface which causes an increase in cutting forces as well as residual stresses.

Additionally, the following interaction plot (Figure 3.18) illustrates that all factors apart from the surface speed and feed rate interact with each other. These interactions occur when the surface speed and feed rate are translated into the machine parameters; they are connected with each other and the spindle speed adjusts accordingly.

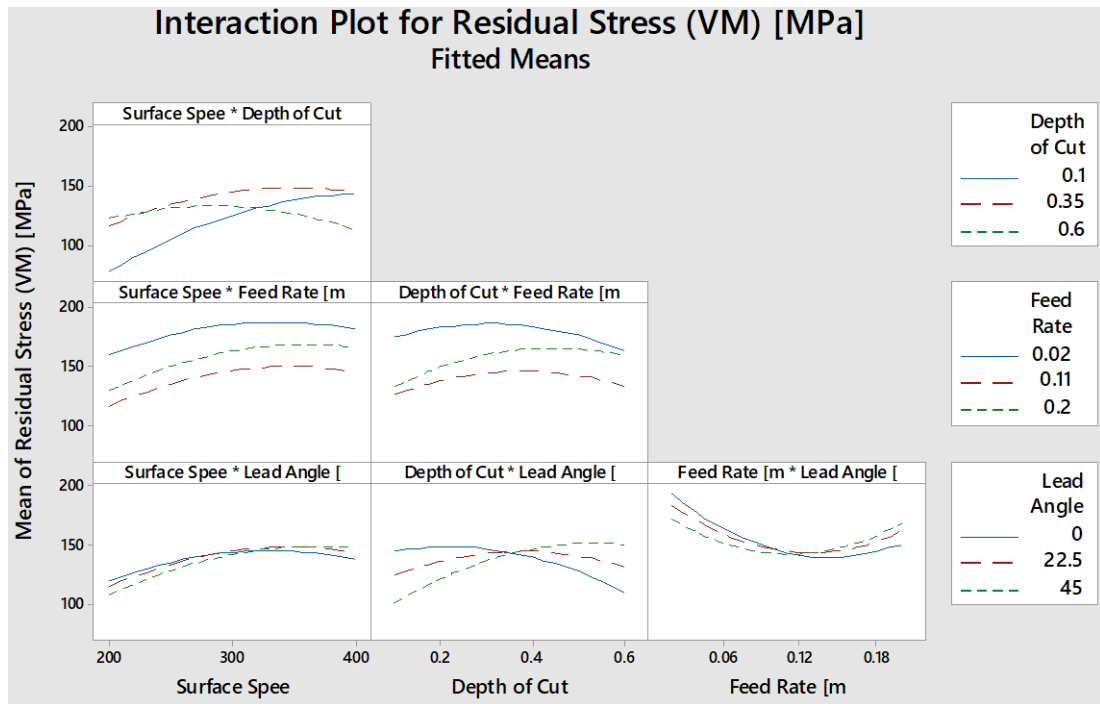


Figure 3.18: Machining parameter interaction plot for residual stress

The surface response model (SRM) is illustrated in Figure 3.19. It shows the two most influential factors for the plane residual stress are the surface speed and feed rate. These two factors were set on hold at 0.35 mm for the depth of cut and 22.5° for the tool lead angle. From this graph we see that like the other factors, a dynamic interaction between the factors exists at the highest and lowest points of the variables - this interaction leads to increased residual stress.

The increased residual stress is due to the heat induction in the workpiece, as the FEM-simulation has revealed, the FE-simulation is discussed in more detail in Chapter 5. The increased surface speed and feed rate cause adiabatic heat induction in the workpiece, and the result is that residual stress (mainly tensile stresses) [46] becomes enclosed in the workpiece during the material removal process.

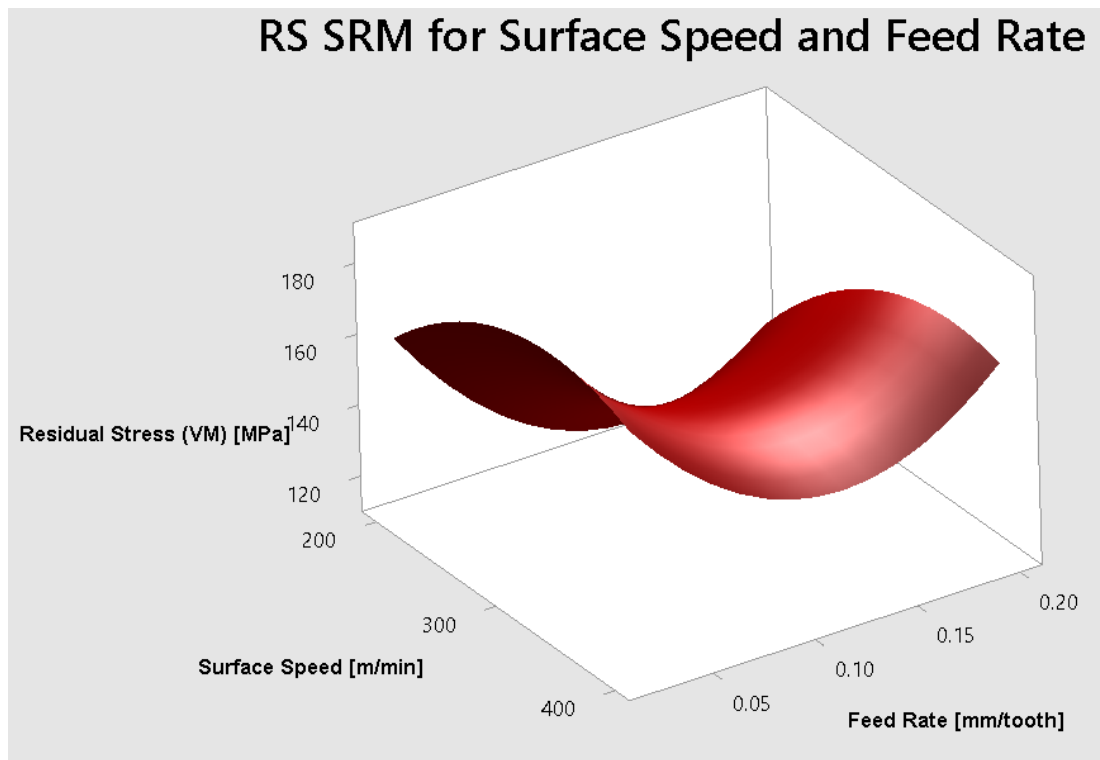


Figure 3.19: SRM on Residual Stress for Surface Speed and Feed Rate

3.4.3 (Micro)hardness

Hardness is also a component of the surface integrity and thus the hardness of the workpieces, therefore the hardness of the machined surface and its cross-section was measured before and after the fatigue testing, as well as before machining.

The average hardness of this selection of workpieces was 49 ± 2 HRC (498 HV) as shown in Figure 3.20. Furthermore, some of the deviations varied around 3 HRC, which is an indication of the variance in the microhardness measuring technique but also the variation within the material. However, the data shows that the part-to-part variation is not significantly different.

After the machining trials, the microhardness of the workpiece was measured again to identify the change of microhardness caused by the machining process. Figure 3.20 shows the measured hardness. This illustrates that the hardness has changed and increased after the machining process.

This change of hardness is due to the adiabatic heating as well as the mechanical movement of the cutter over the surface which compresses the material. However, this increased heat induction results in residual stress, leaving the workpieces in a tensile state.

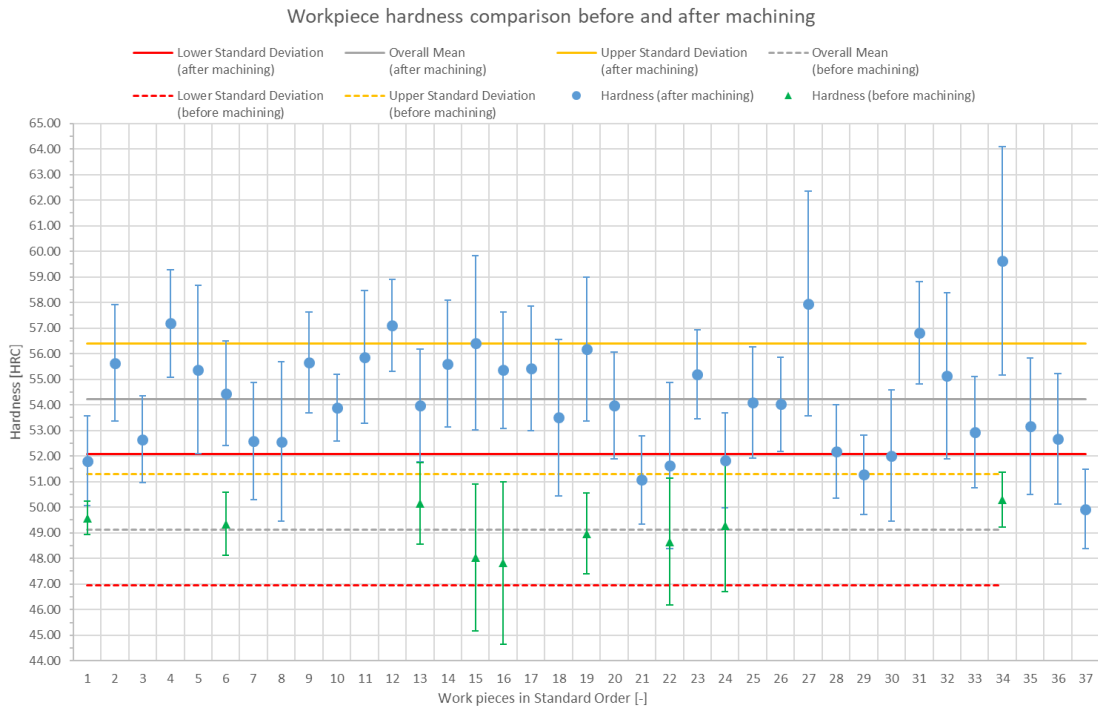


Figure 3.20: Workpiece hardness before and after machining experiments

Furthermore, a several outliers of the measurement can be observed. This is due to various reasons, as there is a part-to-part variation in the material as well as a variation in the measurement of the workpiece. Furthermore it is known, that the microhardness variates in its measurements.

Table 3.15 shows the results of the ANOVA analysis. It can be identified that the depth of cut makes the largest contribution to the hardness.

Table 3.15: Result of ANOVA for Microhardness

Source	Adjusted Sums of Squares	Adjusted mean squares	F-Value	P-Value
Linear				
Surface Speed	1.218	1.218	0.33	0.570
Depth of Cut	11.147	11.1466	3.05	0.095
Feed Rate	2.060	2.0602	0.56	0.461
Lead Angle	0.081	0.0814	0.02	0.883
Square				
Surface Speed * Surface Speed	18.632	18.632	5.10	0.034
Depth of Cut * Depth of Cut	0.074	0.074	0.02	0.888
Feed Rate * Feed Rate	0.803	0.803	0.22	0.644
Lead Angle * Lead Angle	5.272	5.271	1.44	0.243
2-Way				
Surface Speed * Depth of Cut	4.712	4.712	1.29	0.268
Surface Speed * Feed Rate	0.319	0.319	0.09	0.770
Surface Speed * Lead Angle	0.547	0.547	0.15	0.703
Depth of Cut * Feed Rate	0.001	0.001	0.00	0.987
Depth of Cut * Lead Angle	17.193	17.193	4.70	0.041
Feed Rate * Lead Angle	1.849	1.849	0.51	0.484
Error				
Lack-of-Fit	57.874	5.787	3.08	0.034
Pure	22.542	1.879		

Figure 3.21 illustrate the result of the ANOVA analysis. It demonstrates that the surface speed, feed rate and lead angle have a near quadratic behaviour on the microhardness. However, the depth of cut has a near linear behaviour towards the microhardness: when increasing cutting depth, the microhardness of the workpiece reduces. Reduction in the microhardness occurs because the cutter can engage with the material more efficiently and thus induces fewer thermal components during the cut into the workpiece. Adiabatic heating occurs during any cut, but when the cutting tool is not fully engaged with the workpiece material (cutting edge is not in full or only partially in contact with the to-cut-material, due to the angular position or feed rate of the cutting tool) it can start to “rub” the surface and induce heat which changes the microstructure on the surface and therefore the microhardness.

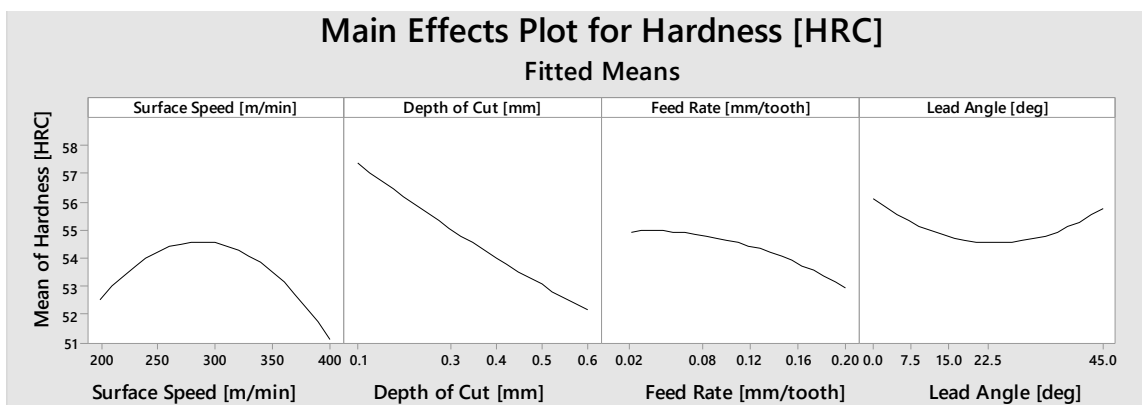


Figure 3.21: Main effects of machining parameter for hardness

Table 3.15 indicates that there is very little or no interaction between surface speed and feed rate, and between feed rate and depth of cut. Figure 3.22 shows the interaction of the all the factors which illustrates that the depth of cut and the lead angle have a substantial interaction.

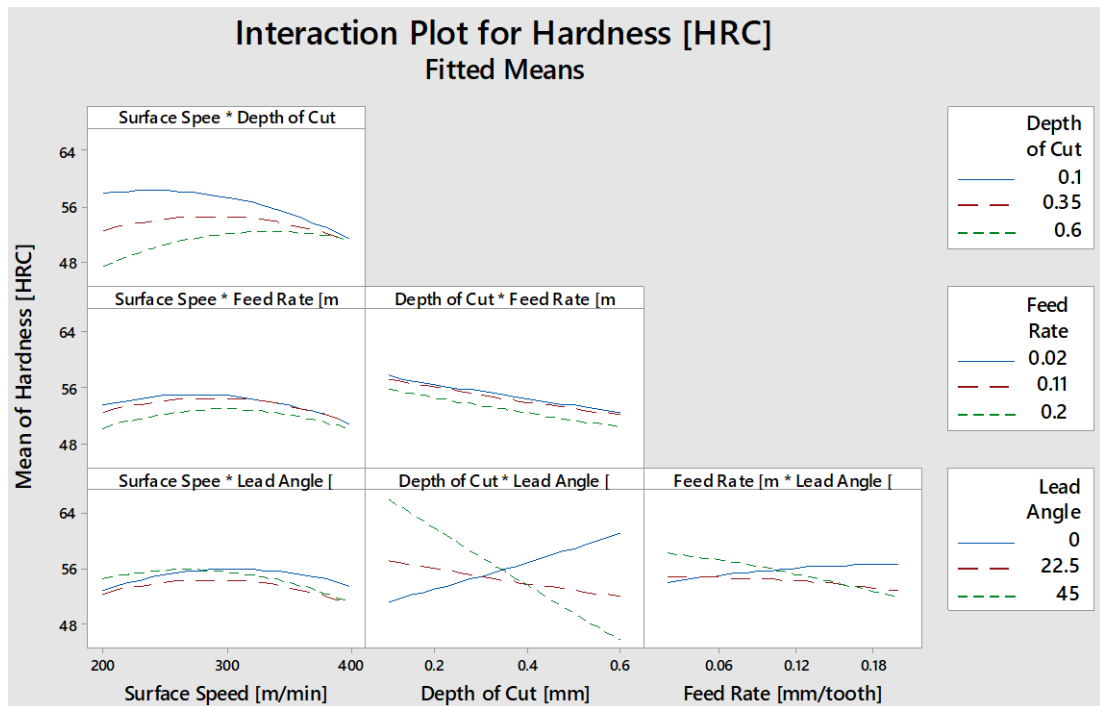


Figure 3.22: Machining parameter interaction plot for microhardness

In general a strong correlation between the factors doesn't exist. This indicates that when a factor changes the hardness value does not change significantly from the expected value due to the influence of other factors.

Figure 3.23 shows the surface response model of the most significant factor. The data shows that a total minimum of the function can be achieved with a maximum lead angle of 45° and a maximum depth of cut of 0.6 mm. However, by minimising one of these factors and maximising the others the maximum hardness can be reached.

SRM for Depth of Cut and Lead Angle

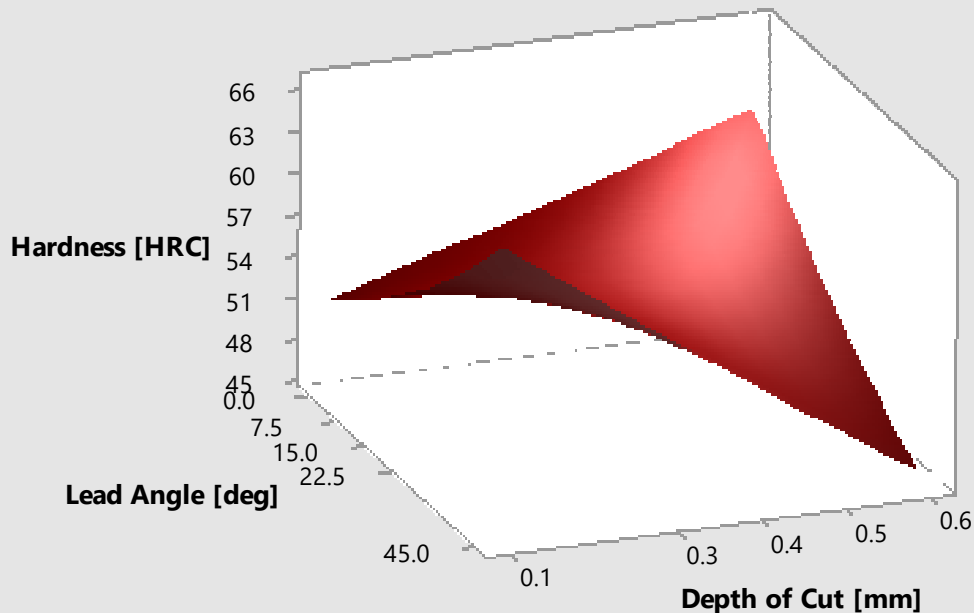


Figure 3.23: Surface Response Model for Depth of Cut and Tool lead Angle of Microhardness

3.4.4 Surface Roughness

The surface roughness is another parameter of surface integrity as presented in sections 2.2.3. and 3.3.3.5. The surface roughness is the most referenced indicator to surface quality, as it can be determined quickly and without adopting expensive or complicated metrology equipment. For this work however, a 3D scan of the surface was conducted to determine the surface roughness as R_a (2D arithmetical mean deviation of the measured roughness profile) and S_a (3D arithmetical mean deviation of the measured roughness profile).

Table 3.16 shows the results of the surface roughness profiles which are presented as R_a , S_a and S_z , (all in μm) where S_z is the profile height of the measured surface roughness profile. All results have a total tolerance of ± 315 nm, as mentioned in Section 3.3.3.5.

Table 3.16: Surface Roughness after Machining

Standard Order	S_a [μm]	R_a [μm]	S_z [μm]	Standard Order	S_a [μm]	R_a [μm]	S_z [μm]
1	0.725	0.722	37.916	20	1.600	1.562	62.427
2	0.840	0.812	97.906	21	0.903	0.818	56.956
3	0.658	0.552	57.828	22	1.265	1.401	61.402
4	1.140	0.963	26.403	23	1.036	0.943	104.48
5	0.626	0.528	61.098	24	1.208	1.128	28.351
6	0.703	0.784	61.448	25	0.473	0.419	57.997
7	1.326	1.098	58.968	26	1.389	1.099	62.187
8	0.734	0.675	47.590	27	2.171	1.995	68.217
9	0.700	0.674	60.962	28	0.926	0.838	59.377
10	1.028	0.895	57.329	29	0.822	0.747	56.155
11	0.916	0.855	53.614	30	1.262	1.182	58.679
12	0.784	0.760	50.069	31	0.947	0.803	56.017
13	1.142	0.958	61.607	32	1.064	1.005	60.741
14	1.066	0.815	47.082	33	0.465	0.423	55.080
15	1.042	0.993	59.963	34	0.948	0.809	61.536
16	0.684	0.697	59.783	35	0.819	0.767	58.652
17	1.184	0.982	60.431	36	1.678	1.604	58.608
18	0.888	0.916	61.313	37	1.366	1.182	56.790
19	0.825	0.892	64.590				

An ANOVA analysis was carried out for the 3D surface roughness profile S_a in Table 3.17 and it was found that the feed rate is the greatest factor in affecting surface roughness S_a , followed by the surface speed, depth of cut and tool lead angle respectively.

Table 3.17: Result of ANOVA for Surface Roughness S_a

Source	Adjusted Sums of Squares	Adjusted mean squares	F-Value	P-Value
Linear				
Surface Speed	0.163	0.163	1.41	0.248
Depth of Cut	0.089	0.089	0.77	0.390
Feed Rate	0.404	0.404	3.49	0.075
Lead Angle	0.017	0.017	0.15	0.703
Square				
Surface Speed * Surface Speed	0.055	0.055	0.48	0.498
Depth of Cut * Depth of Cut	0.027	0.027	0.24	0.632
Feed Rate * Feed Rate	0.146	0.146	1.26	0.274
Lead Angle * Lead Angle	0.027	0.027	0.23	0.634
2-Way				
Surface Speed * Depth of Cut	0.054	0.054	0.46	0.503
Surface Speed * Feed Rate	0.011	0.011	0.10	0.757
Surface Speed * Lead Angle	0.027	0.027	0.25	0.624
Depth of Cut * Feed Rate	0.013	0.013	0.11	0.741
Depth of Cut * Lead Angle	0.120	0.120	1.04	0.319
Feed Rate * Lead Angle	0.024	0.024	0.20	0.655
Error				
Lack-of-Fit	1.003	0.100	0.78	0.649
Pure	1.544	0.129		

Stemming from Table 3.17, Figure 3.24 shows the functions of the machining parameter to the surface roughness. The functions are almost quadratic.

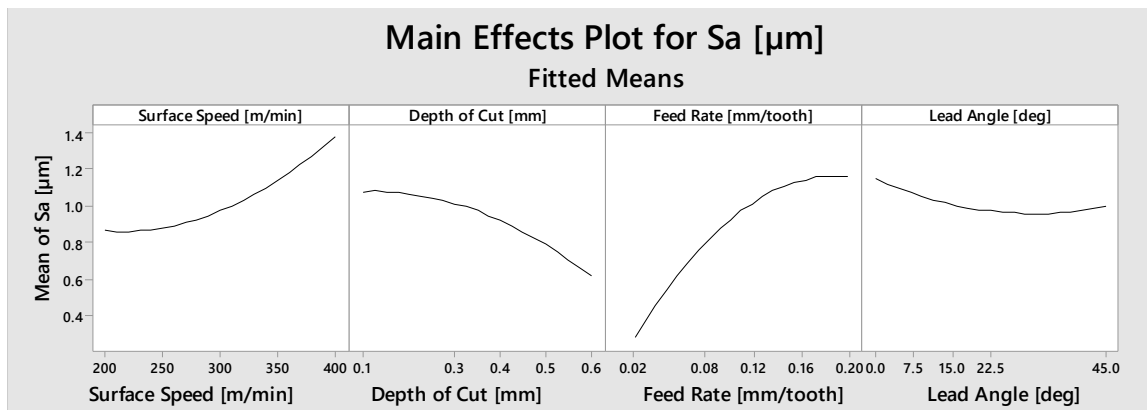


Figure 3.24: Main effects of machining parameter for Surface Roughness (S_a)

Figure 3.25 shows that the depth of cut and lead angle has a strong interaction. However, the surface speed and feed rate as well as depth of cut and feed rate did not interact.

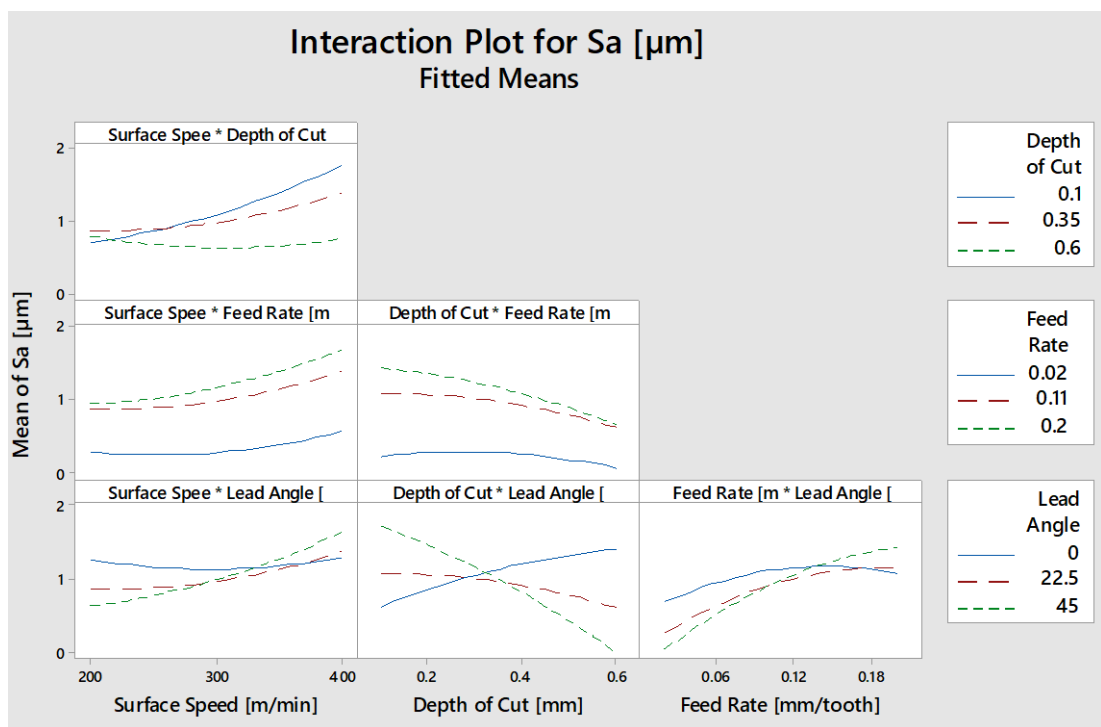


Figure 3.25: Machining parameter interaction plot for hardness

The interaction is not trivial since the feed rate and surface speed are the most influential factors. An increase of feed rate causes an increase in the linear

movement of the workpiece. Because, the relative motion of the workpiece is increased, the material cannot be completely removed as compared to lower feeds and spindle speed. This will increase the value of the machined surface roughness S_a .

Figure 3.26 illustrates the interaction of the depth of cut and the tool lead angle which has the strongest interaction. When both parameters are at their maximum values, a minimum of surface roughness can be achieved, assuming that the surface speed is at 300 m/min and the feed rate at 0.11 mm/tooth are fixed. However, if the depth of cut reduces or the lead angle decreases, the surface roughness increases. This is because of the interaction of the cutter and the workpiece; with any other combination they engage less and so more material is left over on the surface. When both parameters are on a low level, the surface roughness is also decreased as the engagement decreases and the cutter is 'rubbing' along the surface.

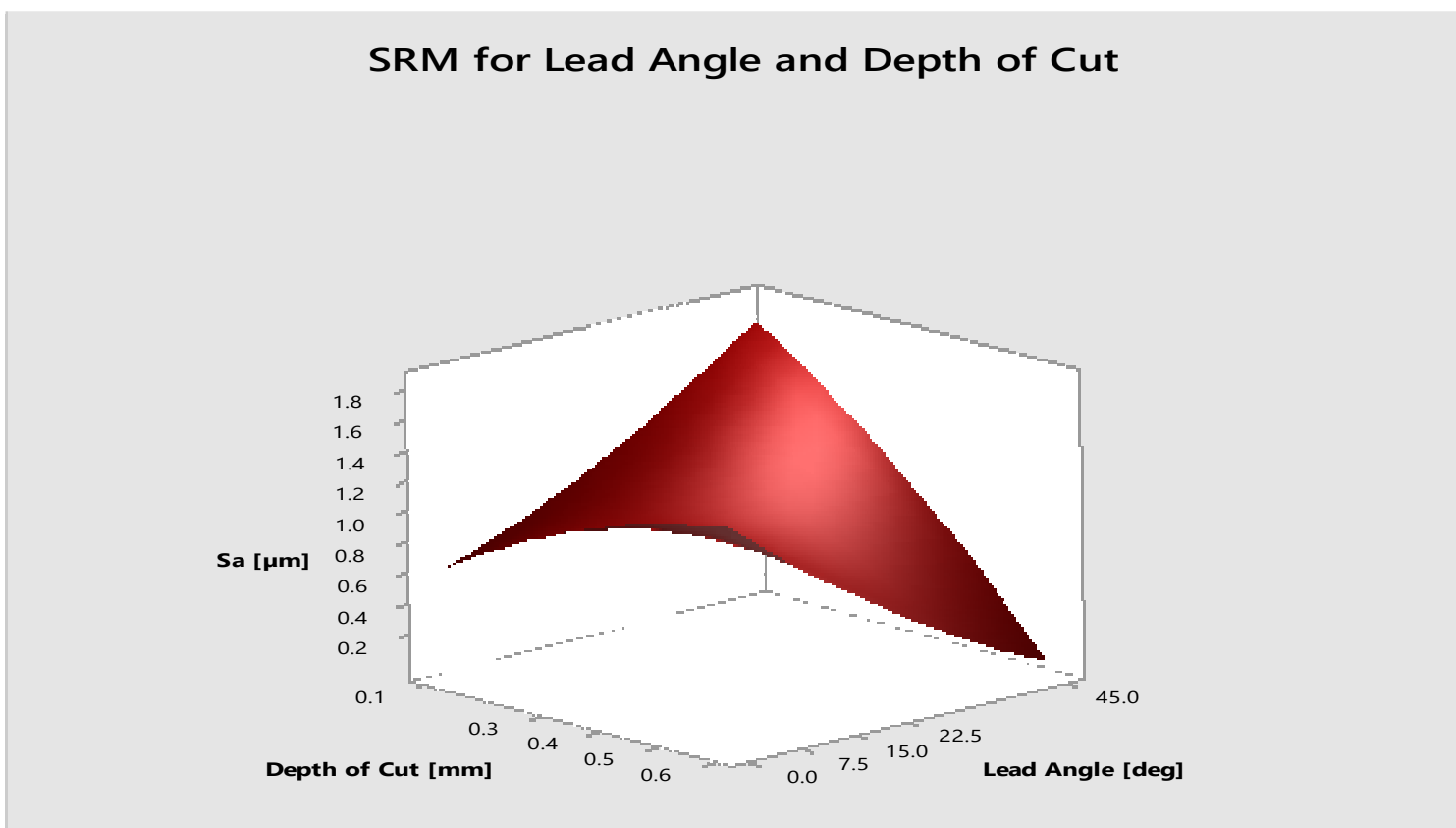


Figure 3.26: SRM for Depth of Cut and Lead Angle of Surface Roughness (S_a)

3.4.5 Macro- & Microstructure

The macro- and microstructure are two components of surface integrity. In this project the macrostructure of the surface was qualitatively analysed first, followed by the microstructure.

Figure 3.27 shows the topology of the workpieces, which are ordered by workpiece number. The figure is also presented in a higher resolution in Appendix III Surface Topology. It was found that the surface topology could not be related to any fatigue life prediction or improvement. Therefore, the macro surface topology will not be discussed any further in the following section of this work. However, the high spatial frequency patterns (which is essentially the surface roughness) are influenced by the machining parameters. The most significant influences of the pattern were found when changing the feed rate and the lead angle.

It was observed that with a lower feed rate the macrostructure becomes finer, as it can be seen in workpieces 3, 19, 24, 35, 36. On the other hand when the feed rate is high the pattern becomes "larger", as it is shown in, i.e. workpieces 4, 9, 23, 29. This behaviour is consistent with the value of the surface roughness. With the change of the tool lead angle, the topology changes to typical patterns within the used lead angle, as shown in workpieces 12, 13, 14, 17, 18, 28 at a lead angle of 15°. Additionally, it was observed that any an increase in the lead angle will lead to increase of the pattern angle.

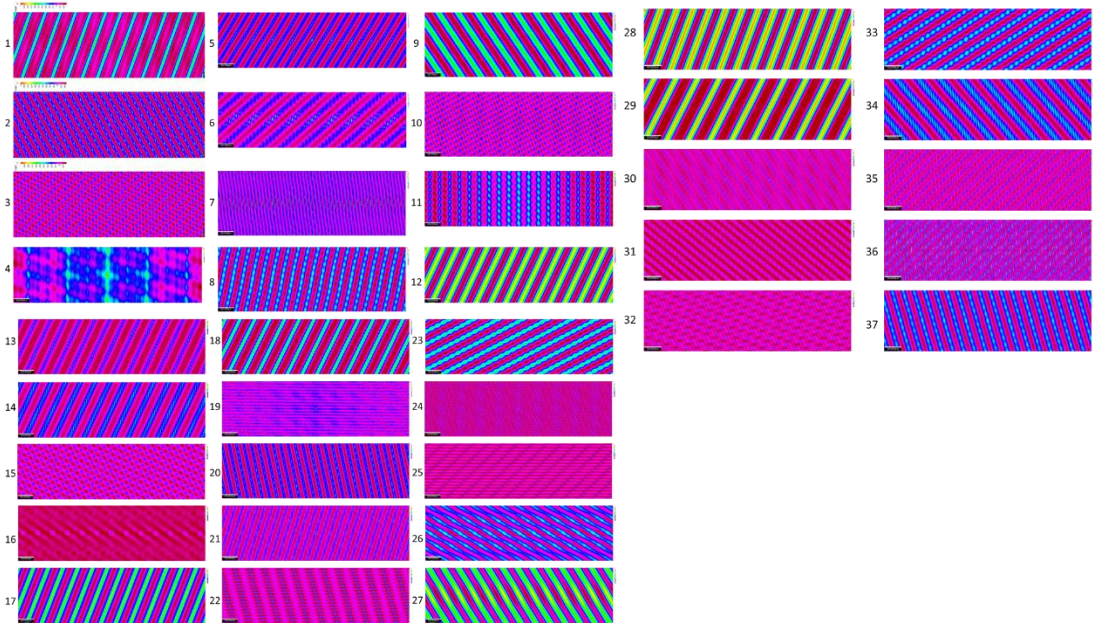


Figure 3.27: Surface topography of machined surfaces

Figure 3.28 shows an example of the microstructured surface of a workpiece after machining and before fatigue testing. It shows that there are no visible crack initiation points. However, the machined pattern can be identified from the topology analyses.

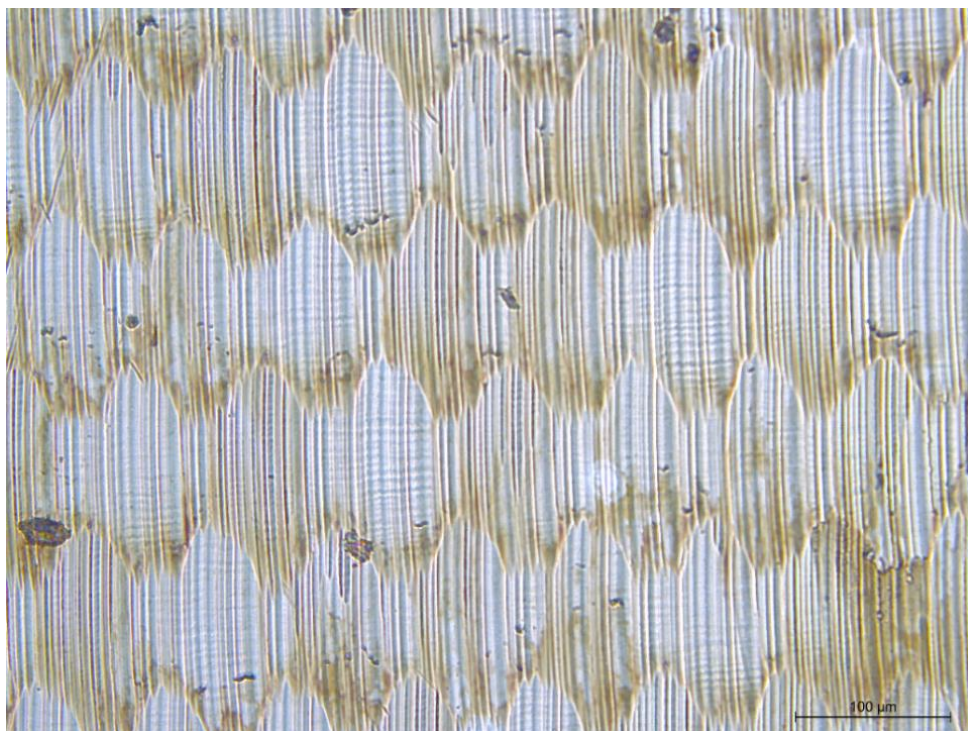


Figure 3.28: Surface Microstructure of Fatigue Workpiece 24

The microstructure of the workpiece is homogeneous before any machining operation has been conducted. As shown in Figure 3.29, the grain structure continues to be homogeneous from the workpiece edge to the bulk material. However, some porosity throughout the material can be seen, which can influence the performance of the material and therefore workpiece. The porosity can come from the supplier's heat treatment process. However, the pores are small, with the maximum size of less than $2\ \mu\text{m}$ and in average $0.6\ \mu\text{m}$. Furthermore it can be seen, that the pores are homogenously distributed, which also contributes to a less severe effect cause by porosity during the fatigue. In this research no action against the porosity was taken since the experiments should reflect the fact that manufacturers do not typically do not take any action to reduce the porosity unless it is severe.

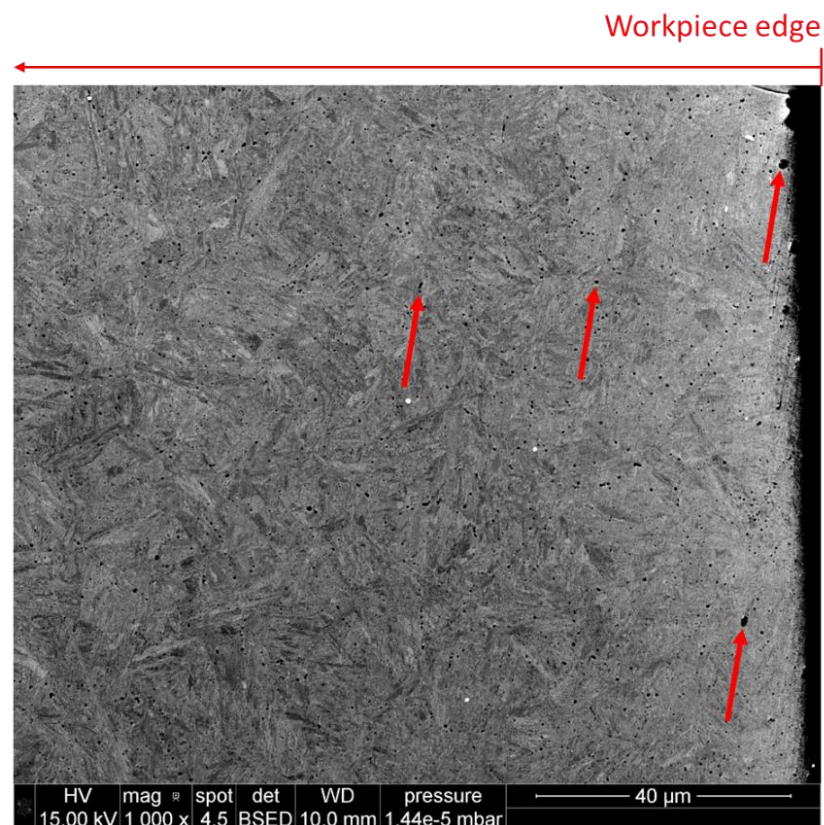


Figure 3.29: Workpiece microstructure of raw material

After the machining experiment a few sample workpieces were taken for analysis in order to examine if the machining process had any significant effect on the microstructure. Figure 3.30 illustrates that there was no noteworthy

change of microstructure from the workpiece surface into the bulk material. Therefore, only random sample workpieces were inspected, at this stage.

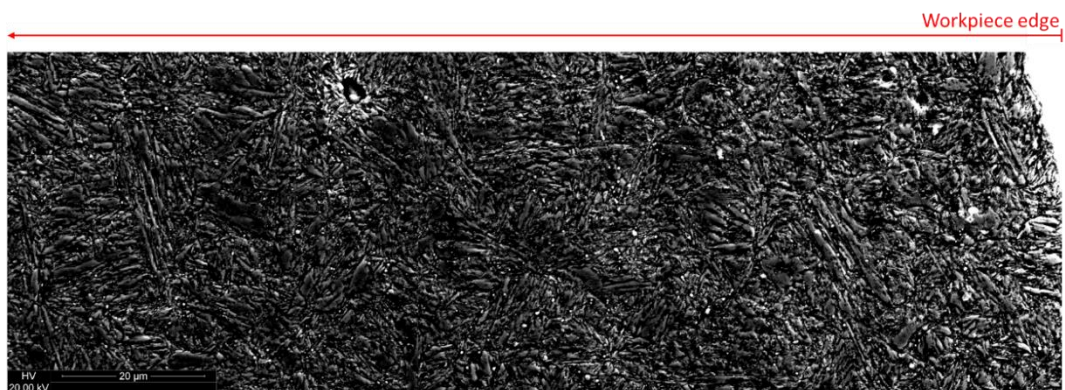


Figure 3.30: Microstructure of fatigue workpiece after machining

3.5 Summary

In this chapter the machining experiments were discussed and presented. At the start the design of experiments was presented along with the experimental set-up; this included the boundary condition for this experiment. The experimental procedure and the measurement equipment and procedure of the surface integrity (SI) were then introduced. Near the end the results in the form of surface integrity, including the cutting force from the machining experiment, were illustrated and analysed. For all outcomes ANOVA analyses were carried out to identify the most influential factor for every SI parameter and to identify and understand the behaviour of the interaction of every factor in every SI-parameter. It was found that the tool lead angle had the most significant impact on the cutting force. The residual stress was mostly influenced by the surface speed, as was the microhardness. However, it was found that the feed rate had the most significant influence on both surface roughness and microstructure / topology. These results on the surface integrity are significant as they will influence the fatigue life of the workpiece which will be studied in the following chapter. A good understanding of the influence of machining parameter is also crucial for the optimisation of machining process to obtain long fatigue life which will be studied in Chapter 6.

Chapter 4 Experimental Evaluation of Fatigue Life

This chapter concerns, the experiment to determine the fatigue performance of the machined component. It includes the experimental setup, design iterations and experimental results.

4.1 Introduction

Literature has shown that in fatigue testing the four-point bending experiment is the closest approximation to the real forming and forging applications [47, 48, 96]. Most of the publications on this subject used room temperature and high cycle fatigue [7, 8, 18, 47, 48, 96, 140]. However, it is more critical to test the material under an elevated temperature due to its working environment. Furthermore, in the process the high cycle fatigue is not as critical as low cycle fatigue due to its much shorter life cycle and increased costs. Therefore, the fatigue tests were carried out in this study instead of the real forming test in order to demonstrate how different machining strategies impact die life.

As an essential part of this work, a four-point cyclic fatigue experiment was carried out to simulate the fatigue performance on parts using different machining strategies. The experiment supports the development of the prediction model for fatigue life and optimisation model for milling process. Afterwards, the fatigue life can be evaluated through surface integrity instead of machining parameters, because there is no direct link between fatigue life and the machining parameters.

4.2 Experimental set-up and procedure

The four-point cycle fatigue was carried out on a Zwick Roell HA250 under an elevated temperature of 250 °C, and a low cycle fatigue load was applied. In this experiment, 85 % of the relative Ultimate Tensile Strength (UTS) in elevated temperature was applied. The UTS of AISI H13 can reach up to 1990 MPa in room temperature [145] (and a yield strength $R_{p0,2}$ of 1660 MPa), and at the elevated temperature of 250 °C the UTS reduces to around 1700 MPa (around 85 % of UTS in room temperature, Yield Strength is around 1410 MPa). The load can be calculated from the cross-section of the workpiece multiplied with applied stress; this results into a maximum load of 175 kN whereby 1445 MPa is 85 % of the UTS (at elevated temperature) and 120 mm² (15 mm x 8 mm) the cross-section (1445 MPa · 120 mm²). Therefore, the test could be carried out on the fatigue limit of the workpiece and material. The minimum load of 17.4 kN was applied. This left a force ratio of 0.1 and the values are shown in Table 4.1.

Table 4.1: Fatigue performance setup parameter

UTS [MPa]	Max Stress [MPa]	Max Load [kN]	Min Stress [MPa]	Min Load [kN]	Stress / load ratio [-]	Elevated Temperature [°C]	Frequency [Hz]
1990	1445	175	145	17.4	0.1	250°C	4

The machine runs on a cycle frequency of 4 Hz to reduce the test time as much as possible, but it maintains the consistent stress ratio throughout the experiment. However, higher frequencies were tested in preliminary trials but the machine was not able to maintain force cycles required.

In Figure 4.1 the force flow of the test rig is schematically presented. Due to the force flow it can assume that at the location of the interaction with the workpiece and die will be the failures typically occurred. Furthermore, this examination ensures that the force flow is equally distributed through the workpiece.

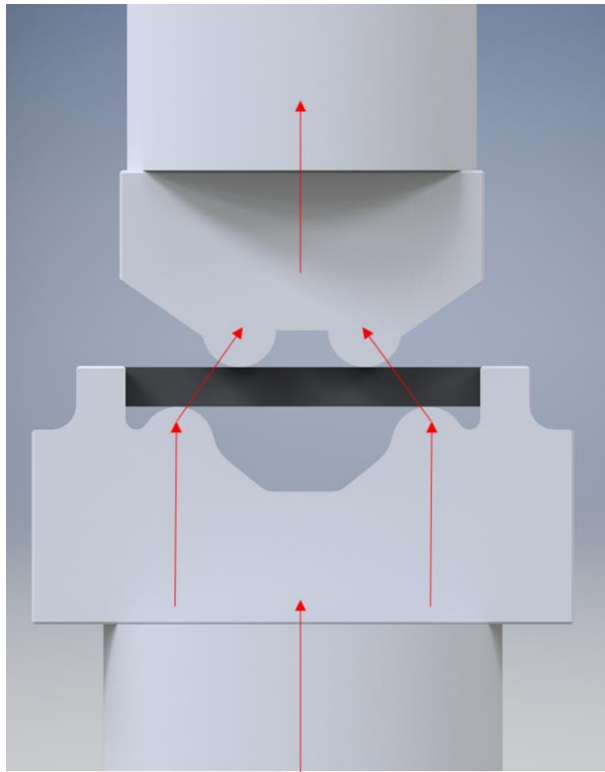


Figure 4.1: Force flow in four-point bending test

4.2.1 Equipment and Tools

The fatigue tests were carried out by performing a four-point bend test. The four-point bending test is the closest test to cyclic fatigue behaviour in a forming die. For the experiment a Zwick Roell HA250 was used, with a maximum load of 250 kN. The experiment was carried out at an elevated temperature in an environmental chamber from Severnts (EC2112). The complete fatigue experimental set-up is shown in Figure 4.2.

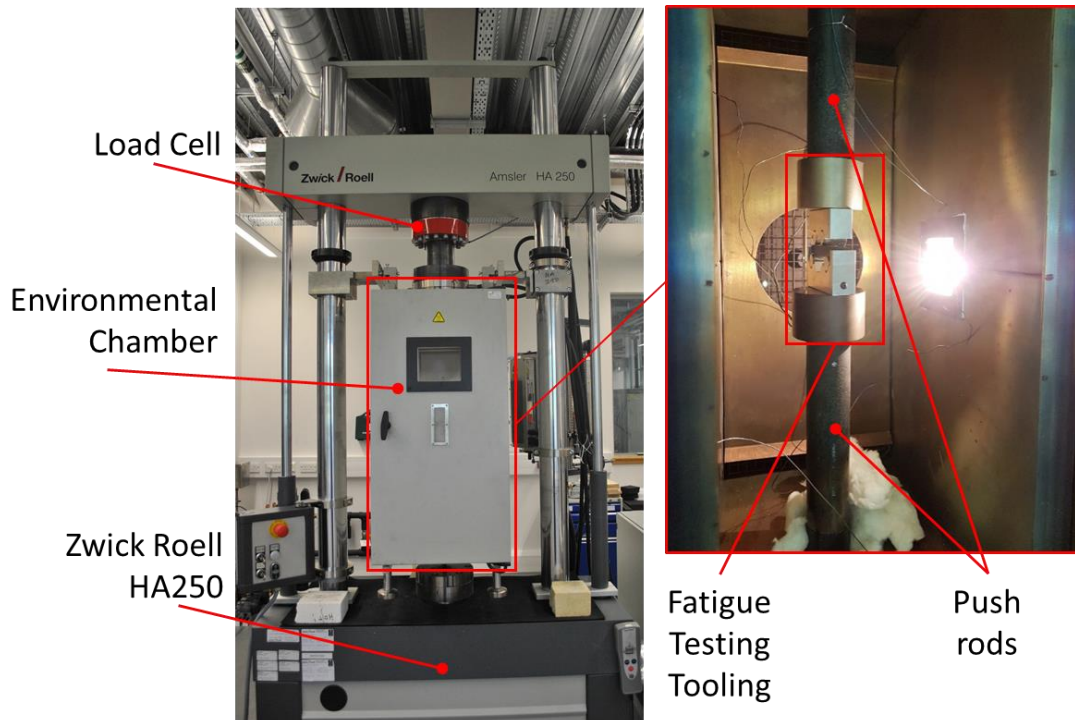


Figure 4.2: Fatigue Testing Set-up

Figure 4.2 shows the environmental chamber attached to the hydraulic press. The pushing rods are holding the fatigue workpiece fixture and the workpiece. The environmental chamber can be closed to maintain the elevated temperature.

For this part of the work the four-point bending tooling was central. Quotes for standard tool rigs from Zwick-Roell were obtained, but other tooling for this set-up was available more cheaply and was also a more accurate solution than the general tooling from the OEM. The design took several iterations to allow a good and robust experimental procedure.

The test tooling was designed to have individual parts, based on a modular system. This allows the end-user to quickly and easily change worn parts or change parts with a different geometry without the need to replace the entire fixture. The complete test rig consisted of 10 parts.

The tooling was manufactured from AISI D2 and sourced by Cogne UK Ltd. It comprised the average composition shown in Table 4.1. AISI D2 (X155CrMoV121, 1.2379) is generally used for cold working environments such as rolling dies, blanking dies and cold rolling rolls. For this project a more robust and hard steel than AISI H13 in a reasonable price range needed to be selected. Therefore, AISI D2 was selected to withstand the high forces during the forming experiment.

Table 4.2: AISI D2 - Material composition - as received material

C	Si	Mn	S	P	Cr	Mo	V	Ni	Cu
1.47	0.36	0.32	0.01	0.024	11.60	0.80	0.77	0.0	0.0

Based on the recommended guidelines by the material manufacturer, heat treatment was carried out to harden the material after the machining process. In Figure 4.3, the Temperature-Time-Table is illustrated.

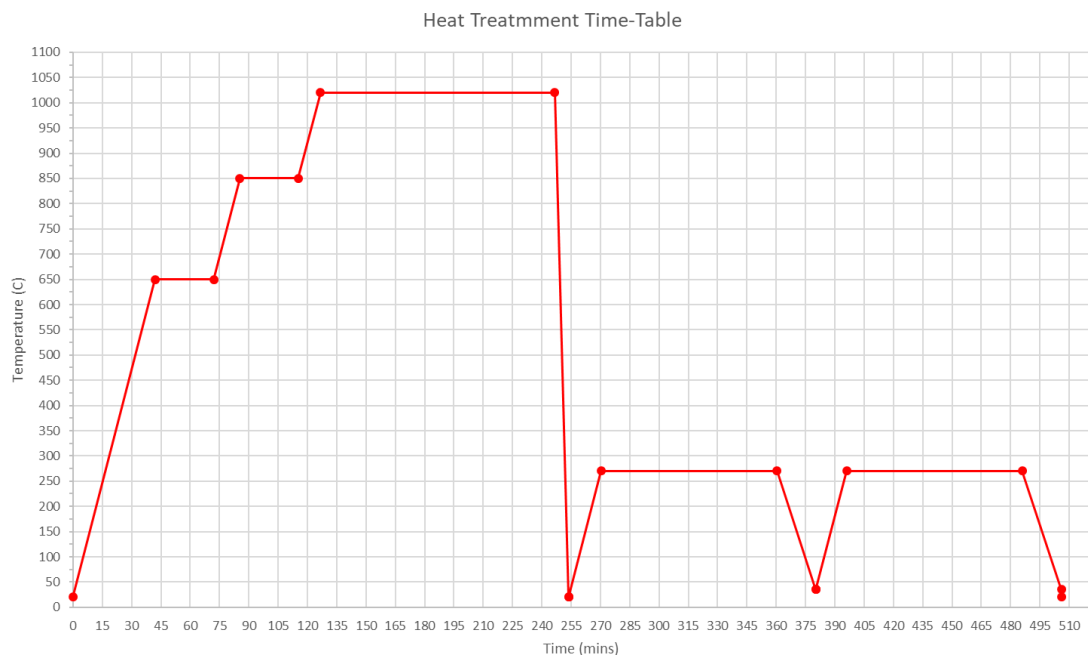


Figure 4.3: Heat treatment temperature-time-table

The heat treatment itself was carried out in a precision vacuum oven on site. The part was preheated in different stages and at different dwelling times. Figure 4.3 shows that once the Austenitizing temperature of 1020 °C was reached it was maintained for about 2 hrs to make sure all the parts were thoroughly heated. These were then gas quenched using 2-6 bar Nitrogen (N₂). After quenching, the parts were twice tempered up to 270 °C. A hardness of 58 HRC in the 4-point bend test rig was targeted to ensure the test rig could withstand the low cycle fatigue pressure when deforming AISI H13 workpieces.

As mention above, the working temperature for this experiment was set to 250 °C also to avoid a change in microstructure of the dies, as the dies were tempered on a higher temperature. An increase of the experimental temperature of 250 °C would cause a loss of the features derived from tempering, such as hardness and toughness, as shown in Figure 4.4. The derived hardness is based on the solution temperature and the tempering temperature.

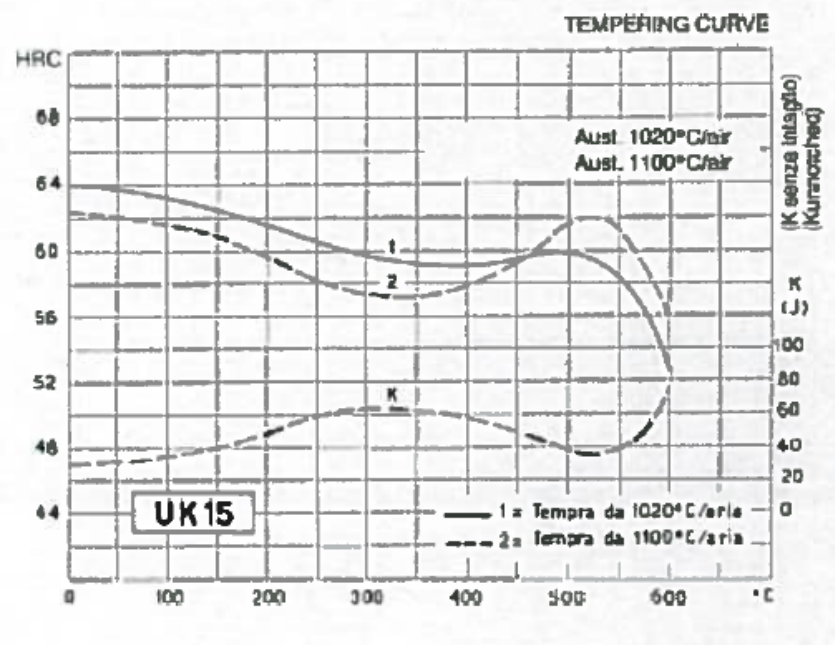


Figure 4.4: Tempering Curve [146]

Following heat treatment the hardness of the components were measured and compared with the hardness of the received material. The results are shown in Table 4.3.

Table 4.3: Fatigue die hardness [HRC] before and after heat treatment

Material as received	Lower tool base	lower tool	Fatigue toolbar	Upper tool	Upper tool base
22	58.0	57.8	58.4	57.8	59.5

Table 4.3 shows that the material was received in a softened state to manufacture components efficiently; after heat treatment the hardness increased significantly to the targeted 58 HRC.

The first test rig was manufactured as shown in Figure 4.5 using the above-described material heat treatment.

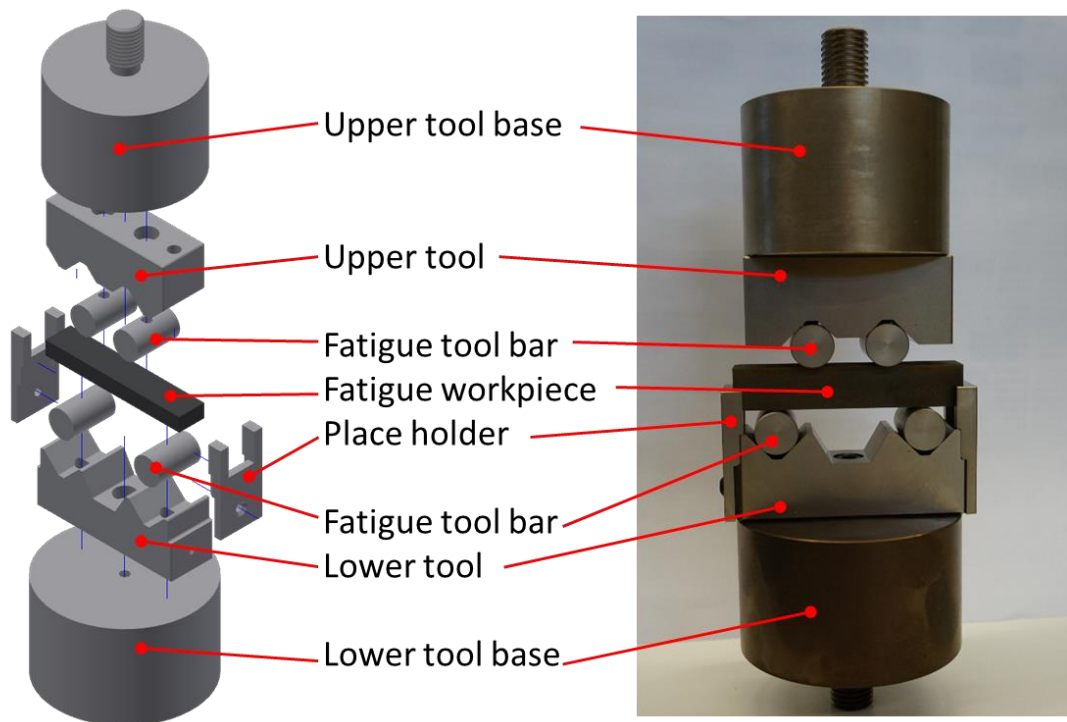


Figure 4.5: Four-point bend test rig – first die design

The advantage of this design was its modularity; the balance of parts meant they could be exchanged at low cost. However, it was found that after running a preliminary trial on this test rig the shear forces were simply too high for the set parameters on this test rig; the result was a broken test rig. The final state of the bottom die can be seen in Figure 4.6.

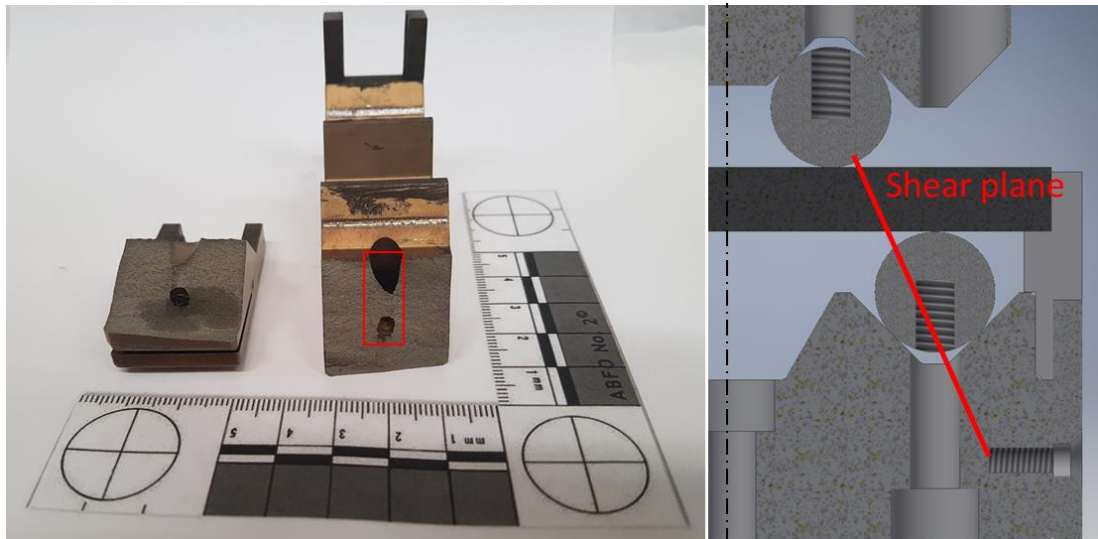


Figure 4.6: Breakage of the 1st design of the four-point bending die

It is evident from this analysis that the crack has propagated from the tapered screw holes where the test rig had its weak point. This is indicated by the red line in Figure 4.6.

The next design iteration considered these shear forces during the cyclic fatigue experiment and gave them a higher priority. All parts were entirely redesigned, excluding the tool base. In the second design iteration, a different approach was used. All parts were made from one solid block, as shown in Figure 4.7. This new design had the advantage of the manufacturing easiness; the shapes can be cut by EDM and the hole for the workpiece guidance and centre hole can be machined and drilled (reduced production time). Furthermore, its robustness under fatigue cycles has increased significantly, because no tapered holes exist in the identified shear plane of the experiment. However, the disadvantage of this design is that the parts are not replaceable. If a feature fails or wears out the complete unit needs to be replaced.

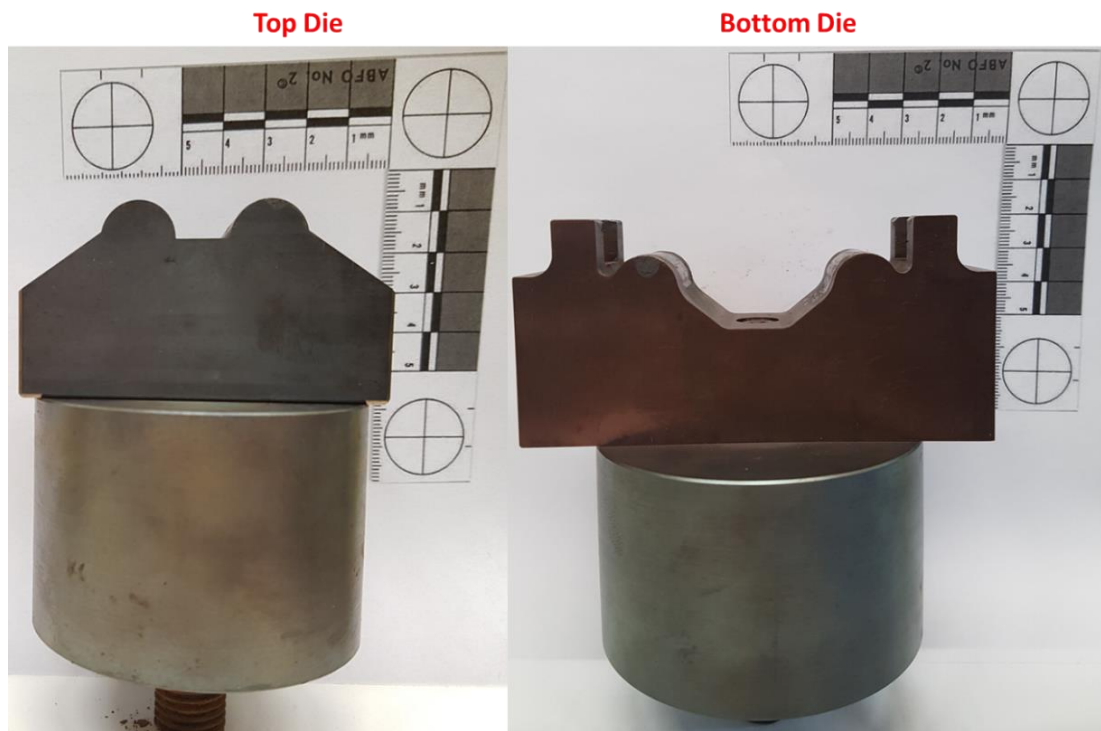


Figure 4.7: Second design iteration of the four-point bending die

4.2.1 Experimental procedure

All workpieces were measured before running the trials on the machine. This would ensure accurate results in terms of dimensions and potentially explain outliers. A variation of the measured dimension can be found in Figure 4.8. All shown measurements illustrate an average of four measured points on the workpiece – an example is shown at the top left corner. Furthermore, the findings show that the critical dimensions have a maximum variation of 0.06 mm for thickness and 0.07 mm for the width of the workpiece. The average value of all workpieces was calculated for length, thickness and width and came out at 79.98 mm, 8.00 mm and 14.97 mm respectively.

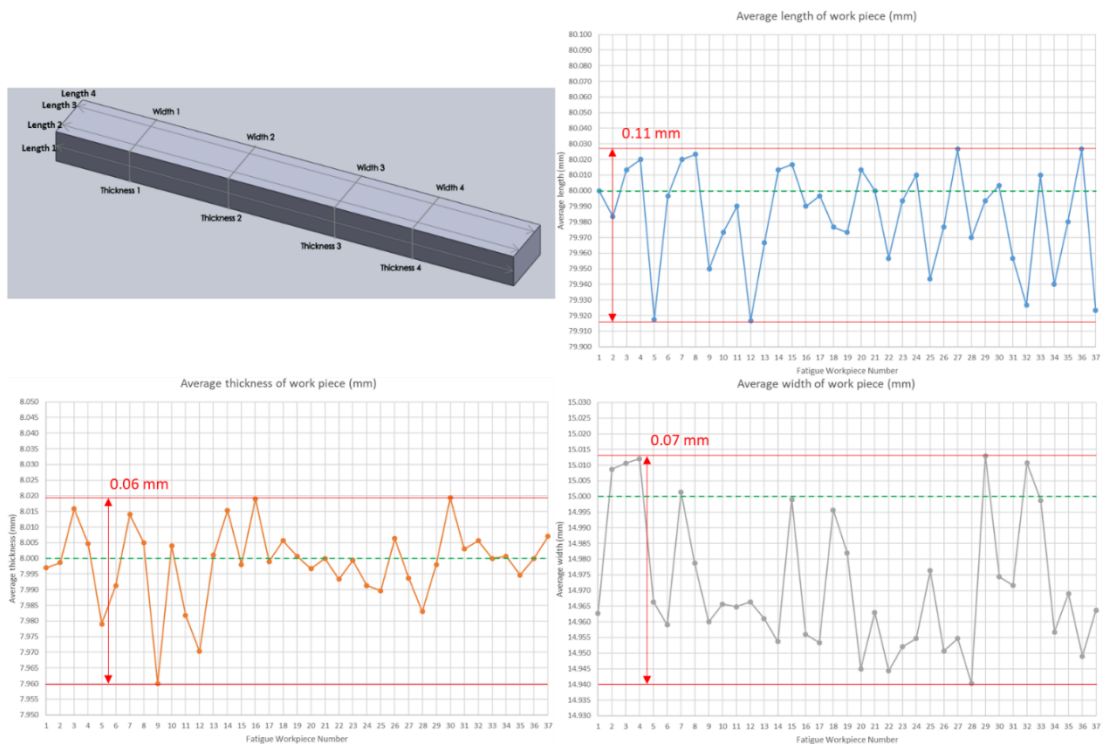


Figure 4.8: Geometrical measurements of fatigue workpieces before fatigue testing

The experimental procedure was standardised to ensure comparable results throughout the entire experiment. The following steps were implemented:

1. Preheat chamber to a constant level of 250 °C.
2. Selection of workpiece according to DoE.
3. Prepare to place the sample in the chamber.
4. Open heating chamber.
5. Place workpiece precisely in the middle of the bottom die.
6. Align top and bottom die parallel to each other.
7. Close heating chamber.
8. Wait until the temperature of 250 °C has been reached.
9. Soak workpiece with a temperature of 250 °C for 12 minutes.
10. Start cycle fatigue experiment.

The soaking time was applied to achieve a more equal condition within the workpiece from the start, as different temperature distribution in the work piece could influence the results.

The start of a recorded cycle can be found in Figure 4.9. Before reaching 55 % (99 kN) of the total load the force increases linearly by 1 kN/s.

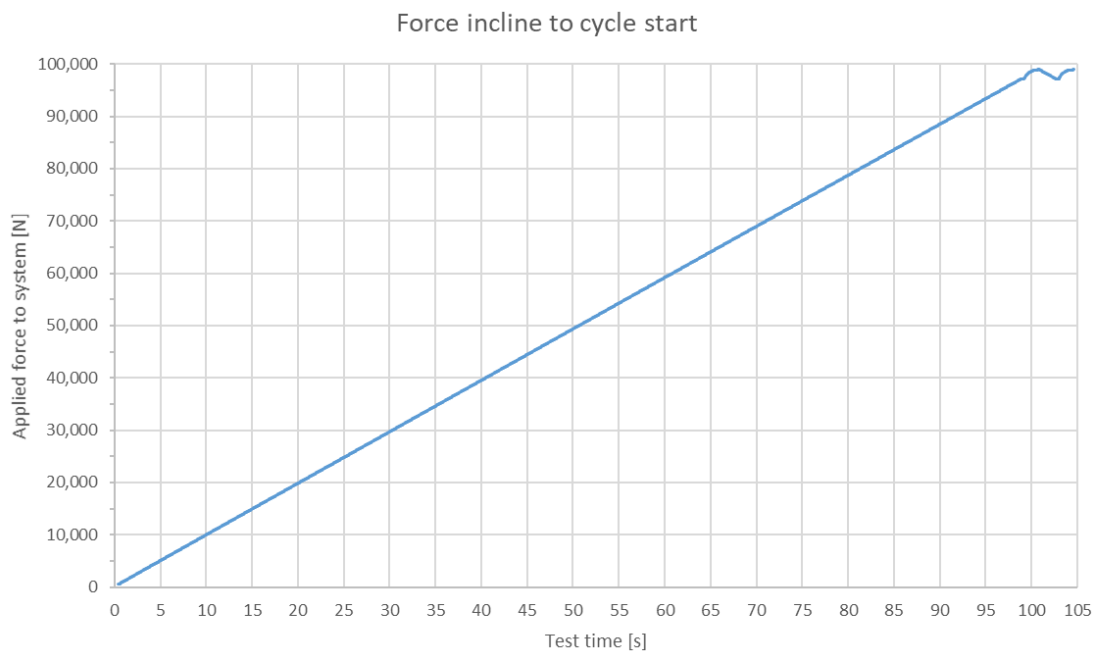


Figure 4.9: Force incline rate to start of the experiment

From Figure 4.10 it can be seen that the force builds up gradually in the first few cycles and then stabilise at the target values. The cycle intervals were set to a sine-wave formation. The increase towards the final force has no effect on the results since the applied forces are lower than the experimental set values of 175 kN. The lower boundary reaches 15 kN, which is around 2.5 kN under the set value. However, the difference of 2.5 kN will have no impact on the test results as it relates to the amplitude (160 kN) which has a margin of less than 2 %.

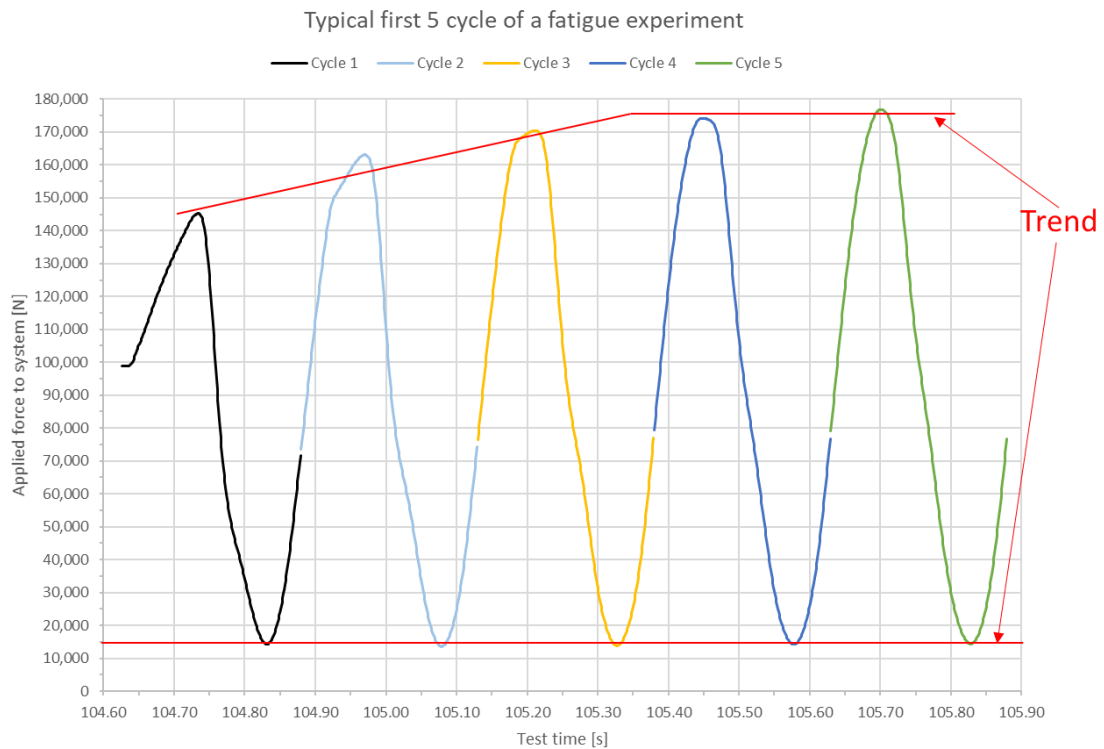


Figure 4.10: First five cycles of fatigue experiment

4.3 Analysis of the Influence of Surface Integrity on Fatigue Life

Fatigue life is an important economic factor to budget tooling costs. Under critical conditions tool life is hugely reduced and replacing them incurs further expense. Therefore, extending tool life is essential in reducing the overall production cost of a forming and forging product. These critical conditions were simulated and analysed in the fatigue test conducted as part of the experiments. The workpieces were stressed at an elevated temperature of 250 °C until a total failure of the workpiece occurred. The fatigue test is carried out with the same parameters.

Table 4.4 lists the measured surface integrity and the fatigue life.

Table 4.4: The Central Composite Design of the experiment for fatigue tests

Standard Order	Surface Speed	Depth of Cut	Feed Rate	Lead Angle	S _a [μm]	S _z [μm]	Hardness [HRC]	Residual Stress [MPa]	Cycle [-]
1	1	-1	-1	-1	0.725	37.916	51.82	165.75	25443
2	-1	1	-1	-1	0.840	97.906	55.64	113.74	10406
3	-1	-1	1	-1	0.658	57.828	52.65	103.04	17572
4	1	1	1	-1	1.153	26.403	57.18	115.29	4855
5	-1	-1	-1	1	0.626	61.098	55.38	158.42	4506
6	1	1	-1	1	0.703	61.448	54.45	147.96	48194
7	1	-1	1	1	1.326	58.968	52.59	150.59	6199
8	-1	1	1	1	0.734	47.590	52.57	109.34	5236
9	0	0	0	0	0.700	60.962	55.66	130.19	3071
10	0	0	0	0	1.028	57.329	53.90	114.23	6453
11	-1	-1	-1	-1	0.916	53.614	55.87	130.71	4598
12	1	1	-1	-1	0.784	50.069	57.10	113.21	12245
13	1	-1	1	-1	1.142	61.607	53.98	108.17	3622
14	-1	1	1	-1	1.066	47.082	55.61	125.97	5293
15	1	-1	-1	1	1.042	59.963	56.42	159.22	14894
16	-1	1	-1	1	0.684	59.783	55.36	181.53	4803
17	-1	-1	1	1	1.184	60.431	55.42	119.38	5550
18	1	1	1	1	0.888	61.313	53.50	159.77	10082
19	0	0	0	0	0.825	64.590	56.17	181.39	3669
20	0	0	0	0	1.600	62.427	53.98	113.02	5045
21	-2	0	0	0	0.903	56.956	51.07	121.46	5375
22	2	0	0	0	1.265	61.402	51.62	145.89	4813
23	0	-2	0	0	1.036	104.480	55.19	133.68	5365
24	0	2	0	0	1.208	28.351	51.83	146.98	4752
25	0	0	-2	0	0.473	57.997	54.09	173.96	6016
26	0	0	2	0	1.389	62.187	54.03	208.02	2940
27	0	0	0	-2	2.171	68.217	57.96	198.11	4117
28	0	0	0	2	0.926	59.377	52.19	161.02	5491
29	0	0	0	0	0.822	56.155	51.27	120.47	4384
30	0	0	0	0	1.262	58.679	52.02	153.30	10575

Table 4.4 shows that the overall average fatigue performance lasts around 7150 cycles. During the analysis obvious outliers were not considered.

A relation between the surface roughness and fatigue life was studied, in the first instance. Regression Analysis was carried out to determine the most influential factor. The results from the regression analysis are shown in Table 4.5. In this analysis, the most influential elements were the surface roughness (S_a), hardness and Von-Mises residual stress; the cyclic fatigue does not have a direct link to the machining parameter [20]. Table 4.5 shows the coefficients of the regression analysis and these results can be used to model a cyclic fatigue prediction, whether linearly or polynomial.

Table 4.5: Regression Analysis of Cyclic Fatigue

Term	Coefficients	Standard Error Coefficient	T-Value	P-Value
<i>Constant</i>	21629	47421	0.46	0.652
<i>Surface Roughness S_a [μm]</i>	-7646	5062	-1.51	0.143
<i>Hardness [HRC]</i>	-153	884	-0.17	0.864
<i>Residual Stress (VM) [MPa]</i>	20.1	60.6	0.33	0.743

From the regression analysis, it can be concluded that the surface roughness is the most significant aspect in fatigue, followed by the residual stress and hardness, respectively. This information can be used in the optimisation and prediction model.

In the following two graphs (Figure 4.11 and Figure 4.12) outliers were removed from the visual graph, however not from the equation.

In the following Figure 4.11 the relationship between fatigue life and the surface roughness S_a is shown. The graph illustrates that with decreasing surface roughness the fatigue life increases.

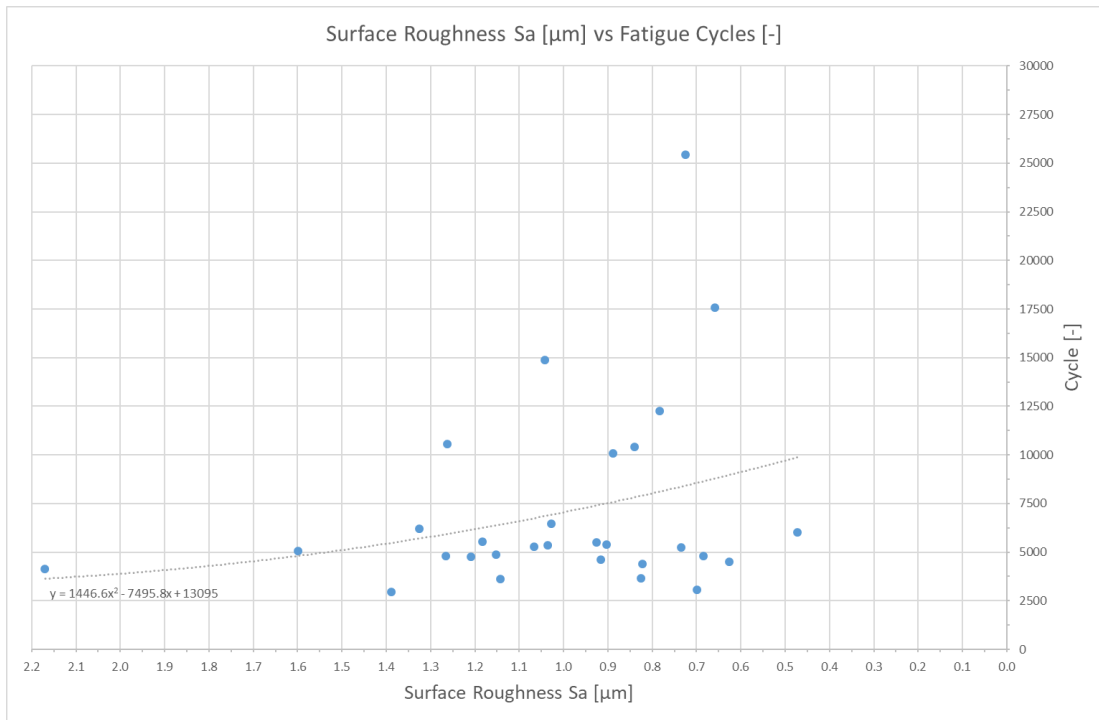


Figure 4.11: Interaction of Surface Roughness S_a [μm] and Fatigue Cycles [-]

The increase of fatigue life combined with a decrease in surface roughness is expected since the smoother the surface the fewer the defects, and therefore the fewer the number of crack initiation points.

Figure 4.12 shows the relationship of microhardness and fatigue cycles. The illustration shows that with increasing hardness the fatigue cycles are decreasing. The harder the material the greater the UTS strength of the workpiece. However, it also reduces the ductility of the workpiece due to the increased ratio of Martensite in the material. Figure 4.14 illustrates that the characteristic lamellar Martensite structure is more prevalent on the left side (higher hardness) than it is on the right side (lower hardness).

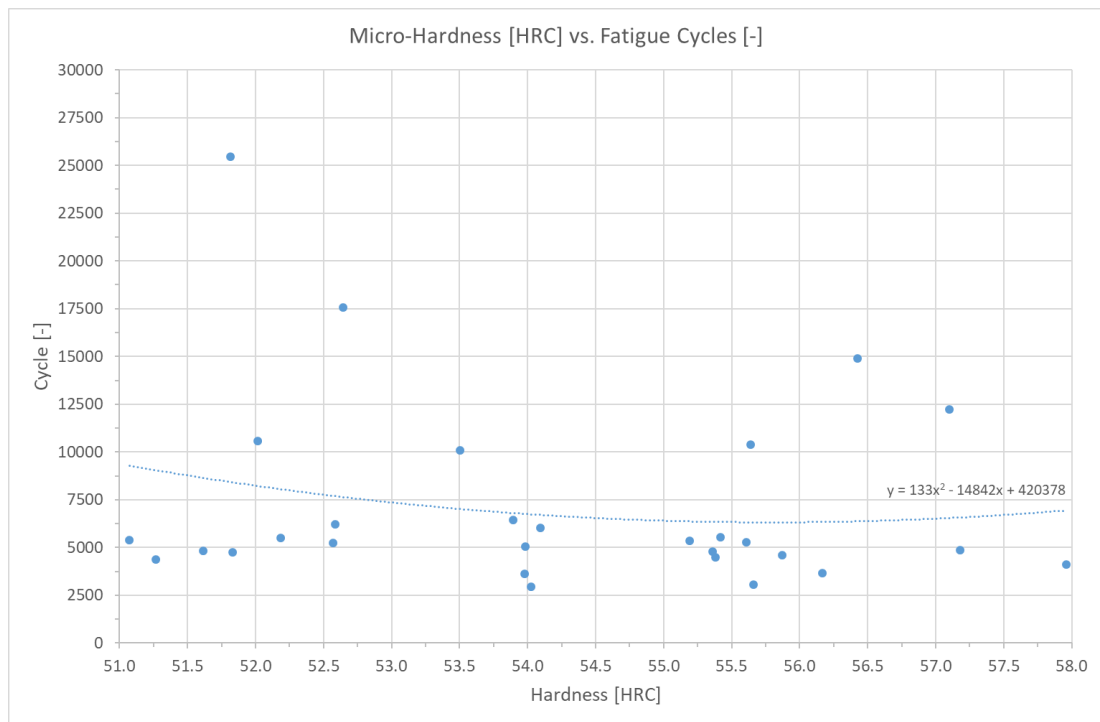


Figure 4.12: Interaction of Micro-Hardness [HRC] and Fatigue Cycles [-]

Figure 4.13 (a) shows the cross-section hardness map of the unformed material. A comparison between both states shows that the material hardness changes during the cycle test due to the high pressure and temperature during the experiment.

In Figure 4.13 (b) a cross-section hardness maps of a deformed workpiece (after fatigue test) workpiece is shown. The hardness was measured using 0.5 kgf and a distance between the measurements of 0.5 mm in x- and y-direction. The hardness map shows that the cycles have softened the material overall. The top part of the workpiece increases in terms of hardness, whereas at the bottom half it decreases. This change of hardness is due to the position of the workpiece in the fatigue rig: the bottom side of the workpiece is elongated and the top half is higher compressed. This deformation causes a change in the microstructure.

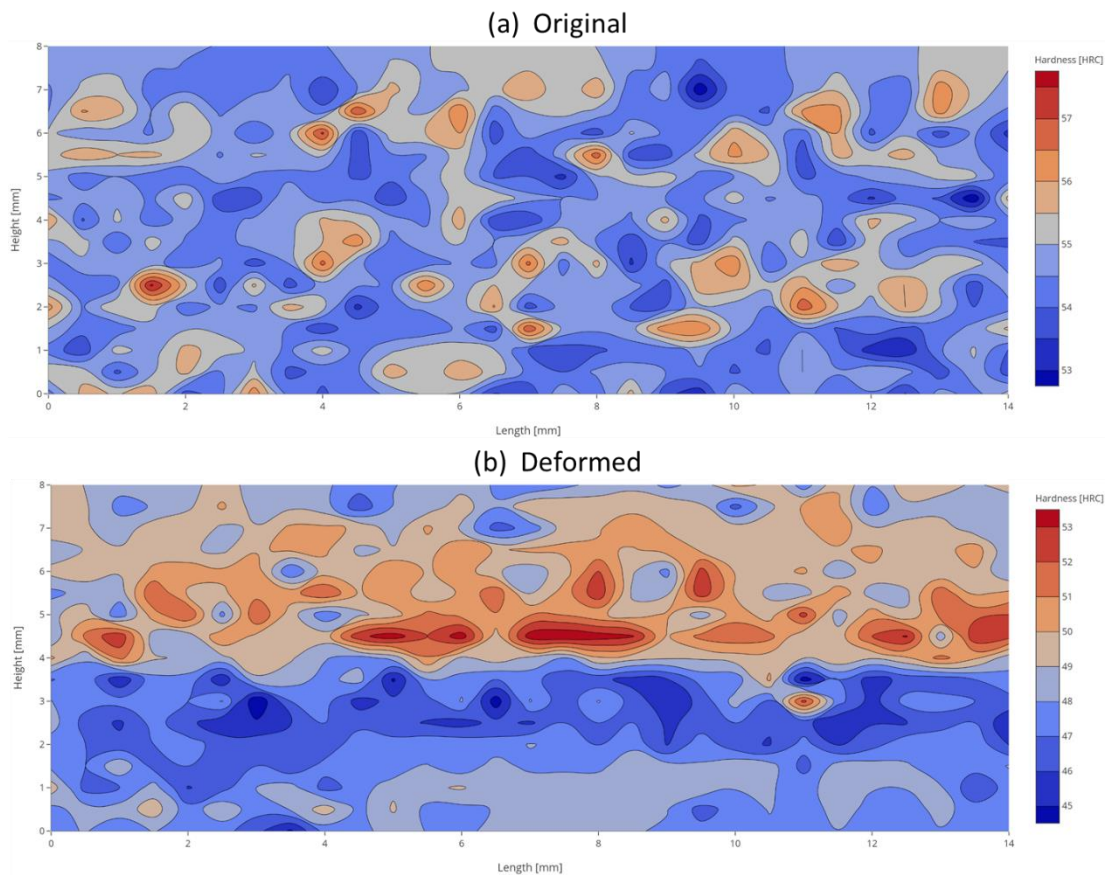


Figure 4.13: Hardness Cross-section original and deformed comparison

As mentioned in Figure 4.14, the microstructure of different hardness is illustrated. In the left picture a harder workpiece is displayed, and on the right a softer one. In the left image we see an increased number of the lamellar martensitic structure – this increases the hardness typically in a material. However, harder steel combined with an increase in the number of the martensitic lamella make the material more brittle (this was discussed in section 2.2.2). During the cycle fatigue testing these lamellar structure break down and the material softens. The image to the right shows a similar softer material-state of the same steel AISI H13. It is evident that this grain structure is less lamellar martensitic.

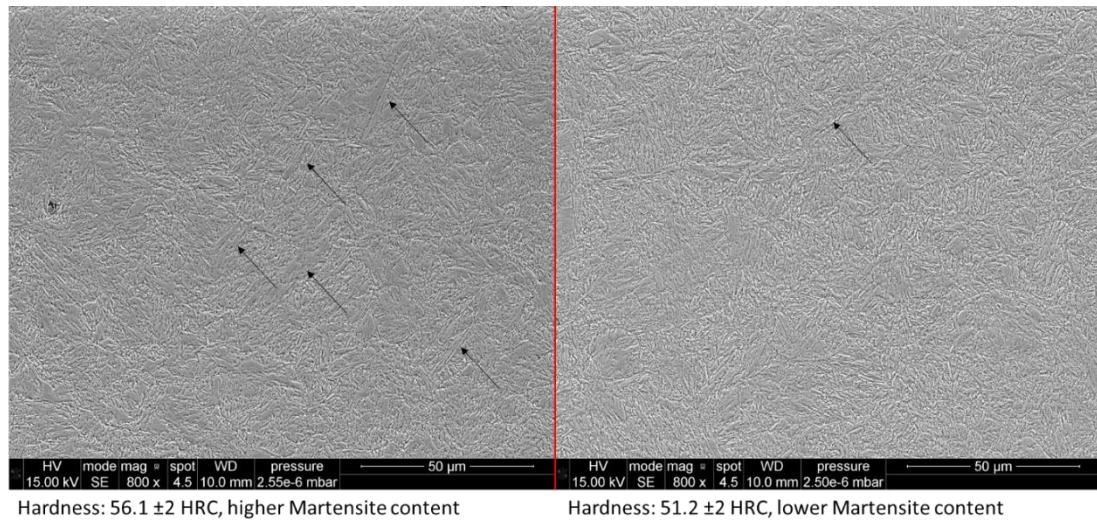


Figure 4.14: Microstructure of workpieces with high (left) and lower (right) Martensite content

The inspection of the workpiece showed that the fatigue cycles increased the so-called material drag which is a disorientation of the workpieces subsurface microstructure, initially caused by machining, this can be seen in Figure 4.15. The comparison (Figure 4.15) shows that the fatigue cycles increase the disorientation, this change of structure can cause a shift in the material behaviour. This irregularity was found in all workpieces to the same extent. However, the lamellar orientation of the material introduces more potential for surface defects.

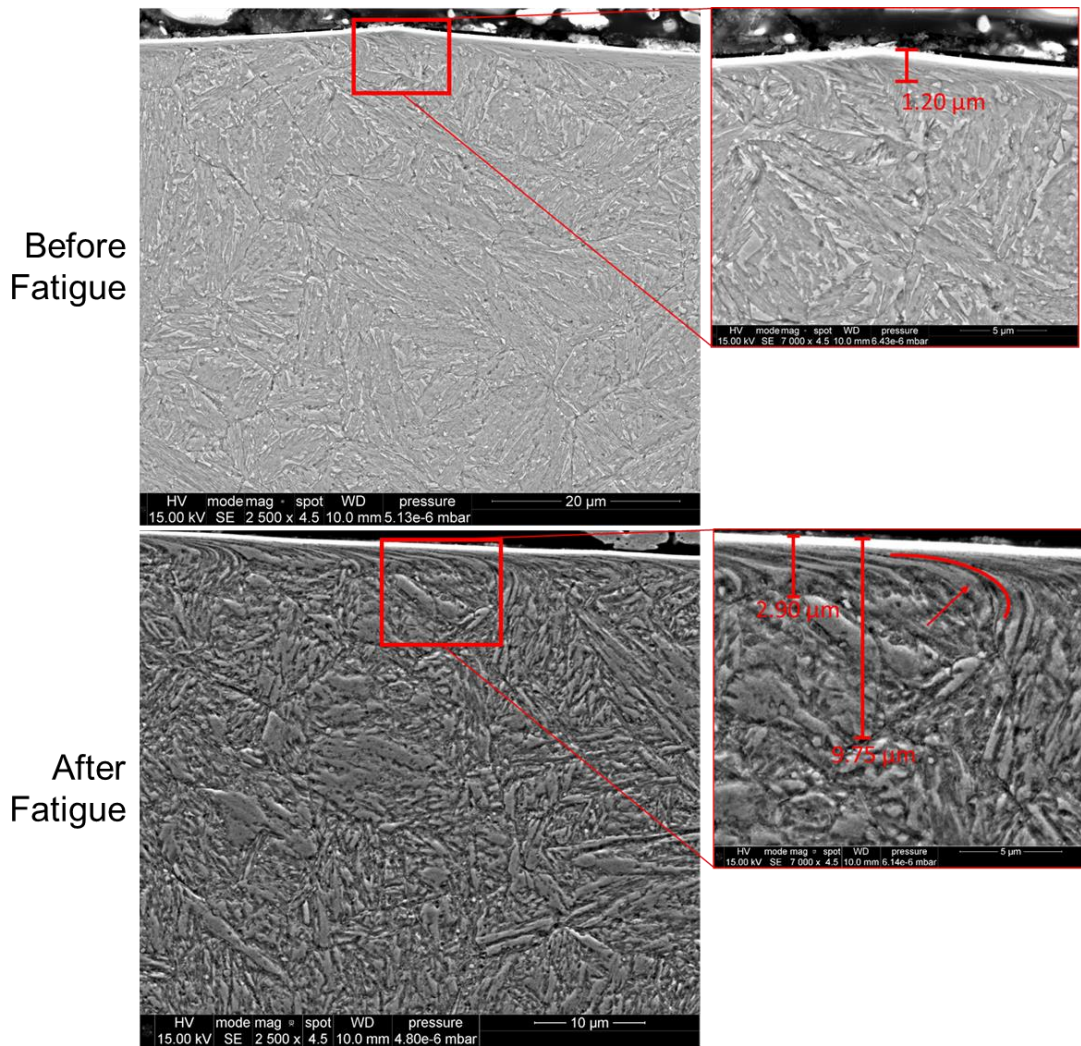


Figure 4.15: Workpiece surface drag microstructure deformation

Recent literature (section 2.3) shows that residual stress has a high impact on fatigue life, as compressive stresses are working in favour of fatigue life and enhancing the cycle resistance. However, most of the experiments were carried out in room temperature as well as a high cycle fatigue setup. In this experiment, elevated temperature and low cycle fatigue setup were used. Figure 4.16 shows that the change of the plane-residual stress does not influence the fatigue cycles significantly (outliers removed).

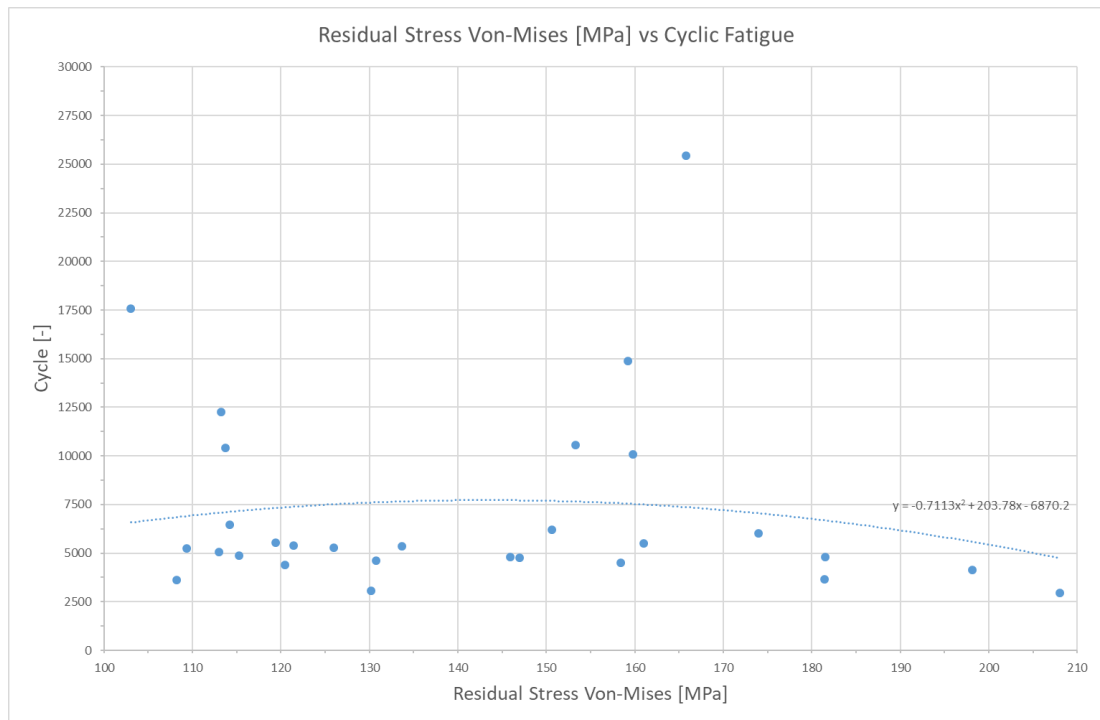


Figure 4.16: Interaction of Residual Stress (VM) [MPa] and Fatigue Cycles [-]

4.3.1 Fractography

Fractography can be defined as: “fracture is the process of separation or fragmentation of a solid body under the action of loads or stresses, thus creating new surfaces, which are referred to like them ‘fractured surface’” [57]. Fractures can be categorised into two categories:

1. Brittle Fracture, where little or no plastic deformation is present,
2. Ductile Fracture, where plastic deformation is present.

The brittleness is correlated to the material properties such as hardness, tensile strength and fatigue life, as presented in 4.3.

A fracture consists of three stages of failure: the crack nucleation, crack propagation, and the final stage. Figure 4.17 shows a general fracture model featuring the three stages above. The progress of the crack becomes more evident at the bottom of the picture, where a change in the topology of the crack is shown, i.e. “beach marks” develop mainly in the propagation phase.

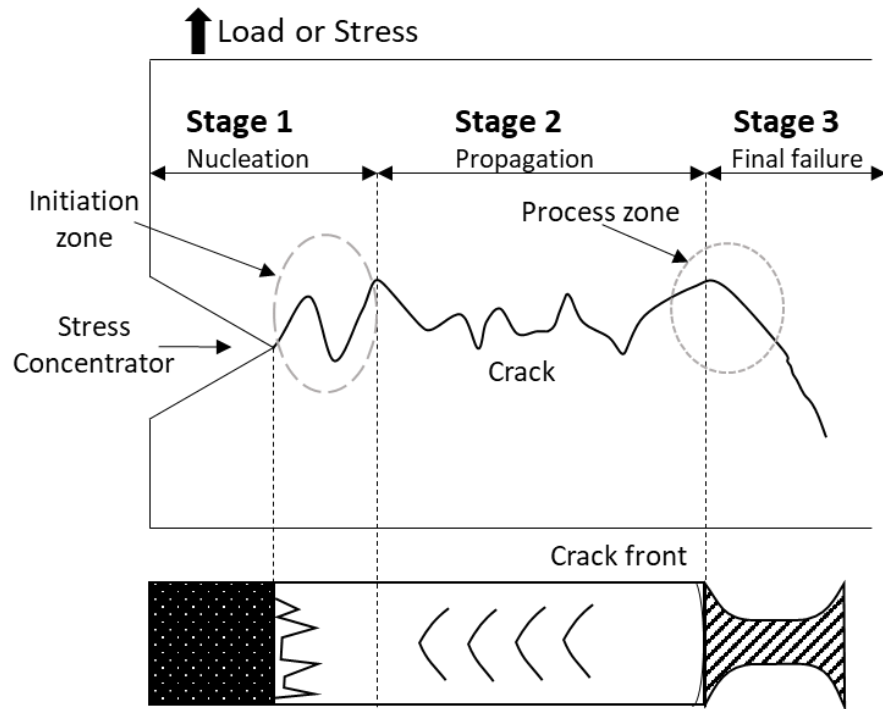


Figure 4.17: Fracture Model (based on [57])

The understanding of the fracturing process allows for reconstruction of the fracture mechanism within the analysed workpieces. A series of workpieces was analysed and exemplary samples taken. Since the fractured surface was not damaged by the process investigation was possible.

The surface of workpiece No. 5 was analysed and can be seen in Figure 4.18. The illustration shows an overview of the fatigued surface and location of the microscale analysis in the SEM. The cracks show the distinctive characteristics of the fatigue fracture with shear and ductile fracture zones. All following SEM figures can be found in a higher resolution in Appendix VI Underpinning Microstructure Data.

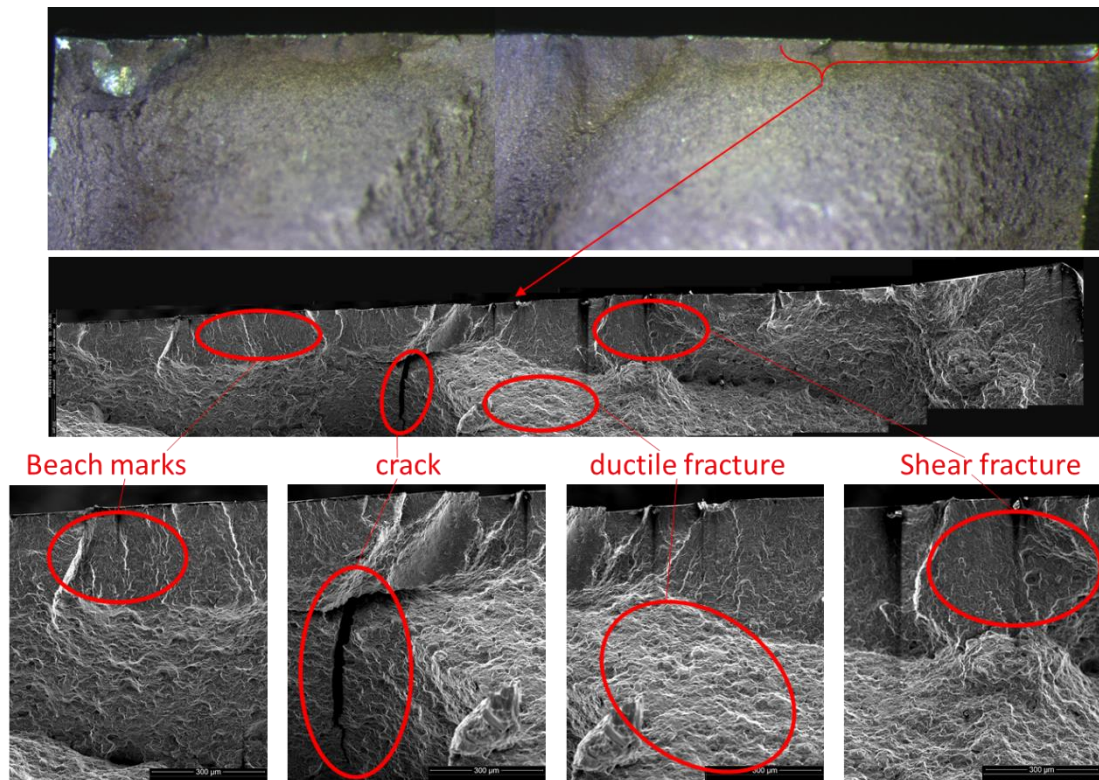


Figure 4.18: Exemplary fracture surface

The fracture in Figure 4.18 shows characteristic signs of fatigue cracking. In the shear area typical beach marks can be found; this is an indication for crack propagation and initiation. Beach marks are defined by the changes in load and environment when a crack starts and stops in its spread [57]. Furthermore, multiple cracks can be identified. The cracks have different sizes and a different impact on the workpiece about their fracture behaviour. The crack indicated in Figure 4.18 defines the line between shear and ductile fracture. However, the indicated breaks in Figure 4.19 are microcracks; these can develop towards a macrocrack and lead to the fracture of the workpiece. From these cracks a clear crack and fatigue propagation can be seen in Figure 4.19. Dimples can also be seen – these are common and an indication of ductile fractures.

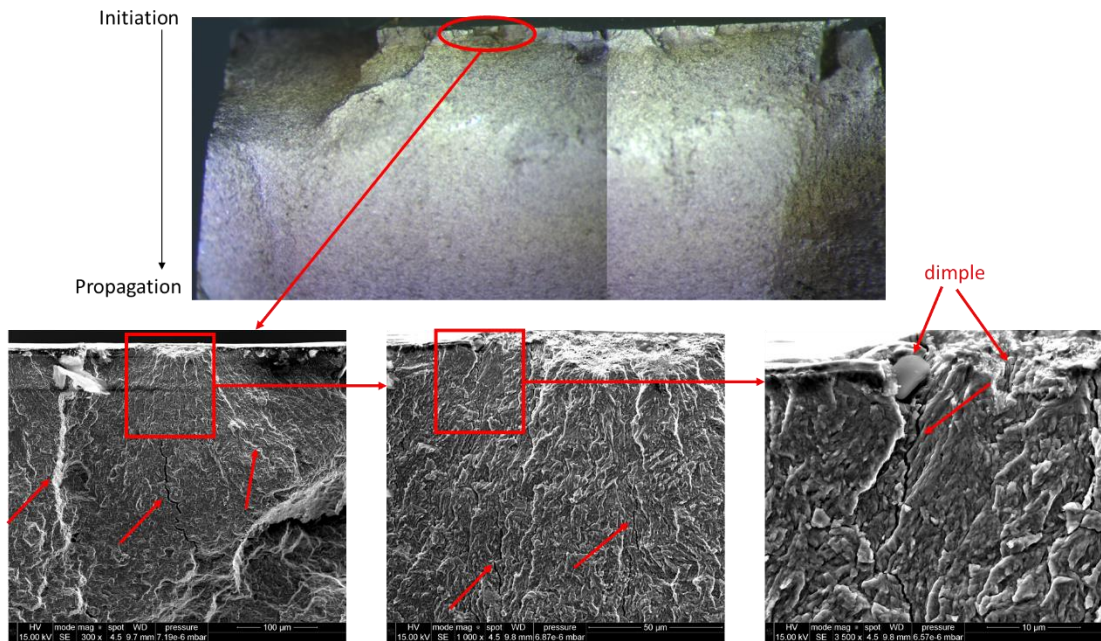


Figure 4.19: Crack propagation from dimple of the fractured surface

In the fractography example shown in Figure 4.20 a characteristic shear zone and the ductile zone can be seen, as well as the beach marks. Other examined samples have shown similar results. Therefore it can assume that these figures are representative examples of all fractures, propagations and crack initiations, and are comparable depending on the machined surface.

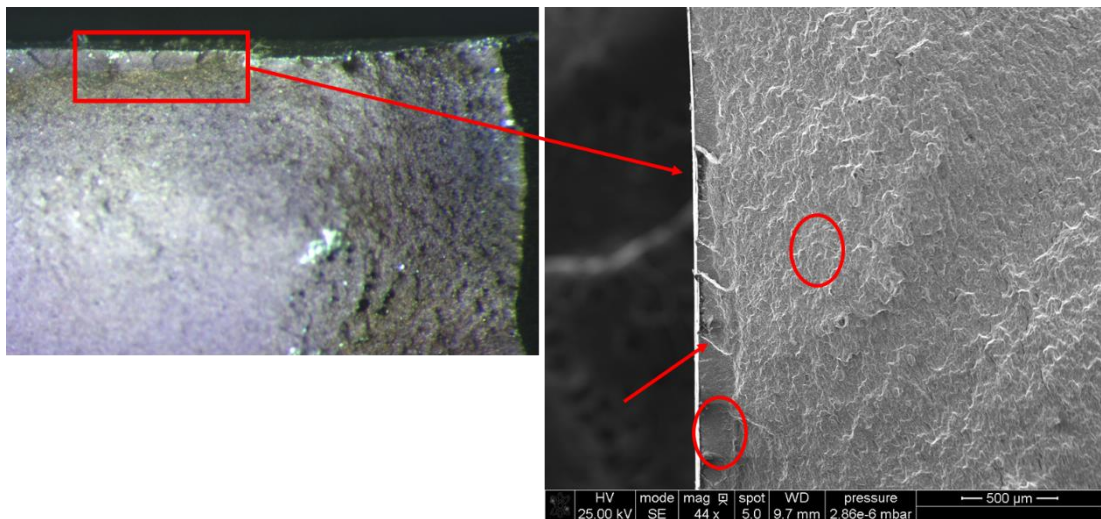


Figure 4.20: Fractured surface showing beach marks and ductile fracture

4.4 Summary

In this chapter the influence of the different surface integrity parameter has been discussed and analysed. Fractography has been carried out to describe the fatigue process. It was found that surface roughness was the most influential factor in fatigue life, due to the related surface defects. When the surface roughness increases the possibility of crack initiation points increases, which lead to an earlier crack and finally fatigue. The hardness also played a role in fatigue life since the workpiece was loaded close to the UTS. In testing low-cycle fatigue performance it was observed that soft and more ductile workpiece surfaces had a higher fatigue life than harder and more brittle workpiece surfaces. It was also found that the residual stress did not have a significant impact on the fatigue life because the applied stresses on the workpiece exceeded those remaining in the workpiece: the remaining stresses were overtaken by the applied stresses.

Chapter 5 Modelling & Simulation of 3D-Milling Process

In this chapter the FE modelling for the milling process is developed and discussed. At the beginning of this chapter an introduction of the overall FE-Model of this work is given. Following the FE-Model development and its material parameter, scripts to set up the simulation and the validation strategy to the model are explained. This is supported by the development of a subroutine which includes a new material model (this was published in [107]). At the end of this chapter the modelling of surface integrity is presented.

5.1 Introduction

This chapter aims to develop a framework and prediction model for the surface integrity of workpieces and ultimately to increase its fatigue resistance. The work includes the validation of the 3D-FEM (Finite Element Model) in its residual stress state, surface roughness and cutting forces. Based on this, the development of a soft prediction model for surface integrity can be pursued.

The investigation of the theory and behaviour of cutting strategies and surface integrity will support the optimisation of the cutting process and enhance the fatigue resistance of the machined workpieces. Recent research has led to published work on more simplified FE models in milling of difficult-to-machine materials, such as AISI H13 [48, 51, 111, 147].

In this chapter a more comprehensive material model featuring a 3D-FE-Model and framework (including a subroutine) was developed. The advantage is that the 3D model can represent a multi-cutting-edge engagement during the cutting process, and this has a significant impact on force and consequently on stress and temperature. Additionally, the 3D-Model helps our understanding of the machining process during the cut, which is very difficult to analyse in a physical experiment.

As previously discussed four influencing factors are central to this work. These factors are feed rate, surface speed, depth of cut and lead angle with five levels each. The combination of these factors and levels led to 625 (5^4) simulations in a full factorial experimental design. However, over 600 simulations would be excessive and impossible to run within the given calculation time, so a fractional factorial design was applied to the FE-simulation.

The fractional factorial simulation covers over 180 simulations. The completed simulations were compared and validated by the process since over 30 strategies were physically machined while cutting force was recorded by a Kistler dynamometer. The surface residual stress, surface roughness and cutting force were measured and compared. A soft prediction model was developed using the validated simulation as its basis.

5.2 Description of the 3D FE model for End-Milling

Finite element (FE) simulation of machining processes is often used to gain good understanding of the physical formation of stresses.

Figure 5.1 shows the general setup of FE-model which implemented using ABAQUS 6-14, adding additional material subroutines. ABAQUS was chosen because it can seamlessly implement subroutines and scripts to achieve a consistent set up of the Model as well as continue running the simulations.

The ball-nose cutter was initially scanned using a GOM 3D-scanner to increase simulation accuracy. The cutting tool was modelled using rigid shell elements to reduce the calculation time. The workpiece elements were modelled using an 8-node thermally coupled brick, trilinear displacement and temperature, reduced integration, and hourglass control elements (C3D8RT). Element deletion of the workpiece elements was activated. In the simulation the standard Coulomb friction model was used to simulate the friction coefficient between the workpiece and the tool. The interaction of the heat transfer and thermal conductance between workpiece and tool was considered

using the Abaqus. The data entered was taken from previous in-house experiments. The workpiece also had a predefined boundary condition set to room temperature.

The FE-Model ran in ABAQUS explicit using a subroutine; this implements a newly developed material model based on the hardening process, which encounters the temperature, hardness and residual stress of the model in order to achieve a precise prediction model. This model is further discussed in section 5.3.1.

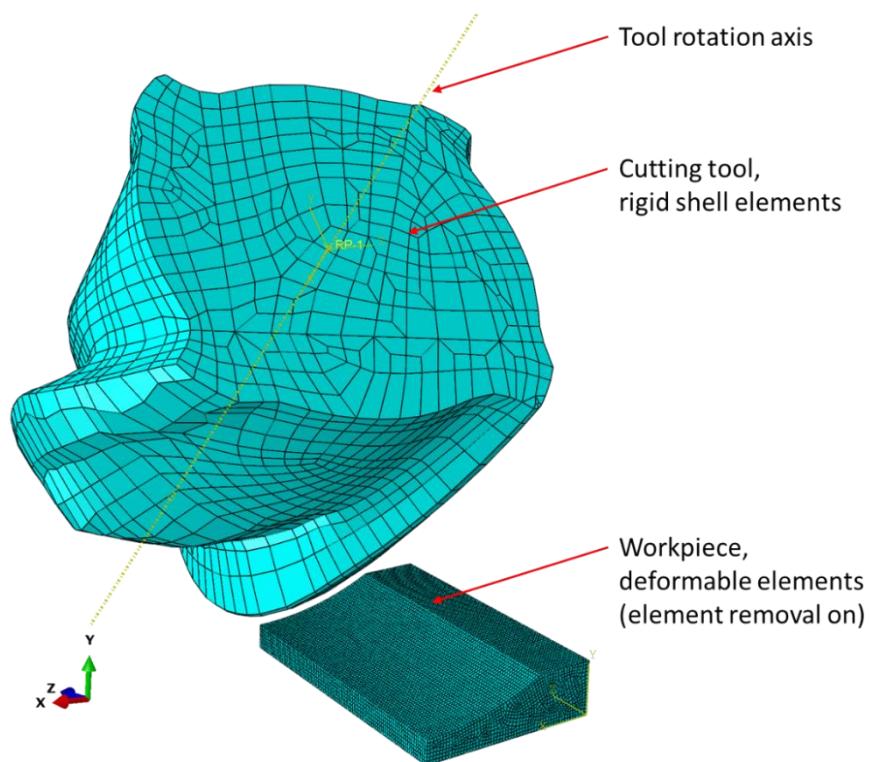


Figure 5.1: General FEM Setup

Figure 5.1 shows the setup. This model used two axes: one rotational axis on the cutting tool which goes through the centre point of the cutting tool, and the other axis which is on the corner of the workpiece. The tool rotates around its axis, simulating the rotational movement of the tool. The axis of the workpiece moves the workpiece to simulate the movement of the machining bed. Additionally, it can be seen that the workpiece was modelled using a slope, which imitates the previous cut. This was necessary because if slotting was

used then different results would emerge and the FE-model would not be representative. The movements mentioned above - tool rotation and the workpiece's linear movement - are defined in the boundary condition.

The step time was automatically calculated in the setup-script as it varied, depending on the feed and speeds; accurate calculation of the step-time can reduce unnecessary calculation time of the simulation.

During the setup of the simulation various sets were also generated to achieve a more traceable FE-Model; this also supports the final analysis.

5.2.1 Material parameters

The project focused on difficult-to-machine materials, therefore a selection of hard materials was selected. A broad range of materials are available for tooling, and these can be categorised into four types of tool steels: alloyed and unalloyed cold work steels, hot work steels, and high-speed steels [148]. A small range of tool steel material is given in Table 5.1.

Table 5.1: Material composition as an average

Name	% C	% Si	% Mn	% Cr	% Mo	% V
<i>D2</i>	1.60	0.35	0.30	11.50	0.60	0.30
<i>H13</i>	0.40	1.00	0.40	5.30	1.40	1.00
<i>H10</i>	0.32	0.30	0.30	3.00	2.80	0.50

This work focused on AISI H13 (or, X40CrMoV5-1), which is hot-worked steel and is regarded as a high-alloy. It has good resistance to hot wear and possesses excellent toughness, even when deforming larger cross-sections. The material composition of the material is listed in Table 5.1.

As far as the material properties in the FE-Model go, the parameter can be expressed in the general Johnson-Cook equation, where parameters are

shown in Table 5.2. Additionally, it is compared to AISI D2 which is cold work tool steel (AISI D2 was used as the fatigue test rig material).

Table 5.2: Johnson-Cook Parameter for selected materials

Material	HRC	A (MPa)	B (MPa)	C	n	m	T_m (°K)	Source
<i>D2</i>	62±1	1,766	904	0.012	0.312	3.38	1,733	[115]
<i>H13</i>	46	674.8	239.2	0.027	0.28	1.3	1,760	[112]

The cutting tool material was introduced, using a basic set of material properties and describes the elements in its basic form. The cutting tool elements do not need to be described in detail because they were set as rigid shell elements. Table 5.3 shows the mechanical properties of the cutting tool core material Tungsten-Carbide as well as the workpiece material AISI H13.

Table 5.3: Mechanical material properties

Material	Density [kg/m³]	Young's Modulus [GPa]	Poisson Ratio [-]	Specific heat [J/kg°C]	Thermal Conductivity [W/m°C]	Source
<i>Tungsten Carbide</i>	11,900	534	0.22	400	50	[149]
<i>H13</i>	7,800	210	0.29	565	37.2	[87]

As mentioned above, the friction model in the FEM is a prominent feature due to its influence on the prediction model. It interacts directly with the cutting tool and workpiece, heat induction and different shear forces, and the resulting residual stresses.

Previous work has shown that the Coulomb friction coefficient delivers a good agreement to predict the friction in FE [108, 150]. A derivate model of the Coulomb friction coefficient is the Zorev friction model, which can be described as followed in equation (5.1) [151]:

$$\begin{aligned} s &= \mu p \quad \text{when } \mu p < \tau_{max} \\ s &= \tau_{max} \quad \text{when } \mu p \geq \tau_{max} \end{aligned} \quad (5.1)$$

where s is the friction coefficient, p the normal pressure and τ the equivalent shear stress. In this simulation the constant friction factor of 0.48 was used, which was found by [19] and recommended by the tool manufacturer in using this tool and workpiece material combination.

5.2.2 Scripting Model (Python)

As described in the introduction of this chapter, a fractional factorial approach was chosen. To produce a large batch of simulations a script was required using the python interface from Abaqus.

The script consists of seven files and the file interaction and working principle which are illustrate in the framework diagram – the high-resolution diagram can be found in Appendix IX Script Framework. It sets up the FE-simulation automatically and analyses precisely all simulations in the same way. The automatisisation has the advantage of consistency and comparison, as well as reduced analysis time for similar problems.

The script includes file consistency checks and naming. The split of the code into different files makes it easier to apply changes to the model, especially in the material model, material properties or boundary conditions of the FE-Simulation. These script files can be found in Appendix VII Script.

5.2.3 Validation Strategy

To achieve a precise and correct model in finite element simulations a validation strategy must be implemented, to verify the simulations. Figure 5.2 depicts the developed validation-strategy.

The simulations were first run on a smaller scale until they were validated. Adjustments in the material model, as well as a subroutine, were then successfully completed. After reasonable results were achieved the results were compared with the experiment, after which a large-scale simulation was carried out. As mentioned above, a fractional factorial approach for FEM was applied and resulted in over 180 simulations. Preliminary simulation results have been published and validated in the three papers see [105-107].

The validation strategy shown in Figure 5.2 confirms the simulation based on residual stress, cutting forces and surface roughness. At the beginning of the simulation a selection of adjustable parameters as well as non-adjustable parameters were identified. Adjustable parameters are factors which can be modified to validate the FEM and to match the experiments, such as friction coefficient, workpiece geometry, and material parameter. These adjustments are necessary due to the variation in the material and external real-world influences on the used literature parameter. The non-adjustable parameters were the factors investigated in the experiment, and comprised depth of cut, feed rate, surface speed and lead angle.

The friction coefficient is a significant factor in the validation strategy because the friction coefficient has a direct influence on all observed parameters. The development of a suitable material model, which acts as the basis of all other FE adjustments, is discussed further in section 5.3.

Once the results from the cutting force - residual stress and surface roughness - are less than 30-35% of the mean-squared error (MSE) the model can be confirmed as validated and with the achieved precision.

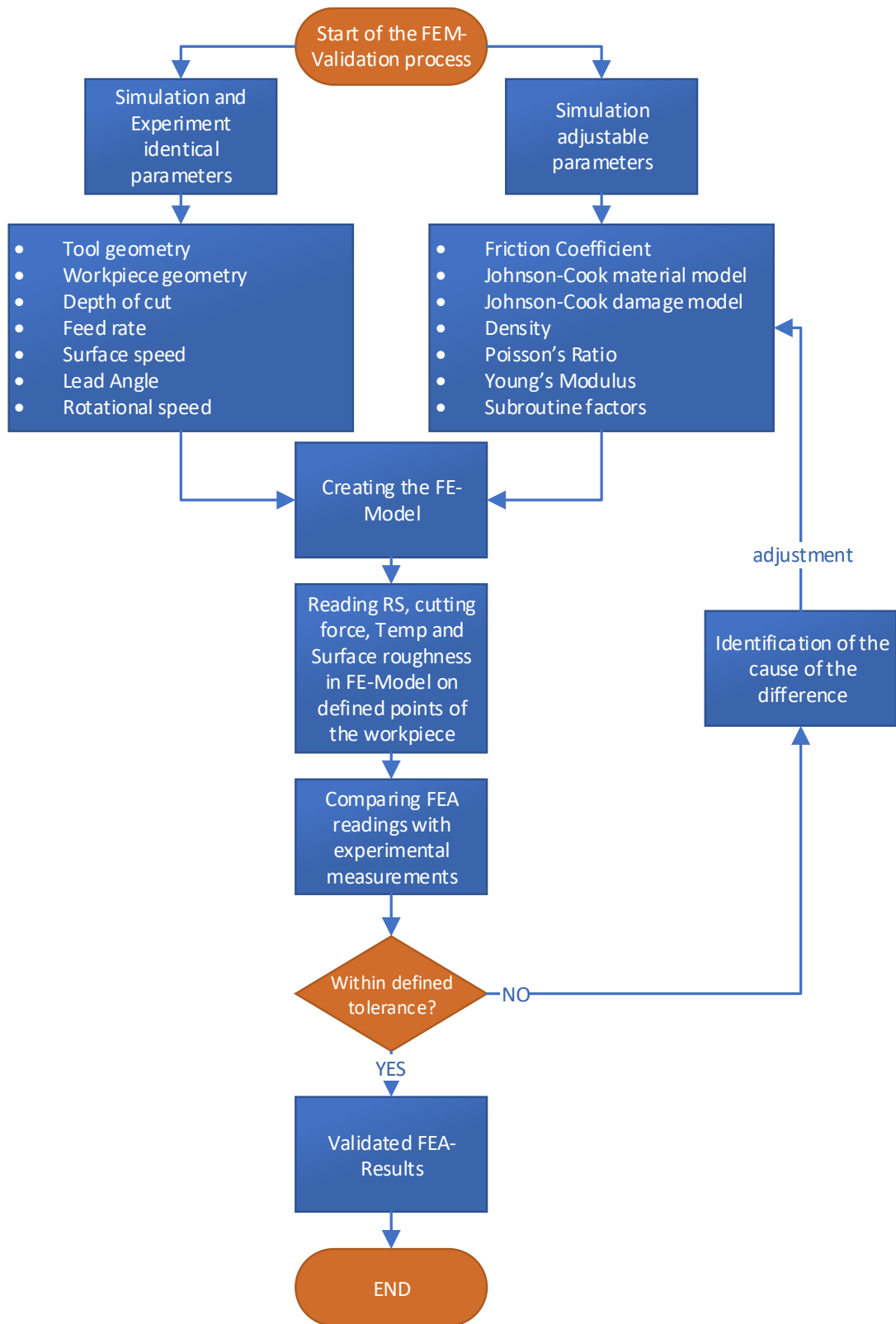


Figure 5.2: FEM Validation strategy

5.3 Finite Element Material Model

The material model is the most critical feature of a numerical simulation. In the past decade many researchers [6, 23, 82, 103, 104, 116] have investigated the material model description to achieve an ever-more-precise prediction model. Standard functions are often implemented into the simulation software, such as ABAQUS, DEFORM or ANSYS. However, those material models are often not described in enough depth. Consequently, many researchers are developing subroutines to describe the material model more accurately; FEM platforms like ABAQUS allow the user to implement different interface subroutines and to accomplish this.

This research used the Johnson-Cook material model as the basis for the material model description because it can describe high strain rates which occurring during machining processes. The material model in ABAQUS supports the basic Johnson-Cook model. The complete model was programmed in a subroutine and was discussed in more detail in Section 2.5.2.1. In addition to this, a more detailed structure of the subroutine is shown in the following section 5.3.1.

A further consideration in the model is the hardening and temporary softening of the material during the removal process on the workpiece surface. During the machining process the material temperature increases due to excessive deformation, and as a result of the adiabatic heating effect the workpiece material temporarily reduces in ultimate tensile strength (UTS). This reduction of the UTS affects the cutting force as well as the residual stress state in the workpiece afterwards. The material softens temporarily and is consequently more easily removed; this also causes a drop in the cutting force. Furthermore, compressive stresses are lowered as the material does not withstand the deformation as it would in a cold state; however tensile stresses rise.

Other material parameters applying standard FE-calculation, such as Conductivity, Johnson-Cook Damage, Density, Elastic, Expansion, Inelastic

Heat Fraction and Specific Heat were used. These values were taken from the literature and are listed in Table 5.4.

Table 5.4: FEM material parameters

Conductivity	Conductivity [-]	Temperature [°C]
	17.6	20
	24.3	215
	24.4	350
	24.5	475
	24.7	605
Expansion	Expansion [mm]	Temperature [°C]
	1.04E-05	93
	1.13E-05	204
	1.24E-05	316
	1.31E-05	427
	1.35E-05	538
Specific Heat	Specific Heat [-]	Temperature [°C]
	4.60E+08	20
	5.48E+08	500
	5.90E+08	600
Johnson-Cook Damage		
	d_1	-0.8
	d_2	2.1
	d_3	-0.5
	d_4	0.0002
	d_5	2.7
	T_m	1480
	T_r	20
	$Strain_{ref}$	1
Density	7.80E-09	
Youngs Modulus	2.11E+05	
Poisson's ratio	0.28	
Inelastic heat fraction	0.90	

5.3.1 Subroutine (VUHARD)

A material hardening model was written in an ABAQUS subroutine, whereby the VUHARD interface was used, and which describes the hardening process. The interface connects in the simulation to the *Define K^{el}* “environment”, where the yield stress is the feedback to the system. This can be seen in Figure 5.3, where the overall flow system of Abaqus (Standard) is mapped.

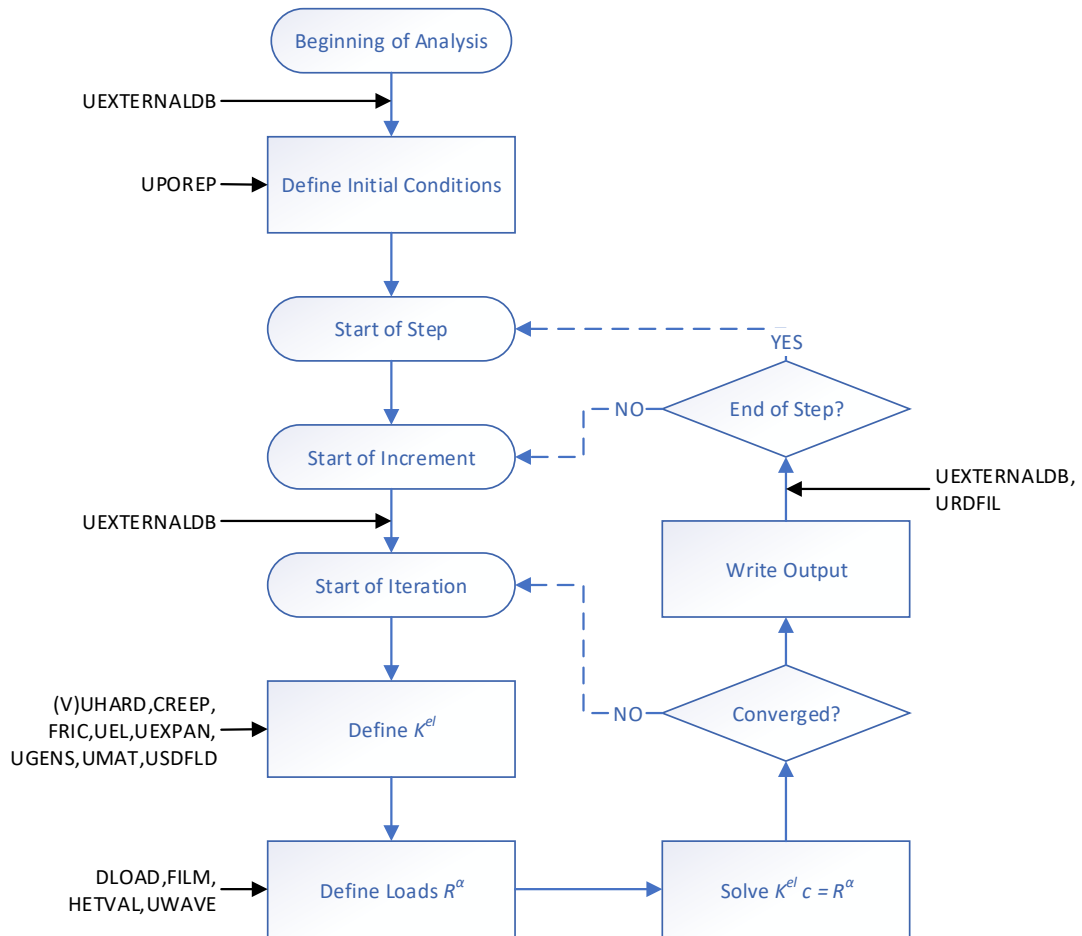


Figure 5.3: Flow in Abaqus / Standard (based on [152])

The developed model was based on the principle of Umbrello’s model [51]. However, it was based on the ultimate tensile strength (UTS), where the yield criterion changes. Additionally, a material removal criterion was added. The material removal criterion is based on the UTS. The UTS changes with the temperature and therefore the current temperature in the FEM was initialised

with room temperature of 20 °C. The current UTS in the element was calculated using a 3rd-grade polynomial regression of physical tensile stress data at different temperatures. If the flow stress exceeds the UTS the elements are deleted, unless a separation criterion within ABAQUS has been applied beforehand. The workflow principle of the above-described removal criterion is shown in Figure 5.4 (this workflow is published in [106]). The source code for the subroutine can be found in Appendix VII Subroutine.

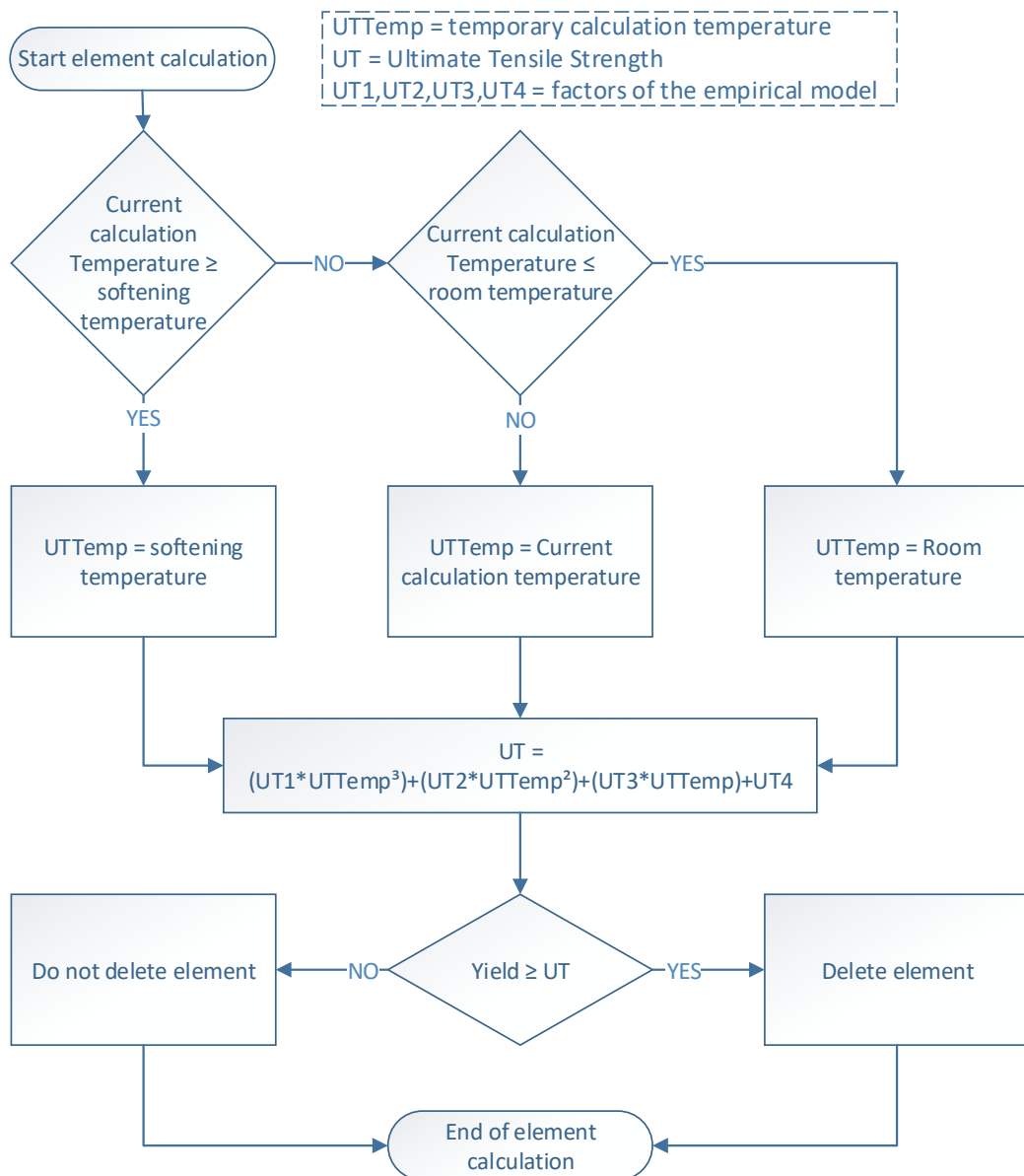


Figure 5.4: UTS deletion criteria principle

5.4 Modelling of Surface Integrity

In this section, exemplary FE-Models results are shown, discussed and validated. The simulation was validated by cutting force, residual stress and surface roughness. Furthermore, the general mechanism during the cutting process can be analysed.

5.4.1 Temperature

In this section the development of the temperature is explained. It can be assumed that from the validated simulation, the temperature investigation during the cutting process verifies the explanations for the residual stress as well as cutting forces behaviour. The temperature development during the cutting process is an essential part of the FE-analysis.

Figure 5.5 shows an example of a simulation and its temperature development during the cutting process. When the first flute engages with the material its temperatures reaches up to around 420 °C, whereby the connected (Von-Mises) residual stress rises around 1500 MPa (around the current UTS). The second flute follows the first flute almost instantly, and that affects the temperature in the material which is carried over to the 2nd engagement since the surface does not have enough cooldown time. Therefore, the peaks on the second flute engagement can reach in this example up to around 880 °C, which decreases the UTS further and causes peaks of residual stresses at this stage of around 1390 MPa (current UTS) for the material removal.

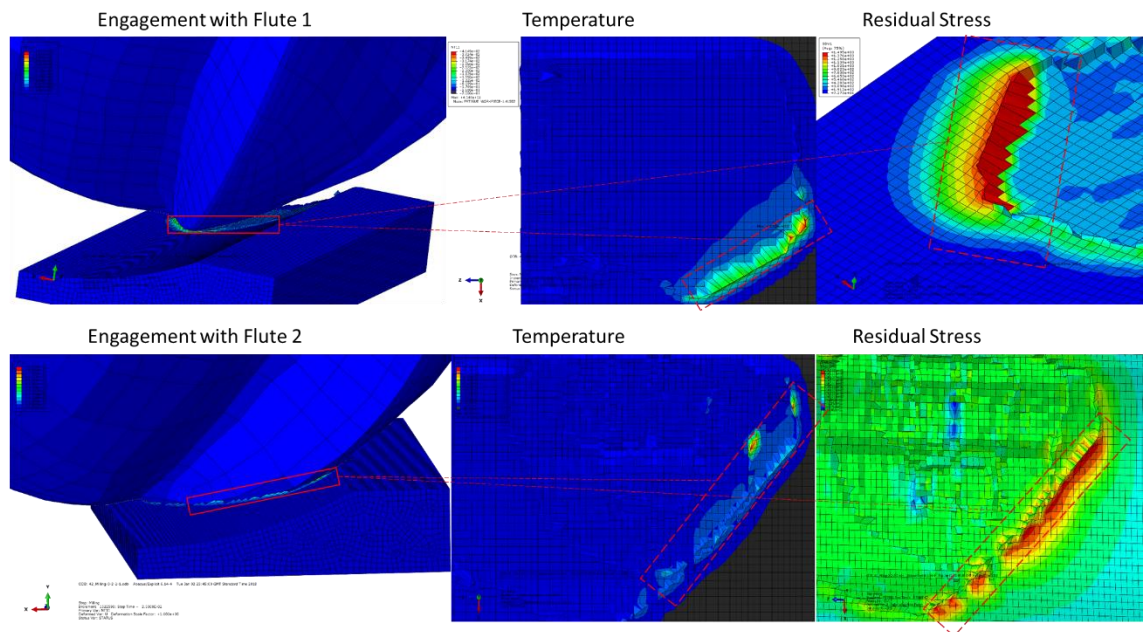


Figure 5.5: FE Temperature and residual stress development

After the investigation of all simulations the average temperature was measured at around 250 °C during the FEM; however, peak temperatures reached up to 1000 °C during the cutting process. The induced stresses of high temperatures (above 250 °C) by machining were not influenced by the operating temperature during the fatigue test since the fatigue test operating temperature was set to 250 °C.

Figure 5.6 shows the correlation of the cutting parameters and the temperature. The lead angle is the most influencing machining parameter for the temperature due to its interaction with all other parameters, and is shown in the graph. Furthermore, it was observed that all parameters interacted with each other. The (adiabatic) heating during the cutting process is expected to be influenced by all factors, just as the cutting force is influenced by other parameters. In this example an increase of the feed rate causes a local increase of the temperature, and so the material can be removed because less resistance is given by the UTS; with an increased feed rate measured nodal temperature on average reduces as the workpiece has less time to absorb the temperature.

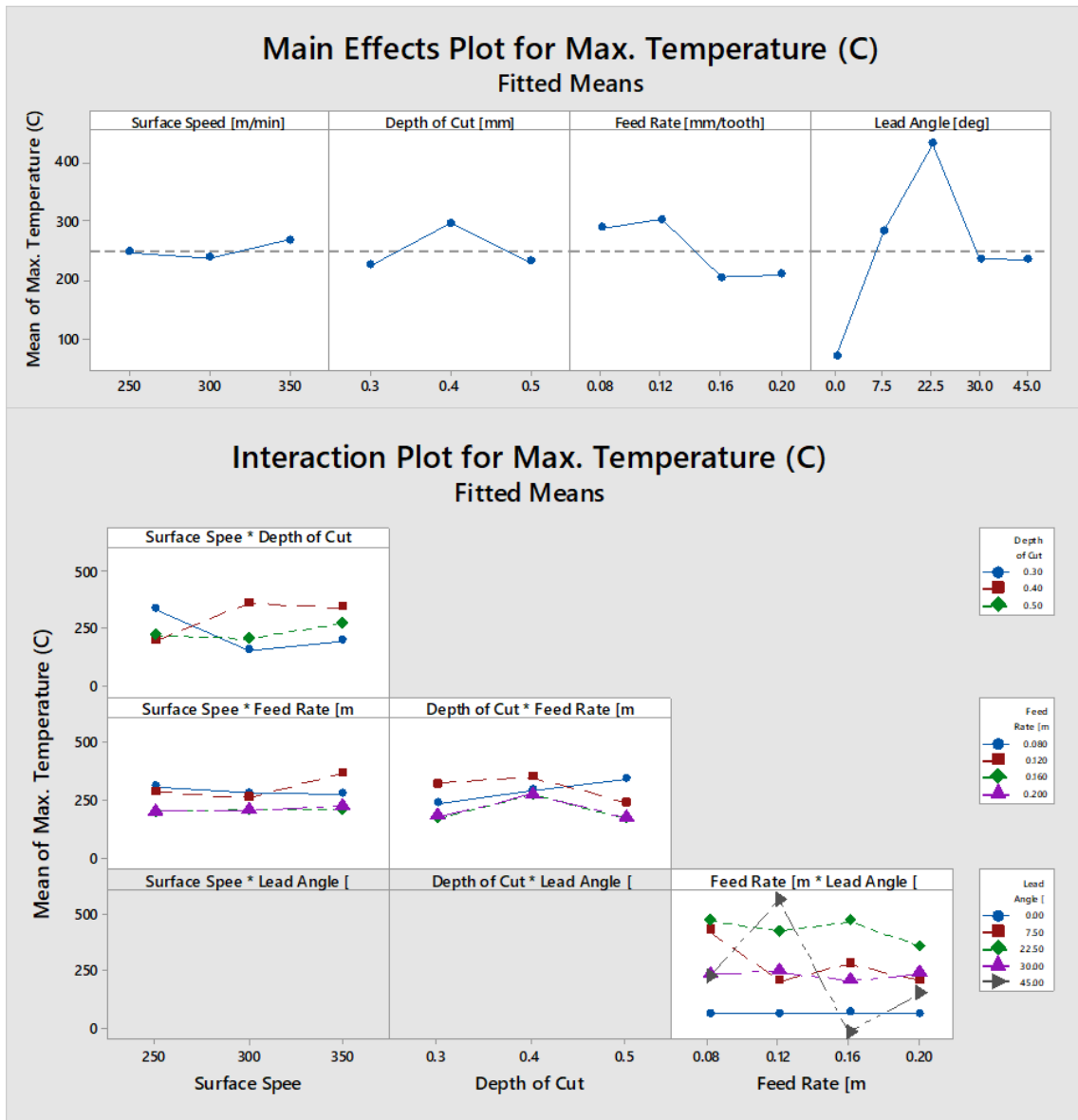


Figure 5.6: Effect and interaction plots for Temperature on machining

5.4.2 Cutting Forces

The cutting force of the FE-Model was compared with the measurements of the experiment. Figure 5.7 illustrates the comparison between the experimental results and the FE predicted results and it can be seen the results are similar: the mean error for the simulation to physical experiments is around 20%, or less than 7.6 N in total average value.

The overall cutting forces were not unusually low during the finishing and cutting processes of hardened material such as AISI H13. The reduced cutting forces were also due to the coating of the cutter - the cutter has a reduced friction coefficient compared to conventional cutters as well as sharp cutting edges. Furthermore, the feeds and speeds are comparatively high when using a shallow depth of cut; the cutting process described is precise. The cutting force differs by a small margin between simulation and recorded cutting forces. A small difference of a few Newton-meter has a correspondingly high impact on the percentage difference between the simulation and experiment.

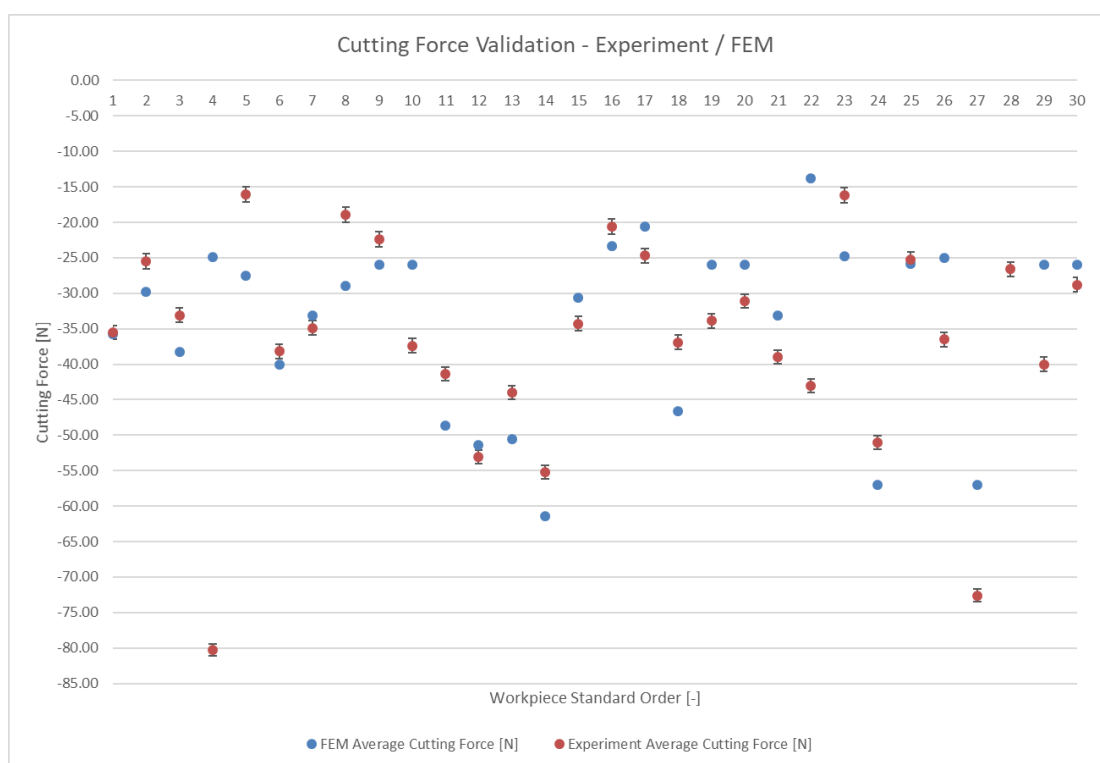


Figure 5.7: Cutting Force - Experiment vs. Simulation Comparison

An ANOVA analysis was applied to the FE simulated results which were found to have a similar pattern to those in the experiment. This can be seen in Table 5.5 where the lead angle is the most influential factor, followed by the depth of cut, surface speed and feed rate respectively.

The difference of the significance of the parameter of in the simulation is down to the FEM setting. The depth of cut and the surface speed have a higher impact than the feed rate; this is translated into the rotational speed of the cutter. A higher depth of cut profile calculates a higher cutting force as well as the transversal movement of the component, which is directly linked to the surface speed. Nevertheless, if these influencing factors have changed their ranking in the simulation, the prediction of the cutting force is still accurate and follows the trend from the experiment. Therefore, it can be concluded from the statements above that the simulation is accurate, under its current condition, in predicting the cutting forces during the machining process, and is therefore valid in predicting cutting forces.

Additionally, in Figure 5.8 the main effect plot and interaction plot is shown. The main effects are trend similar to the machining trials, when changing parameter. The interaction plots show that all factors influence each other, however it can be clearly seen, that the interaction is different from the machining trials. This is caused by the calculation approximation in the simulation.

Table 5.5: ANOVA for FEM machining parameter on Cutting force

Source	Adjusted Sums of Squares	Adjusted mean squares	F-Value	P-Value
Linear				
Surface Speed	138.71	138.706	0.96	0.344
Depth of Cut	176.85	176.852	1.22	0.287
Feed Rate	0.02	0.016	0	0.992
Lead Angle	480.05	480.053	3.31	0.089
Square				
Surface Speed * Surface Speed	1.62	1.617	0.01	0.917
Depth of Cut * Depth of Cut	249.7	249.701	1.72	0.209
Feed Rate * Feed Rate	0.11	0.109	0	0.978
Lead Angle * Lead Angle	439.12	439.117	3.02	0.102
2-Way				
Surface Speed * Depth of Cut	1.24	1.241	0.01	0.928
Surface Speed * Feed Rate	32.22	32.216	0.22	0.644
Surface Speed * Lead Angle	269.12	269.121	1.85	0.193
Depth of Cut * Feed Rate	18.66	18.655	0.13	0.725
Depth of Cut * Lead Angle	67.58	67.579	0.47	0.505
Feed Rate * Lead Angle	0.17	0.171	0	0.973
Error				
Lack-of-Fit	2177.92	217.792		
Pure	0	0		

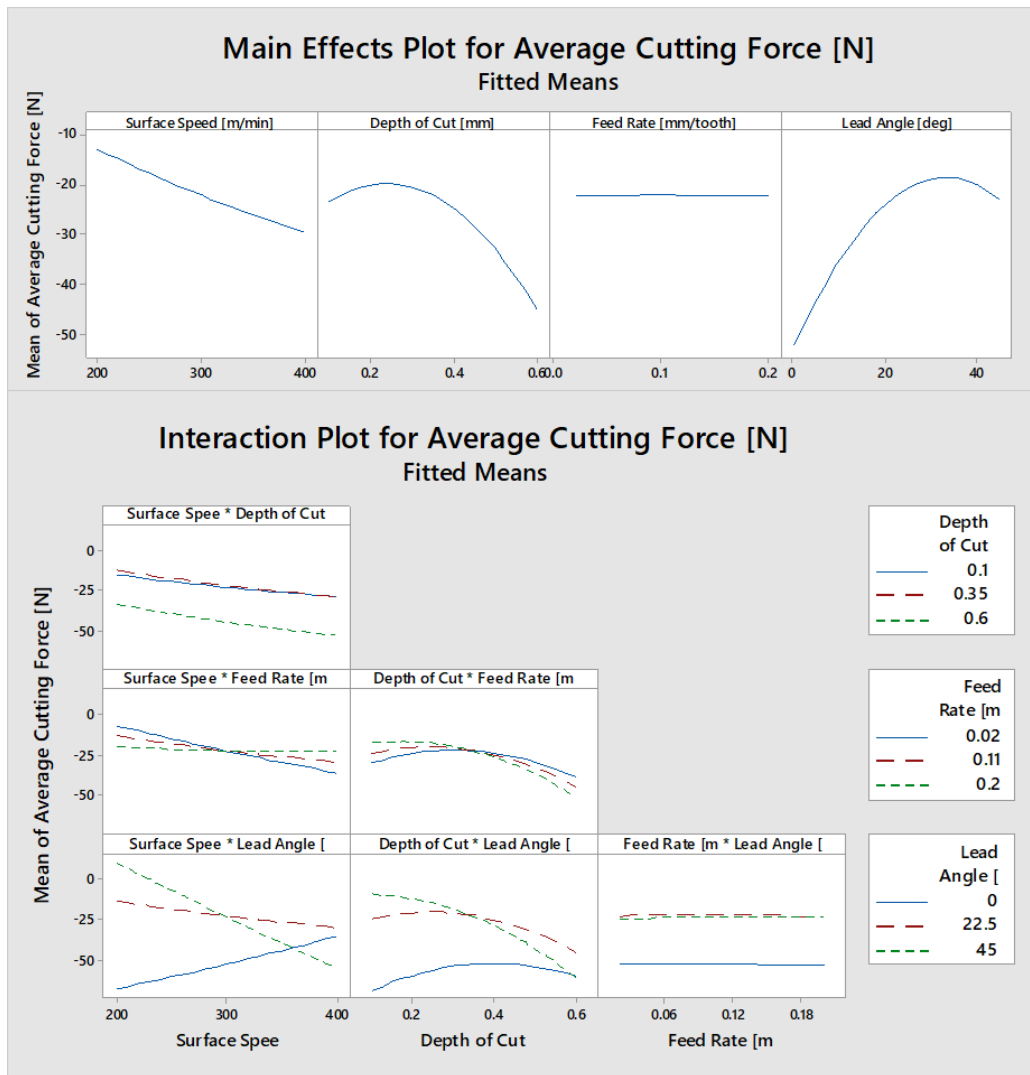


Figure 5.8: Effect and interaction plots on cutting forces during machining

5.4.3 Residual Stress

The residual stress is used to validate the simulation and to predict values in the neural network as input values. Figure 5.9 shows the average Von-Mises residual stress values of the simulation in comparison with the experiments. The residual stress results are Von-Mises calculated values and are determined by using the subroutine with the full Johnson-Cook formula in the FE-Model.

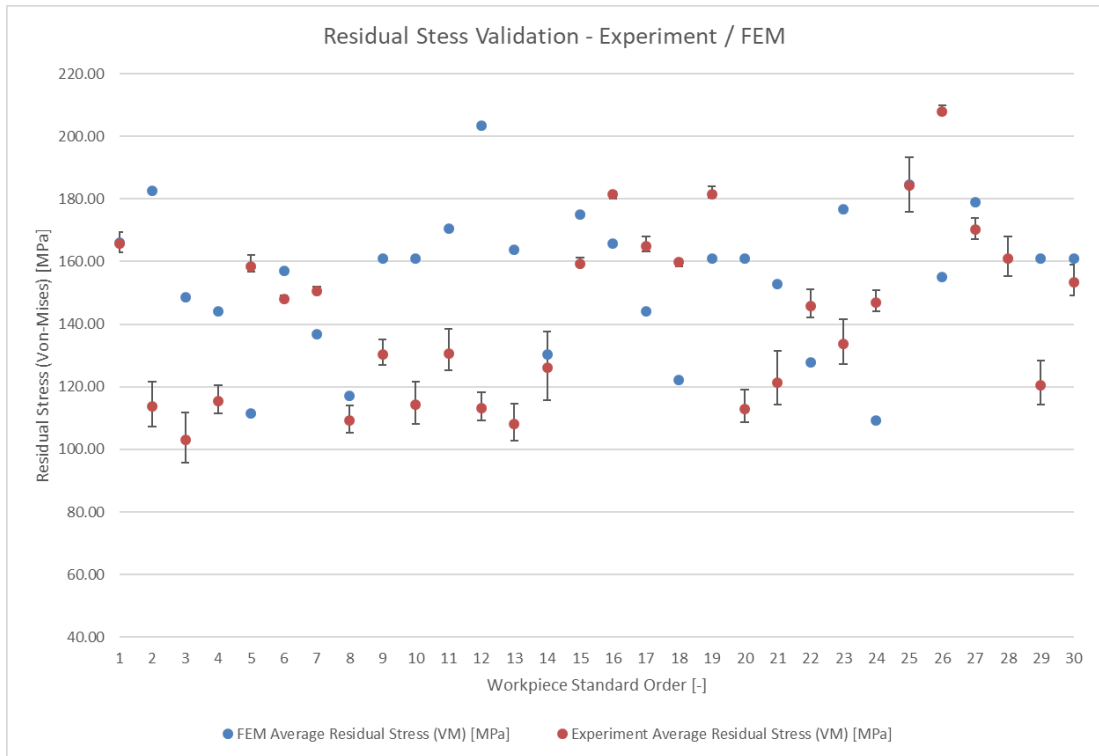


Figure 5.9: Residual stress comparison between experiments and FEM

Figure 5.9 shows that the correlation and trending between FEM and experiments are close. A correlation with an overall MSE between the simulation and experiments of 20% was achieved; this correlates to an average error of around 30 MPa.

The published work [107] shown in Figure 5.10 clearly illustrates the development of the residual stress during the cutting process. Figure 5.10 also demonstrates that the residual stress is set to begin at 72 MPa, and in this particular example rises to around 130 MPa after the material has been removed. After the cut, when the temperature decreases the residual stress state decreases slightly too, and the workpiece remains in its final stress state.

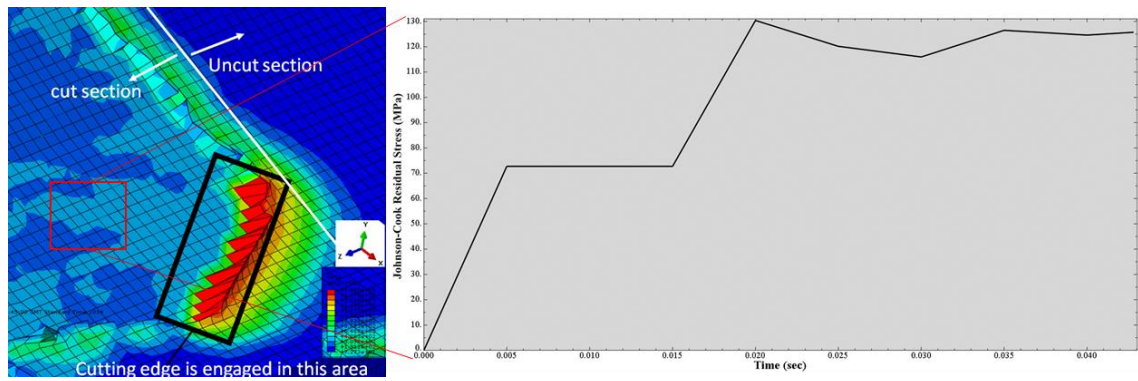


Figure 5.10: Residual stress development in the cutting process [107]

In the example above, as in other examples elsewhere, the fall in the area of measured tolerances proves the accuracy of the performed FE-Model.

The ANOVA analysis in Table 5.6 showed that the influencing factors are the same as those in the experiments. From the simulation it became evident that the lead angle influences the residual stress significantly. It was found that the elements are dragged away from the workpiece, which causes an increase of the residual stress due to the distortion and increased heat induction of the component.

In Figure 5.11 the effect and interaction plots are outlined. The effect plots show a similar behaviour to the main effect plots from the machining experiment; however, the in the FEM lead angle plays a more significant and different role than compared with the experiment. This is due to the distortion of the elements described above. However, the overall influence and prediction of the process is still authentic. The interaction plots closely match the experimental plots and this shows that the interaction in the simulation and the experiments behave in the same way.

Table 5.6: ANOVA for FEM machining parameter on Von-Mises residual stress

Source	Adjusted Sums of Squares	Adjusted mean squares	F-Value	P-Value
Linear				
<i>Surface Speed</i>	149.7	149.72	0.43	0.523
<i>Depth of Cut</i>	91.6	91.63	0.26	0.617
<i>Feed Rate</i>	105.6	105.63	0.30	0.591
<i>Lead Angle</i>	13.6	13.62	0.04	0.846
Square				
<i>Surface Speed * Surface Speed</i>	633.4	633.42	1.81	0.199
<i>Depth of Cut * Depth of Cut</i>	156.5	156.51	0.45	0.514
<i>Feed Rate * Feed Rate</i>	48.7	48.74	0.14	0.715
<i>Lead Angle * Lead Angle</i>	2464.8	2464.84	7.03	0.018
2-Way				
<i>Surface Speed * Depth of Cut</i>	81.3	81.34	0.23	0.637
<i>Surface Speed * Feed Rate</i>	122.4	122.44	0.35	0.563
<i>Surface Speed * Lead Angle</i>	3.7	3.66	0.01	0.920
<i>Depth of Cut * Feed Rate</i>	1704.7	1704.68	4.86	0.044
<i>Depth of Cut * Lead Angle</i>	17.6	17.62	0.05	0.826
<i>Feed Rate * Lead Angle</i>	137.3	137.31	0.39	0.541
Error				
<i>Lack-of-Fit</i>	5263	526.3		
<i>Pure</i>	0	0		

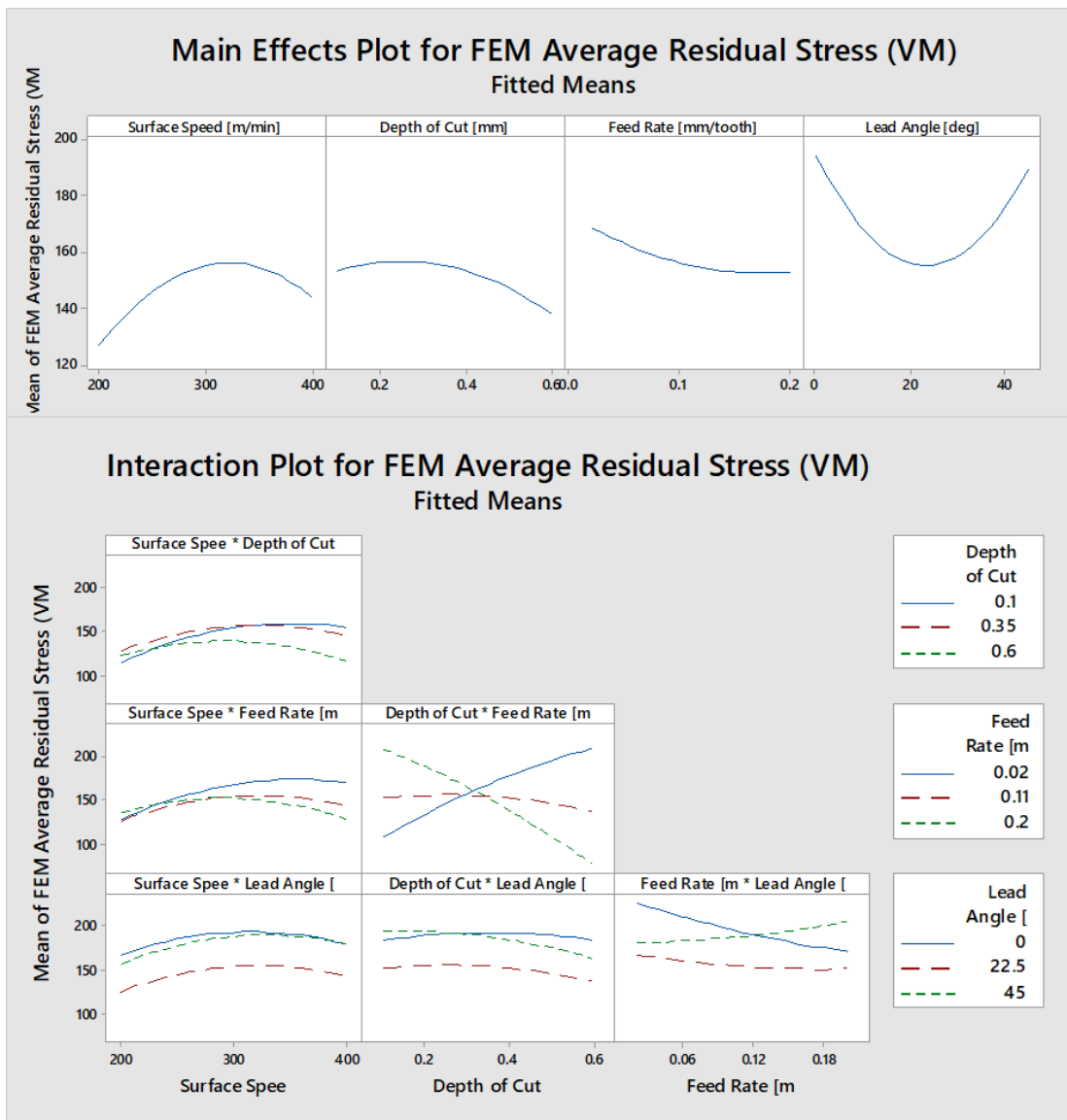


Figure 5.11: Effect and interaction plots on Residual Stress during machining

5.4.4 Surface Roughness

In the following section the surface roughness prediction is discussed. In the physical environment the surface roughness results from several different parameters, such as step over, lead angle, feed rate, surface speed and its resulting RPM on the spindle. The surface roughness pointed out in this research does not include the step over factor since it can be neglected when kept constant and when measuring R_a in the cutting direction. The deformation of the elements can be measured in Abaqus using “U – Translation”, whereby

the translation is measured towards the original position of the element. The absolute translation vectors perpendicular to the machined surface were used and averaged to create a relative displacement value towards the mean of the displacement. In the final step the calculation of the standard surface roughness R_a can be pursued. This method allows it to predict the surface roughness precisely within an accuracy of 77% which correlates to $0.2 \mu\text{m}$, whereby the measuring tolerance of the optical surface roughness machine is $0.315 \mu\text{m}$. The average surface roughness formula was introduced in section 2.2.3 and stated in equation (2.2).

In Figure 5.12 the surface roughness (R_a) is compared between the FEM and experiments. It can be seen that most of the values are within the measuring tolerances of the optical microscope. This accurate prediction allows it to use these verified values in the soft prediction model as input variables.

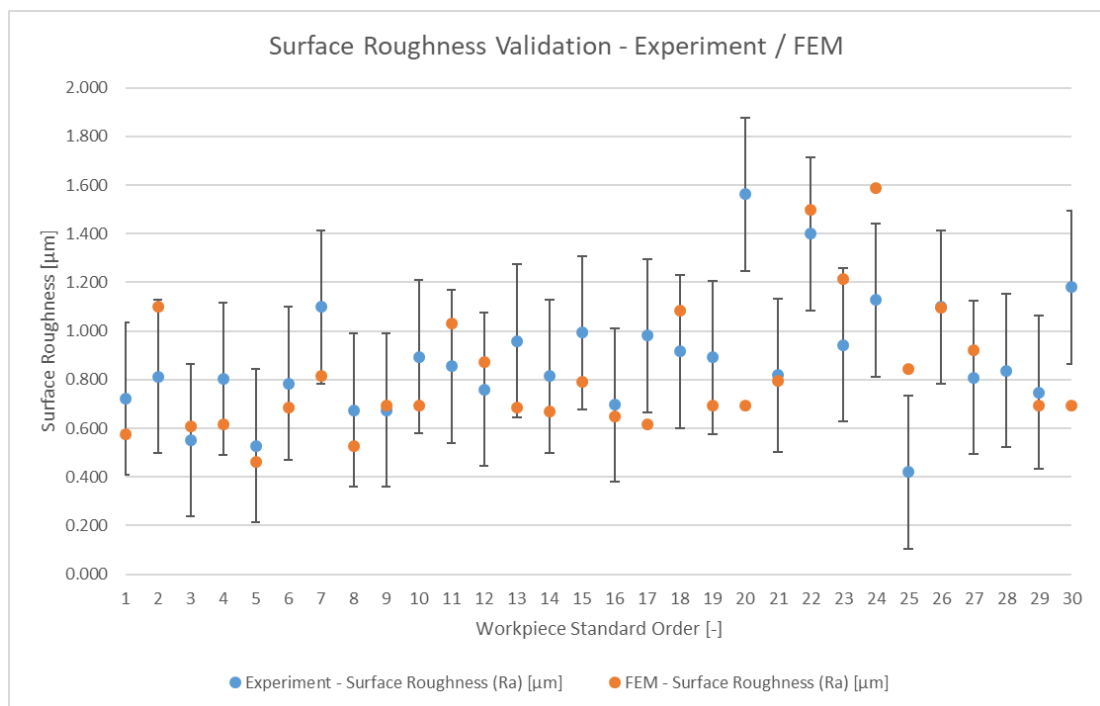


Figure 5.12: Comparison of surface roughness obtained by FEM and Experiment

An ANOVA analysis was carried out and found behaviour similar to the experiments (R_a). The surface speed and feed rate were the most influencing factors, followed by the lead angle and depth of cut. Similar behaviour was seen in the experiment - the values in this regression are close to each other. Figure 5.13 shows the interaction of the factors to the surface roughness; it can be observed that all factors are influencing each other result, as expected. Furthermore, it is shown in the effect plot that all factors have a strong quadratic behaviour. However, the calculated results from

Table 5.7 show that these are not significantly influential.

Table 5.7 ANOVA for FEM machining parameter on surface roughness (R_a)

Source	Adjusted Sums of Squares	Adjusted mean squares	F-Value	P-Value
Linear				
Surface Speed	0.2274	0.2274	3.24	0.092
Depth of Cut	0.0005	0.0004	0.01	0.937
Feed Rate	0.0680	0.0679	0.97	0.341
Lead Angle	0.1905	0.1905	2.71	0.120
Square				
Surface Speed * Surface Speed	0.1188	0.1188	1.69	0.213
Depth of Cut * Depth of Cut	0.5513	0.5513	7.85	0.013
Feed Rate * Feed Rate	0.0217	0.0217	0.31	0.586
Lead Angle * Lead Angle	0.5839	0.5839	8.32	0.011
2-Way				
Surface Speed * Depth of Cut	0.1188	0.1188	1.69	0.213
Surface Speed * Feed Rate	0.5513	0.5513	7.85	0.013
Surface Speed * Lead Angle	0.0217	0.0217	0.31	0.586
Depth of Cut * Feed Rate	0.5839	0.5839	8.32	0.011

<i>Depth of Cut * Lead Angle</i>	0.0007	0.0007	0.01	0.924
<i>Feed Rate * Lead Angle</i>	0.1336	0.1336	1.90	0.188
Error				
<i>Lack-of-Fit</i>	1.0530	0.1053		
<i>Pure</i>	0	0		

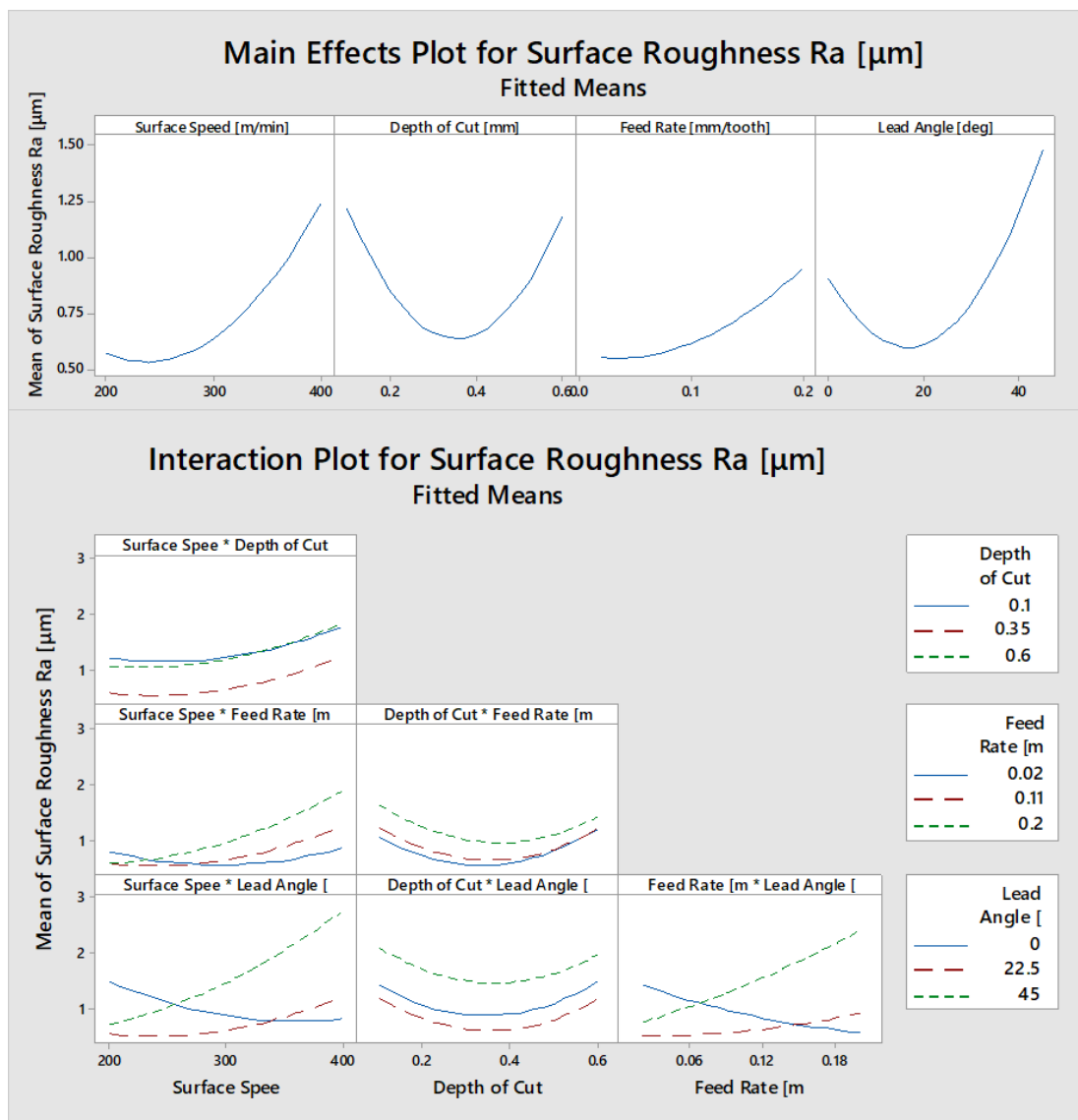


Figure 5.13: Effect and interaction plots for surface roughness on machining

5.5 Summary

Overall it can be concluded from this chapter that a highly accurate FE-model has been developed and verified, which can be used for input variables to the soft prediction model for machining optimisation. This chapter developed a FEM framework to improve and run multiple machining setups. The framework allows the end user to set up numerous FE-simulations in a comparable way and allows them to analyse the simulation in the same way. The big advantage is that all results are comparable since the same method / points of measurement are selected for the analysis.

A validation model of the simulation was developed and implemented to verify the simulation. This new model produced a more accurate machining simulation of residual stress and cutting forces. This newly developed model showed that an accurate prediction of a 3D-milling process is possible. The outcome was that the developed simulations are highly accurate and can predict the surface roughness with an accuracy of 77% and the residual stress with an accuracy of 80%. Furthermore, the cutting force can be predicted with an overall MSE of 20%. Information on the temperature distribution during the machining process was also analysed.

Critically, this FE-model greatly reduces experimental costs in develop an in-depth understanding of the machining process. Furthermore, when running simulations on parallel-computer the calculation time and overall process time is shorter when compared to similar experiments.

Chapter 6 Modelling & Optimisation of Fatigue Life

In this chapter, the optimisation of the end-milling process is developed and discussed. A soft prediction model was firstly developed and validated to predict and optimise the values gained from the experiments and the simulation. After the development of the model the soft prediction model was used to generate optimum surface integrity values and predict the fatigue performance of the optimised surface along with the output of the machining parameters for such a surface. At the end of this chapter testing and validation of the optimised values is discussed. To achieve this goal the Artificial Neural Network (ANN) was used to predict the results and the Genetic Algorithm (GA) to optimise the process.

6.1 Developing Soft Prediction Model

The soft prediction model was developed in Matlab (R2017a) Toolbox Neural Network (Ver. 10.0). In Figure 6.1 a visual overview of the principle of the optimisation model is shown. The complete soft prediction model contains two neural networks and one genetic algorithm. As illustrated, the first neural network will develop the prediction of the surface integrity based on the simulation and experimental outcome, whereby the cutting parameters are the input for this network. Based on this network the genetic algorithm will evolve and generate outcomes for the optimum surface integrity. Afterwards, the second neural network, which was trained by the outcome of the fatigue experiment will predict the fatigue performance based on surface integrity.

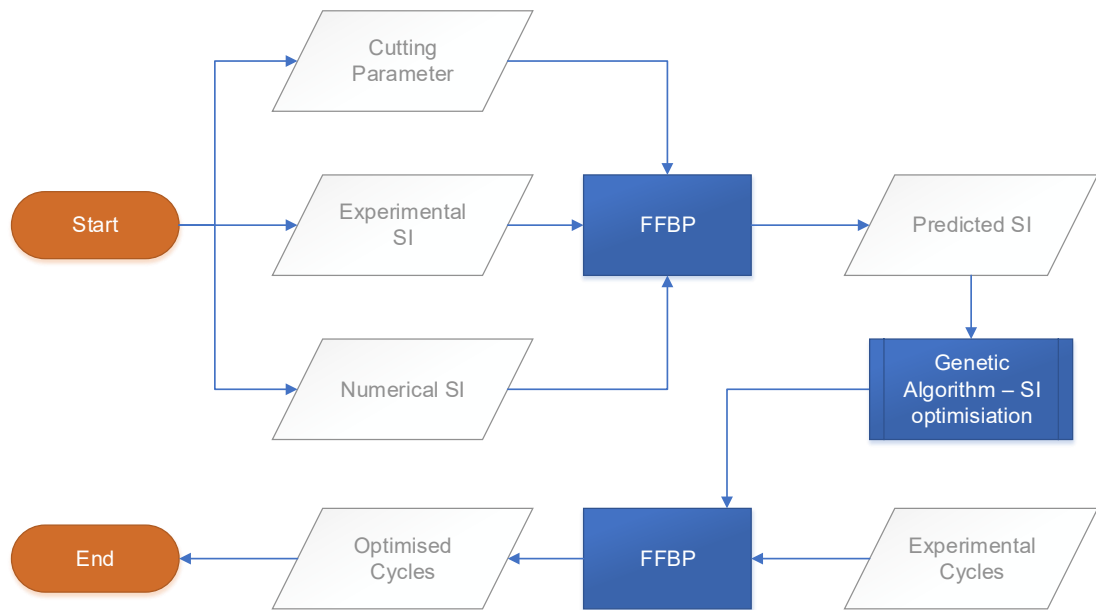


Figure 6.1: Soft prediction model - the optimisation process

6.1.1 Creating an Artificial Neural Network

As mentioned in section 0, the general principle of a neural network is based on the human brain structure. There are several types of neural networks, and in this research utilised the FFBP (feedforward backpropagation) network and RBF (Radial Basis Function) network type. The performance of both networks was compared by measuring regression accuracy as well as the Mean Squared Error (MSE).

A sequential order of networks was tested with three hidden layers and ranged from 1 to 10 neurons in each layer; which resulted in 1000 tested networks. The training, validation and test ratio of those FF (feed forward) networks was 70:15:15 respectively. Figure 6.2 shows the best structure of the FF network. The optimum combination does not always contain the most neurons in every single layer. For this reason the sequential test combination was carried out.

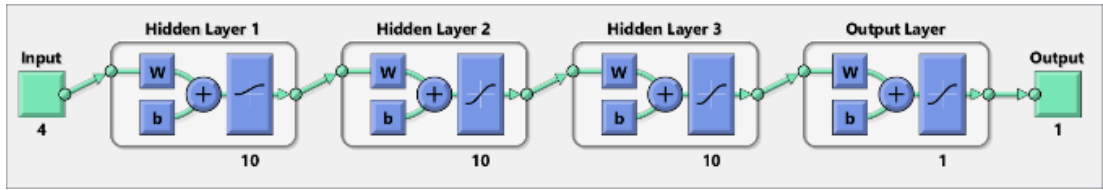


Figure 6.2: FF Network structure

This network consists of an input layer, three hidden layers with each 10 neurons and an output layer. Every tested network was trained 200 times to achieve a consistent outcome. It was found that when the activation functions of the hidden layers use a combination of activation functions, this increases the performance of the network. The best performance was achieved when the first hidden layer was set to a Log-Sigmoid activation function (equation (6.1)); the following two hidden layers and the output layer pertain to a hyperbolic-tangent sigmoid activation function (equation (6.2)).

$$\text{logsig}(x) = \frac{1}{1 + e^{-x_i}} \quad (6.1)$$

$$\text{tansig}(x) = \frac{e^{x_i} - e^{-x_i}}{e^{x_i} + e^{-x_i}} \quad (6.2)$$

The training of the neural network was based on the backpropagation function. The algorithm can be described as follows. In the first step the input goes through the system, then the MSE (equation (6.3)) is calculated; from the output the sensitivity is propagated back to the first layer and the weights and biases are updated [122].

The MSE is a function for measuring and evaluating the performance in neural networks. It can be defined as follows in equation (6.3):

$$MSE = \frac{1}{n} \sum_{k=1}^n (y_k - t_k)^2 \quad (6.3)$$

Where n indicates the number of total data patterns, y_k is the output generated by the neural network at point k , and t_k is the target value at point k . The calculation of the actual distance between output and target is the Root Mean Squared Error (RMSE), which can be calculated as follows in equation (6.4):

$$RMSE = \sqrt{\frac{1}{n} \sum_{k=1}^n (y_k - t_k)^2} \quad (6.4)$$

Added to the more ‘traditional’ feedforward network with backpropagation (FFBP) is the Radial Basis Function Network (RBF). A general structure of the RBF can be found in Figure 6.3; the network consists of an input layer, one hidden layer and an output layer. The hidden layer has 37 neurons (the same amount as the entire experiment).

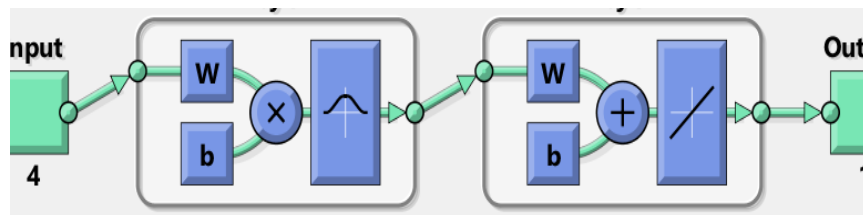


Figure 6.3: RBF Network structure

The hidden layer uses a Gaussian activation function – formula (6.5) where x_i is weighted input vector for the specific neuron i ; c_i is the centre of neuron i and ω_i is the width of neuron i [127].

$$rbf(x) = e^{\left(-\frac{\|x_i - c_i\|^2}{\omega_i}\right)} \quad (6.5)$$

It was found that the RBF performs better within a small given range of training data, but with broader spread data points especially for data interpolation, the RBF performs poorly compared to the FFBP. Therefore the FFBP was used to predict and interpolate the surface integrity and fatigue performance.

6.1.2 Optimisation with Genetic Algorithm

The genetic algorithm is based, as mentioned before in section 2.5.3.2, on the natural genetic evolution and discards the least fit condition in the following generation. This principle supports the development of an optimised output.

Since Genetic Algorithms can optimise one objective they have a significant advantage, compared to regression optimisation. The algorithm is also capable of optimising on multiple objectives, whereby the objectives can be contrary to each other. This so-called multi-objective genetic algorithm, however, cannot be visualised, as there are more than two objectives and variable dimensions. Usually, the GA function is plotted, by a Pareto plot, which indicates the correlation of the objectives.

The genetic algorithm needs defined boundaries to work on within a realistic and optimum level. The nonlinear constraints were evolved from a 4th order regression of the results in using the machining parameter; the constraint can be found in the Matlab-coded formulas ((6.6),(6.7),(6.8)) below.

$$\begin{aligned} c(1) = & (-0.13134 * x(:,1).^2 + 158.1 * x(:,1) * x(:,2) - 69.719 \\ & * x(:,1) * x(:,3) - 1.1179 * x(:,1) * x(:,4) + 0.00055106 \\ & * x(:,1).^3 - 0.81561 * x(:,1).^2 * x(:,2) + 0.41529 \\ & * x(:,1).^2 * x(:,3) + 38.984 * x(:,1) * x(:,2) * x(:,3) \\ & + 0.016616 * x(:,1).^2 * x(:,4) - 6.7745 * x(:,1) * x(:,2) \\ & * x(:,4) - 1.2565 * x(:,1) * x(:,3) * x(:,4) + 996.52 \\ & * x(:,2) * x(:,3) * x(:,4) - 1.1582e - 06 * x(:,1).^4 \\ & + 0.0023615 * x(:,1).^3 * x(:,2) - 0.74851 * x(:,1).^2 \\ & * x(:,2).^2 + 97.135 * x(:,1) * x(:,2).^3 - 0.00052979 \\ & * x(:,1).^3 * x(:,3) - 0.11359 * x(:,1).^2 * x(:,2) * x(:,3) \\ & - 0.10743 * x(:,1).^2 * x(:,3).^2 - 2.8697e - 05 \\ & * x(:,1).^3 * x(:,4) + 0.0017578 * x(:,1).^2 * x(:,2) \\ & * x(:,4) + 7.6171 * x(:,1) * x(:,2).^2 * x(:,4) \\ & + 0.0027643 * x(:,1).^2 * x(:,3) * x(:,4) - 2.3892 \\ & * x(:,1) * x(:,2) * x(:,3) * x(:,4)) \end{aligned} \quad (6.6)$$

$$\begin{aligned}
c(2) = & (0.00020744 * x(:,1).^2 - 0.20683 * x(:,1) * x(:,2) - 0.0010168 \\
& * x(:,1) * x(:,3) + 0.0022568 * x(:,1) * x(:,4) - 5.9257e \\
& - 07 * x(:,1).^3 + 0.00076777 * x(:,1).^2 * x(:,2) + 9.5776e \\
& - 08 * x(:,1).^2 * x(:,3) + 0.30607 * x(:,1) * x(:,2) * x(:,3) \\
& - 4.1889e - 05 * x(:,1).^2 * x(:,4) + 0.021648 * x(:,1) \\
& * x(:,2) * x(:,4) + 0.015042 * x(:,1) * x(:,3) * x(:,4) \\
& - 13.914 * x(:,2) * x(:,3) * x(:,4) + 1.5703e - 09 \\
& * x(:,1).^4 - 3.9518e - 06 * x(:,1).^3 * x(:,2) + 0.0023002 \quad (6.7) \\
& * x(:,1).^2 * x(:,2).^2 - 0.39705 * x(:,1) * x(:,2).^3 + 3.7933e \\
& - 07 * x(:,1).^3 * x(:,3) - 0.0012786 * x(:,1).^2 * x(:,2) \\
& * x(:,3) - 1.6367e - 05 * x(:,1).^2 * x(:,3).^2 + 8.117e - 08 \\
& * x(:,1).^3 * x(:,4) - 2.2718e - 05 * x(:,1).^2 * x(:,2) \\
& * x(:,4) - 0.018644 * x(:,1) * x(:,2).^2 * x(:,4) - 4.8688e \\
& - 05 * x(:,1).^2 * x(:,3) * x(:,4) + 0.046437 * x(:,1) \\
& * x(:,2) * x(:,3) * x(:,4)) * -1
\end{aligned}$$

$$\begin{aligned}
c(3) = & (0.004439 * x(:,1).^2 - 0.42475 * x(:,1) * x(:,2) + 0.95028 \\
& * x(:,1) * x(:,3) - 0.00026253 * x(:,1) * x(:,4) - 1.351e \\
& - 05 * x(:,1).^3 - 0.0021216 * x(:,1).^2 * x(:,2) \\
& - 0.0071018 * x(:,1).^2 * x(:,3) - 1.2593 * x(:,1) * x(:,2) \\
& * x(:,3) - 0.00010926 * x(:,1).^2 * x(:,4) + 0.078345 \\
& * x(:,1) * x(:,2) * x(:,4) - 0.074636 * x(:,1) * x(:,3) \\
& * x(:,4) + 65.292 * x(:,2) * x(:,3) * x(:,4) + 1.0837e - 08 \\
& * x(:,1).^4 - 1.0353e - 07 * x(:,1).^3 * x(:,2) + 0.0036323 \quad (6.8) \\
& * x(:,1).^2 * x(:,2).^2 + 0.50644 * x(:,1) * x(:,2).^3 + 1.2911e \\
& - 05 * x(:,1).^3 * x(:,3) + 0.0030571 * x(:,1).^2 * x(:,2) \\
& * x(:,3) + 0.002371 * x(:,1).^2 * x(:,3).^2 + 2.0247e - 07 \\
& * x(:,1).^3 * x(:,4) + 1.3962e - 05 * x(:,1).^2 * x(:,2) \\
& * x(:,4) - 0.10986 * x(:,1) * x(:,2).^2 * x(:,4) \\
& + 0.00020148 * x(:,1).^2 * x(:,3) * x(:,4) - 0.19583 \\
& * x(:,1) * x(:,2) * x(:,3) * x(:,4)) * -1
\end{aligned}$$

Where $c(1)$ is the constraint for residual stress, $c(2)$ for the surface roughness and $c(3)$ for the hardness. The statements of $x(:,1)$, $x(:,2)$, $x(:,3)$, $x(:,4)$ refers to surface speed, depth of cut, feed rate and lead angle, respectively.

The machine also has physical limitations. Therefore the machine parameter needs to set a range of lower and upper bounds. In the following Table 6.1, the bounds on the machine parameter can be found.

Table 6.1: Bounds for Genetic Algorithm

<i>Bound</i>	Surface Speed [m/min]	Depth of Cut [mm]	Feed Rate [mm/tooth]	Lead Angle [deg]
<i>Lower Bound</i>	200	0.1	0.02	0
<i>Upper Bound</i>	400	0.6	0.20	45

6.1.3 Validation Strategy of Soft Prediction Model

The validation of the soft prediction was tested on several stages, as illustrated in Figure 6.4. In the first stage surface integrity was predicted to a known outcome based on experimental results. However, this data was unknown to the network, before. The second stage predicted parameters, which were outside of the physical experimental range; results from FEA simulation were then predicted. If this passed then the optimisation ran, and experiments were carried out to verify the predicted results.

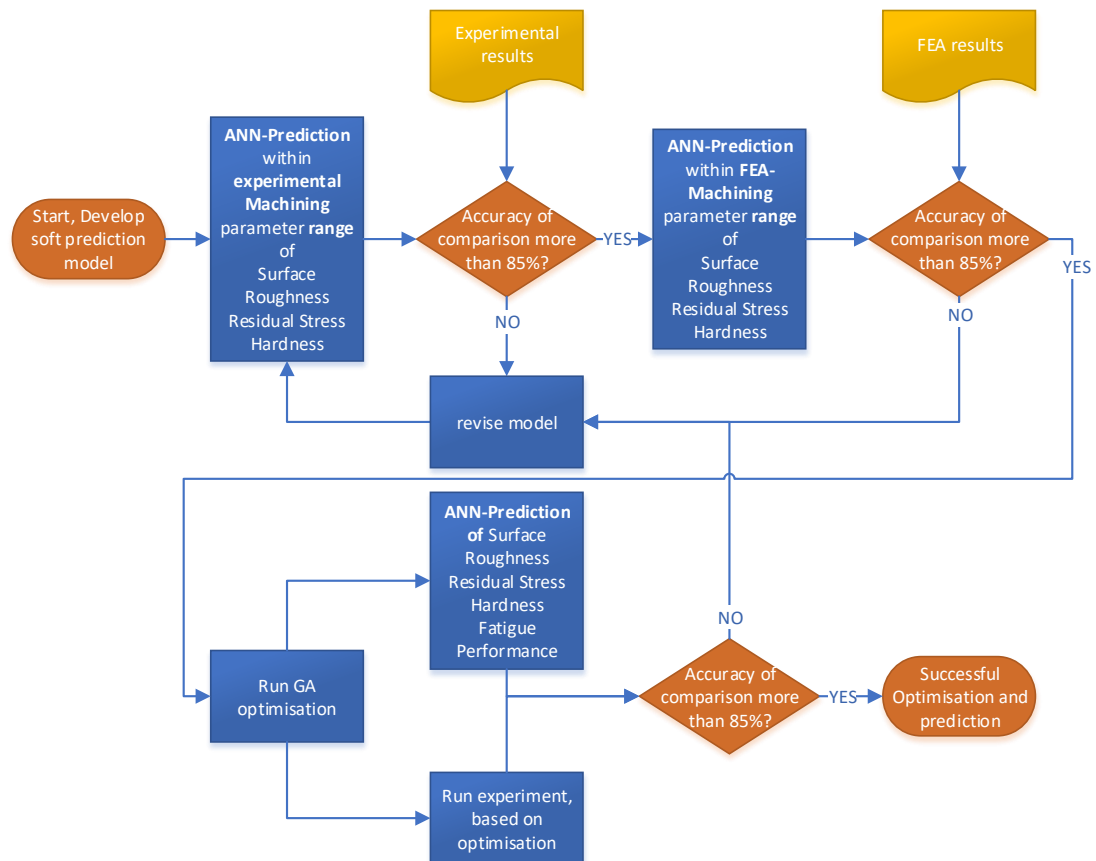


Figure 6.4: Soft prediction validation model

The revision of the model included restricting, programming and changing the initial values and weights for the starting point of the prediction and optimisation model. Figure 6.4 shows the validation model and it is based on the surface integrity values including fatigue life.

6.2 Experimental studies for optimised process

To validate the optimisation discussed, the general setup of the experiments was the same, as already shown in Chapter 3 and Chapter 4. For the optimisation, the machining parameter was changed to optimise the surface integrity and consequently the fatigue life. This chapter discusses the outcome of the optimised parameter.

6.2.1 The Parameter for Optimised Process

The soft prediction model was explained in the previous section. Once the values entered in the system, the optimised parameter were retrieved. In this section, the results gained from the prediction model are shown.

To run the prediction model, the validated FEA was used to predict a complete picture of the model. The predicted residual stress and surface roughness were taken from the FEA simulation. However, the hardness values were taken from the experiments and interpolated by using the RBF to the number of data points equal to the FEA. These values support the prediction in the FFBP network, which then feeds into the GA for optimisation.

Figure 6.5 illustrates the relationship between the target values (physically measured results) and the predicted values. At this stage, a correlation of 72.5% can be achieved, whereby three components are predicted at the same time: the surface roughness, hardness and the residual stress.

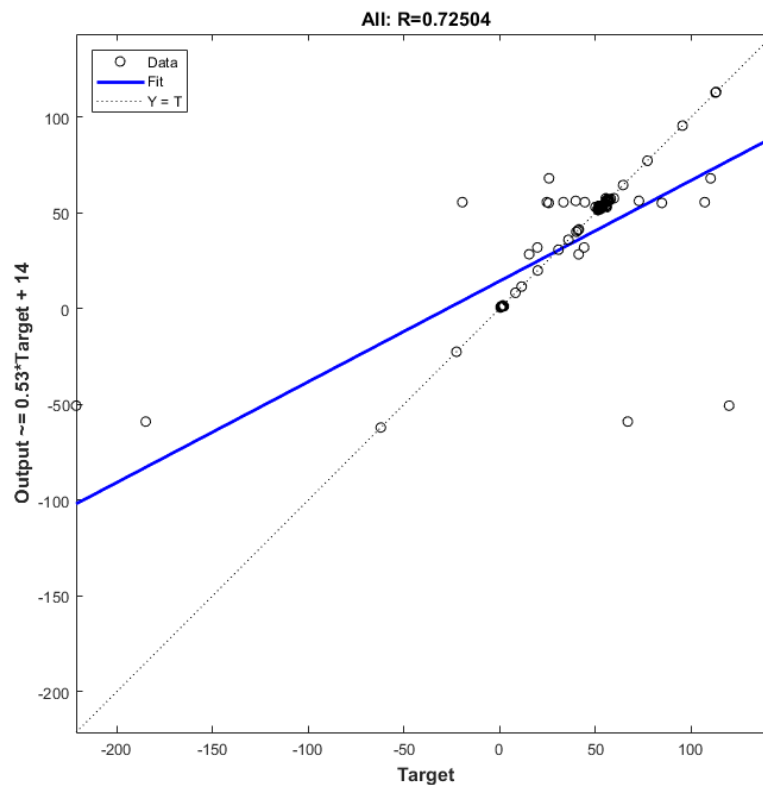


Figure 6.5: Correlation regression of target values and predicted values

In the second stage of the optimisation, a new network has been trained to predict the fatigue life of the components using the optimum predicted surface integrity, within the given boundaries. The network was trained by physically measured surface integrity and fatigue life performance. In Figure 6.6 the evolution of this new neural network to predict the fatigue performance is clear.

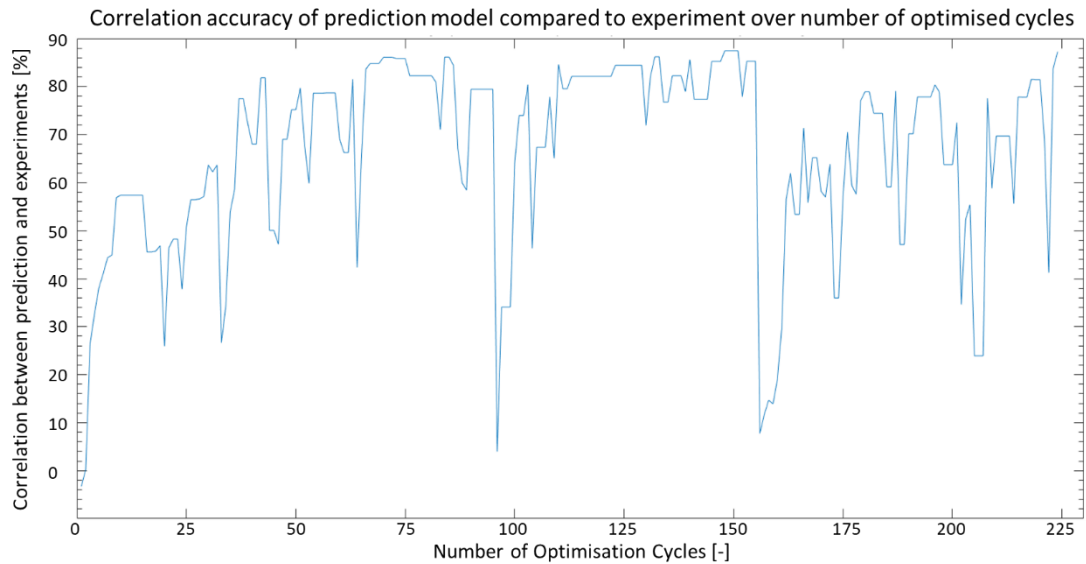


Figure 6.6: Optimisation evolution of soft prediction model

This new network can achieve an accuracy of over 87% to predict fatigue life performance based on surface integrity. In Figure 6.7 the regression model of the prediction model can be seen. This regression plot illustrates the training, validation and testing values respectively, compared to the target values (the measured output of the fatigue performance).

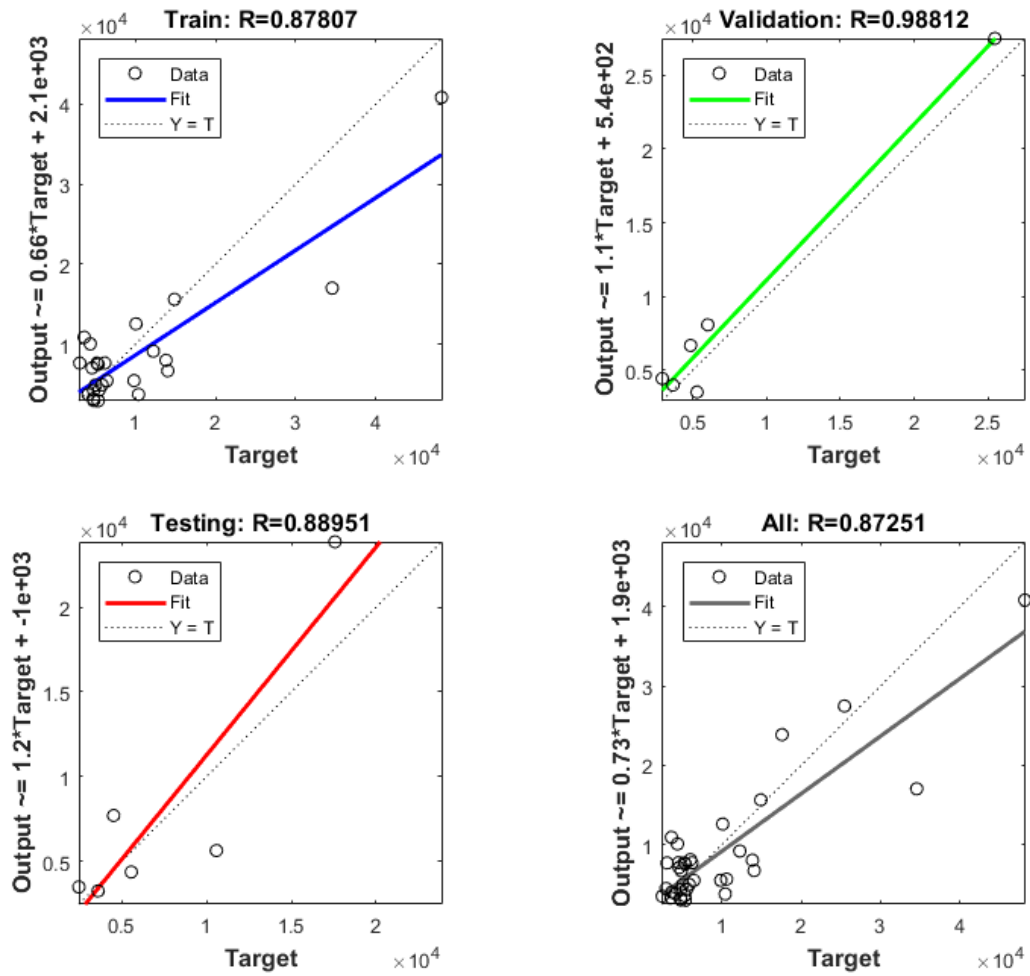


Figure 6.7: Optimisation regression model

As a result of this soft prediction model, the neural network gave multiple responses toward the optimisation. In Table 6.2, the results of the prediction are evident.

Table 6.2: Outcome of the optimisation process

Cycles [-]	Residual Stress (S11) [MPa]	Sa [μm]	Hardness [HRC]	Surface Speed [m/min]	Depth of Cut [mm]	Feed Rate [mm/tooth]	Lead Angle [deg]
3462	62.03	0.928	53.35	243	0.40	0.08	13.69
3631	62.50	0.899	53.52	243	0.40	0.07	13.68
4375	76.29	0.872	53.74	238	0.39	0.06	16.45
4550	47.73	0.960	53.19	250	0.42	0.05	17.76
4610	15.38	0.944	54.60	346	0.48	0.04	19.55
5725	6.47	0.976	55.13	347	0.49	0.04	16.69
6929	85.61	0.840	54.02	233	0.37	0.06	14.96
7233	82.38	0.833	54.02	234	0.37	0.06	13.91
7316	56.16	0.849	54.02	232	0.41	0.06	13.47
7662	70.32	0.814	54.19	232	0.37	0.05	13.40
14050	-31.56	1.003	54.72	310	0.53	0.04	18.14
15234	26.21	1.030	52.86	297	0.44	0.07	18.00
16092	-26.72	0.991	54.61	312	0.51	0.04	17.81
16375	33.93	1.048	52.78	319	0.44	0.08	20.11
19389	42.48	0.979	53.14	270	0.39	0.06	16.04

The highest two cycle-results in Table 6.2 were used in further experimental validation trials to verify the optimisation process. These optimum cutting conditions are more than two times the average value of the conducted experiments and more than 3.5 times higher than the often used standard values for end milling processes of AISI H13.

Furthermore, to test if this soft prediction model is more robust than a standard regression model, experimental values were optimised using a surface response model.

The optimisation of the surface response model was carried out in Minitab 18; and the optimisation process can be found in the following Figure 6.8.

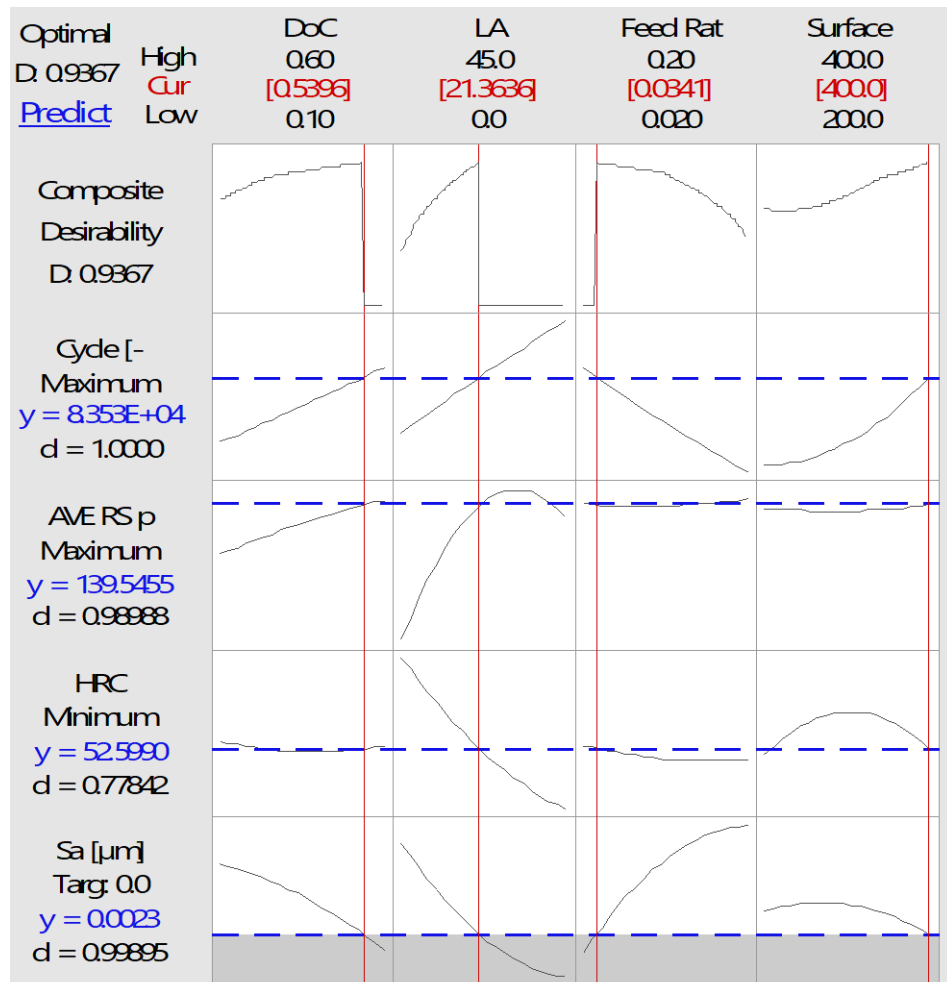


Figure 6.8: Surface response optimisation

For the physical validation trials three different sets of optimisation values were conducted. These are listed in Table 6.3.

Table 6.3: Optimised cutting parameters and tool lead angle values

	Trial Name	Surface Speed [m/min]	Depth of Cut [mm]	Feed Rate [mm/tooth]	Lead Angle [deg]
GA & ANN 1	Validation 1	319	0.44	0.0788	20.112
GA & ANN 2	Validation 2	270	0.39	0.0589	16.045
Surface Response	Validation 3	400	0.54	0.0341	21.364

6.2.2 Experimental Results and Discussion of Optimised Process

In this chapter, the results for the validation experiments were presented and discussed. The experimental procedure and general condition were kept the same to ensure comparability of the experimental results. The only variable parameters were the machining parameters to be investigated; this was discussed before. In the following section, the surface integrity results are presented, followed by the fatigue experiment results.

6.2.2.1 Machining Experiment

The residual stress was measured for the validation experiment, whereby the optimisation was targeting to minimise the residual stress to compressive (negative) stress components. Table 6.4 shows the results of the measured residual stress, whereby predicted references to the soft prediction model.

Table 6.4: Optimised validation results for Residual stress [MPa]

<i>Trial Name</i>	Residual Stress (S11) [MPa]	Predicted Residual Stress (S11) [MPa]	Residual Stress (VM) [MPa]	Predicted Residual Stress (VM) [MPa]
<i>Validation 1</i>	-182.7 ± 12.2	33.93	178.41 ± 9.0	158.47
<i>Validation 2</i>	34.7 ± 14.3	42.48	171.01 ± 11.2	159.66
<i>Validation 3</i>	67.6 ± 16.5	139.55	226.85 ± 11.1	161.14

It can be observed that the residual stress value has been generally reduced, and in Validation 2 especially the predicted values are within the measured tolerances. However, the stress vectors for Validation 1 and 3 are lower than the predicted values. Furthermore, the plane residual stress prediction is within the tolerances of Validation 1 and 2.

In the next step, the surface hardness was measured. The hardness was one of the critical components for fatigue life and is therefore essential to optimise the surface hardness to retain an optimum result. The results of the hardness

measurement and the predicted (target) values are shown in Table 6.5. The predicted values and the measured values correlate well.

Table 6.5: Optimised validation results for Microhardness [HRC]

<i>Trial Name</i>	(average) Hardness [HRC]	Predicted Hardness [HRC]
<i>Validation 1</i>	53.03 ± 2.55	52.78
<i>Validation 2</i>	51.45 ± 3.20	53.14
<i>Validation 3</i>	52.08 ± 1.66	52.60

The surface roughness was conducted before the fatigue experiment. Table 6.6 shows the results.

Table 6.6: Optimised validation results for surface roughness S_a [μm]

<i>Trial Name</i>	(average) S_a [μm]	Predicted S_a [μm]
<i>Validation 1</i>	1.19	1.05
<i>Validation 2</i>	1.04	0.98
<i>Validation 3</i>	1.22	0.00

The results of Table 6.6 show that the correlation of the predicted surface roughness and the measured results are very close. Furthermore, it can be seen that the predicted results from the surface response model are not as close as the prediction of the neural network prediction.

Overall, it was found that this soft prediction model has an excellent correlation between the prediction results and the measured results. It was found that the surface response model, which based on the regression model, cannot achieve as accurate a correlation as the neural network.

6.2.2.2 Fatigue Experiment

This section explains the predicted cycles based on surface integrity. The same conditions as in the previous fatigue experiments were applied. The results of the fatigue experiment can be found in Table 6.7. These values are an average of the conducted experiments; each parameter set has been repeated three times.

Table 6.7: Optimisation validation results for fatigue performance

<i>Trial Name</i>	Cycles [-]	Predicted Cycles [-]
<i>Validation 1</i>	15362	16375
<i>Validation 2</i>	20111	19389
<i>Validation 3</i>	15968	83530

The table above shows that the setting for “Validation 2” in the optimisation process is the most promising parameter selection. Furthermore, it’s clear that the predicted value for Validation 1 and 2 are close to the measured value. However, the less robust surface response model optimisation has a considerably lower outcome than predicted. This outcome proves the originally stated hypothesis that the SRM is a less robust and accurate model for predicting these findings when comparing the results with the central point of the DoE (Surface Speed 300 m/min, Depth of Cut 0.4 mm, Feed Rate 0.12 mm/tooth, Lead Angle 15 deg.), the overall cycle performance improved from 5500 Cycles to over 20100 Cycles (on average), due to improved surface conditions, like surface roughness, residual stress, and hardness.

6.2.3 FEA results of the optimised process

In this section the FE-simulation of the optimised process is presented. As in other sections the simulation followed and was compared and validated by comparing it with the experiments. However, the stress development prediction of the simulation was analysed to determine if predicted

improvements/trends in the simulation can be observed. Table 6.8 shows the results of the FEM.

Table 6.8: Simulation results of optimised validation runs

<i>Trial Name</i>	FEM Residual Stress (VM) [MPa]	Target Residual Stress (VM) [MPa]	Measured Residual Stress (VM) [MPa]	FEM Surface roughness (R_a)	Measured roughness (R_a)
<i>Validation 1</i>	123.88	158.47	178.41 ± 9.0	0.67	0.505
<i>Validation 2</i>	175.02	159.66	171.01 ± 11.2	0.53	0.269
<i>Validation 3</i>	204.25	161.14	226.85 ± 11.1	0.31	0.166

The values suggest a strong correlation between the residual stress of the simulation and the targeted (predicted values). However, when comparing the FEM results with the surface roughness values of the experiment (R_a) the values are not as precise as anticipated. Yet a trend can be noticed. The offset of the compared surface roughness can have multiple reasons. During the simulation the cutter deforms the elements too much as the “optimised” depth of cut does not exactly match the element structure; this can cause a higher distortion and therefore a higher FEM predicted surface roughness, as shown in Figure 6.9. This problem could be resolved when running the same simulation in a much finer mesh resolution. However, the calculation time increased significantly.

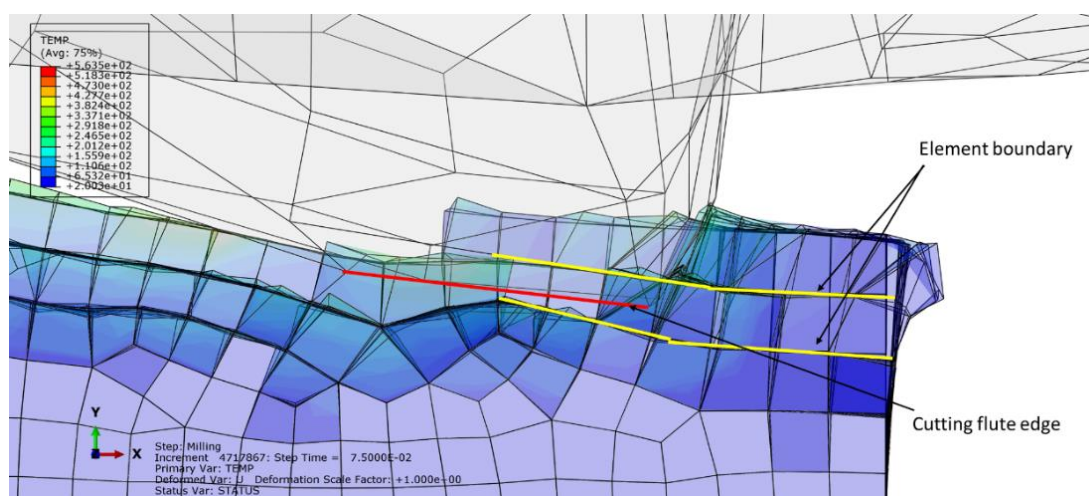


Figure 6.9: Element boundaries in validation simulation

The overall performance of the FEM is within the validation range; the simulation can therefore be used to predict and analyse the machining process and support understanding of the process.

6.3 Summary

In this chapter the development of the neural network and the genetic algorithm was presented. It was found that a Feed Forward Neural network with Backpropagation (FFBP) is the most reliable and accurate type of neural networks. The FFBP was used to predict results based on experimental and finite element analysis inputs. These predictions for surface integrity (SI) were used and optimised in a genetic algorithm (GA) to optimise the SI. Once the SI had been optimised, another FFBP network was trained to predict the outcome for the fatigue performance on the workpiece based on experimental results. The combination of neural networks and genetic algorithm is a highly accurate method to predict the surface integrity and fatigue life, in this thesis an accuracy of 72.5% and 87% was achieved.

The two best outcomes were taken for a validation trial, which was also presented in this chapter. Furthermore, a Surface Response Model (SRM) optimisation was also taken for the validation process and then compared with the neural network prediction models. The result was that the SRM was not as accurate and robust as the FFBP. It was also found that the FFBP prediction achieved a close value towards the measured values of the validation trials.

Chapter 7 Conclusions and future work

This chapter summarises the findings of this research and its contribution to the knowledge in field of precision milling. Considerations for possible future work are given at end of this chapter.

7.1 Conclusions

Precision machining is currently one of the most common manufacturing processes, for making high-precision forging and forming dies made from alloys, metals, or composite materials. The die machining is a challenging and cost-intensive process since complex geometry and high surface finishing are required. Manufacturers often use dies with coatings and/or treatments to prolong fatigue life, in order to help reduce production costs as it avoids machine downtime and lowers die manufacturing costs. Additionally, some formed components like aerofoils or big screw heads require very high accuracy in terms of their surface integrity and geometrical accuracy; therefore, industries are interested in defining new ways for reducing die manufacturing costs, at the same time, still benefiting from a longevity of the manufactured die.

This work investigated the influencing factors of such critical processes on surface integrity, to enhance die fatigue life by optimising the machining process parameter, which in turn optimises the surface integrity. To achieve this goal, this research applied numerical simulations (using ABAQUS), soft prediction models (using Artificial Neural Networks) and experiments (machining and fatigue experiments). This enabled a study of the finishing process during the manufacturing using a variety of parameters, such as surface speed, depth of cut, feed rate and tool lead angle; these machining parameters were used to investigate the optimum surface integrity.

The key findings of this research are concluded as follow:

1. It was found that, the tool lead angle had the most significant impact on the cutting force during the machining experiments. The residual stress and microhardness were mostly influenced by the surface speed. However, the feed rate had the most significant influence on both surface roughness and microstructure. These results on the surface integrity are noteworthy as they are influencing the fatigue life of the component.
2. On the fatigue life performance, it was found that surface roughness was the most influential factor, due to the related surface defects. Because the increase of surface roughness increases the possibility of crack initiation points, which lead to an earlier crack and finally fatigue. Furthermore, it was also found, that the hardness influenced the fatigue life, due to the high loads during the fatigue test. Testing on low-cycle fatigue, it was observed that soft and more ductile workpiece surfaces had a higher fatigue life than harder and more brittle workpiece surfaces. It was also found that residual stress did not have a significant impact on fatigue life because the applied stresses on the workpiece exceeded those remaining in the workpiece.
3. The newly developed model found that the developed simulations are highly accurate and can predict the surface roughness with an accuracy of 77% and the residual stress with an accuracy of 80%. Furthermore, the cutting force can be predicted with an overall MSE of 20%.
4. Using the Artificial Neural Network, it was discovered, that a Feed Forward Neural network with Backpropagation (FFBP) is the most reliable and accurate type of neural networks. The FFBP was used to predict results based on experimental and finite element analysis inputs. The combination of neural networks and genetic algorithm is a highly accurate method to predict the surface integrity and fatigue life, in this thesis an accuracy of 72.5% and 87% was achieved.
5. The results of this research found that the optimisation process, on average, doubled the fatigue duration when compared to standard parameters (central point in Design of Experiments). It was found that a surface speed of 270 m/min, a feed rate of 0.0589 mm/tooth, a depth of cut

of 0.39 mm and a lead angle of 16.045° provide an optimum surface for increased fatigue performance.

The objectives stated in chapter 1.2 have been successfully achieved, and they were discussed in more detail as follows.

1. A prediction model was successfully developed to predict the surface integrity and fatigue life for forming and forging dies produced by precision milling. Based on the predicted surface integrity, the fatigue life under an elevated temperature and high loads on the components was predicted. This prediction model can be applied recursively, by entering different machining parameters that will predict the SI and vice versa a given SI can identify the machining parameter.
2. A comprehensive and novel FE-model was developed to simulate a high-speed end-milling process accurately in a 3D FEM environment. Based on a material hardening subroutine the novel model calculated the residual stress accurately along with the cutting forces. Using the current temperature, the model calculates in the element the Ultimate Tensile Strength; this influences the residual stress and cutting forces during the cutting process. Furthermore, the surface roughness was calculated from the FEM. The FE-simulations were validated by experiments.
3. The soft prediction model was developed and validated by experiments and FEM. It was used to develop a more sophisticated picture of the process and ultimately to optimise it. Genetic algorithm optimisation was used to identify one of the best solutions within the given boundaries of physics and mechanics. The optimised results were validated by specific physical experiments.
4. A generic framework was developed to carry out similar predictions for other materials and/or process parameters such as the type of milling or turning. The FEM can be easily adjusted to different materials or boundary conditions.

7.2 Contribution to Knowledge

This research presented an original and innovative work for the optimisation of precision milling process to improve the SI of produced forming and forging dies, thereby increase its fatigue life. Below are listed its four major contributions to knowledge.

1. Understanding of influence on process parameter on surface integrity and fatigue life

This thesis developed an *understanding and built a bridge between machining parameter and fatigue life*. In general, the machining parameter influencing the forging and forming die's surface integrity in a non-linear environment and furthermore the surface integrity to the fatigue life; this relationship is not trivial but cannot be directly linked to the machining parameter. The contribution from this thesis was able to develop a framework that allows predicting the surface integrity and linking this to the fatigue life, and then backwards developing the corresponding machining parameter.

2. Development of a new framework to enhance fatigue life of precision milled forming and forging dies through optimisation of the machining strategy.

In this thesis, a *framework for optimisation of machining strategy to enhance the fatigue life of the machined forming and forging dies* was developed. The framework is applicable to other machined alloy parts. Furthermore, the simulation and soft prediction models are not limited by workpiece material, cutting tool material or cutter type. They can be used and easily implemented into programmed setup files and run complex 3D machining simulations and evaluate automatically afterwards.

3. Development of a new material model for precise FEM simulation.

A new material model for accurate FEM simulations was developed and verified. This new material model was developed as a subroutine to be implemented into ABAQUS. However, the principle can also be applied with other FEM simulation software. The model is based on the temperature of the element and its correlated Ultimate Tensile Strength (UTS). It calculates the current temperature in the element based on the friction and interaction as well as the previous increment. The UTS changes with different temperatures; this causes a change of the resistance of the material which influences the residual stress due to the applied force on the element and therefore the induced heat. The material model decides if the current yield is higher than the current UTS to remove the element, as it is assumed that the elements cannot withstand a higher yield than the current UTS. This material model can also be applied to other materials. However, tensile test data needs to be acquired for the simulated material; this will allow the implementation the 3rd-grade polynomial regression. Additionally, a new script is develop to run extensive amount of FEM simulation. This research work carried out over 180 verified 3D-simulations on end milling. A comprehensive prediction model as well as a theoretical understanding of the process to validate the newly developed material model was then produced. It was used to understand the mechanisms of machining with a multiple flute engagement. This extensive amount of simulation could only achieved by scripts; the script setup allows for further similar simulations with different materials or cutters in future.

4. A newly developed neural network and genetic algorithm combination to precisely determine surface integrity and optimise it to achieve a better fatigue life.

This work also *developed a new combination of neural network and optimisation* for fatigue life performance. An artificial neural network (ANN)

was first developed to use simulation and experimental outcome to predict the surface integrity accurately. The model was then applied to the entire network in order to find optimum surface integrity within given boundaries such as the physical boundaries of the surface itself as well as boundaries of the machine. The multi-objective genetic algorithm evolves over generations to find optimum surface integrity (SI), which is defined by residual stress, surface roughness and hardness. Once an optimum SI is found the model trains a new ANN to produce the cutting strategy that delivers the optimum surface. The advantage is flexibility - the model can be applied to any other multi-objective optimisation and prediction with minor adjustments to the boundary conditions.

In addition, the contributions of the thesis to industrial practice are:

1. Finding of a set of optimum cutting parameters for a precision milling difficult-to-machine material

Using the optimisation model described above, the optimum cutting condition for AISI H13 was established using a four-flute ball nose cutter. This data can be used and applied in the industry directly and will significantly save time and costs in die manufacturing.

2. Development of a new fatigue testing rig

Moreover, a new fatigue testing rig is developed in this thesis to incorporate a four-point bending test. The production cost of the test-rig is low and it is flexible enough to meet ASTM standards such as a three-point bending test rig. Companies and research institutes such as the AFRC (Advanced Forming Research Centre) has been already benefiting from this test rig, which is 20 times cheaper than the original manufacturer's test platform. It therefore, can be applied in industry to save costs and resources.

7.3 Limitations and Future Work

In this research the objective was to optimise a current process by adjusting the process parameters in a newly developed framework and improving the process by better understanding its scientific and technological principles. This was achieved by using modelling, material testing and analysis, etc. However, it would be beyond the scope of this project to investigate all possible process parameters. Therefore some limitations, as well as possible solutions, have been identified as follows:

Repeatability of measurement: Due to limited time and budget restrictions, only a limited number of samples were used in the experiments. Although, by comparing the result with the existing literature it the testing data obtained was equitable. It is suggested to increase the number of test samples, in order to improve the accuracy of the result.

Raw material quality: The quality and conditions of the raw material used plays a vital role in machining since it can cause variations in the outcome of the suggested parameter. It must be borne in mind that repeatability might suffer under this circumstance, but not the developed framework. Therefore, it is advisable to control the raw material input in precision machining.

Although beyond the scope of this research some future researches for gaining wider academic benefit and creating larger industrial impact are suggested as:

Expanding the research of the developed framework: The developed framework is effective and robust to develop the optimum cutting condition for other materials as well as other influencing parameters. This research methodology and developed framework could be expanded to include other novel materials and different cutting processes such as face milling, slotting and grinding, to help determine the best cutting condition for each process.

Implementation to Industry 4.0: Future development could bring this research forward and implement it into Industry 4.0, as part as intelligent optimising process in the machine or CAM system. The machine system is

feeding back into the optimisation framework, whereby it continuously improves the machining process. A primary sample in Figure 7.1 shows where this research could be implemented as hardware in the loop tool.

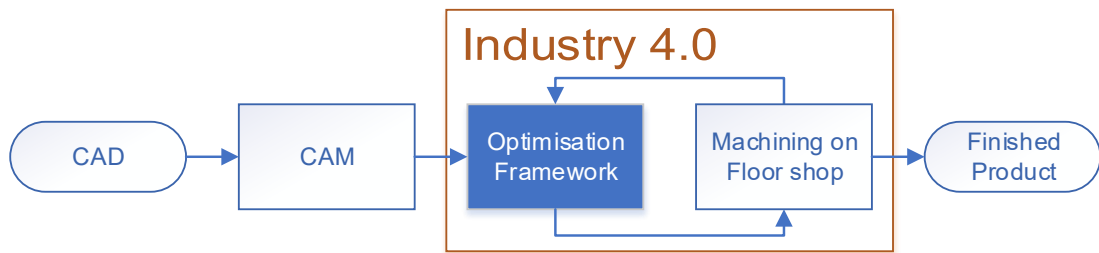


Figure 7.1: Implementation to Industry 4.0 - Basic Schematic

CAM Implementation: Part of the Industry 4.0 revolution would involve implementation of this research in developing a CAM system. FE-software would generate the data necessary for automatically calculating and developing optimum cutting strategies. These would be applied to the developed parts of the process to increase fatigue life performance. Figure 7.2 below demonstrates how this framework could be implemented into Siemens NX using Abaqus software.

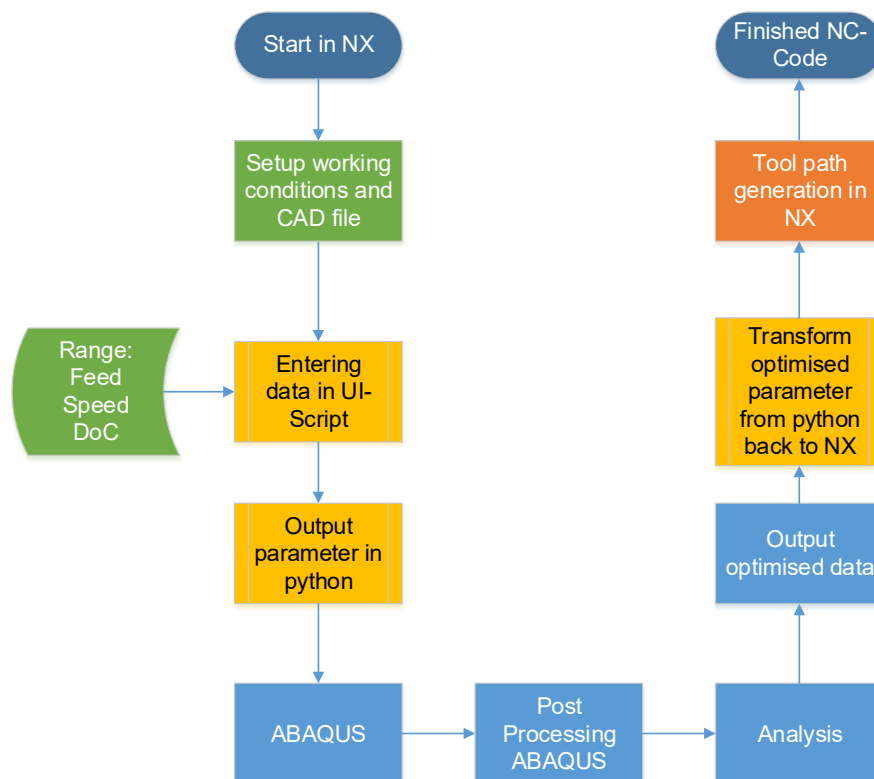


Figure 7.2: NX implementation

List of References

1. Kocańda, A., et al., *Numerical analysis of lateral forces in a die for turbine blade forging*. 2009. **9**(4): p. 49-54.
2. Forging, D. *Cast vs Forged Crankshaft*. 11/03/2019]; Available from: <http://www.dropforging.net/cast-vs-forged-crankshaft.html>.
3. Schuler. *Die competence for body panel & hot stamping parts*. 2019 11/03/2019]; Available from: <http://pdf.aeroexpo.online/pdf/schuler-pressen-gmbh/die-competence-body-panel-hot-stamping-parts/170485-6158.html>.
4. Groseclose, A., et al., *Estimation of die stresses and wear in warm forging of steel pinion shafts*. ERC for Net Shape Manufacturing, Report No. ERC/NSM-08-R-34, The Ohio State University, 2009.
5. Jomaa, W., V. Songmene, and P. Bocher, *Surface Finish and Residual Stresses Induced by Orthogonal Dry Machining of AA7075-T651*. *Materials*, 2014. **7**(3): p. 1603-1624.
6. Buchkremer, S., et al., *FE-simulation of machining processes with a new material model*. *Journal of Materials Processing Technology*, 2014. **214**(3): p. 599-611.
7. Li, W. and Y. Guo. *Residual stress and fatigue properties of AISI H13 steel by sustainable dry milling*. in *ASME 2012 International Manufacturing Science and Engineering Conference collocated with the 40th North American Manufacturing Research Conference and in participation with the International Conference on Tribology Materials and Processing*. 2012. American Society of Mechanical Engineers.
8. Li, W. and Y. Guo. *The effects of PVD coated tool flank wear and process parameters on surface integrity in hard milling AISI H13 steel*. in *STLE/ASME 2010 International Joint Tribology Conference*. 2010. American Society of Mechanical Engineers.
9. Guo, Y., W. Li, and I. Jawahir, *Surface integrity characterization and prediction in machining of hardened and difficult-to-machine alloys: a state-of-art research review and analysis*. *Machining Science and Technology*, 2009. **13**(4): p. 437-470.
10. Fritz, A.H. and G. Schulze, *Fertigungstechnik*. 2010, Heidelberg Dordrecht London New York: Springer.
11. Field, M., J.F. Kahles, and W.P. Koster, *Surface finish and surface integrity*. *ASM Handbook.*, 1989. **16**: p. 19-36.
12. Field, M. and J. Kahles, *The surface integrity of machined-and ground high-strength steels(Surface integrity of machined and ground high strength steels)*. 1964, 1964: p. 54-77.
13. Field, M. and J. Kahles, *Review of surface integrity of machined components*. *CIRP Annals-Manufacturing Technology*, 1971. **20**: p. 153-163.

14. Field, M., J.F. Kahles, and J. Cammett, *Review of measuring methods for surface integrity*. CIRP, 1972. **21**(2): p. 219-238.
15. Rossini, N., et al., *Methods of measuring residual stresses in components*. Materials & Design, 2012. **35**: p. 572-588.
16. Brinksmeier, E., et al., *Nondestructive testing for evaluating surface integrity*. Annals of the CIRP, 1984. **33**(2): p. 489-509.
17. Brinksmeier, E., E. Minke, and L. Nowag. *Residual stresses in precision components*. in *The 5 th International Conference on Industrial Tooling*. 2003.
18. Axinte, D. and R. Dewes, *Surface integrity of hot work tool steel after high speed milling-experimental data and empirical models*. Journal of Materials Processing Technology, 2002. **127**(3): p. 325-335.
19. Özel, T. and T. Altan, *Determination of workpiece flow stress and friction at the chip-tool contact for high-speed cutting*. International Journal of Machine Tools and Manufacture, 2000. **40**(1): p. 133-152.
20. Jawahir, I., et al., *Surface integrity in material removal processes: Recent advances*. CIRP Annals-Manufacturing Technology, 2011. **60**(2): p. 603-626.
21. Davim, J.P., *Machining: fundamentals and recent advances*. 2008: Springer Science & Business Media.
22. Batalha, G., et al., *Residual stresses modelling in hard turning and its correlation with the cutting forces*. Journal of Achievements in Materials and Manufacturing Engineering, 2007. **24**(1): p. 350-356.
23. Maranhão, C. and J. Davim, *Residual Stresses In Machining Using FEM*. Rev. Adv. Mater. Sci, 2012. **30**: p. 267-272.
24. Takacs, M. and B.Z. Farkas, *Hard Cutting of AISI D2 Steel*. 2014.
25. Klocke, F. and W. König, *Fertigungsverfahren 1: Drehen, Fräsen, Bohren*. Vol. 1. 2008: Springer-Verlag.
26. Buchkremer, S. and F. Klocke, *Compilation of a thermodynamics based process signature for the formation of residual surface stresses in metal cutting*. Wear, 2017. **376**: p. 1156-1163.
27. Wojciechowski, S., et al., *Application of signal to noise ratio and grey relational analysis to minimize forces and vibrations during precise ball end milling*. Precision Engineering, 2018. **51**: p. 582-596.
28. Bolar, G., A. Das, and S.N. Joshi, *Measurement and analysis of cutting force and product surface quality during end-milling of thin-wall components*. Measurement, 2018. **121**: p. 190-204.
29. Xu, Z., et al., *The influence of shot peening on the fatigue response of Ti-6Al-4V surfaces subject to different machining processes*. International Journal of Fatigue, 2018. **111**: p. 196-207.
30. Karpuschewski, P.B., *Zerspantechnik - Teil 1*. 2014, Universität Magdeburg.

31. Nie, G.-C., et al., *An experimental study of the white layer formation during cryogenic assisted hard machining of AISI 52100 steel*. Procedia CIRP, 2018. **77**: p. 223-226.
32. Bosheh, S.S. and P.T. Mativenga, *White layer formation in hard turning of H13 tool steel at high cutting speeds using CBN tooling*. International Journal of Machine Tools and Manufacture, 2006. **46**(2): p. 225-233.
33. Pan, Z., Y. Feng, and S.Y. Liang, *Material microstructure affected machining: a review*. Manufacturing Review, 2017. **4**: p. 5.
34. Papazoglou, E.L., A.P. Markopoulos, and D.E. Manolakos, *Experimental research on EDM of AISI O1 tool steel and study of the surface white layer formation*. Procedia Structural Integrity, 2018. **10**: p. 235-242.
35. Zhang, S., J. Li, and H. Lv, *Tool Wear and Formation Mechanism of White Layer When Hard Milling H13 Steel under Different Cooling/Lubrication Conditions*. Advances in Mechanical Engineering, 2014. **6**: p. 949308.
36. Zhang, S., T.C. Ding, and J.F. Li, *MICROSTRUCTURAL ALTERATION AND MICROHARDNESS AT NEAR-SURFACE OF AISI H13 STEEL BY HARD MILLING*. Machining Science and Technology, 2012. **16**(3): p. 473-486.
37. Miller, N. *Martensite: Definition, Transformation & Microstructure*. 2018 01/12/2018]; Available from: <https://study.com/academy/lesson/martensite-definition-transformation-microstructure.html>.
38. Wikipedia, U.-. *Martensite*. 2018 01/12/2018]; Available from: <https://en.wikipedia.org/wiki/Martensite>.
39. Berglund, P.L. *Martensite*. 2006 01/12/2018]; Available from: <http://threeplanes.net/martensite.html>.
40. Gilibert, Y. and G. Verchery, *Influence of Surface Roughness on Mechanical Properties Of Joints*, in *Adhesive Joints: Formation, Characteristics, and Testing*, K.L. Mittal, Editor. 1984, Springer US: Boston, MA. p. 69-84.
41. Xia, Y., et al., *Effect of surface roughness in the determination of the mechanical properties of material using nanoindentation test*. Scanning, 2014. **36**(1): p. 134-149.
42. Dong, W.P., P.J. Sullivan, and K.J. Stout, *Comprehensive study of parameters for characterising three- dimensional surface topography: III: Parameters for characterising amplitude and some functional properties*. Wear, 1994. **178**(1): p. 29-43.
43. Stout, K.J. and L. Blunt, *Three Dimensional Surface Topography*. Three Dimensional Surface Topography, ed. K.J. Stout and L. Blunt. 2000, Oxford: Butterworth-Heinemann.
44. Wikipedia, U.-. *ISO_25178*. 2018 02/10/2018]; Available from: https://en.wikipedia.org/wiki/ISO_25178.
45. Petropoulos, G.P., C.N. Pandazaras, and J.P. Davim, *Surface texture characterization and evaluation related to machining*, in *Surface integrity in machining*. 2010, Springer. p. 37-66.

46. Davim, J.P., *Surface integrity in machining*. Vol. 1848828742. 2010: Springer.
47. Li, W., et al. *Surface integrity and fatigue strength of hard milled surfaces*. in *ASME 2011 International Manufacturing Science and Engineering Conference*. 2011. American Society of Mechanical Engineers.
48. Axinte, D. and R. Dewes, *High-speed milling of AISI H13 hot-work tool steel using polycrystalline cubic boron nitride ball-nose mills: From experimental investigations and empirical modelling to functional testing of the machined surfaces*. Proceedings of the Institution of Mechanical Engineers, Part B: Journal of Engineering Manufacture, 2010. **224**(1): p. 15-24.
49. Wang, J.J. and M. Zheng, *On the machining characteristics of H13 tool steel in different hardness states in ball end milling*. The International Journal of Advanced Manufacturing Technology, 2003. **22**(11-12): p. 855-863.
50. Vaz Jr, M., et al., *Modelling and simulation of machining processes*. Archives of computational methods in engineering, 2007. **14**(2): p. 173-204.
51. Umbrello, D., et al., *Hardness-based flow stress for numerical simulation of hard machining AISI H13 tool steel*. Journal of Materials Processing Technology, 2008. **199**(1-3): p. 64-73.
52. Materials, A.S.f.T., *ASTM E384-16: standard test method for microindentation hardness of materials*. 2016, ASTM West Conshohocken.
53. Materials, A.S.f.T., *ASTM E140: Standard Hardness Conversion Tables for Metals Relationship Among Brinell Hardness, in Vickers Hardness, Rockwell Hardness, Superficial Hardness, Knoop Hardness, Scleroscope Hardness, and Leeb Hardness, ASTM international E140-12b*. 2013, ASTM West Conshohocken.
54. Materials, A.S.f.T., *ASTM E92-17: Standard Test Methods for Vickers Hardness and Knoop Hardness of Metallic Materials*. 2017, ASTM West Conshohocken.
55. Instruments, N. *Microhardness Testing*. 2018 [01/12/2018]; Available from: <https://www.nanoscience.com/techniques/mechanical-testing/microhardness-testing/>.
56. Materials, A.S.f.T., *ASTM E18-18: Standard Test Methods for Rockwell Hardness of Metallic Materials*. ASTM West Conshohocken.
57. González-Velázquez, J.L., *Fractography and Failure Analysis*. Vol. 3. 2018: Springer.
58. Oila, A. and S.J. Bull, *Assessment of the factors influencing micropitting in rolling/sliding contacts*. Wear, 2005. **258**(10): p. 1510-1524.
59. Verdu, C., J. Adrien, and J.-Y. Buffière, *Three-dimensional shape of the early stages of fatigue cracks nucleated in nodular cast iron*. Materials Science and Engineering: A, 2008. **483**: p. 402-405.
60. Radaj, D. and M. Vormwald, *Ermüdungsfestigkeit: Grundlagen für Ingenieure*. 2007: Springer-Verlag.

61. Dowling, N.E., *Mechanical behavior of materials: engineering methods for deformation, fracture, and fatigue*. 2013: Pearson.
62. Suresh, S., *Fatigue of materials*. 1998: Cambridge university press.
63. Hütte eV, A.V., H. Czichos, and M. Hennecke, *Hütte-Das Ingenieurwissen*. 2007: Springer-Verlag.
64. Schott, G., *Werkstoffermüdung-Ermüdungsfestigkeit*. 2009: Wiley-VCH.
65. Lange, K. and H. Meyer-Nolkemper, *Werkstoffe und Halbzeug*, in *Gesenkschmieden*. 1977, Springer. p. 78-106.
66. Luig, H. and T. Bobke, *Beanspruchung und schadensarten an schmiedegesenen*. Tribologie und Schmierungstechnik, 1990. **37**(2): p. 76-81.
67. Doege, B.-A.B.E. and B.-A. Behrens, *Handbuch umformtechnik*. 2010: Springer.
68. Thalmair, S., *Thermomechanische Ermüdung von Aluminium-Silizium-Gusslegierungen unter ottomotorischen Beanspruchungen*. 2009: Shaker.
69. Minichmayr, R., et al., *Thermo-mechanical fatigue life assessment of aluminium components using the damage rate model of Sehitoglu*. International Journal of Fatigue, 2008. **30**(2): p. 298-304.
70. Beck, T., *Isothermes und thermisch-mechanisches Ermüdungsverhalten von Al₁tn₂O₁tn₃ (Saffil) kurzfaserverstärkten Aluminium-Gußlegierungen für Verbrennungsmotoren*. 2000: Shaker.
71. Chen, S. and I. Jawahir. *The influence of cutting edge radius on surface integrity and size effects in dry turning of automotive aluminum alloy A356 with diamond tools*. in *Proc. of the 11th CIRP Conf. on MMO, Gaithersburg, MD, USA*. 2008.
72. Cui, X., et al., *Surface roughness and chip formation in high-speed face milling AISI H13 steel*. The International Journal of Advanced Manufacturing Technology, 2012. **61**(1-4): p. 1-13.
73. Philip, S., P. Chandramohan, and P. Rajesh, *Prediction of surface roughness in end milling operation of duplex stainless steel using response surface methodology*. Journal of engineering science and technology, 2015. **10**(3): p. 340-352.
74. Samanta, B., *Surface roughness prediction in machining using soft computing*. International Journal of Computer Integrated Manufacturing, 2009. **22**(3): p. 257-266.
75. Beatrice, B.A., et al., *Surface roughness prediction using artificial neural network in hard turning of AISI H13 steel with minimal cutting fluid application*. Procedia Engineering, 2014. **97**: p. 205-211.
76. DIN, *Manufacturing Processes Chip Removal–Part 0: General; Classification, Subdivision, Terms and Definitions*. 2003, Deutsches Institut Fuer Normung EV Berlin.

77. DIN, *Manufacturing processes chip removal - Part 3: Milling; Classification, subdivision, terms and definitions*. 2003, Deutsches Institut fuer Normung EV Berlin.
78. Markopoulos, A.P., *Finite element method in machining processes*. 2012: Springer Science & Business Media.
79. Avallone, E.A., T. Baumeister, and A.M. Sadegh, *Marks' standard handbook for mechanical engineers*. Vol. 9. 1996: McGraw-Hill New York.
80. Chen, C.-H., Y.-C. Wang, and B.-Y. Lee, *The effect of surface roughness of end-mills on optimal cutting performance for high-speed machining*. *Strojniški vestnik-Journal of Mechanical Engineering*, 2013. **59**(2): p. 124-134.
81. Li, B., et al., *Influence of edge hone radius on cutting forces, surface integrity, and surface oxidation in hard milling of AISI H13 steel*. *The International Journal of Advanced Manufacturing Technology*, 2018. **95**(1): p. 1153-1164.
82. Arfaoui, S., F. Zemzemi, and Z. Tourki, *A numerical-analytical approach to predict white and dark layer thickness of hard machining*. *The International Journal of Advanced Manufacturing Technology*, 2018. **96**(9): p. 3355-3364.
83. Lee, P. and Y. Altıntaş, *Prediction of ball-end milling forces from orthogonal cutting data*. *International Journal of Machine Tools and Manufacture*, 1996. **36**(9): p. 1059-1072.
84. Wojciechowski, S., P. Twardowski, and M. Pelic, *Cutting forces and vibrations during ball end milling of inclined surfaces*. *Procedia CIRP*, 2014. **14**: p. 113-118.
85. Lamikiz, A.d., et al., *Cutting force estimation in sculptured surface milling*. *International Journal of Machine Tools and Manufacture*, 2004. **44**(14): p. 1511-1526.
86. Byrne, G., D. Dornfeld, and B. Denkena, *Advancing cutting technology*. *CIRP Annals-Manufacturing Technology*, 2003. **52**(2): p. 483-507.
87. Suresh, R., et al., *State-of-the-art research in machinability of hardened steels*. *Proceedings of the Institution of Mechanical Engineers, Part B: Journal of Engineering Manufacture*, 2013. **227**(2): p. 191-209.
88. Davim, J.P., *Machining of hard materials*. 2011: Springer Science & Business Media.
89. Wang, F., et al., *Three-dimensional finite element modeling of high-speed end milling operations of Ti-6Al-4V*. *Proceedings of the Institution of Mechanical Engineers, Part B: Journal of Engineering Manufacture*, 2013: p. 0954405413509375.
90. Elbestawi, M., et al., *High-speed milling of dies and molds in their hardened state*. *CIRP Annals-Manufacturing Technology*, 1997. **46**(1): p. 57-62.
91. Dikshit, M.K., A.B. Puri, and A. Maity, *Analysis of cutting force coefficients in high-speed ball end milling at varying rotational speeds*. *Machining Science and Technology*, 2017. **21**(3): p. 416-435.

92. Zhang, Q., S. Zhang, and J. Li, *Three dimensional finite element simulation of cutting forces and cutting temperature in hard milling of AISI H13 steel*. Procedia Manufacturing, 2017. **10**: p. 37-47.
93. Tönshoff, H., C. Arendt, and R.B. Amor, *Cutting of hardened steel*. CIRP Annals-Manufacturing Technology, 2000. **49**(2): p. 547-566.
94. Klocke, F., E. Brinksmeier, and K. Weinert, *Capability profile of hard cutting and grinding processes*. CIRP Annals-Manufacturing Technology, 2005. **54**(2): p. 22-45.
95. Luo, X., *DM948 - Advanced Materials and Production Technology*, in *Hard Turning*. 2015, University of Strathclyde.
96. Li, W., Y. Guo, and C. Guo, *Superior surface integrity by sustainable dry hard milling and impact on fatigue*. CIRP Annals-Manufacturing Technology, 2013. **62**(1): p. 567-570.
97. Moussaoui, K., et al., *Influence of milling on the fatigue lifetime of a Ti6Al4V titanium alloy*. Metals, 2015. **5**(3): p. 1148-1162.
98. Obiukwu, M., et al. *The Effect of Surface Finish on the Low Cycle Fatigue of Low and Medium Carbon Steel*. in *International Conference on Mechanical and Industrial Engineering, Harare, Zimbabwe*. 2015.
99. Javidi, A., U. Rieger, and W. Eichseder, *The effect of machining on the surface integrity and fatigue life*. International Journal of Fatigue, 2008. **30**(10): p. 2050-2055.
100. Zhang, Z.-p., et al., *Microstructure Variation and Hardness Diminution During Low Cycle Fatigue of 55NiCrMoV7 Steel*. Journal of Iron and Steel Research, International, 2007. **14**(6): p. 68-73.
101. Casagrande, A., G.P. Cammarota, and L. Micele, *Relationship between fatigue limit and Vickers hardness in steels*. Materials Science and Engineering: A, 2011. **528**(9): p. 3468-3473.
102. Clough, R.W. *The Finite Element Method in Plane Stress Analysis*. in *Conference papers [of the] Conference on Electronic Computation*. 1960. Pittsburgh, PA, USA: American Society of Civil Engineers.
103. Klein, B., *FEM: Grundlagen und Anwendungen der Finite-Element-Methode im Maschinen-und Fahrzeugbau*. 7. ed. 2012: Vieweg+ Teubner Verlag. 3.
104. Hatzenbichler, T., O. Harrer, and B. Buchmayr, *Entwicklungsstand und Nutzen der FEM-Simulation von Massivumformprozessen*. BHM Berg- und Hüttenmännische Monatshefte, 2006. **151**(11): p. 469-474.
105. Reimer, A., S. Fitzpatrick, and X. Luo, *A full factorial numerical investigation and validation of precision end milling process for hardened tool steel*, in *Euspen's 17th International Conference & Exhibition*. 2017, Euspen: Hannover, Germany.
106. Reimer, A., et al. *Numerical Investigation of Mechanical Induced Stress during Precision End Milling Hardened Tool Steel*. in *Solid State Phenomena*. 2017. Trans Tech Publ.

107. Reimer, A. and X. Luo, *Prediction of residual stress in precision milling of AISI H13 steel*. Procedia CIRP, 2018. **46**.
108. Franchi, R., A. Del Prete, and D. Umbrello, *Inverse analysis procedure to determine flow stress and friction data for finite element modeling of machining*. International Journal of Material Forming, 2017. **10**(5): p. 685-695.
109. Pantalé, O., et al., *2D and 3D numerical models of metal cutting with damage effects*. Computer Methods in Applied Mechanics and Engineering, 2004. **193**(39–41): p. 4383-4399.
110. Johnson, G.R. and W.H. Cook, *Fracture characteristics of three metals subjected to various strains, strain rates, temperatures and pressures*. Engineering Fracture Mechanics, 1985. **21**(1): p. 31-48.
111. Yan, H., J. Hua, and R. Shivpuri, *Flow stress of AISI H13 die steel in hard machining*. Materials & Design, 2007. **28**(1): p. 272-277.
112. Shatla, M., C. Kerk, and T. Altan, *Process modeling in machining. Part I: determination of flow stress data*. International Journal of Machine Tools and Manufacture, 2001. **41**(10): p. 1511-1534.
113. Shrot, A. and M. Bäker, *Determination of Johnson–Cook parameters from machining simulations*. Computational Materials Science, 2012. **52**(1): p. 298-304.
114. Schwer, L., *Optional Strain-rate forms for the Johnson Cook Constitutive Model and the Role of the parameter Epsilon_0*. LS-DYNA Anwenderforum, Frankenthal, 2007.
115. Becze, E.C., *A thermo-mechanical force model for machining hardened steel*. 2002.
116. Wu, H. and S. Zhang, *3D FEM simulation of milling process for titanium alloy Ti6Al4V*. The International Journal of Advanced Manufacturing Technology, 2014. **71**(5-8): p. 1319-1326.
117. Hancock, J. and A. Mackenzie, *On the mechanisms of ductile failure in high-strength steels subjected to multi-axial stress-states*. Journal of the Mechanics and Physics of Solids, 1976. **24**(2-3): p. 147-160.
118. Márton, T. and F.B. Zsolt, *Theoretical and Experimental Investigation of Machining of AISI H13 Steel*. Advanced Materials Research, 2013. **818**: p. 187-192.
119. Tang, L., J. Huang, and L. Xie, *Finite element modeling and simulation in dry hard orthogonal cutting AISI D2 tool steel with CBN cutting tool*. The International Journal of Advanced Manufacturing Technology, 2011. **53**(9-12): p. 1167-1181.
120. Davim, J.P., et al., *Precision radial turning of AISI D2 steel*. The International Journal of Advanced Manufacturing Technology, 2009. **42**(9-10): p. 842-849.
121. An, L., S. Liu, and H. Zhang. *Study on the Influence of Machining Parameters on Surface Residual Stresses in Dry Turning Inconel718 using FEA and ANN*.

in *Proceedings of the 9th International Conference on Computer and Automation Engineering*. 2017. ACM.

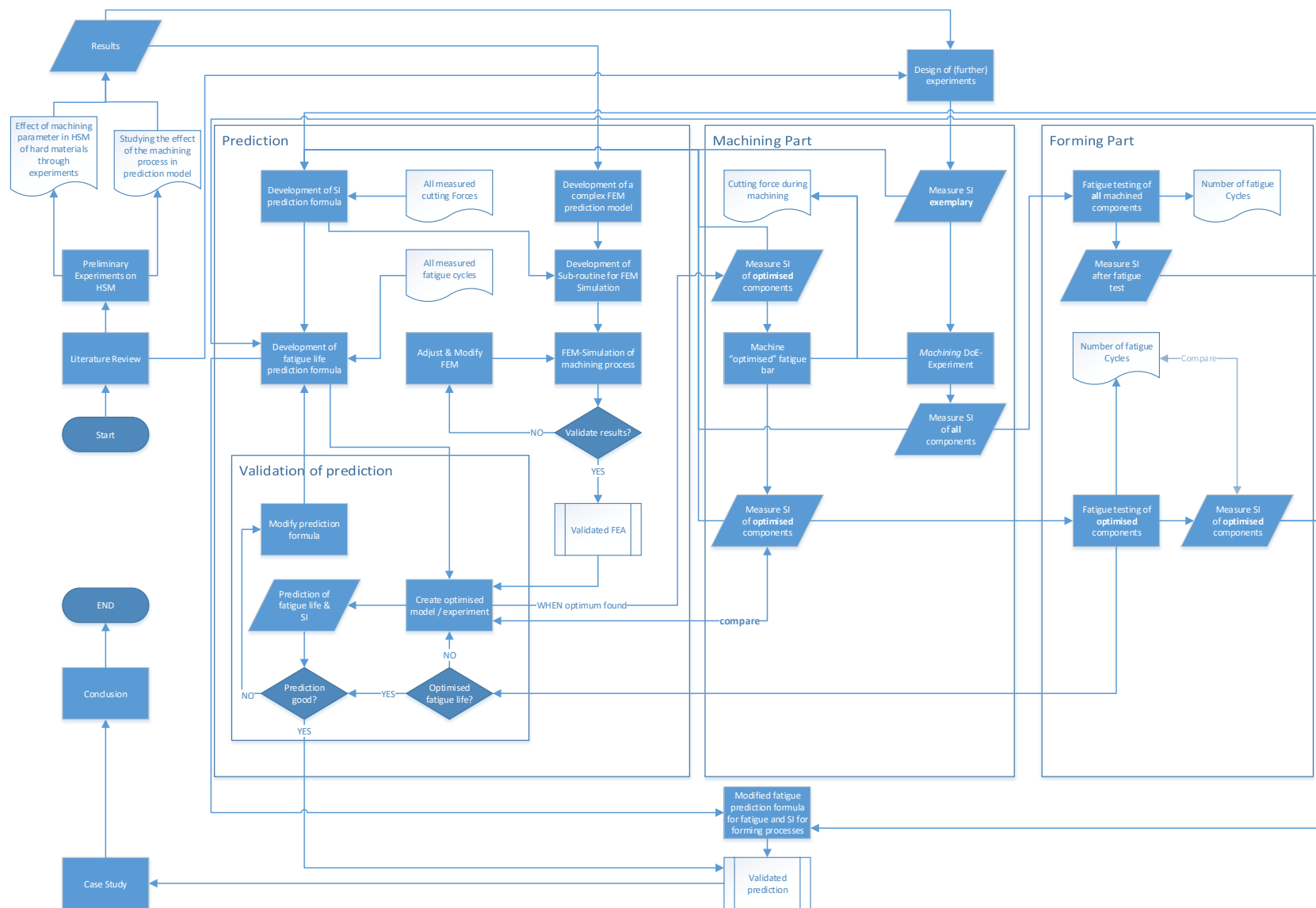
122. Umbrello, D., et al., *A hybrid finite element method–artificial neural network approach for predicting residual stresses and the optimal cutting conditions during hard turning of AISI 52100 bearing steel*. *Materials & Design*, 2008. **29**(4): p. 873-883.
123. Outeiro, J., *Surface integrity predictions and optimisation of machining conditions in the turning of AISI H13 tool steel*. *International Journal of Machining and Machinability of Materials* 7, 2014. **15**(1-2): p. 122-134.
124. Perez, C. and J.D.D. Calderon. *Comparison Between Feed-Forward Back-Propagation and Radial Basis Functions Networks for Roughness Modeling in Face-Milling of Aluminum*. in *ASME 2011 International Mechanical Engineering Congress and Exposition*. 2011. American Society of Mechanical Engineers.
125. Al Hazza, M.H. and E.Y. Adesta. *Investigation of the effect of cutting speed on the Surface Roughness parameters in CNC End Milling using Artificial Neural Network*. in *IOP Conference Series: Materials Science and Engineering*. 2013. IOP Publishing.
126. Outeiro, J., *Optimization of Machining parameters for improved surface integrity of AISI H13 tool steel*. 2012.
127. Xie, T., H. Yu, and B. Wilamowski. *Comparison between traditional neural networks and radial basis function networks*. in *Industrial Electronics (ISIE), IEEE International Symposium*. 2011. IEEE.
128. Abdalla, O.A., et al. *A comparison of feed-forward back-propagation and radial basis artificial neural networks: A Monte Carlo study*. in *Information Technology (ITSim), 2010 International Symposium in*. 2010. IEEE.
129. Reed, R. and I. Marks, RJ (1999). *Neural Smithing. Supervised Learning in Feedforward Artificial Neural Networks*. Cambridge, MA: MIT Press, 1989.
130. Kant, G. and K.S.J.P.C. Sangwan, *Predictive modelling and optimization of machining parameters to minimize surface roughness using artificial neural network coupled with genetic algorithm*. 2015. **31**: p. 453-458.
131. Goldberg, D., *Genetic algorithms in optimization, search and machine learning*. Reading: Addison-Wesley, 1989.
132. Wang, X. and I. Jawahir*, *Optimization of multi-pass turning operations using genetic algorithms for the selection of cutting conditions and cutting tools with tool-wear effect*. *International journal of production research*, 2005. **43**(17): p. 3543-3559.
133. Jabri, A., A. El Barkany, and A. El Khalfi, *Multi-objective optimization using genetic algorithms of multi-pass turning process*. *Engineering*, 2013. **5**(07): p. 601.

134. Kim, S.S., et al., *Real-coded genetic algorithm for machining condition optimization*. The International Journal of Advanced Manufacturing Technology, 2008. **38**(9-10): p. 884-895.
135. Jameel, A., M. Minhat, and M. Nizam, *Using genetic algorithm to optimize machining parameters in turning operation: a review*. International journal of scientific and research publications, 2013. **3**(5): p. 1-6.
136. D'addona, D.M. and R. Teti, *Genetic algorithm-based optimization of cutting parameters in turning processes*. Procedia Cirp, 2013. **7**: p. 323-328.
137. Petkovic, D. and M. Radovanovic, *Using genetic algorithms for optimization of turning machining process*. Journal of Engineering Studies and Research, 2013. **19**(1): p. 47.
138. Gaikhe, V., J. Sahu, and R. Pawade, *Optimization of Cutting Parameters for Cutting Force Minimization in Helical Ball End Milling of Inconel 718 by Using Genetic Algorithm*. Procedia CIRP, 2018. **77**: p. 477-480.
139. Saw, L.H., et al., *Sensitivity analysis of drill wear and optimization using Adaptive Neuro fuzzy –genetic algorithm technique toward sustainable machining*. Journal of Cleaner Production, 2018. **172**: p. 3289-3298.
140. Li, W., Y. Guo, and M. Barkey. *Tool wear influence on surface integrity and fatigue life of hard milled surfaces*. in *ASME/STLE 2011 International Joint Tribology Conference*. 2011. American Society of Mechanical Engineers.
141. Olusanya, A. and M. Hall, *Performance of Adhesive Joints, 1996-1999. Project PAJ 3: Combined Cyclic Loading and Hostile Environments. Report 3. A Guide to the Use of Design of Experiment Methods*. 1997.
142. Zolgharnein, J., A. Shahmoradi, and J.B. Ghasemi, *Comparative study of Box–Behnken, central composite, and Doehlert matrix for multivariate optimization of Pb (II) adsorption onto Robinia tree leaves*. Journal of Chemometrics, 2013. **27**(1-2): p. 12-20.
143. Materials, M. *4 flute Impact Miracle ball nose end mill VF-4MB*. 2018 09/12/2018]; Available from: <http://www.mitsubishicarbide.com/application/files/8114/4643/8982/b163g.pdf>.
144. Kistler. *Kilster Dynanometer*. 2018 08/12/2018]; Available from: www.kistler.com.
145. Matweb. *AISI Type H13 Hot Work Tool Steel*. 2015 12.08.2015]; Available from: http://www.matweb.com/search/datasheet_print.aspx?matguid=e30d1d1038164808a85cf7ba6aa87ef7.
146. Cogne. 2018 10.12.2018]; Available from: <https://www.cogne.co.uk/tool-steel-duplex>.
147. Sulaiman, S., A. Roshan, and S. Borazjani. *Finite Element Modeling and Simulation of Machining of Titanium Alloy and H13 Tool Steel Using PCBN Tool*. in *Applied Mechanics and Materials*. 2013. Trans Tech Publ.

148. Klocke, F. and W. König, *Fertigungsverfahren 4*. 2006: Springer.
149. Davim, J.P., *Dynamic Methods and Process Advancements in Mechanical, Manufacturing, and Materials Engineering*. 2012: Engineering Science Reference.
150. Priyadarshini, A., et al., *Influence of the Johnson Cook material model parameters and friction models on simulation of orthogonal cutting process*. 2012. **4**(1/2): p. 59-83.
151. Ng, E.-G. and D.K. Aspinwall, *Modelling of hard part machining*. Journal of materials processing technology, 2002. **127**(2): p. 222-229.
152. Systems, D., *Writing User Subroutines with ABAQUS*. 2007.

Appendices

Appendix I Framework



Appendix II Kistler Datasheet

Force



Multicomponent Dynamometer

Type 9129AA

-10 ... 10 kN, Cover Plate 90x105 mm

Multicomponent dynamometer for measuring the three components of the resultant force vector and the three components of the resultant moment vector.

- Small design
- Large measuring range
- Small temperature error
- For cutting force measurements
- For general multicomponent force measurements

Description

The dynamometer consists of four 3-component force sensors which are mounted under high preload between the cover plate and the two lateral base plates.

Because of the special mounting of the sensors, a small temperature error is achieved. The force sensors each contain three crystal disks, one of which is sensitive to pressure in the y direction and the two others to shear force in the x or z directions. The forces are measured with practically no displacement. The outputs of the four built-in force sensors are passed to the 9-pole flange socket. Multicomponent force-moment measurements are possible.

The four sensors are mounted with ground isolation. This largely avoids ground loop problems.

The dynamometer is corrosion-resistant and protected against the ingress of cooling lubricant. Used together with connecting cable Type 1687B... or Type 1677A..., the dynamometer is sealed according to degree of protection IP67.

Quartz multicomponent dynamometers measure easily, directly and very accurately.

Application Examples

- Cutting force measurement in superfinishing
- Multicomponent force measurement
- Force measurement in confined spaces
- Measurement of the three cutting forces F_c , F_f , F_p while turning outside and inside diameters on lathes with turret-type tool heads (see data sheet for Type 9129A...)



Technical Data

Max. permitted measuring range (Force application point at cover plate surface)	F_x, F_y, F_z M_x, M_y, M_z	kN N-m	-10 ... 10 -500 ... 500
Calibrated measuring range 100 %	F_x, F_y, F_z	kN	0 ... 10
Calibrated partial meas. range 10 %	F_x, F_y, F_z	kN	0 ... 1
Calibrated partial meas. range 1 %	F_x, F_y, F_z	kN	0 ... 0,1
Overload	F_x, F_y, F_z	%	20
Threshold		N	<0,01
Sensitivity (rated)	F_x	pc/N	≈-8,1
	F_y	pc/N	≈-4,1
	F_z	pc/N	≈-8,1
Linearity, all ranges	F_x, F_y, F_z	±%/FSO	≤±0,3
Hysteresis, all ranges	F_x, F_y, F_z	%/FSO	≤0,3
Crosstalk	$F_z \rightarrow F_x, F_y$	%	≤±2
	$F_x \leftrightarrow F_y$	%	≤±2
	$F_x, F_y \rightarrow F_z$	%	≤±2
Rigidity	c_x, c_z	N/μm	≈1 000
	c_y	N/μm	≈4 000
Natural frequency (Type 9129AA mounted on rigid base)	$f_n(x)$	kHz	≈3,5
	$f_n(y)$	kHz	≈4,5
	$f_n(z)$	kHz	≈3,5
Operating temperature range		°C	0 ... 70
Capacitance	F_x, F_y, F_z	pF	≈180
Isolation resistance		Ω	>10 ¹³
Ground isolation		Ω	>10 ⁹
Degree of protection EN60529			IP67
Weight	Dynamometer	kg	3,2
	Cover plate	kg	2,0
Mounting surface		mm	90x105
Connection			Fischer flange 9 pin neg.

9129AA_000-709e-10.12

Page 1/5

This information corresponds to the current state of knowledge. Kistler reserves the right to make technical changes. Liability for consequential damage resulting from the use of Kistler products is excluded.

©2009 ... 2012, Kistler Group, Eulachstrasse 22, 8408 Winterthur, Switzerland
Tel. +41 52 224 11 11, Fax +41 52 224 14 14, info@kistler.com, www.kistler.com
Kistler is a registered trademark of Kistler Holding AG.

Dimensions

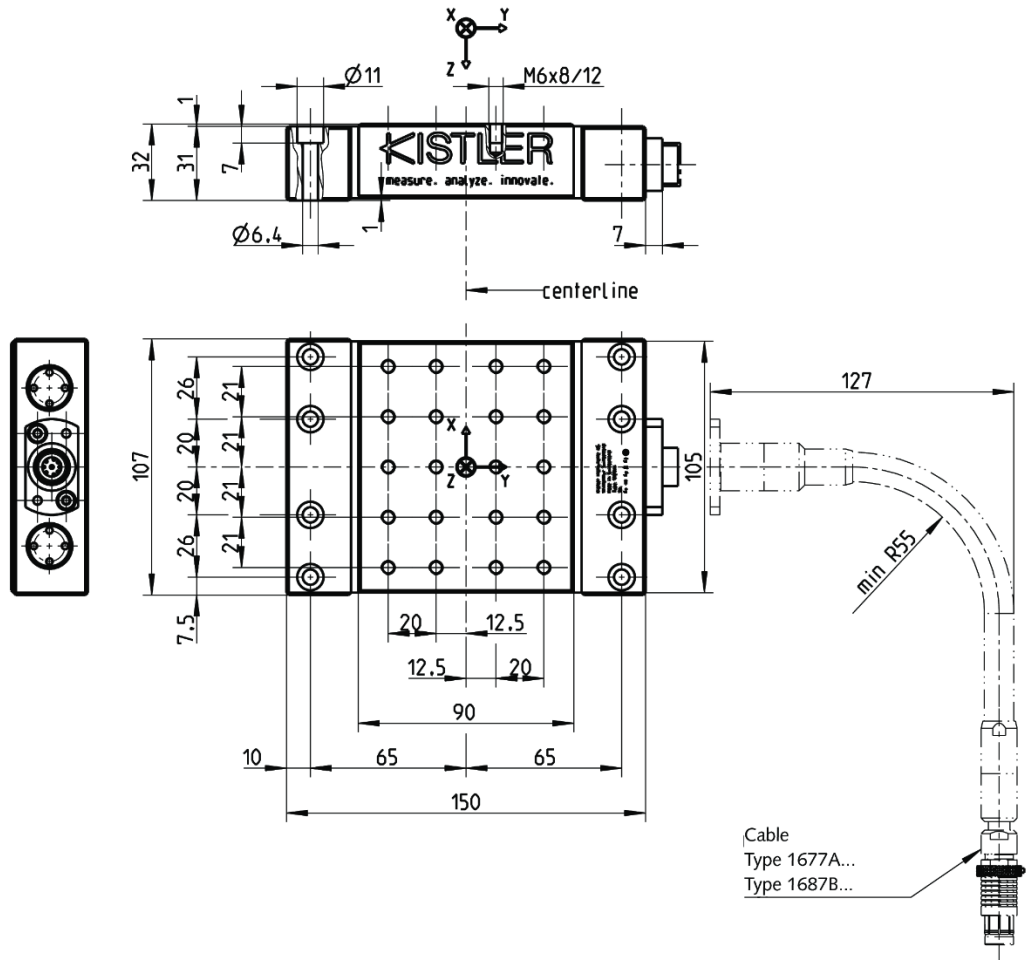
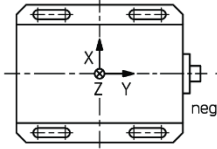


Fig. 1: Dimensions of Type 9129AA

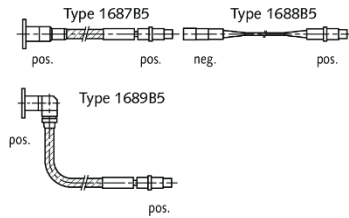
9129AA_000-709e-10.12

3-Component Force Measurement F_x, F_y, F_z with 4-Channel Charge Amplifier

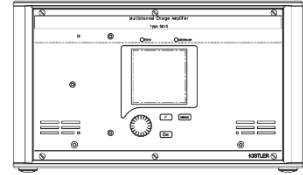
Dynamometer
Type 9129AA



Cable



Charge Amplifier
Type 5070Ax01xx



3 output signals
from charge amplifier

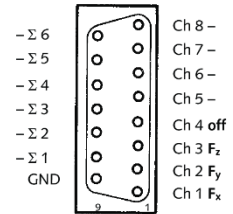
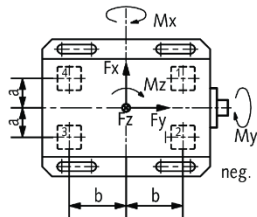


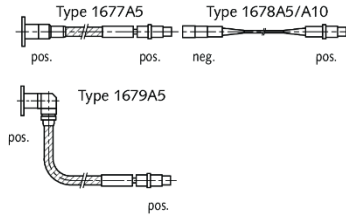
Fig. 2: Example of a measuring system with standard dynamometer

6-Component Force and Moment Measurement $F_x, F_y, F_z, M_x, M_y, M_z$ with 8-Channel Charge Amplifier

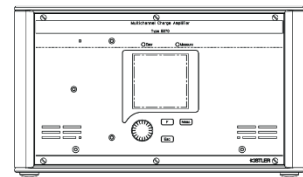
Dynamometer
Type 9129AA



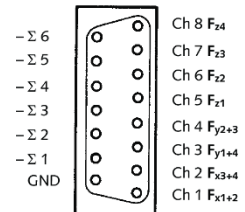
Cable



Charge Amplifier
Type 5070Ax11xx



8 output signals
from charge amplifier



9129AA_000-709e-10.12

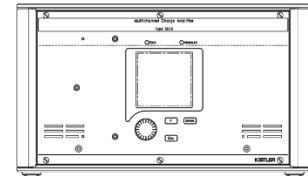
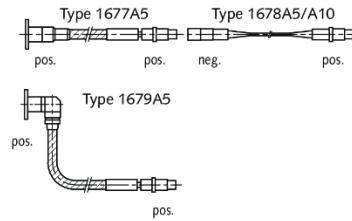
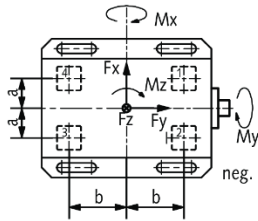
Fig. 3: Example of a measuring system with standard dynamometer

6-Component Force and Moment Measurement $F_x, F_y, F_z, M_x, M_y, M_z$ with 8-Channel Charge Amplifier with 6-Component-Summing Calculator

Dynamometer
Type 9129AA

Cable

Charge Amplifier
Type 5070Ax21xx

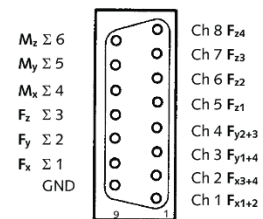


8 output signals from charge amplifier
6 output signals from summing calculator

Fig. 4: Example of a measuring system with standard dynamometer

Values a,b for Type 9129AA:

a mm	b mm
33	50,5



Mounting

The dynamometer can be screwed onto any clean, surface-ground mounting surface, such as on a machine tool table. Mounting on a magnet plate is also possible. Please note that uneven mounting surfaces may cause internal distortion, placing additional heavy load on the individual measuring elements and possibly increased crosstalk.

M6 tapped blind bores are available on the cover plate for mounting the force-introducing components such as workpieces or tool holders. The mounting surfaces of the force-introducing components must be face-ground so that good mechanical connection to the cover plate is achieved.

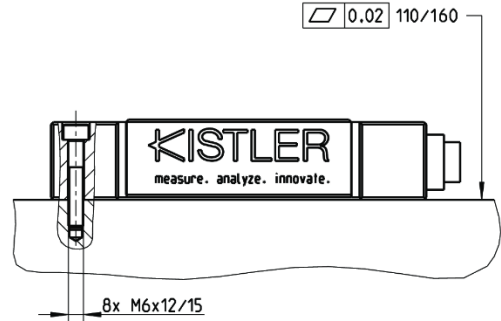


Fig. 5: Mounting the dynamometer

9129AA_000-709e-10.12

Signal Conditioning

A charge amplifier is also needed to build a complete measuring system. The measurement signal is converted into an electrical voltage in the individual channels. The measured value is exactly proportional to the force acting.

The multichannel charge amplifier Type 5070A... has been specially developed for multicomponent force measurement systems.



Fig. 6: Multichannel charge amplifier Type 5070A...

Data Acquisition and Evaluation

Kistler offers with the DAQ system a universal and easy to operate package, consisting of a hardware for the data acquisition and the DynoWare software. For details see data sheet 5697A_000-745.

Included Accessories

- Socket head cap screw M6x35 (8 items)

Art. No.
6.120.110

Optional Accessories

For 3-Component Force Measurements

F_x, F_y, F_z

- Connecting cable, length $l = 5$ m (3 leads)
- Extension cable, length $l = 5$ m (3 leads)

Type
1687B5
1689B5
1688B5

For 6-Component Force and Moment

Measurements $F_x, F_y, F_z / M_x, M_y, M_z$

- Connecting cable, length $l = 5$ m (8 leads)
- Extension cable, length $l = 5$ m (8 leads)

Type
1677A5
1679A5
1678A5

Ordering Code

- Multicomponent dynamometer –10 ... 10 kN, cover plate 95x105 mm

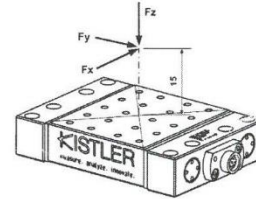
Type 9129AA

Kalibrierschein Calibration Certificate

Type Kistler 9129AA

Serial No. 4957322

Kalibriert durch Calibration Technician	Datum Date	
A. Luder	03. May. 2016	
Referenzgeräte Reference Equipment	Typ Type	Serien-Nr. Serial No.
Gebrauchsnormal Working Standard	Kistler 96017629 Kistler 96017630 Kistler 96017633	4352333 4352310 4352327
Ladungskalibrator Charge Calibrator	Kistler 5395A	605262
Umgebungstemperatur Ambient Temperature	Relative Feuchte Relative Humidity	
°C	%	
23	45	



Messergebnisse Results of Measurement

Kalibrierter Bereich Calibrated Range	Empfindlichkeit Sensitivity	Linearität Linearity	Übersprechen Cross talk	
kN	pC / N	≤ ± %FSO	%	%
F_x 0 ... 10	-8,118	0,03	$F_x \rightarrow F_y$ -0,4	$F_x \rightarrow F_z$ 0,6
F_x 0 ... 1	-8,111	0,05	$F_x \rightarrow F_y$ -0,4	$F_x \rightarrow F_z$ 0,6
F_x 0 ... 0,1	-8,102	0,09	$F_x \rightarrow F_y$ -0,4	$F_x \rightarrow F_z$ 0,7
F_y 0 ... 10	-4,165	0,09	$F_y \rightarrow F_x$ 0,7	$F_y \rightarrow F_z$ 0,4
F_y 0 ... 1	-4,157	0,13	$F_y \rightarrow F_x$ 0,8	$F_y \rightarrow F_z$ 0,3
F_y 0 ... 0,1	-4,142	0,11	$F_y \rightarrow F_x$ 0,8	$F_y \rightarrow F_z$ 0,3
F_z 0 ... 10	-8,133	0,03	$F_z \rightarrow F_x$ 0,1	$F_z \rightarrow F_y$ 0,7
F_z 0 ... 1	-8,123	0,06	$F_z \rightarrow F_x$ 0,1	$F_z \rightarrow F_y$ 0,7
F_z 0 ... 0,1	-8,133	0,14	$F_z \rightarrow F_x$ 0,1	$F_z \rightarrow F_y$ 0,8

Messverfahren Kontinuierliche Kalibrierung, Vergleichsverfahren
Measurement Procedure Continuous Calibration, Comparison Method

Bestätigung Confirmation

Das oben durch die Seriennummer identifizierte Gerät entspricht der Vereinbarung der Bestellung und hält die Herstellertoleranzen gemäss den Spezifikationen der Datenblätter ein, sofern nicht anders auf dem Kalibrierschein vermerkt. Das Kistler Qualitätsmanagement System ist nach ISO 9001 zertifiziert. Das Dokument erfüllt die Anforderungen von EN 10204 Abnahmeprüfzeugnis "3.1". Die aufgeführten Referenzgeräte sind auf nationale Normale rückgeführt. Das Dokument wurde elektronisch erstellt und ist daher ohne Unterschrift gültig.

The equipment identified by Serial No. complies with the agreement of the order and meets the manufacturing tolerances specified in the data sheets, unless otherwise specified on the calibration certificate. The Kistler Quality Management System is certified per ISO 9001. This document fulfils the requirements of EN 10204 Inspection Certificate "3.1". The reference equipment is traceable to national standards. The document was issued electronically and is therefore valid without signature.

Kistler Instrumente AG
Eulachstrasse 22 Tel. +41 52 224 11 11 ZKB Winterthur BC 732 IBAN: CH67 0070 0113 2003 7462 8
PO Box Fax +41 52 224 14 14 Swift: ZKBKCHZZ80A VAT: 229 713
CH-8408 Wintherthur info@kistler.com Account: 1132-0374.628 ISO 9001 certified

www.kistler.com

Seite page 1 / 1

Kalibrierschein Calibration Certificate

Type Kistler 5070A10100 Serial No. 4965397

Bearbeiter Calibration Technician	Datum Date	Geräteinstellungen Instrument settings		
U. Schäffler	25. Feb. 2016	HP Filter HP Filter	LP Filter LP Filter	Ausgangsbereich FS Output Range FS
Referenzgeräte Reference Equipment	Typ Type	Serie Nr. Serial No.	kHz	V
Ladungskalibrator Charge Calibrator	Kistler 5395	1258084	DC (Long)	1,0 ± 10
Umgebungstemperatur Ambient Temperature	Relative Feuchte Relative Humidity	Ladungsverstärker Einschub Serie-Nr. Charge Amplifier Slide-In Unit Serial-No.		
24 °C	40 %	4862303	(Channel 1 - 4)	

Messergebnisse Results of Measurement

Kanal Channel		1	2	3	4
Nullpunktabweichung Offset Voltage	mV	1,2	0,0	-0,3	0,5
Reset-Operate-Sprung Reset-Operate Step	pC	1,00	-0,90	-1,20	-0,70
Drift (Bereich = 200 pC) Drift (Range = 200 pC)	pC/s	0,00	0,00	0,01	0,00
Bereich Range	Abweichung Deviation				
pC 200	%	0,0	0,0	0,0	0,0
pC 1120	%	0,0	0,0	0,0	0,0
pC 6270	%	0,0	0,0	0,0	0,0
pC 35120	%	0,0	0,0	0,0	0,0
pC 200000	%	0,0	-0,1	-0,1	0,0
Abweichung Anzeige Indication Deviation	%	0,0 (für alle Kanäle gleicher Wert) (for all channels same value)			

Bestätigung Confirmation

Das oben durch die Seriennummer identifizierte Gerät entspricht der Vereinbarung der Bestellung und hält die Herstellertoleranzen gemäß den Spezifikationen der Datenblätter ein, sofern nicht anders auf dem Kalibrierschein vermerkt. Das Kistler Qualitätsmanagement System ist nach ISO 9001 zertifiziert. Das Dokument erfüllt die Anforderungen von EN 10204 Abnahmeprüfzeugnis "3.1". Die aufgeführten Referenzgeräte sind auf nationale Normale rückgeführt. Das Dokument wurde elektronisch erstellt und ist daher ohne Unterschrift gültig.

The equipment identified by Serial No. complies with the agreement of the order and meets the manufacturing tolerances specified in the data sheets, unless otherwise specified on the calibration certificate. The Kistler Quality Management System is certified per ISO 9001. This document fulfils the requirements of EN 10204 Inspection Certificate "3.1". The reference equipment is traceable to national standards. The document was issued electronically and is therefore valid without signature.

Kistler Instrumente AG
Eulachstrasse 22
8408 Winterthur
Switzerland

Tel. +41 52 224 11 11
Fax +41 52 224 14 14
info@kistler.com



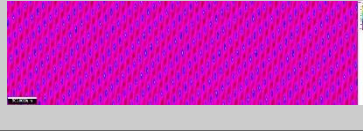

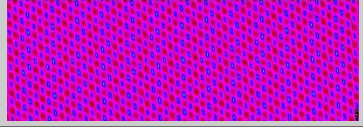
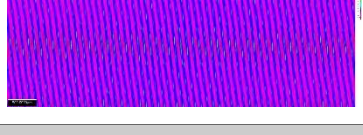


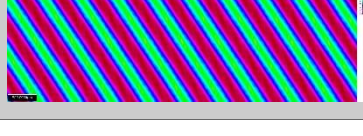
ZKB Winterthur BC 732
Swift: ZKBKCHZ8DA
Account: 1132-0374.628

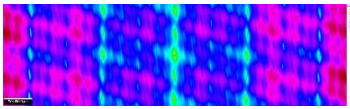

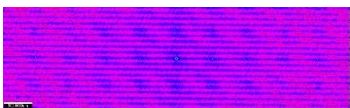


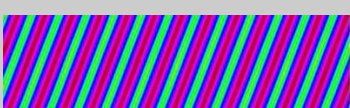



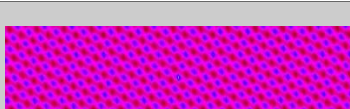

IBAN: CH67 0070 0113 2003 7462 8
VAT: 229 713
ISO 9001 certified

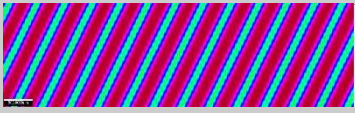



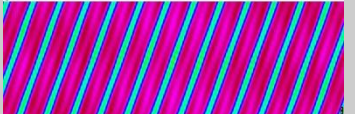





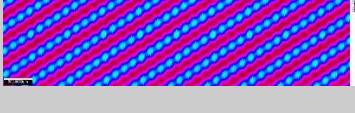
www.kistler.com

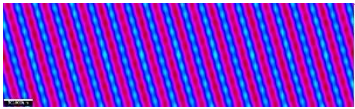

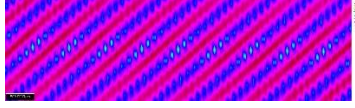
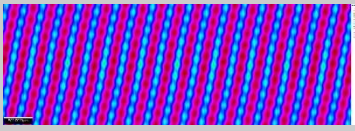

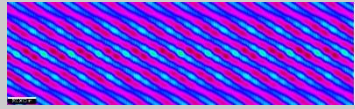
Appendix III Surface Topology

Surface Topology sort by Lead Angle

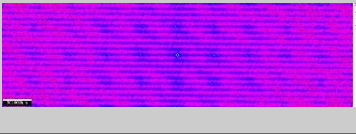



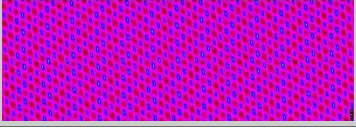


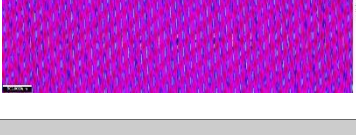

WP #	Std Order	Surface Speed	Depth of Cut	Feed Rate	Lead Angle	Picture
22	27	300	0.4	0.12	0	
25	34	300	0.4	0.12	0	
35	11	250	0.3	0.08	7.5	
30	1	350	0.3	0.08	7.5	
3	2	250	0.5	0.08	7.5	
7	12	350	0.5	0.08	7.5	
32	3	250	0.3	0.16	7.5	
34	13	350	0.3	0.16	7.5	
9	14	250	0.5	0.16	7.5	



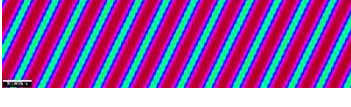
4	4	350	0.5	0.16	7.5	
11	31	350	0.5	0.16	7.5	
19	25	300	0.4	0.02	15	
24	33	300	0.4	0.02	15	
2	23	300	0.1	0.12	15	
17	21	200	0.4	0.12	15	
28	37	200	0.4	0.12	15	
13	9	300	0.4	0.12	15	
12	10	300	0.4	0.12	15	
15	19	300	0.4	0.12	15	
14	20	300	0.4	0.12	15	


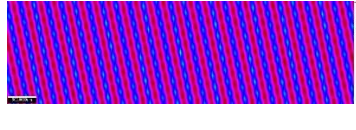
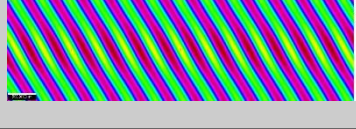
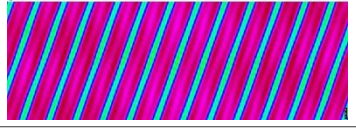

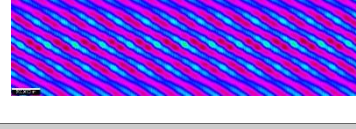


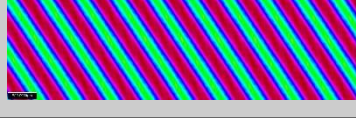
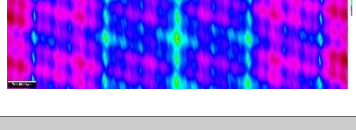

18	29	300	0.4	0.12	15	
21	30	300	0.4	0.12	15	
20	22	400	0.4	0.12	15	
27	36	400	0.4	0.12	15	
1	24	300	0.6	0.12	15	
23	26	300	0.4	0.2	15	
31	5	250	0.3	0.08	22.5	
36	15	350	0.3	0.08	22.5	
10	16	250	0.5	0.08	22.5	
5	6	350	0.5	0.08	22.5	
33	17	250	0.3	0.16	22.5	

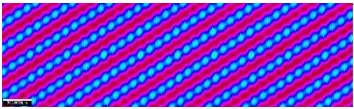
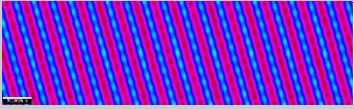

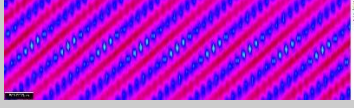
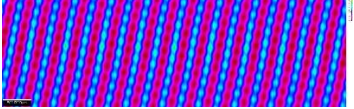

39	32	250	0.3	0.16	22.5	
29	7	350	0.3	0.16	22.5	
6	8	250	0.5	0.16	22.5	
8	18	350	0.5	0.16	22.5	
16	28	300	0.4	0.12	45	
26	35	300	0.4	0.12	45	

Surface Topology sort by Feed Rate

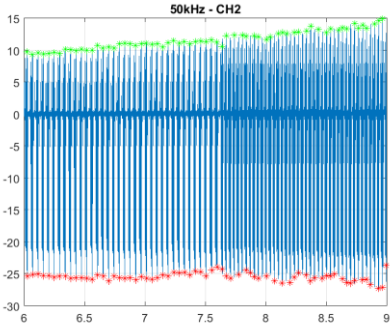
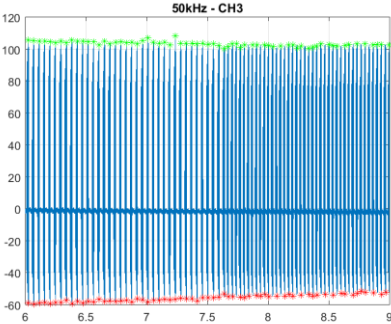
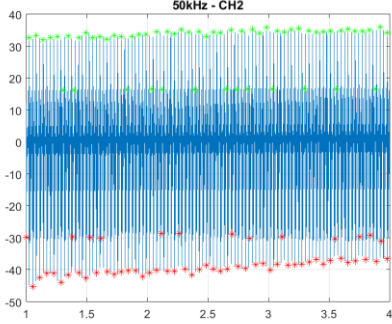
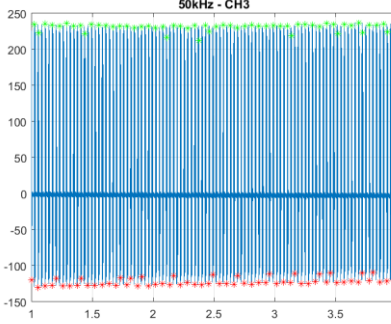
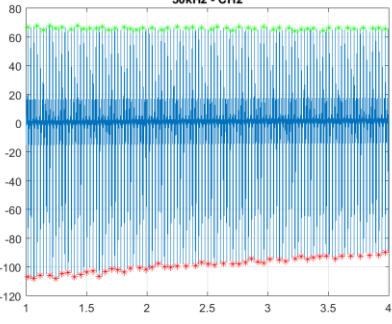
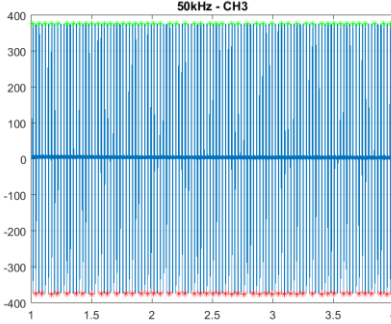
WP #	Std Order	Surface Speed	Depth of Cut	Feed Rate	Lead Angle	Picture
19	25	300	0.4	0.02	15	
24	33	300	0.4	0.02	15	
35	11	250	0.3	0.08	7.5	
30	1	350	0.3	0.08	7.5	
3	2	250	0.5	0.08	7.5	
7	12	350	0.5	0.08	7.5	
31	5	250	0.3	0.08	22.5	
36	15	350	0.3	0.08	22.5	
10	16	250	0.5	0.08	22.5	

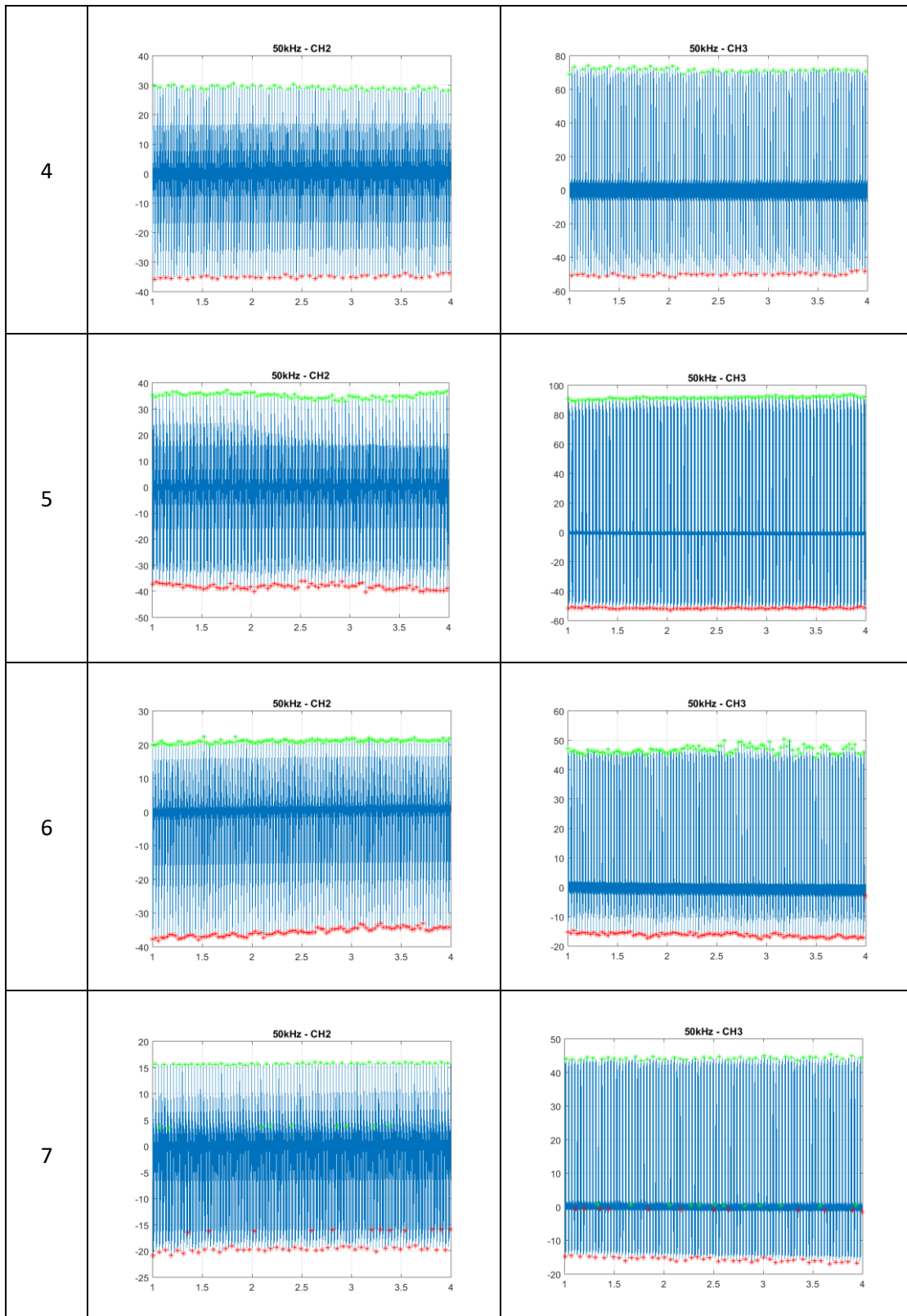
5	6	350	0.5	0.08	22.5	
22	27	300	0.4	0.12	0	
25	34	300	0.4	0.12	0	
2	23	300	0.1	0.12	15	
17	21	200	0.4	0.12	15	
28	37	200	0.4	0.12	15	
13	9	300	0.4	0.12	15	
12	10	300	0.4	0.12	15	
15	19	300	0.4	0.12	15	
14	20	300	0.4	0.12	15	
18	29	300	0.4	0.12	15	

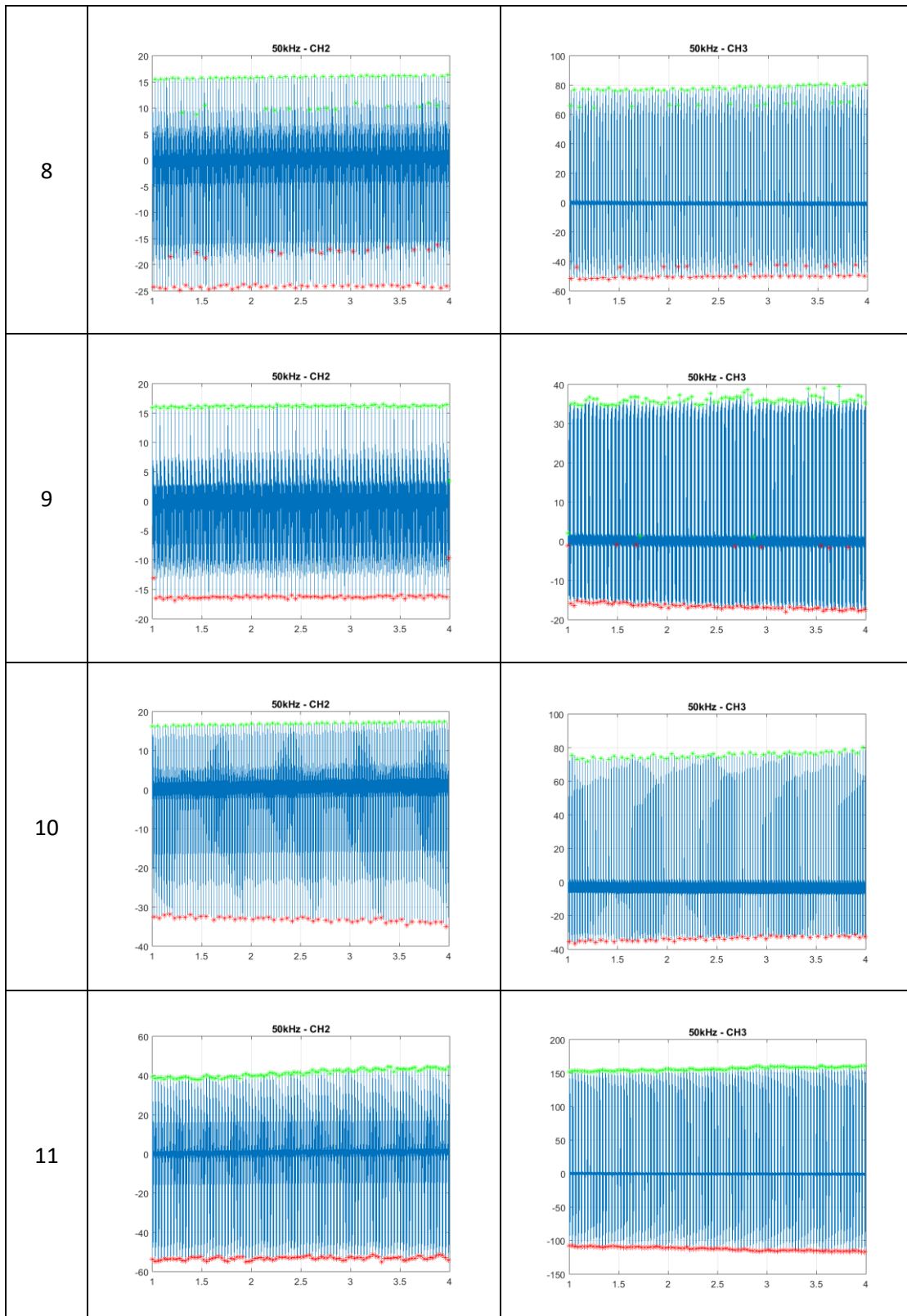
21	30	300	0.4	0.12	15	
20	22	400	0.4	0.12	15	
27	36	400	0.4	0.12	15	
1	24	300	0.6	0.12	15	
16	28	300	0.4	0.12	45	
26	35	300	0.4	0.12	45	
32	3	250	0.3	0.16	7.5	
34	13	350	0.3	0.16	7.5	
9	14	250	0.5	0.16	7.5	
4	4	350	0.5	0.16	7.5	
11	31	350	0.5	0.16	7.5	

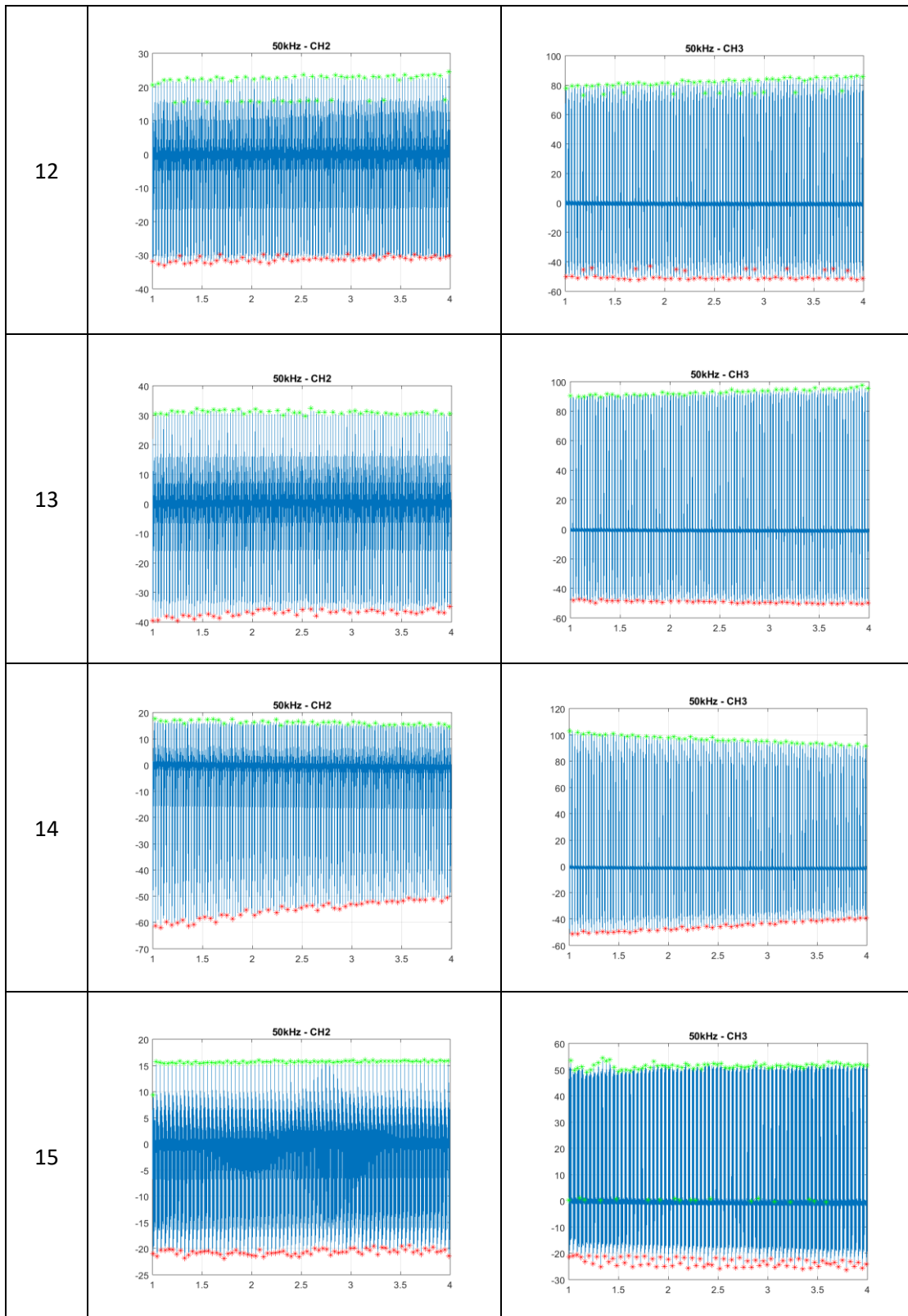
33	17	250	0.3	0.16	22.5	
39	32	250	0.3	0.16	22.5	
29	7	350	0.3	0.16	22.5	
6	8	250	0.5	0.16	22.5	
8	18	350	0.5	0.16	22.5	
23	26	300	0.4	0.2	15	

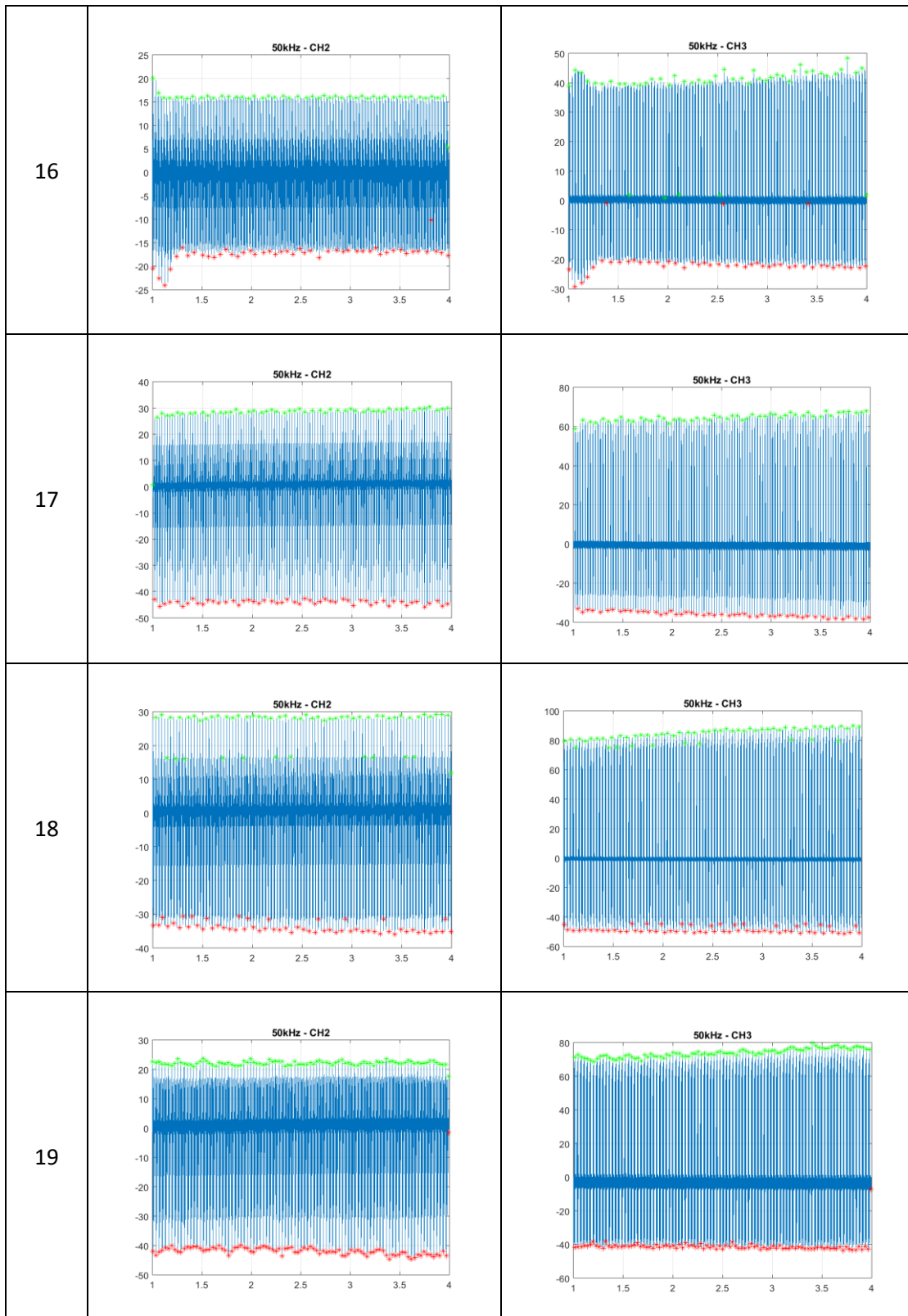
Appendix IV Underpinning Cutting Force Data

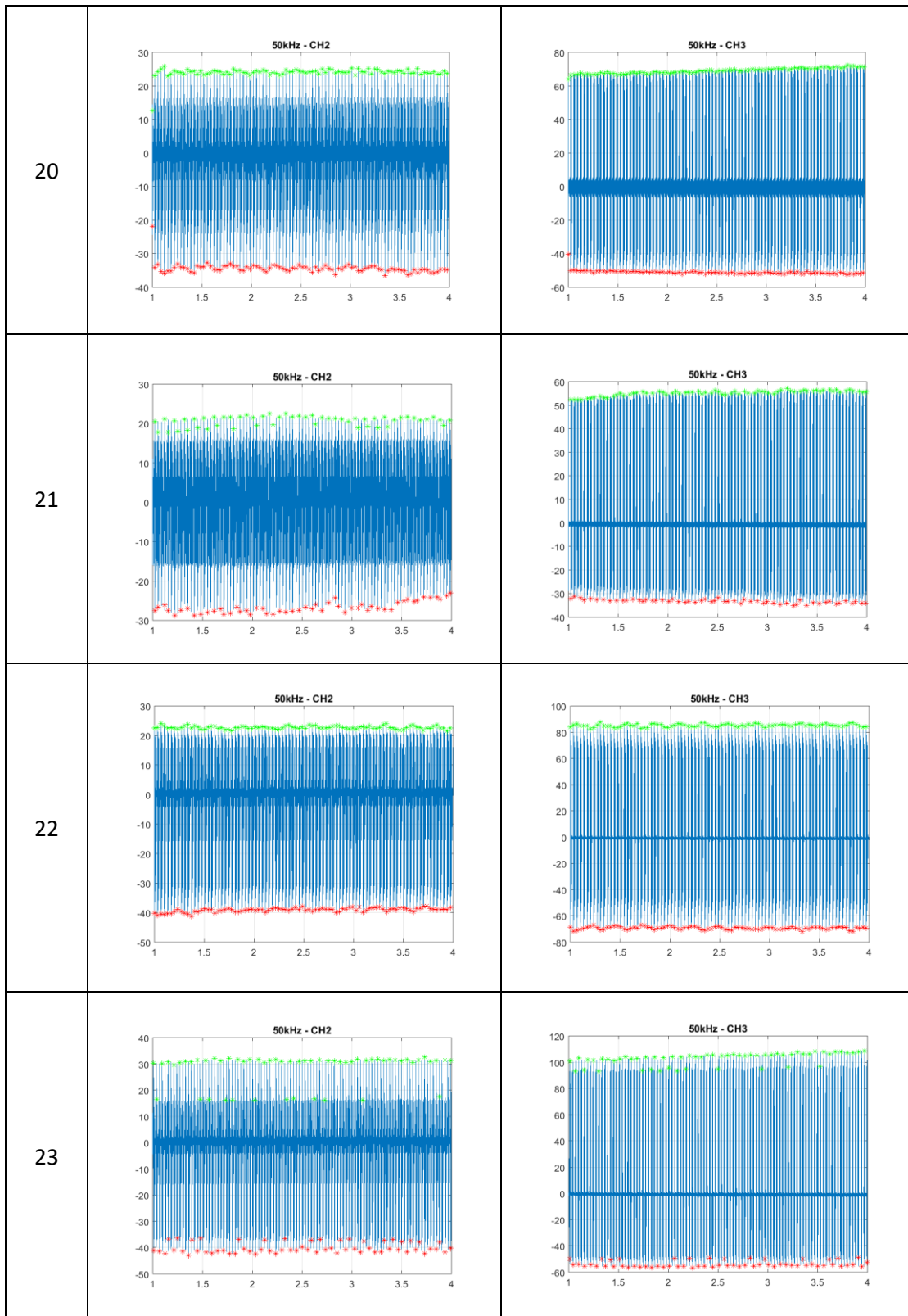
Run Order	Feed Direction	Vertical Direction
1	 <p>50kHz - CH2</p> <p>This plot shows cutting force data for Run 1 in the Feed Direction. The y-axis ranges from -30 to 15, and the x-axis ranges from 6 to 9. It features three data series: a green line at the top (around 10), a blue line oscillating around 0, and a red line at the bottom (around -25).</p>	 <p>50kHz - CH3</p> <p>This plot shows cutting force data for Run 1 in the Vertical Direction. The y-axis ranges from -60 to 120, and the x-axis ranges from 6 to 9. It features three data series: a green line at the top (around 100), a blue line oscillating around 0, and a red line at the bottom (around -50).</p>
2	 <p>50kHz - CH2</p> <p>This plot shows cutting force data for Run 2 in the Feed Direction. The y-axis ranges from -50 to 40, and the x-axis ranges from 1 to 4. It features three data series: a green line at the top (around 30), a blue line oscillating around 0, and a red line at the bottom (around -40).</p>	 <p>50kHz - CH3</p> <p>This plot shows cutting force data for Run 2 in the Vertical Direction. The y-axis ranges from -150 to 250, and the x-axis ranges from 1 to 4. It features three data series: a green line at the top (around 200), a blue line oscillating around 0, and a red line at the bottom (around -120).</p>
3	 <p>50kHz - CH2</p> <p>This plot shows cutting force data for Run 3 in the Feed Direction. The y-axis ranges from -120 to 80, and the x-axis ranges from 1 to 4. It features three data series: a green line at the top (around 60), a blue line oscillating around 0, and a red line at the bottom (around -100).</p>	 <p>50kHz - CH3</p> <p>This plot shows cutting force data for Run 3 in the Vertical Direction. The y-axis ranges from -400 to 400, and the x-axis ranges from 1 to 4. It features three data series: a green line at the top (around 350), a blue line oscillating around 0, and a red line at the bottom (around -350).</p>

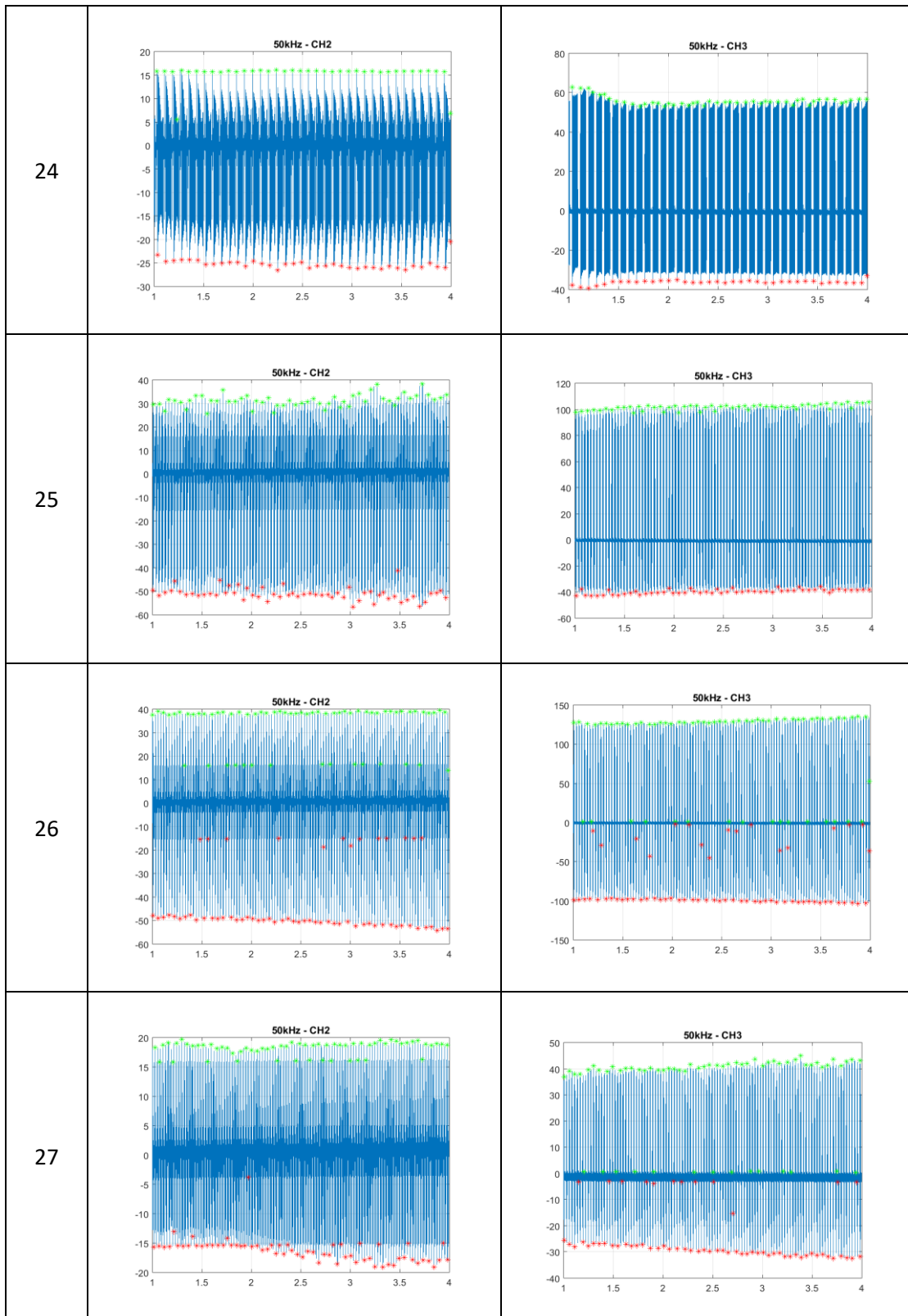


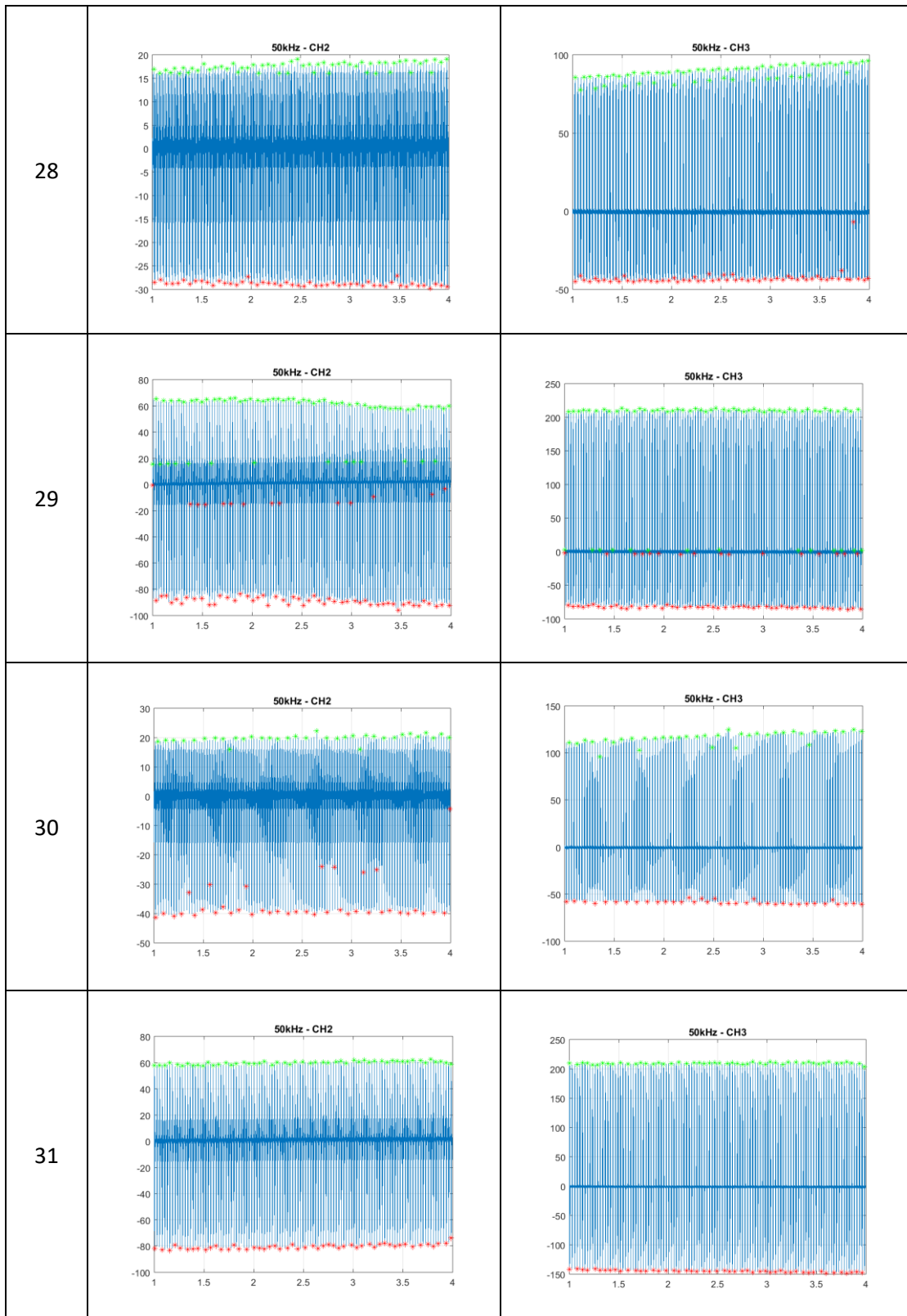


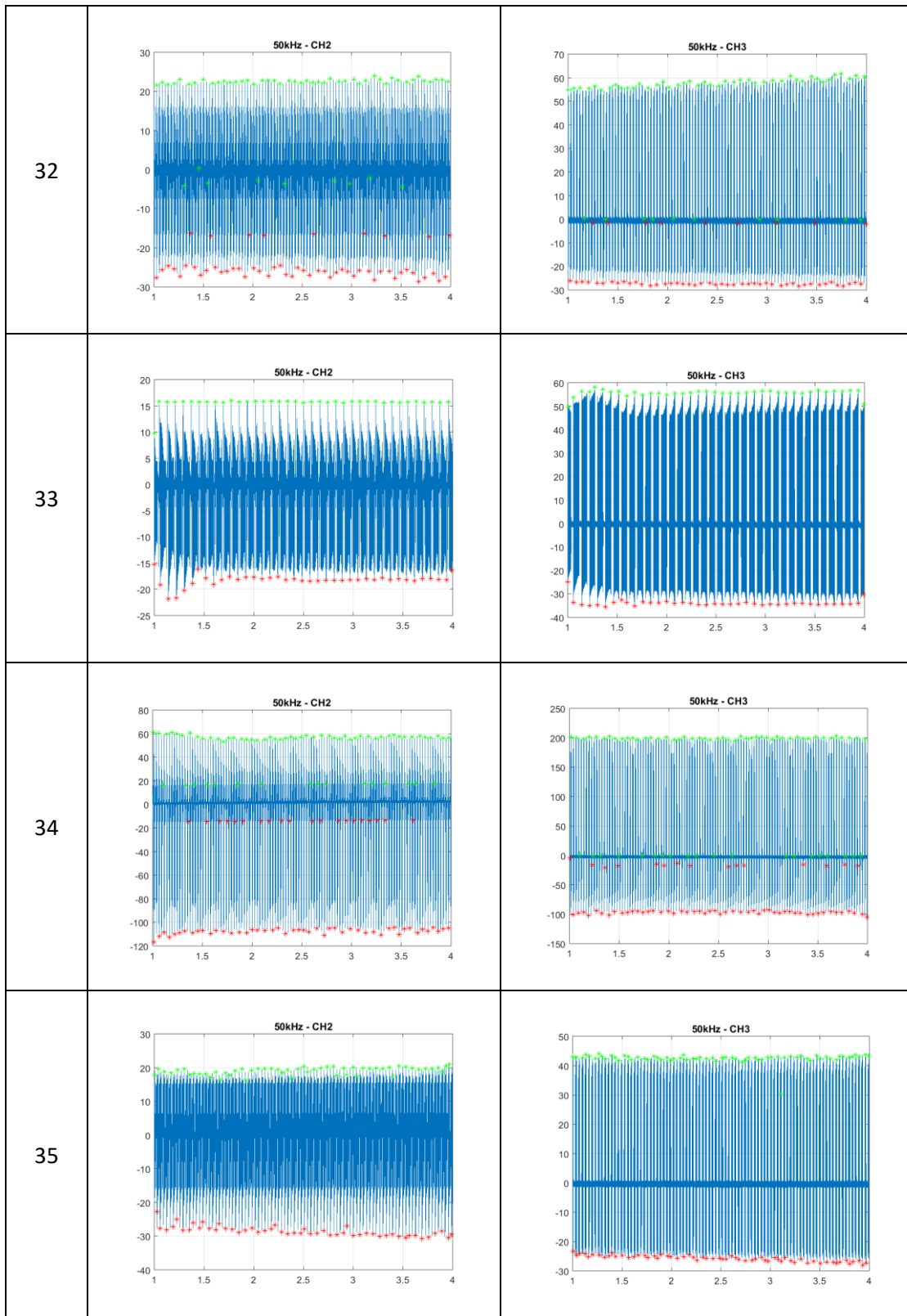




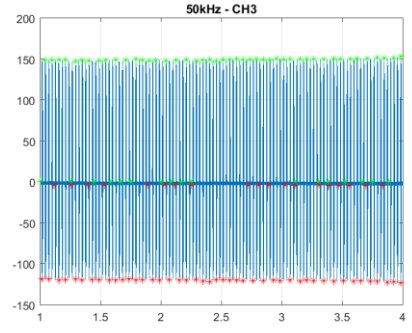
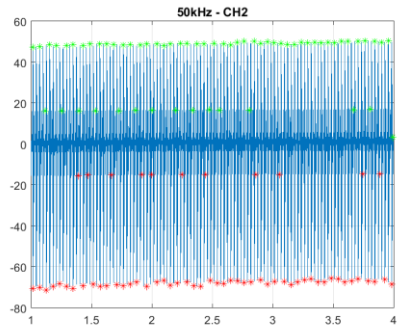




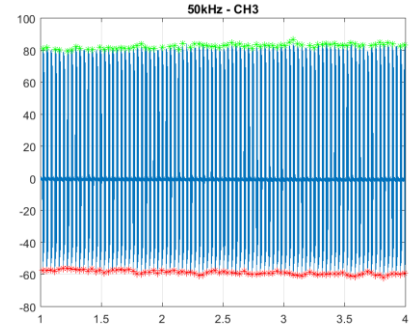
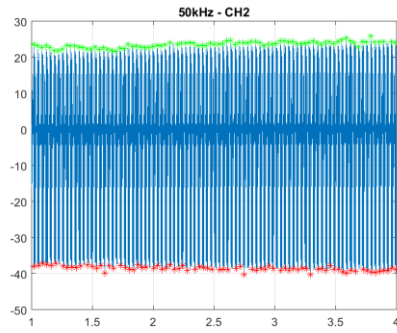




36



37



Appendix V Underpinning Residual Stress Data

WP No	No	X Pos	Y Pos	Phi Pos	Stress	Error Stress	Shear Stress	Error Shear Stress
1	1	0	0	0	63.7	11.4	-67.4	5.4
1	2	0	0	90	104.2	9.1	1.7	4.3
1	3	0	-10	0	56.1	11.9	-70	5.7
1	4	0	-10	90	104.9	6	-2.5	2.9
1	5	0	-20	0	53.1	11.2	-70.5	5.4
1	6	0	-20	90	103.7	6.4	-1	3.1
1	7	0	-30	0	46.3	9.4	-66.8	4.5
1	8	0	-30	90	94.2	6.3	4.6	3
1	9	0	-40	0	56.4	10.3	-71	4.9
1	10	0	-40	90	96.9	5.7	-0.1	2.7
1	11	0	-50	0	53.9	9	-65.3	4.3
1	12	0	-50	90	95.1	7.7	1	3.7
2	13	30	-57.5	0	49.8	11.6	-58.8	5.6
2	14	30	-57.5	90	81	5	-1.3	2.4
2	15	30	-47.5	0	22.8	12.2	-58.5	5.8
2	16	30	-47.5	90	92	5.7	-1.4	2.7
2	17	30	-37.5	0	35	12	-61.5	5.8
2	18	30	-37.5	90	105.7	7.8	0.4	3.7
2	19	30	-27.5	0	20.1	15.2	-61.7	7.3
2	20	30	-27.5	90	81.3	7.2	-0.7	3.4
2	21	30	-17.5	0	-10.1	12	-59.9	5.7
2	22	30	-17.5	90	67.9	4.9	1.5	2.3
2	23	30	-7.5	0	1.4	14.4	-70.6	6.9
2	24	30	-7.5	90	85.4	6.8	-2.4	3.2
3	25	50	-7.5	0	-36.4	7.3	58.9	3.5
3	26	50	-7.5	90	-43.7	4.9	-1.9	2.3
3	27	50	-17.5	0	-13.5	13.2	62.9	6.3
3	28	50	-17.5	90	-36.9	5.6	-2.4	2.7
3	29	50	-27.5	0	-9.6	12.6	65.9	6
3	30	50	-27.5	90	-27.7	6.5	0.3	3.1
3	31	50	-37.5	0	-17.7	10.3	60.1	4.9
3	32	50	-37.5	90	-38.8	5.9	2	2.8
3	33	50	-47.5	0	-16.5	11.9	65.1	5.7
3	34	50	-47.5	90	-36	8	3.6	3.8
3	35	50	-57.5	0	-42.2	12.5	63.5	6
3	36	50	-57.5	90	-23.6	3.9	0.8	1.9
4	37	80	-50	0	33.4	9.9	-61.8	4.7

4	38	80	-50	90	49.8	5.5	2.8	2.6
4	39	80	-40	0	25.5	15.5	-62.9	7.4
4	40	80	-40	90	54.3	5.2	-2.8	2.5
4	41	80	-30	0	28.4	11.6	-62	5.5
4	42	80	-30	90	64	8.6	2.5	4.1
4	43	80	-20	0	20	7.8	-55.9	3.7
4	44	80	-20	90	58.2	9.2	2.4	4.4
4	45	80	-10	0	18.6	9.7	-60.3	4.6
4	46	80	-10	90	74.5	8.4	-7.6	4
4	47	80	0	0	27.2	6	-52.7	2.9
4	48	80	0	90	54.5	9.1	-5.5	4.4
5	1	0	0	0	120.2	10.5	-59.4	5
5	2	0	0	90	54.8	8.3	2.1	4
5	3	0	-10	0	116.5	15.8	-67.8	7.5
5	4	0	-10	90	49.7	5.4	-0.7	2.6
5	5	0	-20	0	114.1	8.9	-60.4	4.3
5	6	0	-20	90	59.1	5.6	1.9	2.7
5	7	0	-30	0	114.2	11.5	-64.7	5.5
5	8	0	-30	90	52.9	5.8	0.6	2.8
5	9	0	-40	0	106.6	12.1	-65.4	5.8
5	10	0	-40	90	52.2	4.3	1.9	2
5	11	0	-50	0	104.6	11.9	-66.6	5.7
5	12	0	-50	90	49.8	6.3	4.8	3
6	13	30	-57.5	0	51	7.2	-59.4	3.4
6	14	30	-57.5	90	14.2	8.2	-2.5	3.9
6	15	30	-47.5	0	36.9	9.4	-60.1	4.5
6	16	30	-47.5	90	16.4	6	0.1	2.9
6	17	30	-37.5	0	35.9	10.8	-60.6	5.2
6	18	30	-37.5	90	11.4	7.2	2.8	3.5
6	19	30	-27.5	0	41.3	8.3	-59.2	4
6	20	30	-27.5	90	15.8	5.1	-0.4	2.5
6	21	30	-17.5	0	42.4	6.3	-60.1	3
6	22	30	-17.5	90	24.3	4.8	-4.1	2.3
6	23	30	-7.5	0	37.1	8.7	-58.2	4.1
6	24	30	-7.5	90	19.7	5.3	1.1	2.5
7	25	50	-7.5	0	29.3	7.5	-54.9	3.6
7	26	50	-7.5	90	-14.4	7.9	-7	3.8
7	27	50	-17.5	0	49.6	6.9	-60	3.3
7	28	50	-17.5	90	-0.7	8.5	-5.5	4.1
7	29	50	-27.5	0	53.7	7.3	-54.7	3.5
7	30	50	-27.5	90	-12.3	4.6	-2.4	2.2
7	31	50	-37.5	0	26.2	10.7	-60.2	5.1
7	32	50	-37.5	90	-18.4	5.2	-1.6	2.5
7	33	50	-47.5	0	44.8	8.2	-57.4	3.9

7	34	50	-47.5	90	-30.3	4	-1.9	1.9
7	35	50	-57.5	0	44.2	12.1	-60.6	5.8
7	36	50	-57.5	90	-17.4	5.3	-2.4	2.5
8	37	80	-50	0	114.7	14.2	-65.7	6.8
8	38	80	-50	90	130.1	7.9	-1.3	3.8
8	39	80	-40	0	104.5	15.7	-63.8	7.5
8	40	80	-40	90	126.4	8.9	-4.5	4.2
8	41	80	-30	0	106.9	12.4	-62	5.9
8	42	80	-30	90	105.7	9.4	2.2	4.5
8	43	80	-20	0	122.6	14.6	-59.8	7
8	44	80	-20	90	125.3	9.7	0.7	4.7
8	45	80	-10	0	115.7	21.2	-66.4	10.2
8	46	80	-10	90	125.5	10.9	-2.6	5.2
8	47	80	0	0	113.7	14	-60.1	6.7
8	48	80	0	90	103	13.9	-1.1	6.6
9	1	0	0	0	-9.3	18.6	-69.6	8.9
9	2	0	0	90	-45.5	5.5	-7.6	2.6
9	3	0	-10	0	-12.3	15.3	-65.6	7.3
9	4	0	-10	90	-62.2	4.4	-3.6	2.1
9	5	0	-20	0	-21.6	13.9	-65.4	6.7
9	6	0	-20	90	-69.3	6.4	1.6	3.1
9	7	0	-30	0	-10.9	13.2	-60.3	6.3
9	8	0	-30	90	-59.1	5.4	-2.4	2.6
9	9	0	-40	0	-26.4	12.7	-62.2	6.1
9	10	0	-40	90	-76.9	4.1	-6.4	1.9
9	11	0	-50	0	-37.1	10.5	-63.3	5
9	12	0	-50	90	-74.6	5.3	-1.1	2.5
10	13	15	0	0	139.4	16.2	-68.4	7.8
10	14	15	0	90	141	8.2	-2.2	3.9
10	15	15	-10	0	150.8	17.1	-68.6	8.2
10	16	15	-10	90	140.4	6.8	0.3	3.3
10	17	15	-20	0	135.7	20.2	-70	9.7
10	18	15	-20	90	122.3	9.2	2.7	4.4
10	19	15	-30	0	134.7	17.2	-66.9	8.2
10	20	15	-30	90	127.2	7.1	0.3	3.4
10	21	15	-40	0	145.9	14.1	-63.1	6.7
10	22	15	-40	90	136.1	4.2	1.3	2
10	23	15	-50	0	152.9	18.9	-70.6	9
10	24	15	-50	90	124.3	5.7	-0.9	2.7
11	25	30	0	0	50	14.5	-59.2	6.9
11	26	30	0	90	40.9	6.5	-0.4	3.1
11	27	30	-10	0	46.8	10.5	-56.4	5
11	28	30	-10	90	30.8	5.4	-4.7	2.6
11	29	30	-20	0	35.7	8.7	-56.5	4.2

11	30	30	-20	90	28.9	5.4	-3.6	2.6
11	31	30	-30	0	28.8	14.3	-58.3	6.8
11	32	30	-30	90	12.8	5	-3.8	2.4
11	33	30	-40	0	33.7	11.7	-57.5	5.6
11	34	30	-40	90	6.4	4.2	-1.3	2
11	35	30	-50	0	20.3	15.3	-55.9	7.3
11	36	30	-50	90	-8.8	7	-1.7	3.3
12	37	45	0	0	41.9	8.9	-53.3	4.3
12	38	45	0	90	52.6	6.4	2.2	3.1
12	39	45	-10	0	45.2	11.8	-60.1	5.6
12	40	45	-10	90	50.4	5.3	4.3	2.5
12	41	45	-20	0	25.9	11	-62.2	5.3
12	42	45	-20	90	49	6	1.1	2.9
12	43	45	-30	0	31.4	12.4	-62.9	5.9
12	44	45	-30	90	42	5.7	-0.5	2.7
12	45	45	-40	0	18.5	13.5	-64.6	6.5
12	46	45	-40	90	43	6.1	-0.7	2.9
12	47	45	-50	0	21.1	12.6	-65	6
12	48	45	-50	90	39	5.9	-0.8	2.8
13	49	60	0	0	65.4	17.8	-69.8	8.5
13	50	60	0	90	-7.5	5.6	2.6	2.7
13	51	60	-10	0	69	15.8	-66.5	7.6
13	52	60	-10	90	-15.8	6.5	0.7	3.1
13	53	60	-20	0	68.7	14	-63.9	6.7
13	54	60	-20	90	-0.9	6.2	2.8	3
13	55	60	-30	0	63.6	8.1	-61.2	3.9
13	56	60	-30	90	-7.5	5.2	-2	2.5
13	57	60	-40	0	63	12.8	-65	6.1
13	58	60	-40	90	-8	6.4	-1	3.1
13	59	60	-50	0	56.9	10.5	-53.5	5
13	60	60	-50	90	-18.8	4.6	-0.2	2.2
14	61	75	0	0	51.7	15	-63.9	7.2
14	62	75	0	90	31.1	7.6	-2.2	3.6
14	63	75	-10	0	64.3	10.7	-60.9	5.1
14	64	75	-10	90	34.7	5.6	-0.1	2.7
14	65	75	-20	0	48.3	12.2	-61	5.8
14	66	75	-20	90	33	4.3	-1.8	2
14	67	75	-30	0	51.5	13.4	-55.7	6.4
14	68	75	-30	90	38.6	4.2	0.1	2
14	69	75	-40	0	44.4	10.4	-57.1	5
14	70	75	-40	90	36.3	4.6	0.1	2.2
14	71	75	-50	0	49.1	12.4	-59.3	5.9
14	72	75	-50	90	28.9	6.8	-1.2	3.2
15	73	90	0	0	99.5	15.2	-61.2	7.3

15	74	90	0	90	171	6.5	-3.9	3.1
15	75	90	-10	0	83.7	11.4	-60	5.4
15	76	90	-10	90	172.9	6.2	-1.1	3
15	77	90	-20	0	106.2	13.9	-63.8	6.6
15	78	90	-20	90	159.6	7	-4.7	3.3
15	79	90	-30	0	93.9	14.3	-60.5	6.8
15	80	90	-30	90	167.9	7.1	3.3	3.4
15	81	90	-40	0	99.3	16.6	-64.8	7.9
15	82	90	-40	90	175.8	5.4	1	2.6
15	83	90	-50	0	90.2	14.6	-60.9	7
15	84	90	-50	90	161.6	7	0.6	3.3
16	85	105	0	0	28.1	13.1	-65	6.2
16	86	105	0	90	117.6	6.1	1.1	2.9
16	87	105	-10	0	21.5	13.7	-67	6.5
16	88	105	-10	90	125.2	6.9	-2	3.3
16	89	105	-20	0	1.3	13.1	-62.5	6.3
16	90	105	-20	90	117.4	5.7	2.1	2.7
16	91	105	-30	0	4	14.7	-65.9	7
16	92	105	-30	90	117.9	7.7	2.4	3.7
16	93	105	-40	0	11	10.8	-66.4	5.2
16	94	105	-40	90	120.8	6.5	-0.1	3.1
16	95	105	-50	0	2.5	12	-63.8	5.7
16	96	105	-50	90	119.9	9.9	-4.2	4.7
17	97	120	0	0	42.4	20.5	-70.4	9.8
17	98	120	0	90	0.7	6.7	0.9	3.2
17	99	120	-10	0	38.8	15.5	-57.2	7.4
17	100	120	-10	90	-5.5	7	-1.9	3.4
17	101	120	-20	0	46.1	15.3	-65.6	7.3
17	102	120	-20	90	13.7	6.9	0.2	3.3
17	103	120	-30	0	34.4	17	-69.2	8.1
17	104	120	-30	90	9.3	4.7	0.4	2.2
17	105	120	-40	0	40.3	18.8	-70.9	9
17	106	120	-40	90	12.7	5.4	2.6	2.6
17	107	120	-50	0	45.1	14.3	-65	6.8
17	108	120	-50	90	10.3	6.5	-2.9	3.1
18	109	135	0	0	52.4	13.6	-64.9	6.5
18	110	135	0	90	64.2	5.1	-0.8	2.5
18	111	135	-10	0	45.4	10.4	-61.4	5
18	112	135	-10	90	34.7	8.6	0.4	4.1
18	113	135	-20	0	37.6	13.2	-60.9	6.3
18	114	135	-20	90	42.2	7.5	0.3	3.6
18	115	135	-30	0	27.8	14.9	-67	7.1
18	116	135	-30	90	35.9	7.1	2.4	3.4
18	117	135	-40	0	38.7	13.4	-67.9	6.4

18	118	135	-40	90	26.3	6	1.4	2.9
18	119	135	-50	0	38	15.5	-69.4	7.4
18	120	135	-50	90	36.6	8	1.9	3.8
19	121	150	0	0	45.1	20.7	-85.6	9.9
19	122	150	0	90	-76.1	4.9	1.1	2.3
19	123	150	-10	0	26.6	13.3	-80.5	6.4
19	124	150	-10	90	-81.9	5.9	1	2.8
19	125	150	-20	0	37.2	13	-80.4	6.2
19	126	150	-20	90	-88	6.1	2.6	2.9
19	127	150	-30	0	15	17	-79.1	8.1
19	128	150	-30	90	-92.4	5.5	1.4	2.6
19	129	150	-40	0	18	14.8	-81.8	7.1
19	130	150	-40	90	-88.6	4.8	0.3	2.3
19	131	150	-50	0	5.2	14.9	-78.4	7.1
19	132	150	-50	90	-99.5	11.3	-5.6	5.4
20	133	165	0	0	31.1	12.9	-56.7	6.2
20	134	165	0	90	104.2	7.8	4.1	3.7
20	135	165	-10	0	31.2	12.2	-55.4	5.8
20	136	165	-10	90	114.3	8.4	3.2	4
20	137	165	-20	0	30	15.4	-64.4	7.4
20	138	165	-20	90	121.1	7.7	4.7	3.7
20	139	165	-30	0	27.3	12.9	-62.1	6.2
20	140	165	-30	90	121.8	5.7	2.9	2.7
20	141	165	-40	0	41.1	14	-59.4	6.7
20	142	165	-40	90	111.7	10.8	4.5	5.1
20	143	165	-50	0	38.7	8.3	-56.3	4
20	144	165	-50	90	124.9	4.3	-4.8	2
21	145	180	0	0	38.6	10.6	-56.9	5.1
21	146	180	0	90	128	7.9	4.7	3.8
21	147	180	-10	0	50	13.4	-56.3	6.4
21	148	180	-10	90	133.2	8.2	5.7	3.9
21	149	180	-20	0	39.5	13.9	-62.9	6.6
21	150	180	-20	90	130.6	8.5	0.1	4
21	151	180	-30	0	30.2	16	-64.7	7.7
21	152	180	-30	90	119	6.4	-2.8	3.1
21	153	180	-40	0	47.6	13	-59.6	6.2
21	154	180	-40	90	132.9	6.7	-1.7	3.2
21	155	180	-50	0	32	16.1	-62.9	7.7
21	156	180	-50	90	111.4	6.7	2.4	3.2
22	157	195	0	0	-215.9	6.5	-7.6	3.1
22	158	195	0	90	-56.5	12.6	-41.3	6
22	159	195	-10	0	-214.1	7.8	-10.4	3.7
22	160	195	-10	90	-60.6	13.2	-41.8	6.3
22	161	195	-20	0	-227.4	7.8	-11.8	3.7

22	162	195	-20	90	-72.1	10.6	-40.6	5.1
22	163	195	-30	0	-232.4	7.5	-12.5	3.6
22	164	195	-30	90	-66.5	13.8	-44.2	6.6
22	165	195	-40	0	-225	10.7	-16.4	5.1
22	166	195	-40	90	-68.8	14.6	-45.7	7
22	167	195	-50	0	-213.3	7.7	-9.8	3.7
22	168	195	-50	90	-66.3	14.4	-43.4	6.9
23	1	0	0	0	87.7	16.8	-61.7	8
23	2	0	0	90	197.9	10.2	5	4.9
23	3	0	-10	0	66.7	12.7	-58.1	6.1
23	4	0	-10	90	199.5	5.7	-2.8	2.7
23	5	0	-20	0	75	14	-62.9	6.7
23	6	0	-20	90	205.3	5.7	0	2.7
23	7	0	-30	0	78.5	14.5	-55.4	6.9
23	8	0	-30	90	210	7.3	-2.9	3.5
23	9	0	-40	0	85.4	13.8	-59.5	6.6
23	10	0	-40	90	223.8	7.7	5.9	3.7
23	11	0	-50	0	69.5	11.9	-57.7	5.7
23	12	0	-50	90	202.6	10.7	-5.3	5.1
24	169	0	-80	0	-41.9	14.4	-71.1	6.9
24	170	0	-80	90	-163.2	7	-3.4	3.4
24	171	0	-90	0	-62.8	8.6	-65.8	4.1
24	172	0	-90	90	-167.9	4.7	1.9	2.3
24	173	0	-100	0	-81.4	9.3	-69.9	4.4
24	174	0	-100	90	-163.6	6.5	3	3.1
24	175	0	-110	0	-72.3	10.9	-71.6	5.2
24	176	0	-110	90	-150.2	5.6	-1.6	2.7
24	177	0	-120	0	-50	12.4	-71.9	5.9
24	178	0	-120	90	-147.9	4.8	3.4	2.3
24	179	0	-130	0	-64.8	11.5	-71.2	5.5
24	180	0	-130	90	-153.8	3.4	0.6	1.6
25	181	15	-80	0	-182.1	5.8	-11.9	2.8
25	182	15	-80	90	-41.4	12	-48.7	5.8
25	183	15	-90	0	-184	6.7	-15.9	3.2
25	184	15	-90	90	-39.3	10.9	-52.3	5.2
25	185	15	-100	0	-181.1	7.7	-15.2	3.7
25	186	15	-100	90	-44.7	12	-51	5.7
25	187	15	-110	0	-179.1	5	-11.2	2.4
25	188	15	-110	90	-32.2	9	-46.9	4.3
25	189	15	-120	0	-184.4	6.1	-7.4	2.9
25	190	15	-120	90	-35.4	12.7	-51.3	6.1
25	191	15	-130	0	-199.3	7.1	-12.6	3.4
25	192	15	-130	90	-46	13.2	-51.5	6.3
26	193	30	-80	0	-7	13.9	-54.5	6.7

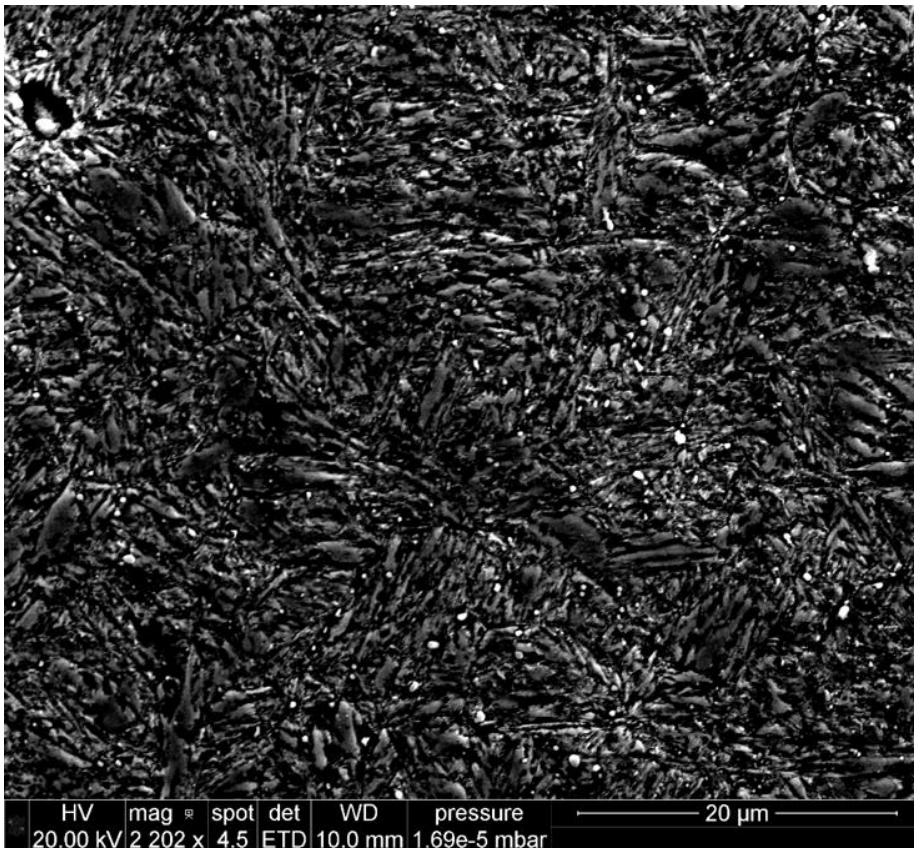
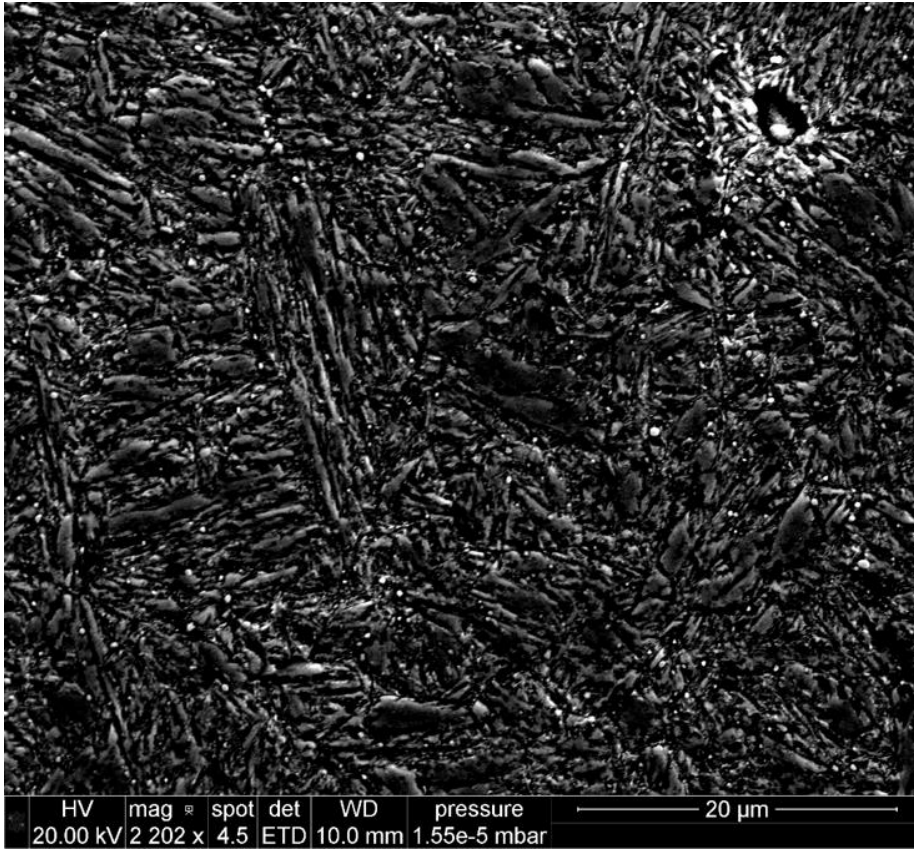
26	194	30	-80	90	65.8	5.5	-0.6	2.6
26	195	30	-90	0	1.7	10.3	-47.8	4.9
26	196	30	-90	90	80.4	8.1	-2.2	3.9
26	197	30	-100	0	-1.2	16.9	-60.7	8.1
26	198	30	-100	90	48.2	6.5	-0.7	3.1
26	199	30	-110	0	27	17.1	-50.8	8.2
26	200	30	-110	90	84.6	6.3	-2.2	3
26	201	30	-120	0	11.1	14.7	-60.5	7
26	202	30	-120	90	80.9	5.3	1.1	2.6
26	203	30	-130	0	17.4	13.5	-56.7	6.5
26	204	30	-130	90	88.4	6.8	-1.9	3.2
27	205	45	-80	0	117.3	12.6	-71.2	6
27	206	45	-80	90	86.3	5.9	2.7	2.8
27	207	45	-90	0	112.2	14.2	-73	6.8
27	208	45	-90	90	83.2	8.9	5.2	4.3
27	209	45	-100	0	117.4	16.7	-71.6	8
27	210	45	-100	90	79.6	7.8	-5.1	3.7
27	211	45	-110	0	108.9	17.6	-74.5	8.4
27	212	45	-110	90	72.8	6.3	-2.8	3
27	213	45	-120	0	110.4	14.4	-70.8	6.9
27	214	45	-120	90	86.3	5.1	2.1	2.4
27	215	45	-130	0	94.5	11.7	-66.5	5.6
27	216	45	-130	90	80.8	6.5	0.8	3.1
28	217	60	-80	0	30.6	17.4	-68.8	8.3
28	218	60	-80	90	13.3	6.9	-5.4	3.3
28	219	60	-90	0	21	12.1	-66.3	5.8
28	220	60	-90	90	7.7	5	3.3	2.4
28	221	60	-100	0	21.3	17.8	-70.4	8.5
28	222	60	-100	90	0.8	5.7	-1.3	2.7
28	223	60	-110	0	11.3	13.9	-67.6	6.6
28	224	60	-110	90	-8.8	5.5	-1.4	2.7
28	225	60	-120	0	25	10.7	-64.4	5.1
28	226	60	-120	90	-3.1	5.6	-2.1	2.7
28	227	60	-130	0	8.5	13	-61.3	6.2
28	228	60	-130	90	-8.4	6.4	-0.4	3
29	229	75	-80	0	108.5	14.3	-63	6.8
29	230	75	-80	90	97.2	5.2	1	2.5
29	231	75	-90	0	108.7	13.5	-63.8	6.5
29	232	75	-90	90	110.5	6.8	2.8	3.2
29	233	75	-100	0	124.1	12.8	-61.8	6.1
29	234	75	-100	90	110.1	9.3	3.7	4.4
29	235	75	-110	0	96.7	11.1	-60.5	5.3
29	236	75	-110	90	95.3	6.5	-2.2	3.1
29	237	75	-120	0	111.4	13.4	-61	6.4

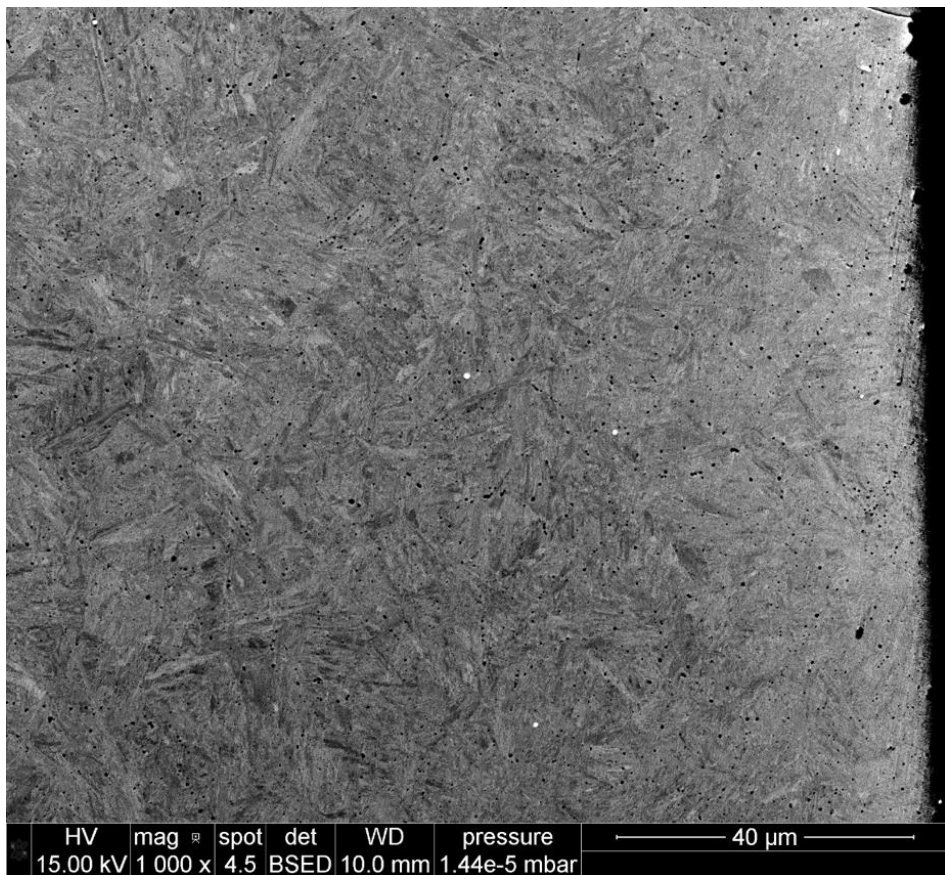
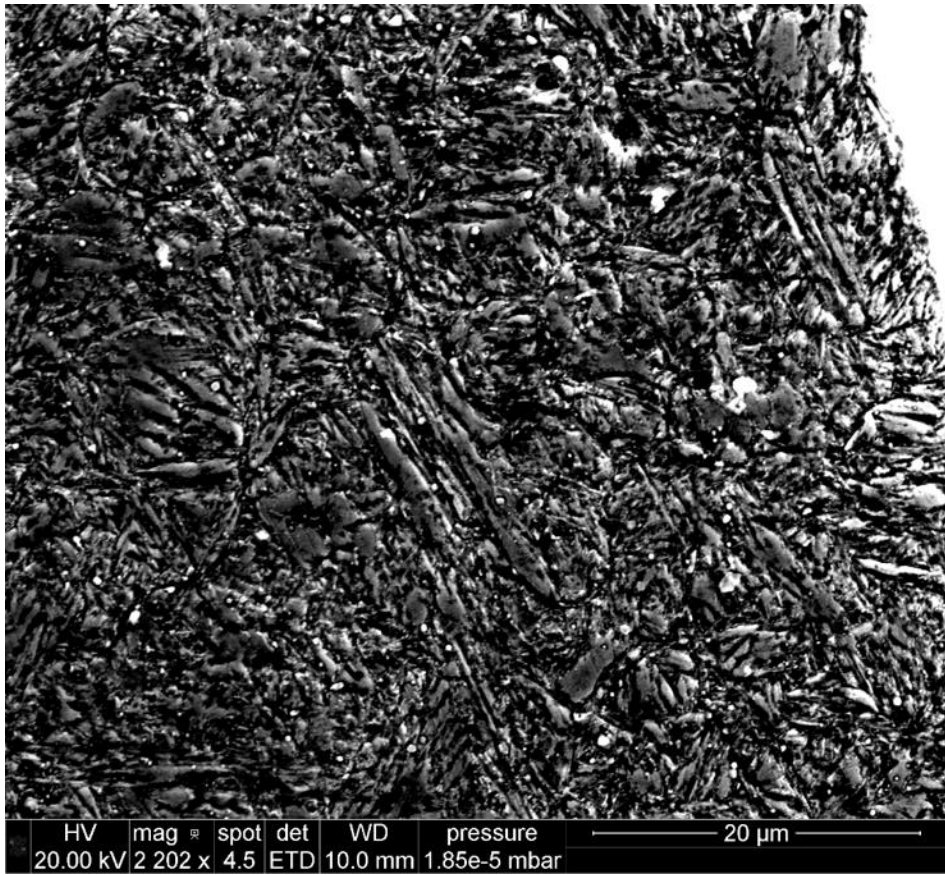
29	238	75	-120	90	113.4	7.2	-1.5	3.5
29	239	75	-130	0	92.9	14.1	-62.9	6.7
29	240	75	-130	90	89.5	7.1	1.3	3.4
30	241	90	-80	0	39.8	11.8	-56	5.6
30	242	90	-80	90	-118.7	3.9	1.1	1.9
30	243	90	-90	0	41.6	9.8	-49.4	4.7
30	244	90	-90	90	-103.2	4.2	-3	2
30	245	90	-100	0	43.4	10.7	-55.8	5.1
30	246	90	-100	90	-106.5	7.1	-3.4	3.4
30	247	90	-110	0	52.1	8.9	-48.8	4.3
30	248	90	-110	90	-109.9	5.4	-0.8	2.6
30	249	90	-120	0	47.5	10.7	-55.7	5.1
30	250	90	-120	90	-103.9	8.4	-5.7	4
30	251	90	-130	0	41.9	9.4	-51.3	4.5
30	252	90	-130	90	-120	6.5	-5.6	3.1
31	253	105	-80	0	82.7	18.3	-68	8.8
31	254	105	-80	90	-30.9	7.3	4.9	3.5
31	255	105	-90	0	80	13	-68.3	6.2
31	256	105	-90	90	-39.6	9.2	-5.6	4.4
31	257	105	-100	0	86.7	15.1	-67.1	7.2
31	258	105	-100	90	-31.3	6.5	-1.6	3.1
31	259	105	-110	0	83	15.6	-67	7.5
31	260	105	-110	90	-32.5	5.4	-0.3	2.6
31	261	105	-120	0	88.9	14.7	-72	7
31	262	105	-120	90	-22.7	4.4	1.5	2.1
31	263	105	-130	0	86.6	15.2	-68.7	7.3
31	264	105	-130	90	-38.4	4.7	2.5	2.2
32	265	120	-80	0	11.6	12.1	-58.4	5.8
32	266	120	-80	90	25.9	5.5	-0.4	2.6
32	267	120	-90	0	26.7	15.2	-60	7.3
32	268	120	-90	90	23.6	5.1	-3.8	2.4
32	269	120	-100	0	20.8	9.6	-52.4	4.6
32	270	120	-100	90	31.3	6.1	-7.3	2.9
32	271	120	-110	0	20.6	13.4	-58.6	6.4
32	272	120	-110	90	16.9	6.1	-3.5	2.9
32	273	120	-120	0	15.7	11	-58.5	5.2
32	274	120	-120	90	35.8	6.2	-3	2.9
32	275	120	-130	0	-3.4	10	-58.6	4.8
32	276	120	-130	90	18.7	8.8	-6.6	4.2
33	277	135	-80	0	61.7	9.5	-54.1	4.5
33	278	135	-80	90	73.4	6.9	3.2	3.3
33	279	135	-90	0	64.7	10.4	-56.2	5
33	280	135	-90	90	82.2	5.9	-4.1	2.8
33	281	135	-100	0	65.8	14.9	-58.1	7.1

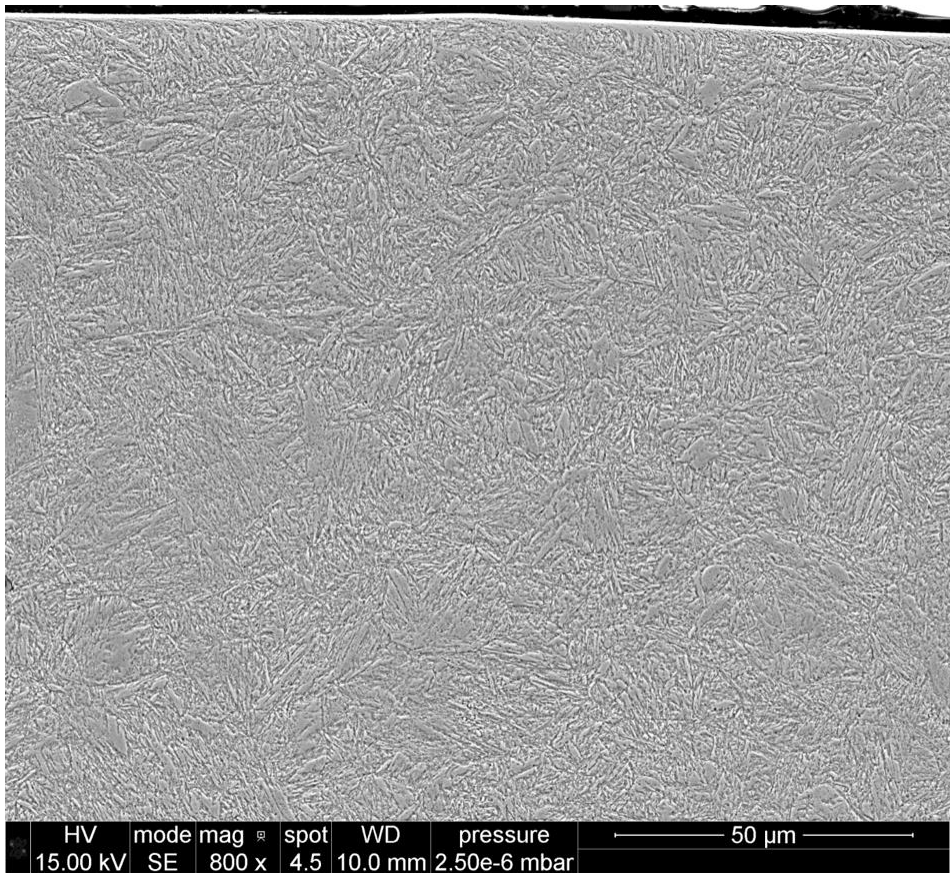
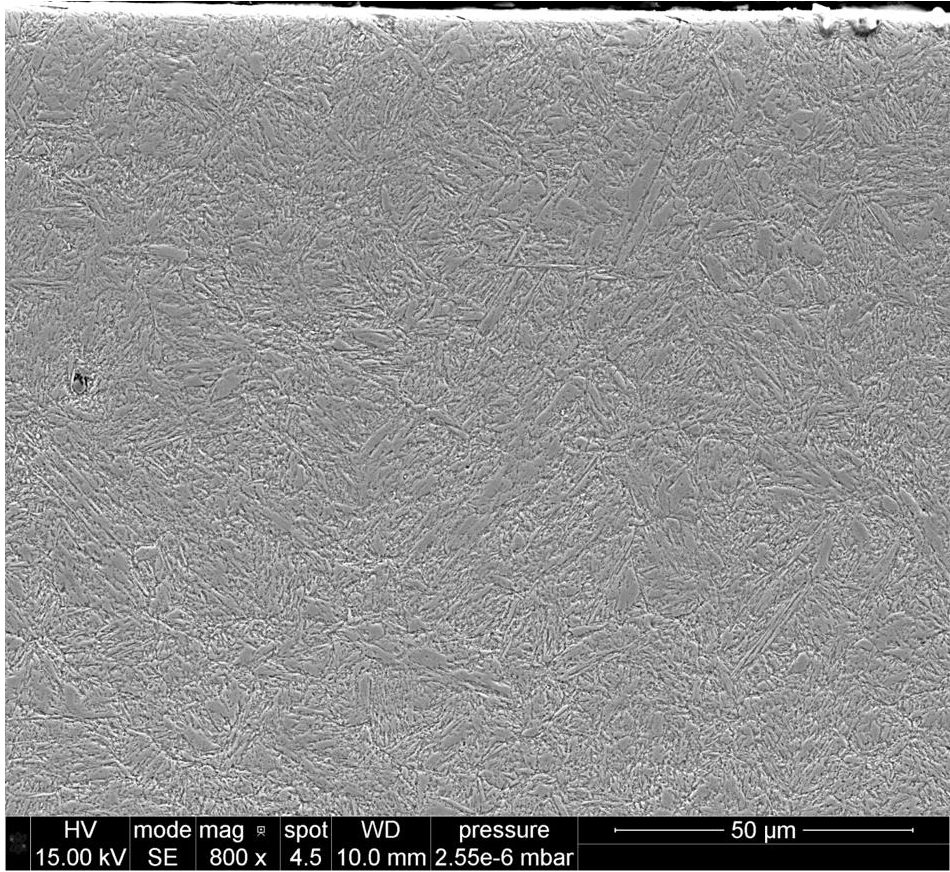
33	282	135	-100	90	73.8	9.1	-1.7	4.3
33	283	135	-110	0	66.6	11.1	-52	5.3
33	284	135	-110	90	75.6	6.3	1.5	3
33	285	135	-120	0	70	9.4	-48.2	4.5
33	286	135	-120	90	92.1	5.6	-1.4	2.7
33	287	135	-130	0	72.2	9.7	-52.6	4.6
33	288	135	-130	90	87.4	7.5	2.7	3.6
34	289	150	-80	0	37.6	10.3	-58.2	4.9
34	290	150	-80	90	-30.6	5.7	-6.4	2.7
34	291	150	-90	0	17.5	11.5	-58.3	5.5
34	292	150	-90	90	-26.9	7.2	0.4	3.5
34	293	150	-100	0	21.2	9.3	-58.5	4.5
34	294	150	-100	90	-7.8	6.7	-0.8	3.2
34	295	150	-110	0	20.9	10.5	-56.1	5
34	296	150	-110	90	-8.6	4.5	-3.4	2.1
34	297	150	-120	0	31.6	10.3	-55.5	4.9
34	298	150	-120	90	-23.9	6	-5.3	2.9
34	299	150	-130	0	25.5	8.2	-54.1	3.9
34	300	150	-130	90	-42.8	4.4	-4.7	2.1
35	301	165	-80	0	46.9	10.6	-61	5.1
35	302	165	-80	90	-41.5	4.3	1.3	2.1
35	303	165	-90	0	37.3	13	-61.2	6.2
35	304	165	-90	90	-33.1	5.7	-5.9	2.7
35	305	165	-100	0	51.9	16.1	-64.8	7.7
35	306	165	-100	90	-29.6	6.1	-2.4	2.9
35	307	165	-110	0	41.9	15.1	-69.4	7.2
35	308	165	-110	90	-49.4	10.8	-7	5.1
35	309	165	-120	0	41.3	24.6	-68	11.8
35	310	165	-120	90	-31.4	5.9	-5.6	2.8
35	311	165	-130	0	44.9	9.5	-57.2	4.6
35	312	165	-130	90	-34.8	7.8	4.7	3.7
36	313	180	-80	0	115.1	17.5	-66.1	8.4
36	314	180	-80	90	89.8	9.4	-6	4.5
36	315	180	-90	0	136.2	16.2	-67	7.7
36	316	180	-90	90	95.5	5.5	-4.8	2.6
36	317	180	-100	0	104.3	18.7	-68.3	8.9
36	318	180	-100	90	99.6	8.1	1.9	3.9
36	319	180	-110	0	122.8	16	-63.5	7.6
36	320	180	-110	90	94.6	8.1	-3.5	3.9
36	321	180	-120	0	119.8	15.1	-67.1	7.2
36	322	180	-120	90	106.1	7.7	-7.7	3.7
36	323	180	-130	0	120.6	17.5	-64.9	8.4
36	324	180	-130	90	94.3	5.7	-0.8	2.8
37	325	195	-80	0	81.2	16.3	-64.6	7.8

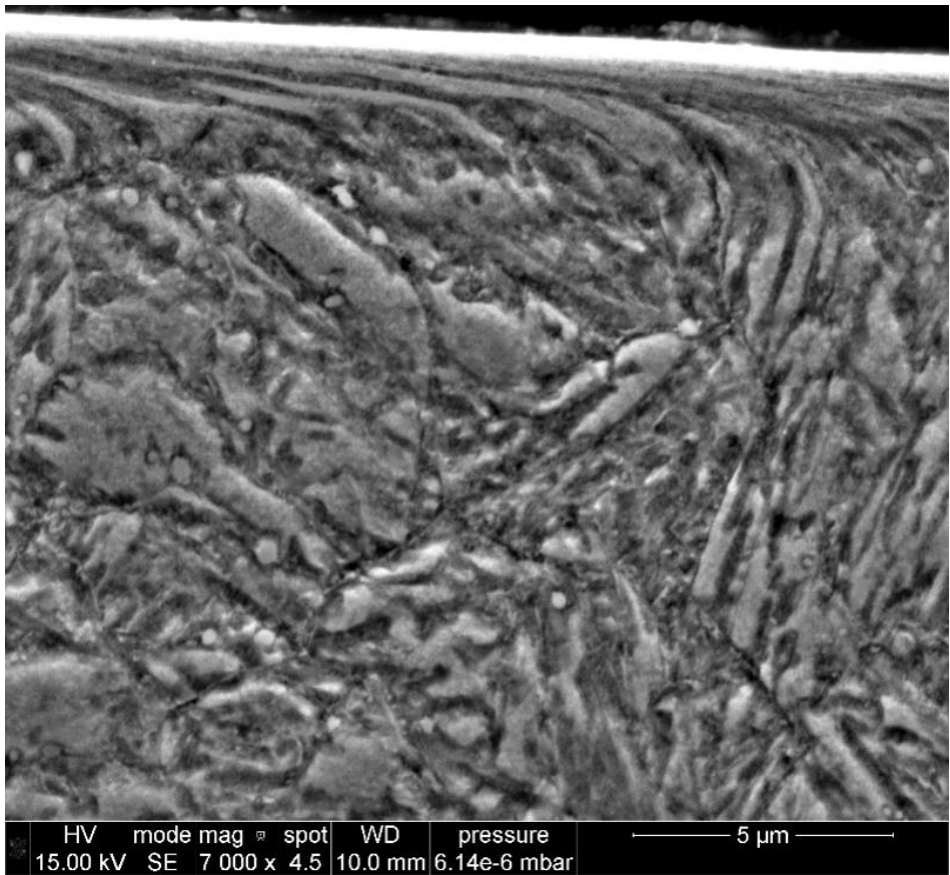
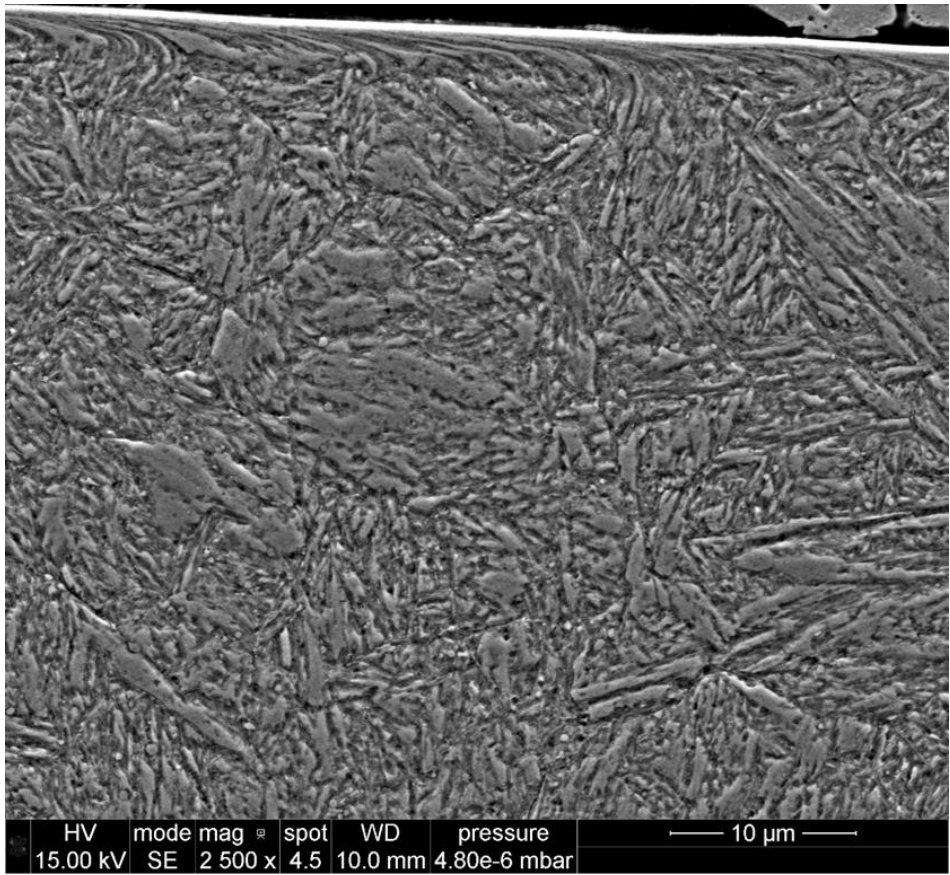
37	326	195	-80	90	139	6.3	1.7	3
37	327	195	-90	0	79.4	11.4	-59.6	5.5
37	328	195	-90	90	152.2	6	0.2	2.9
37	329	195	-100	0	66.5	11.3	-62.2	5.4
37	330	195	-100	90	142.7	8.1	-0.8	3.9
37	331	195	-110	0	73.1	12.5	-64.2	6
37	332	195	-110	90	144.6	8.4	-2.7	4
37	333	195	-120	0	66.7	14.5	-63.3	7
37	334	195	-120	90	132.9	6.6	1.8	3.2
37	335	195	-130	0	69.1	12.2	-62	5.8
37	336	195	-130	90	147.4	7.8	-3.8	3.7

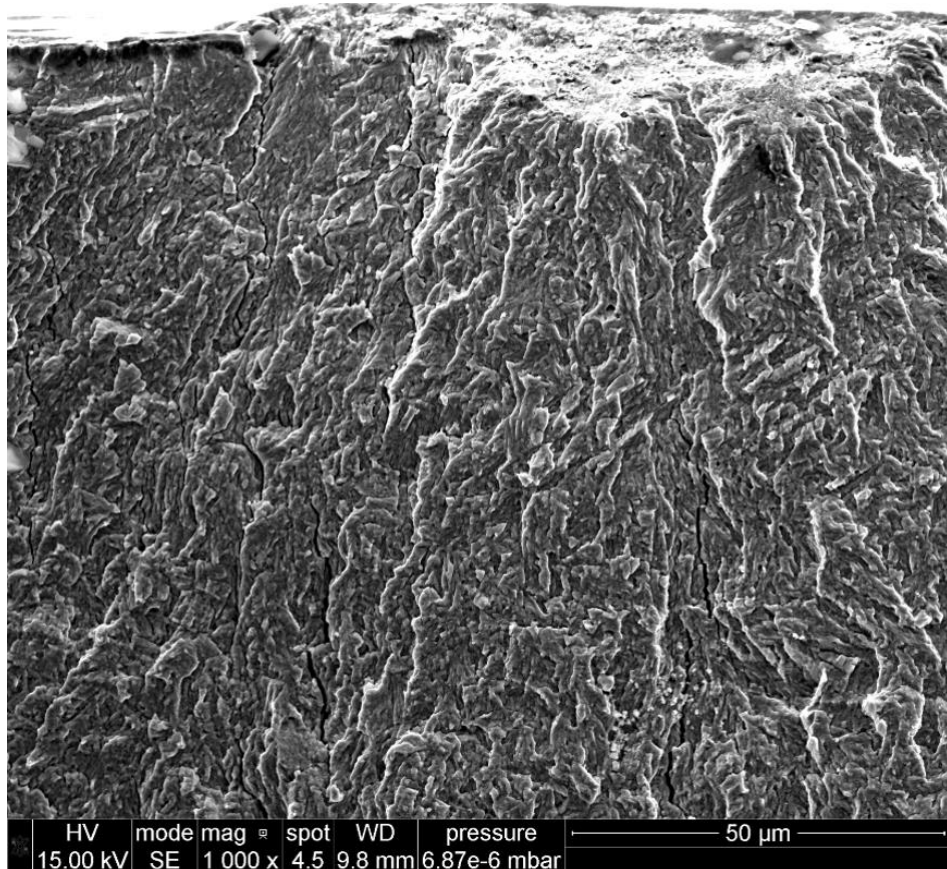
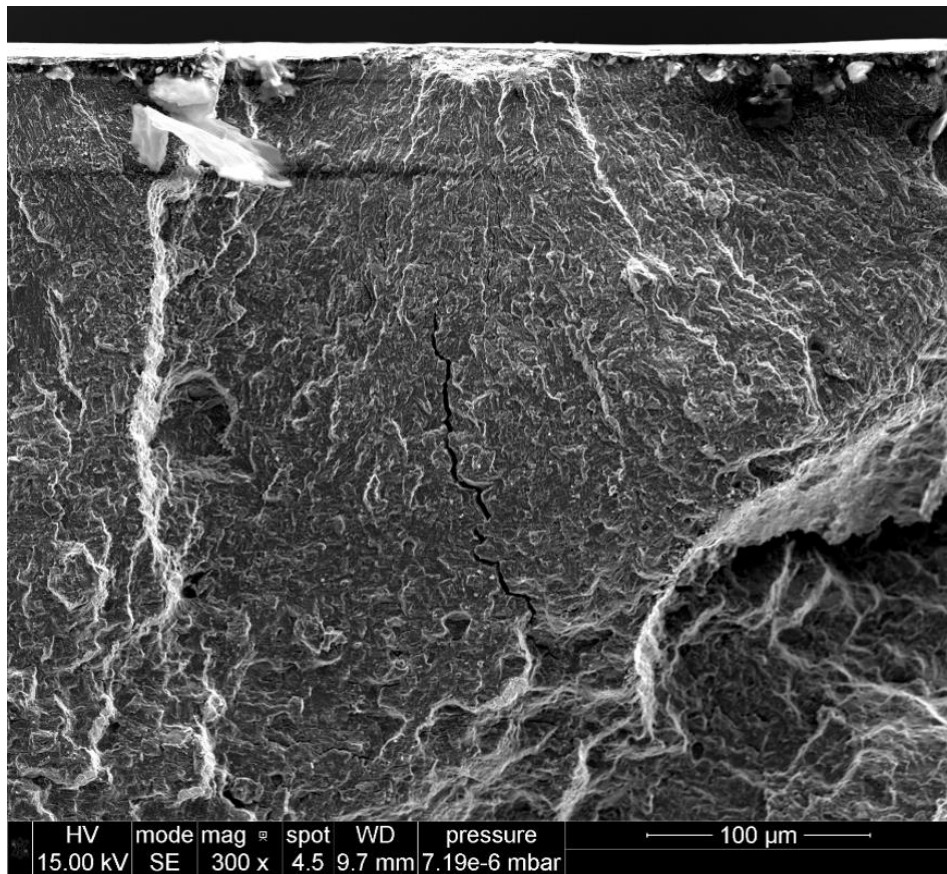
Appendix VI Underpinning Microstructure Data

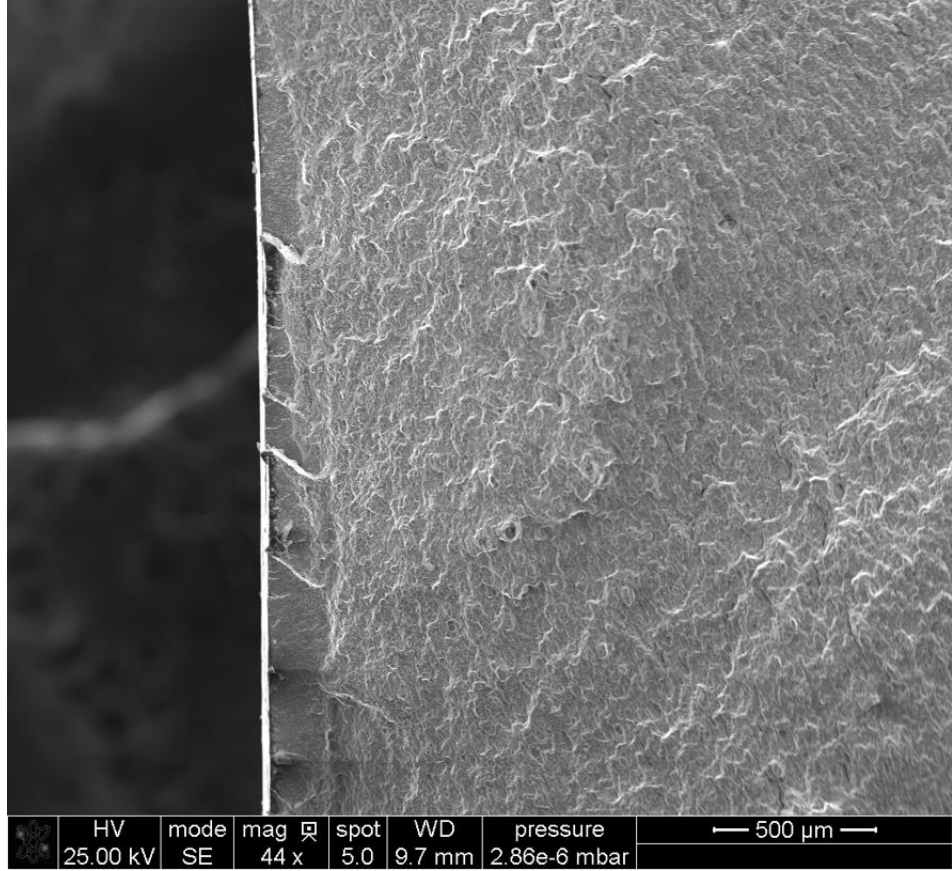
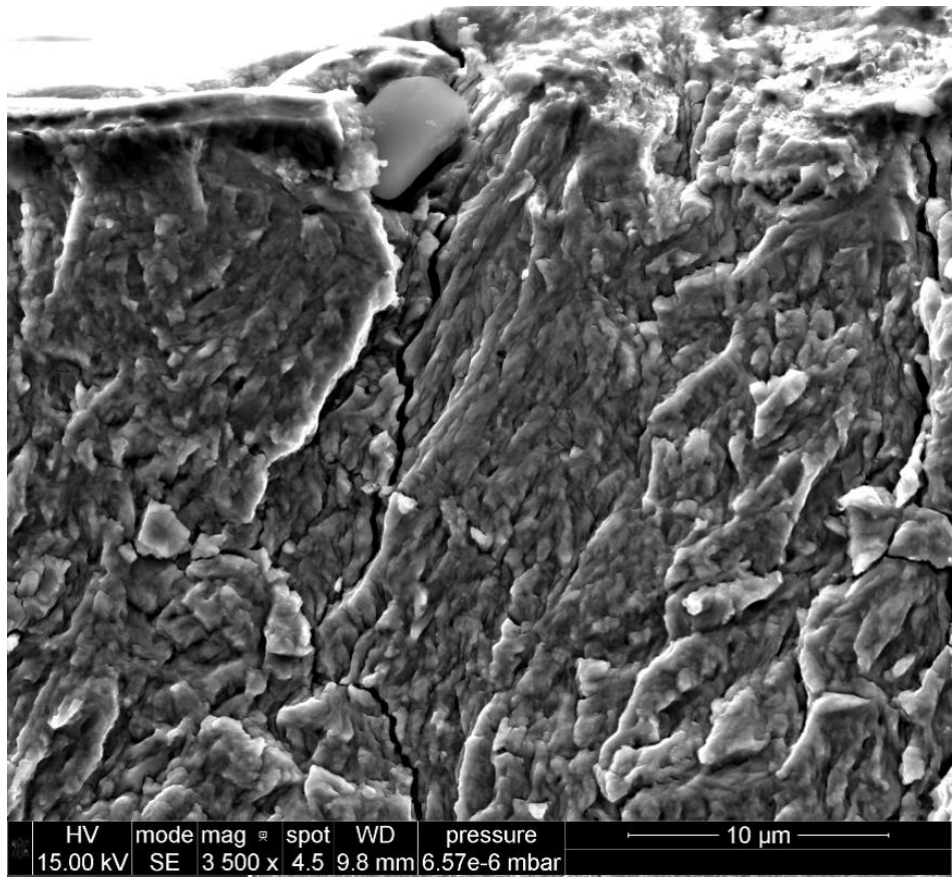


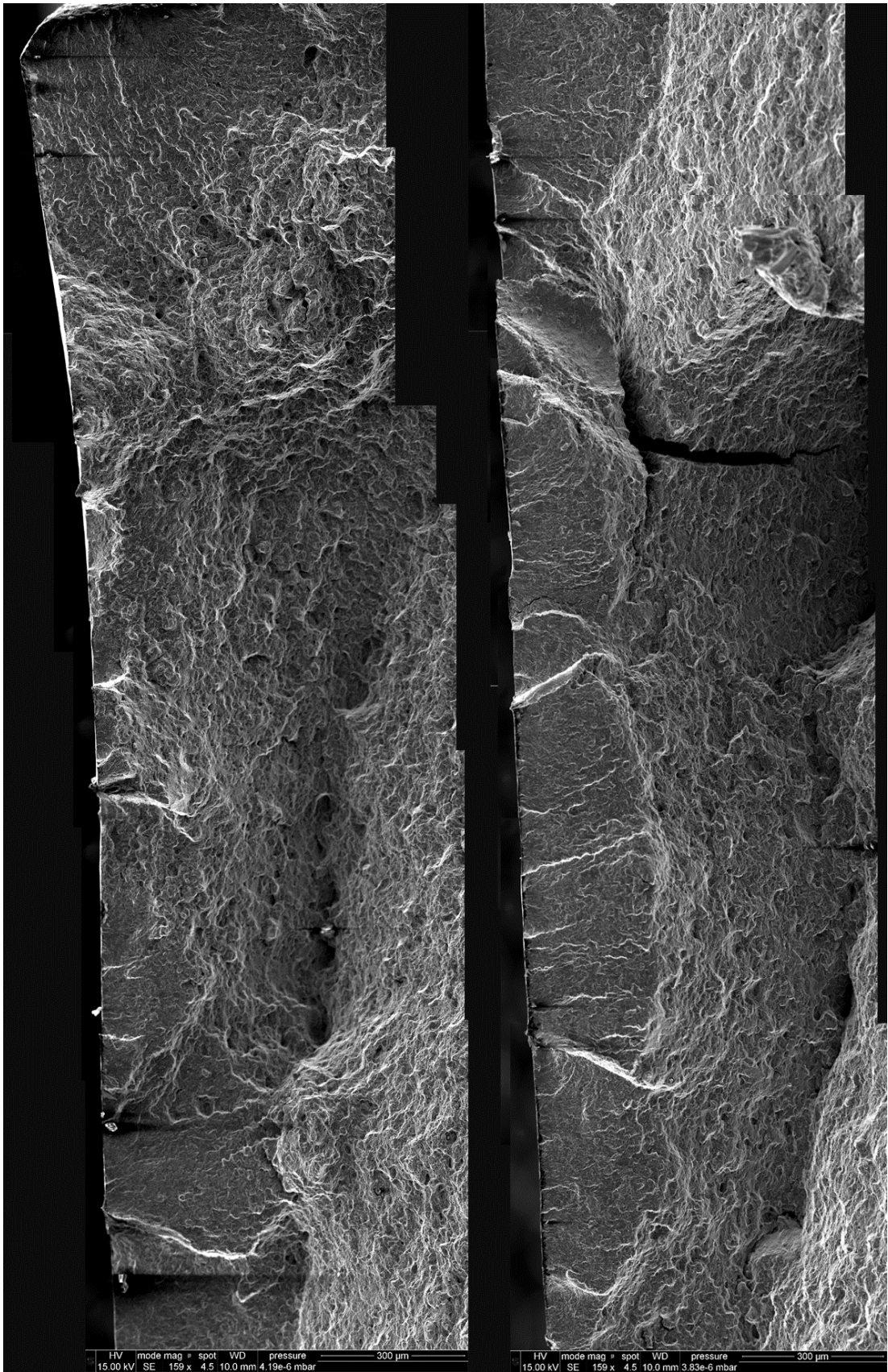


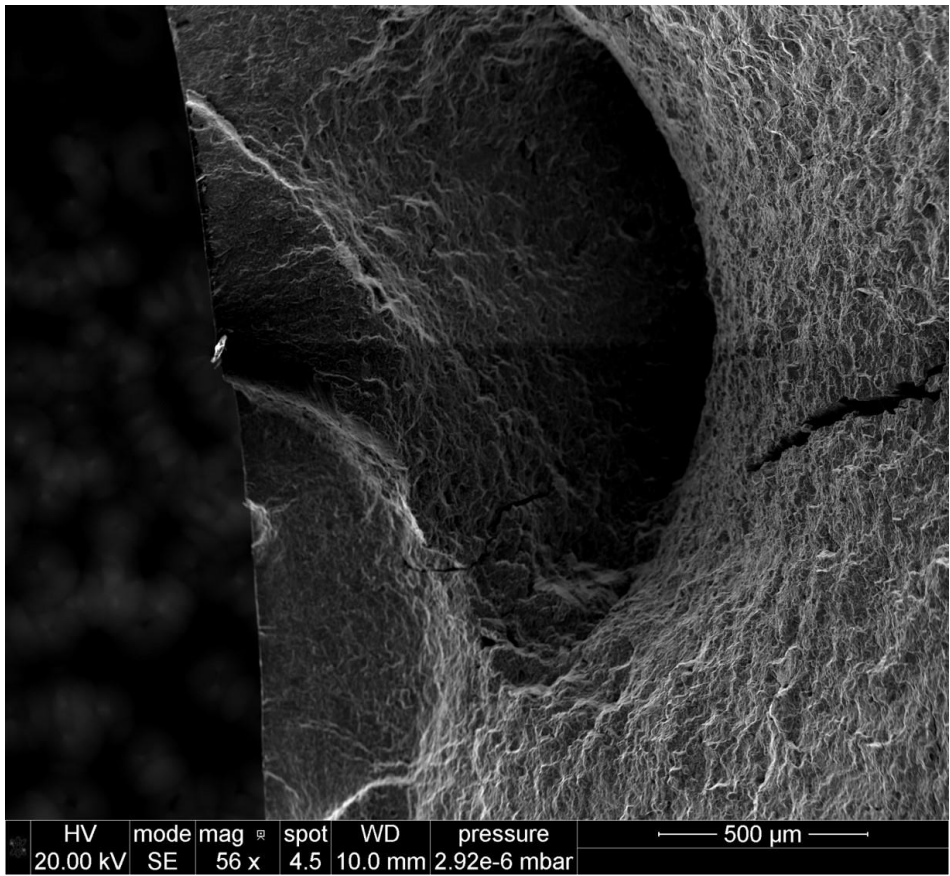
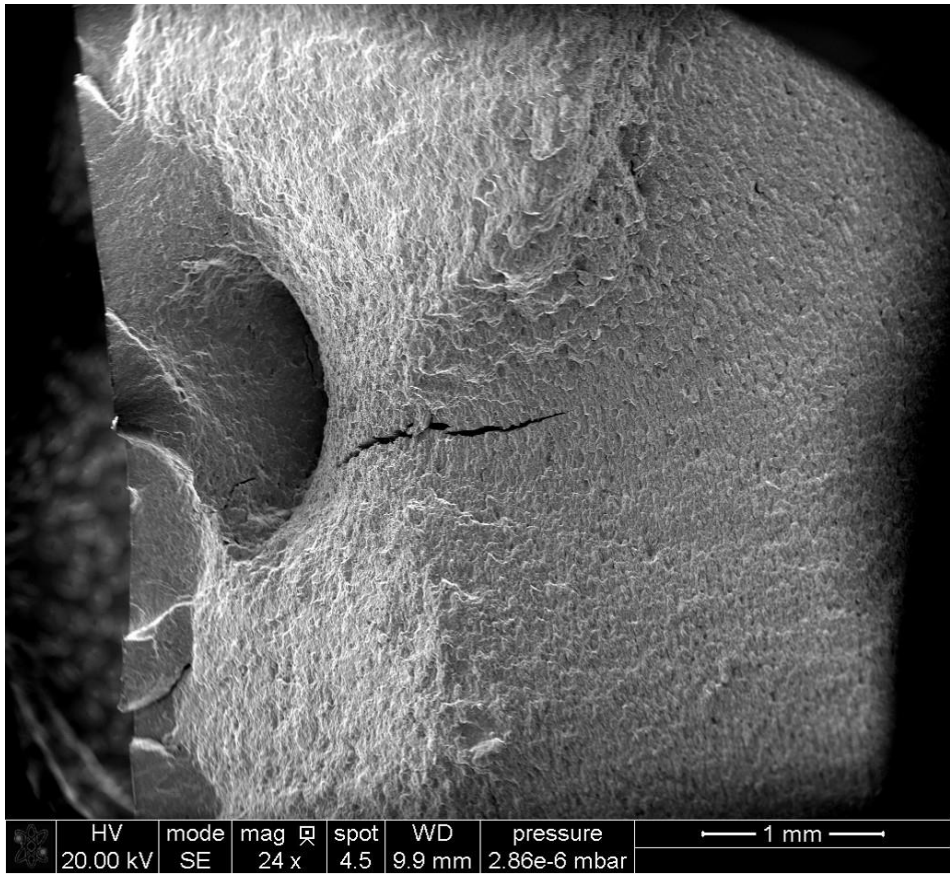


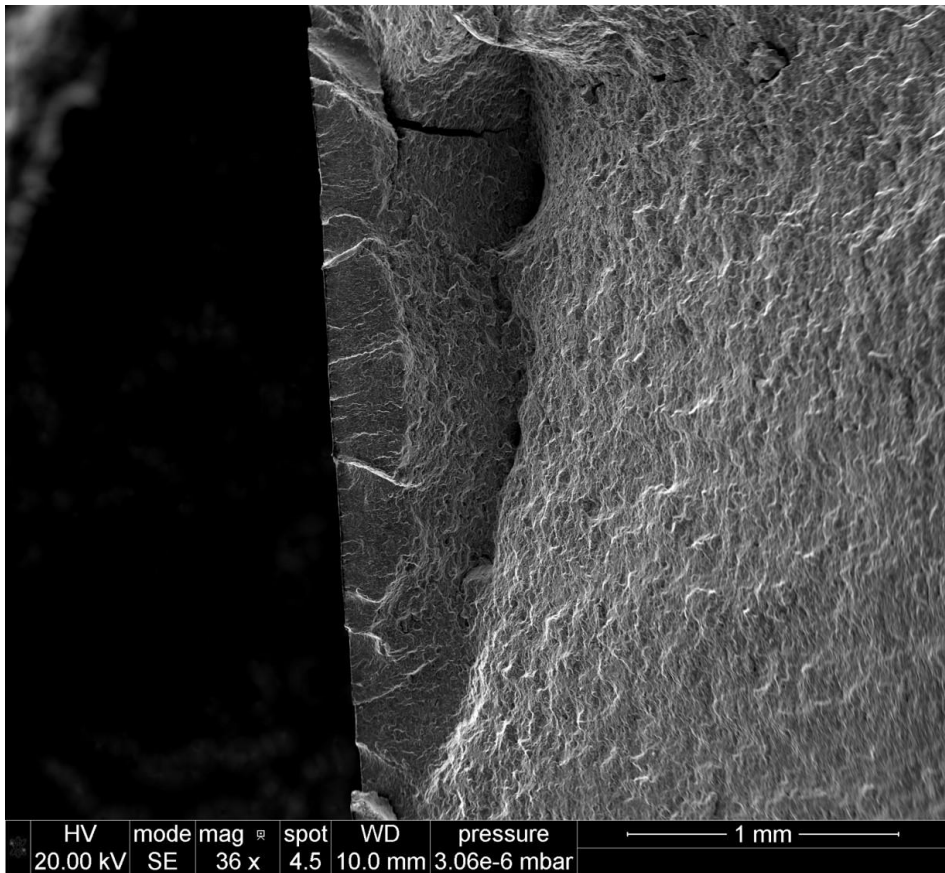
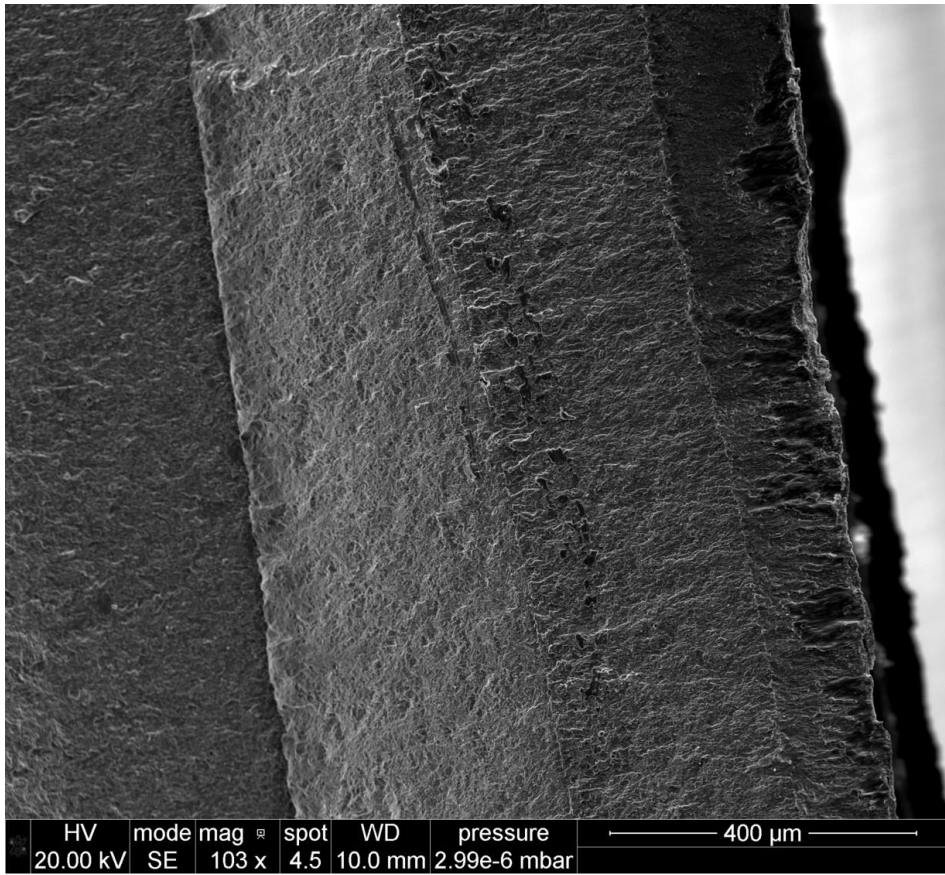


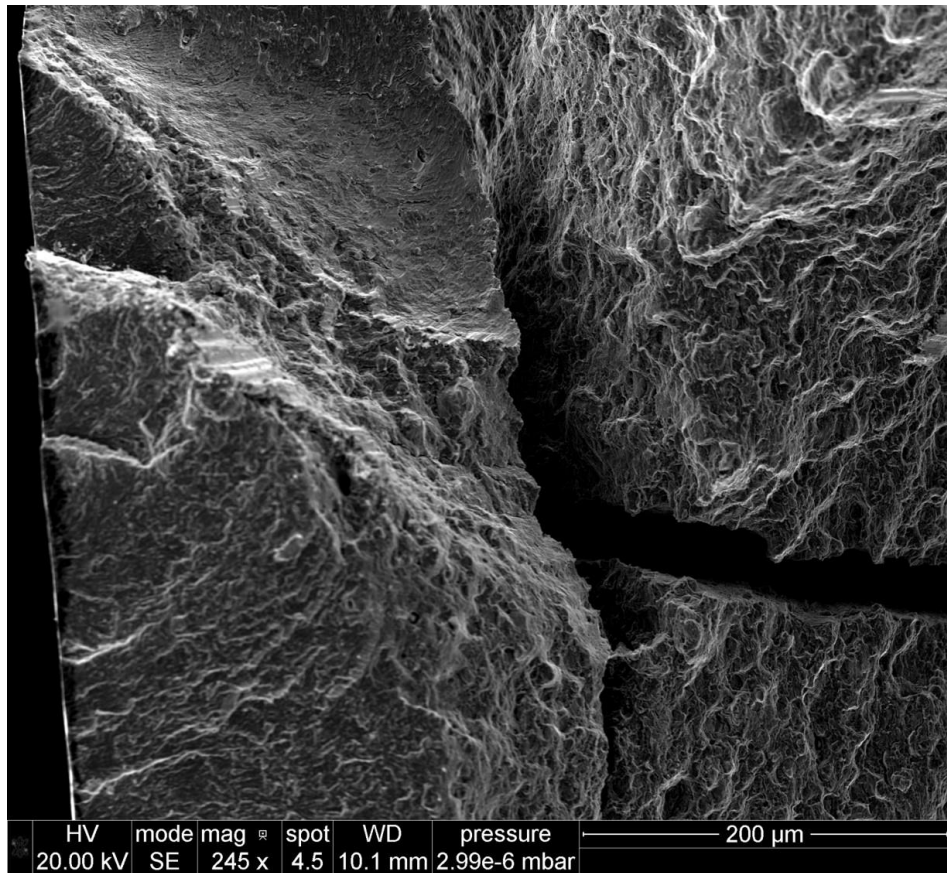
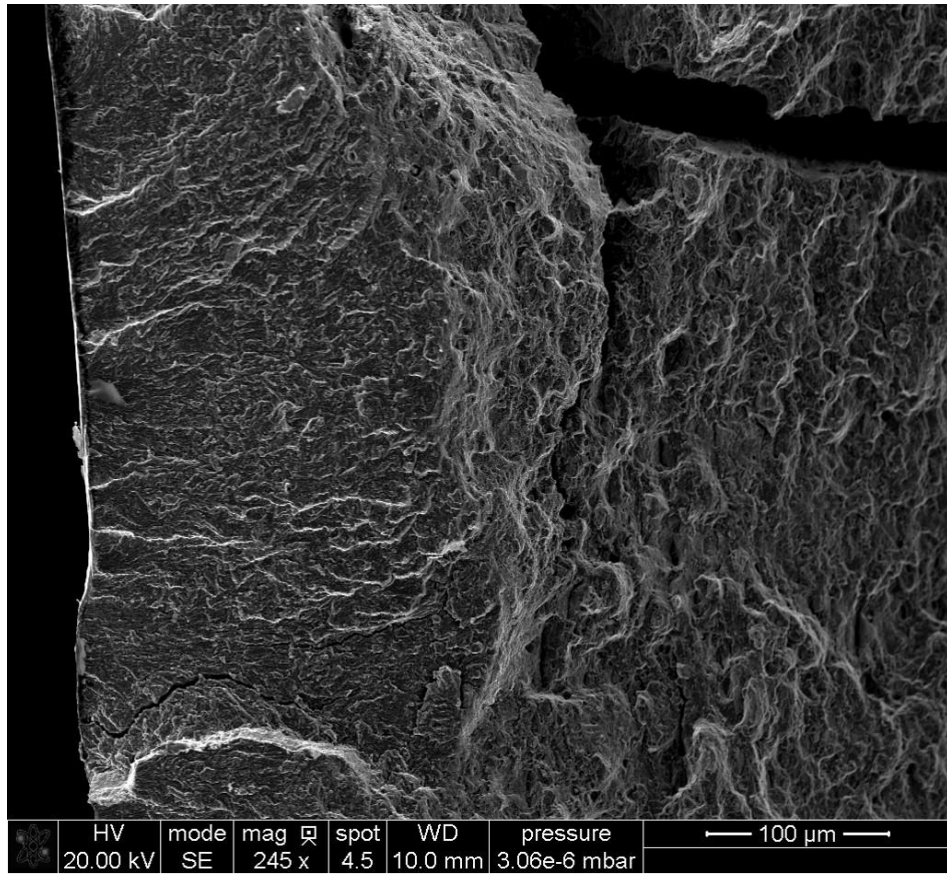


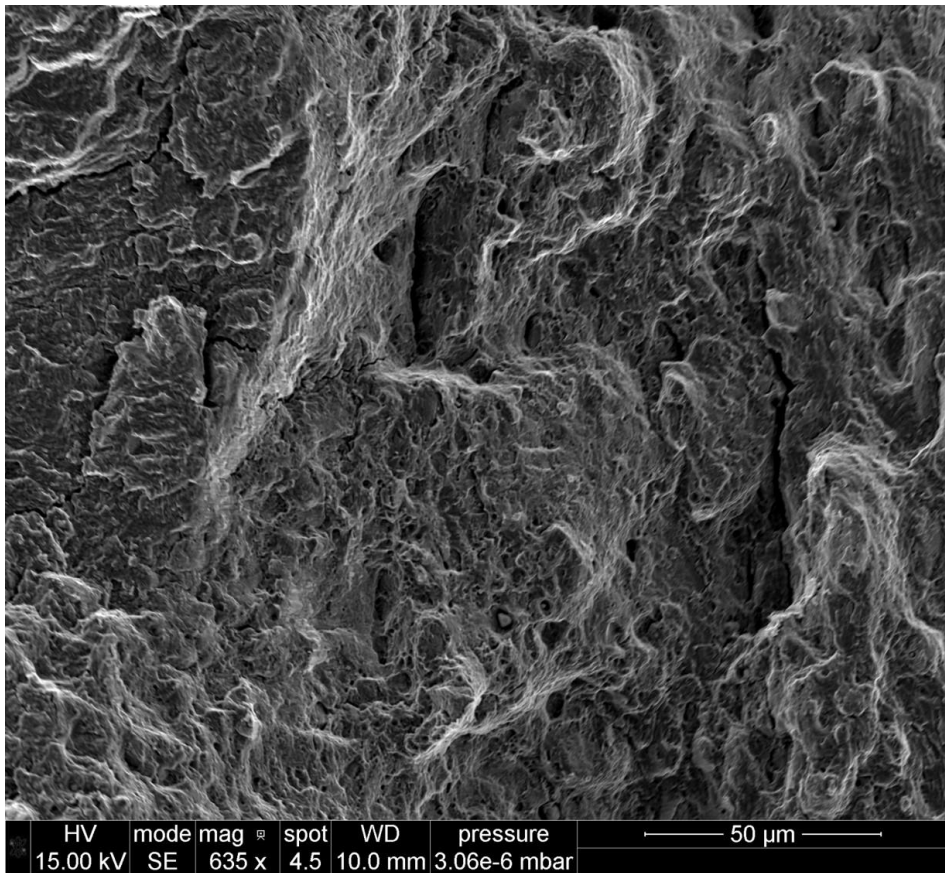
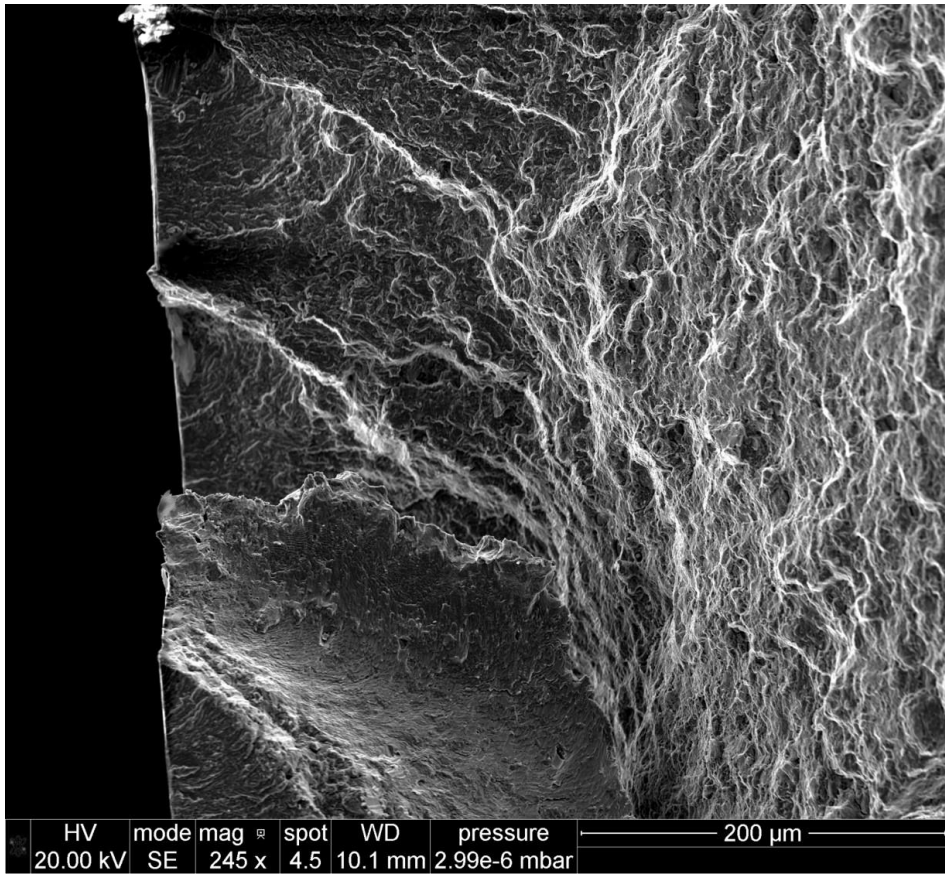


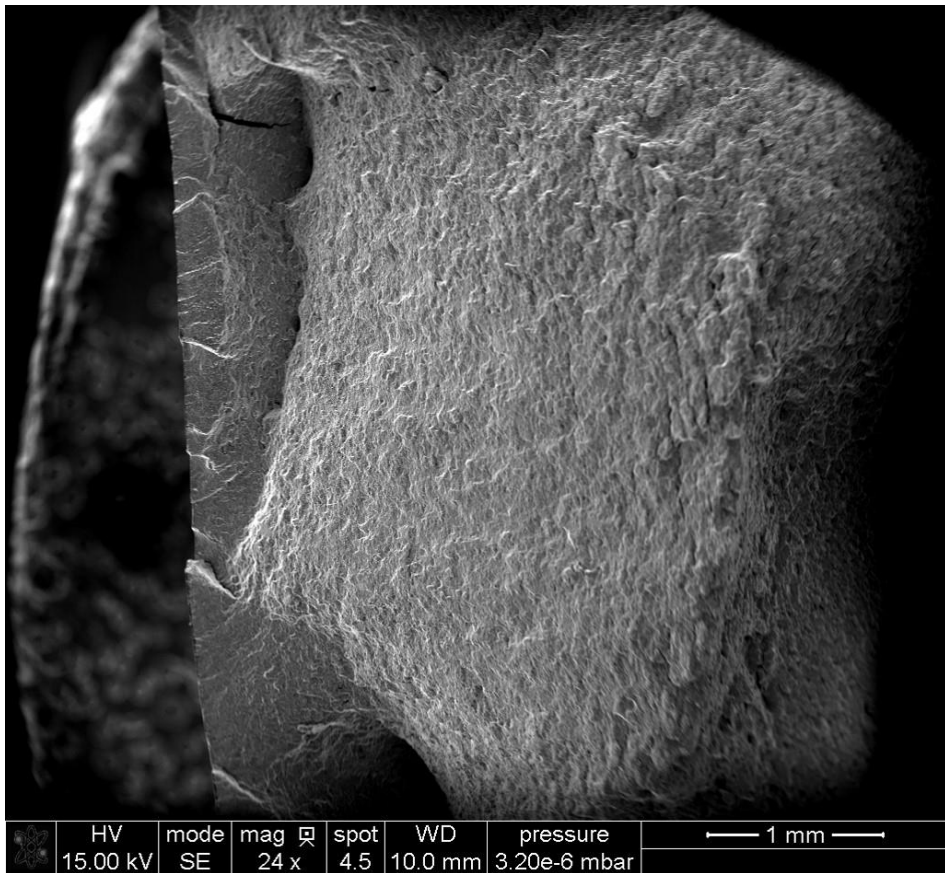
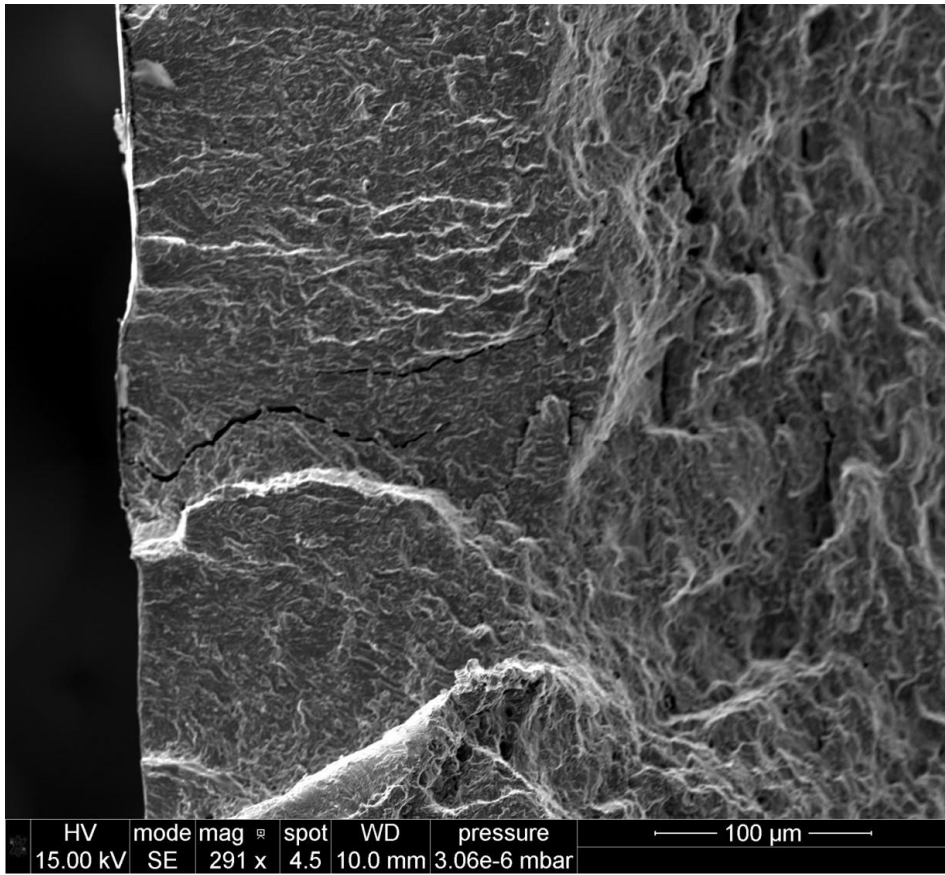


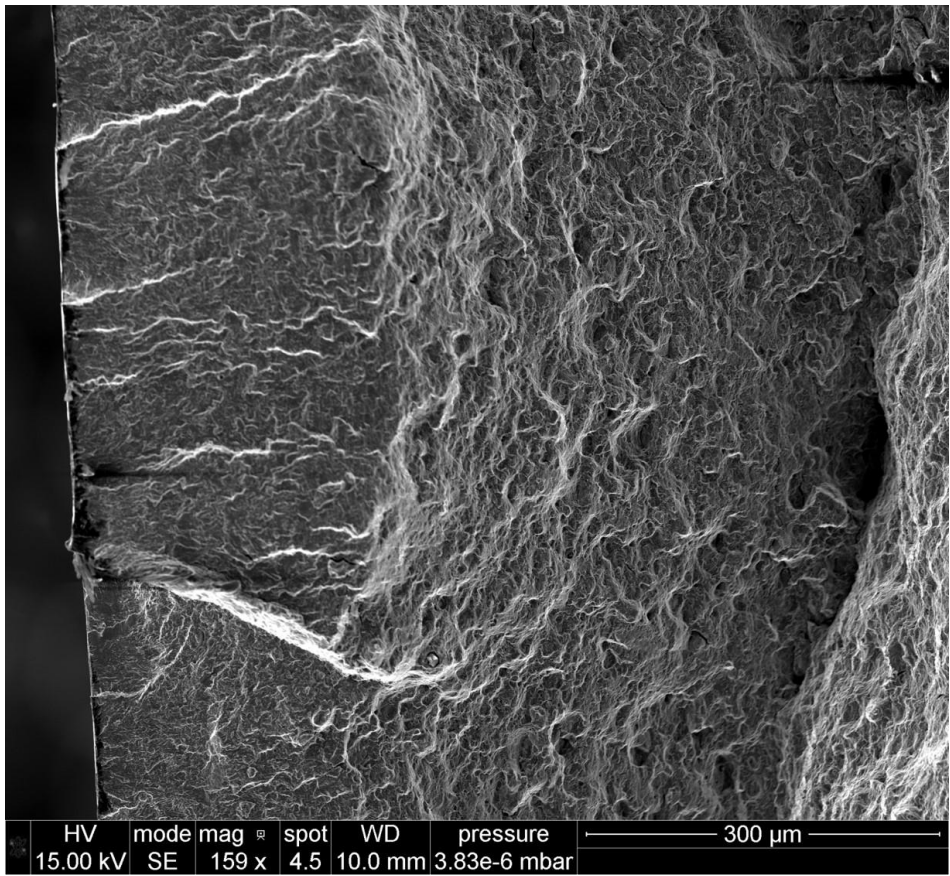
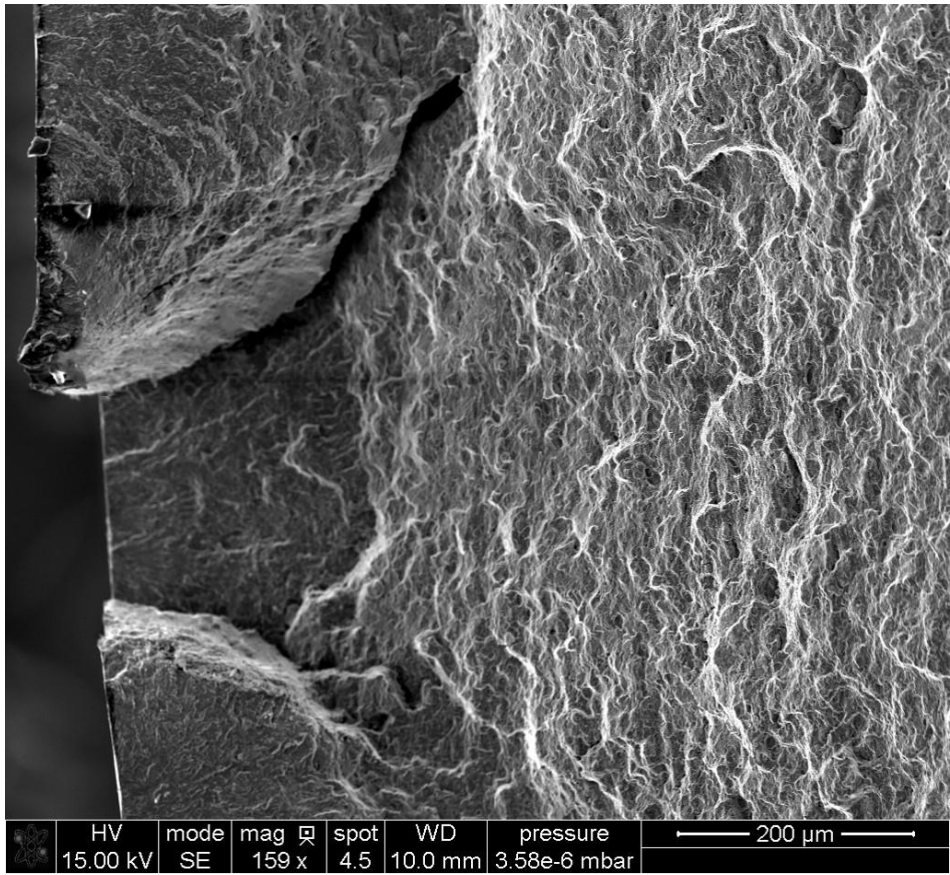


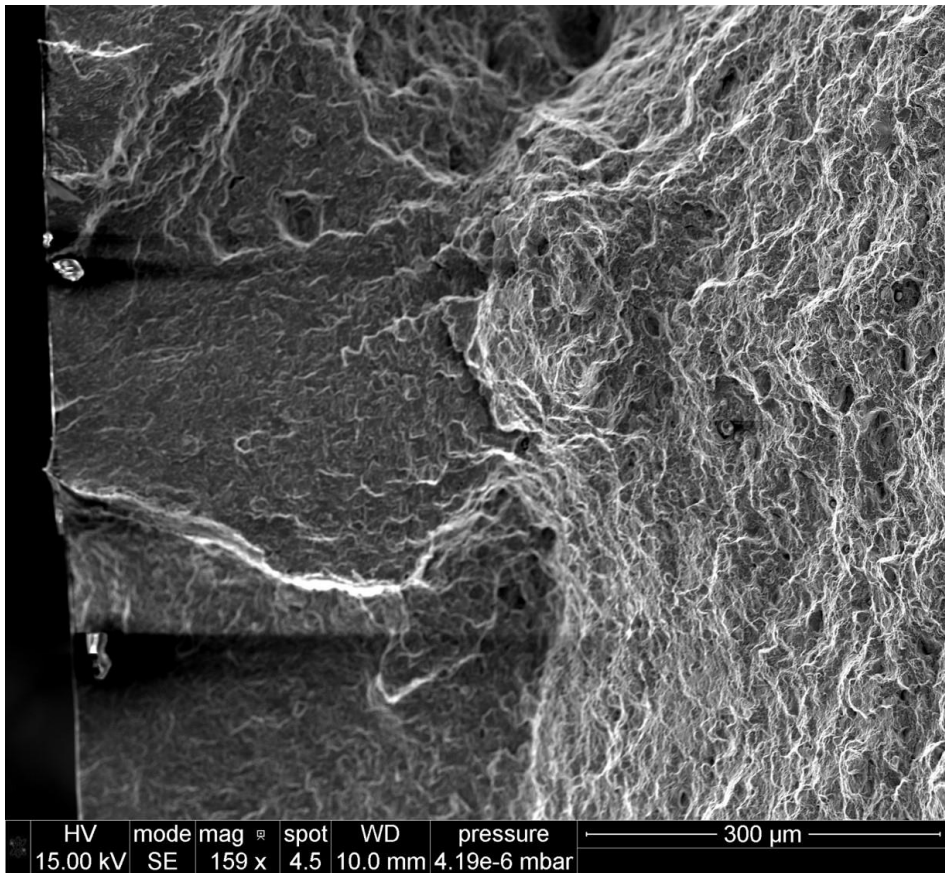
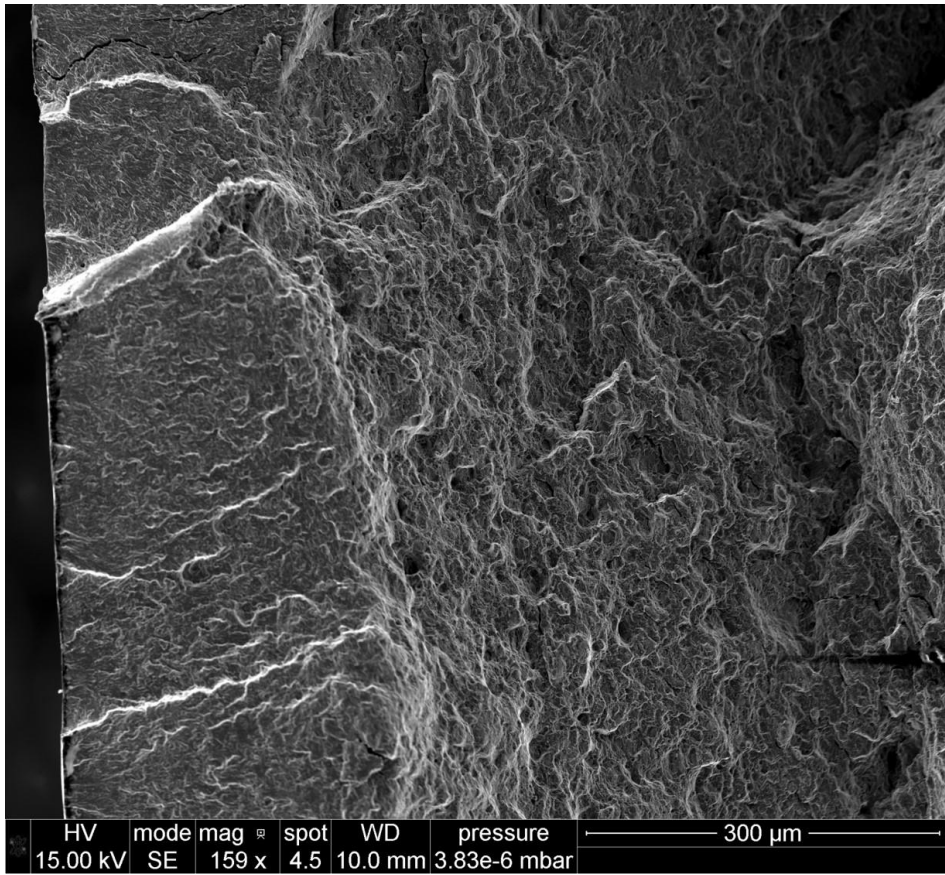


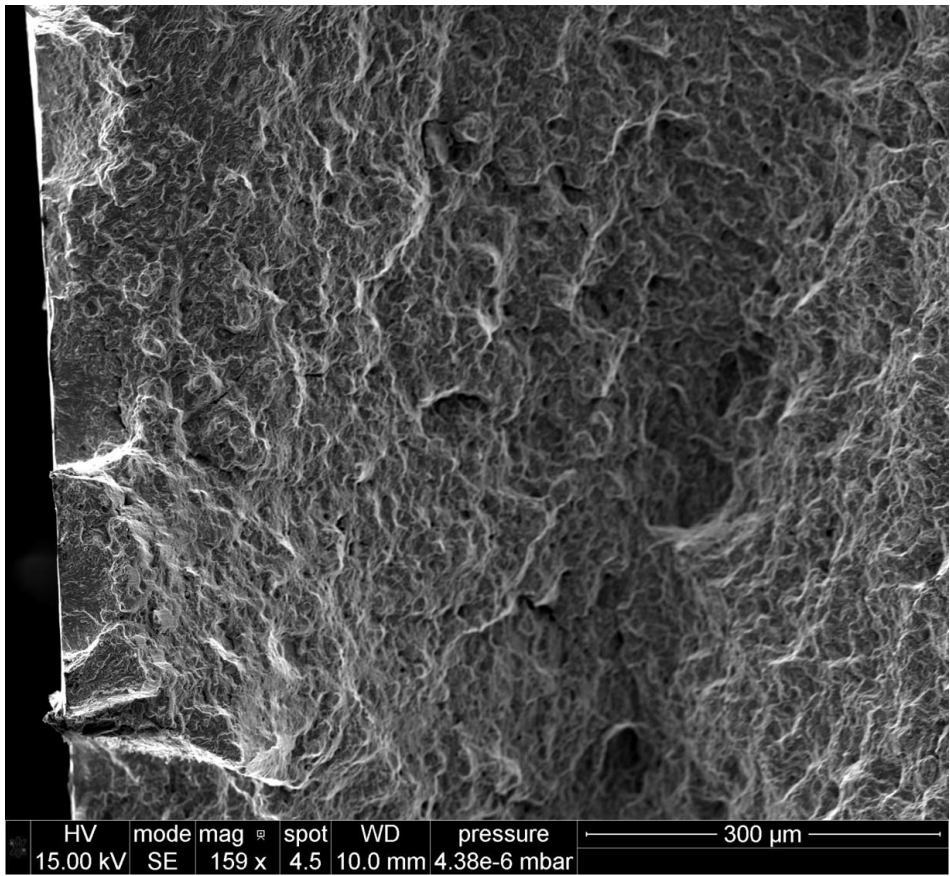
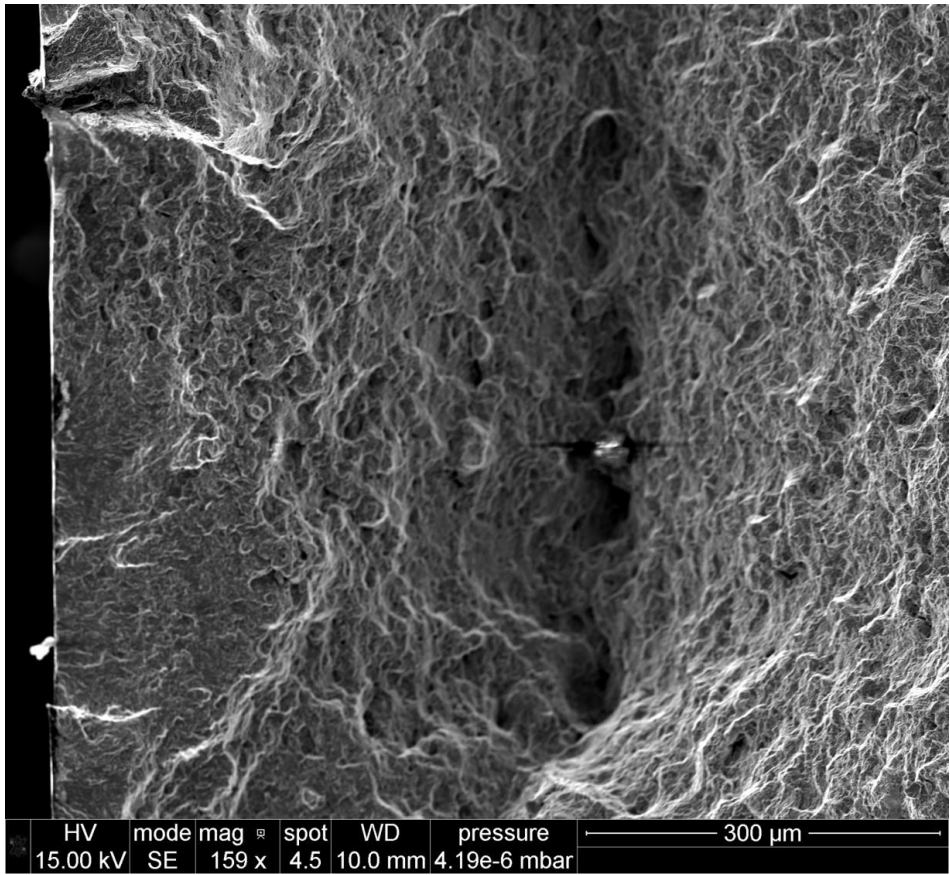


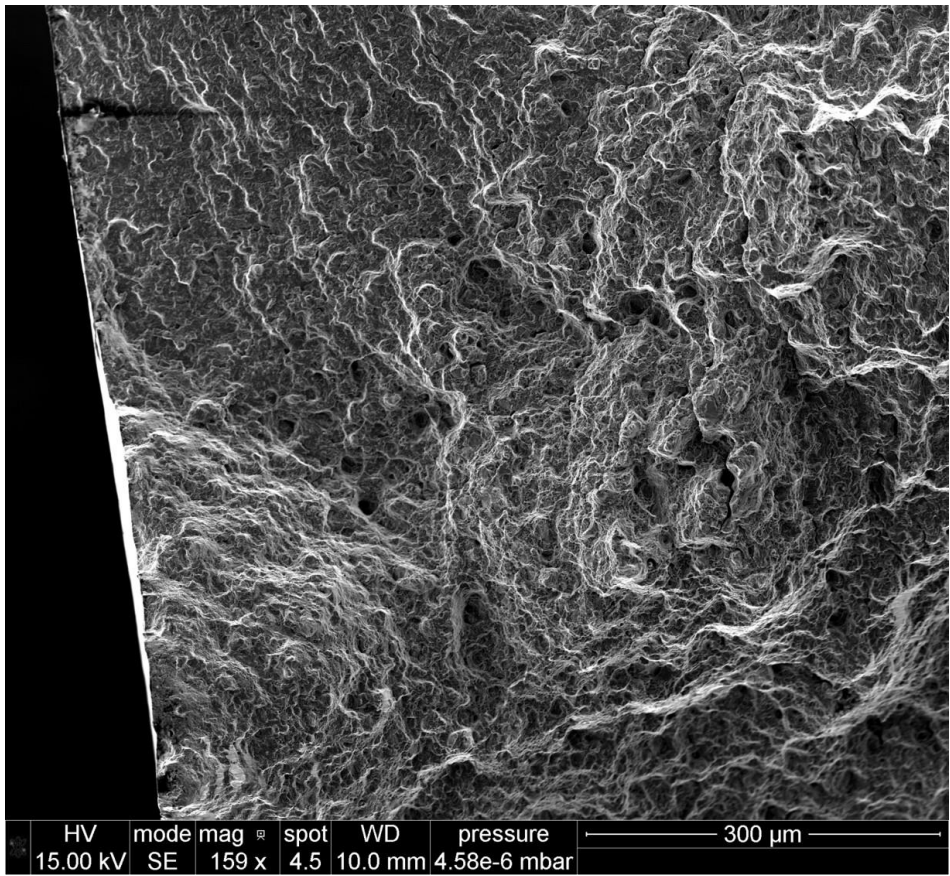
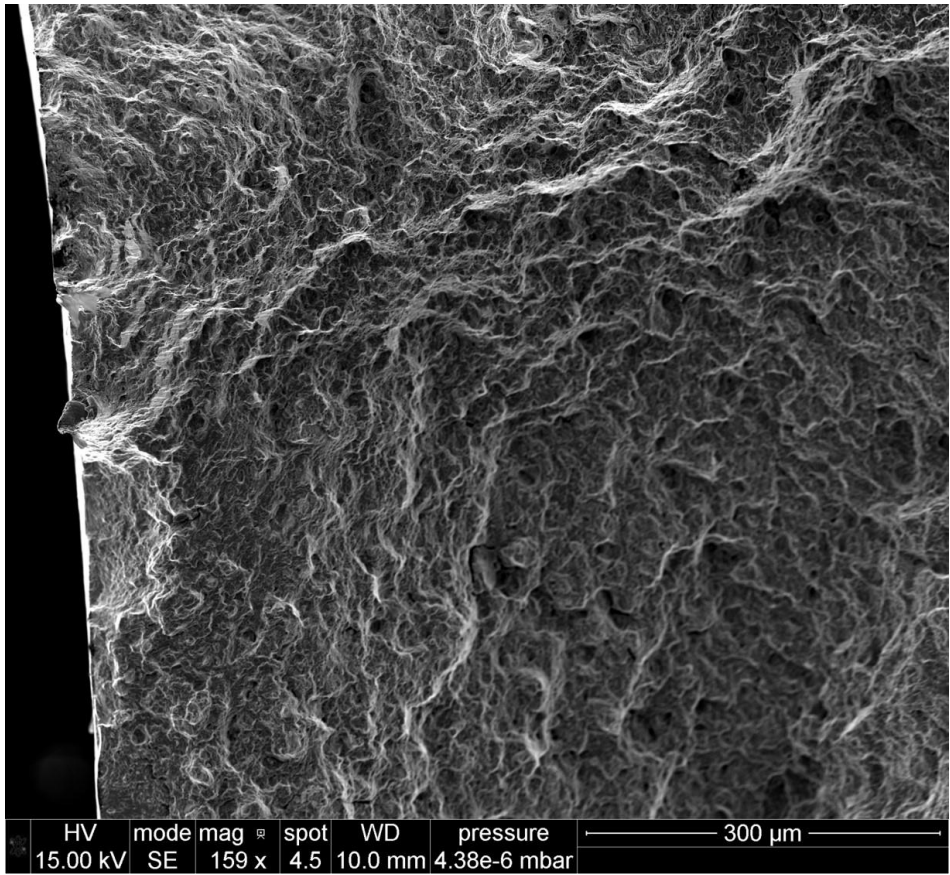


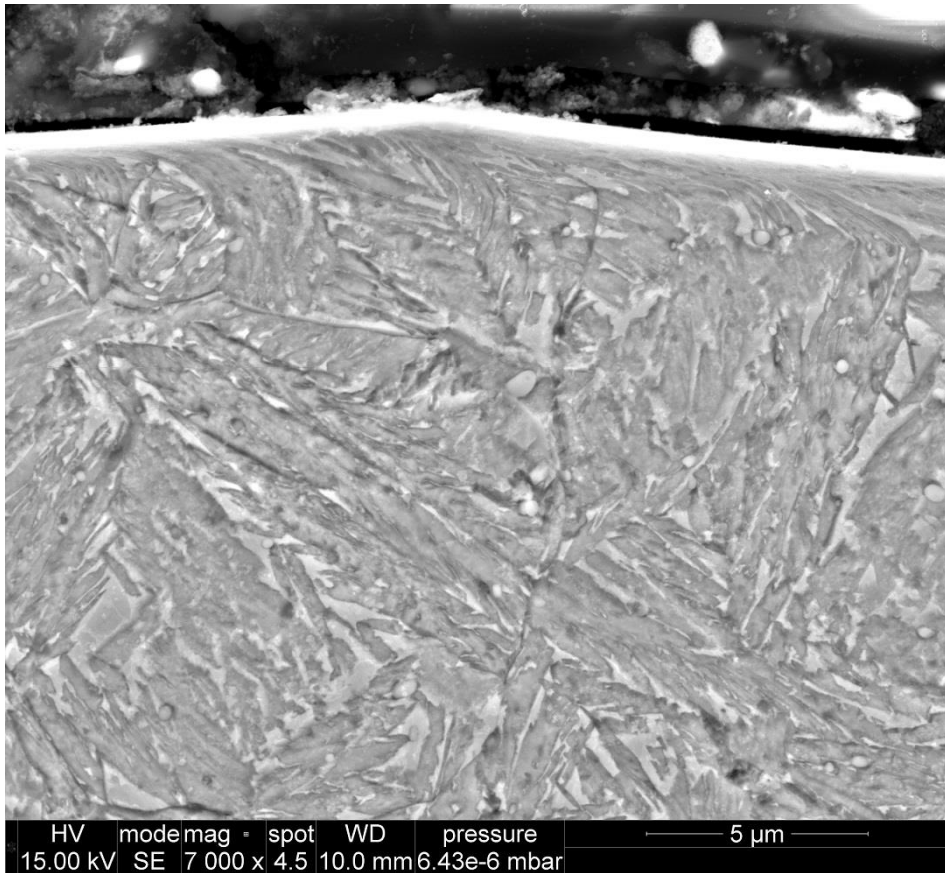
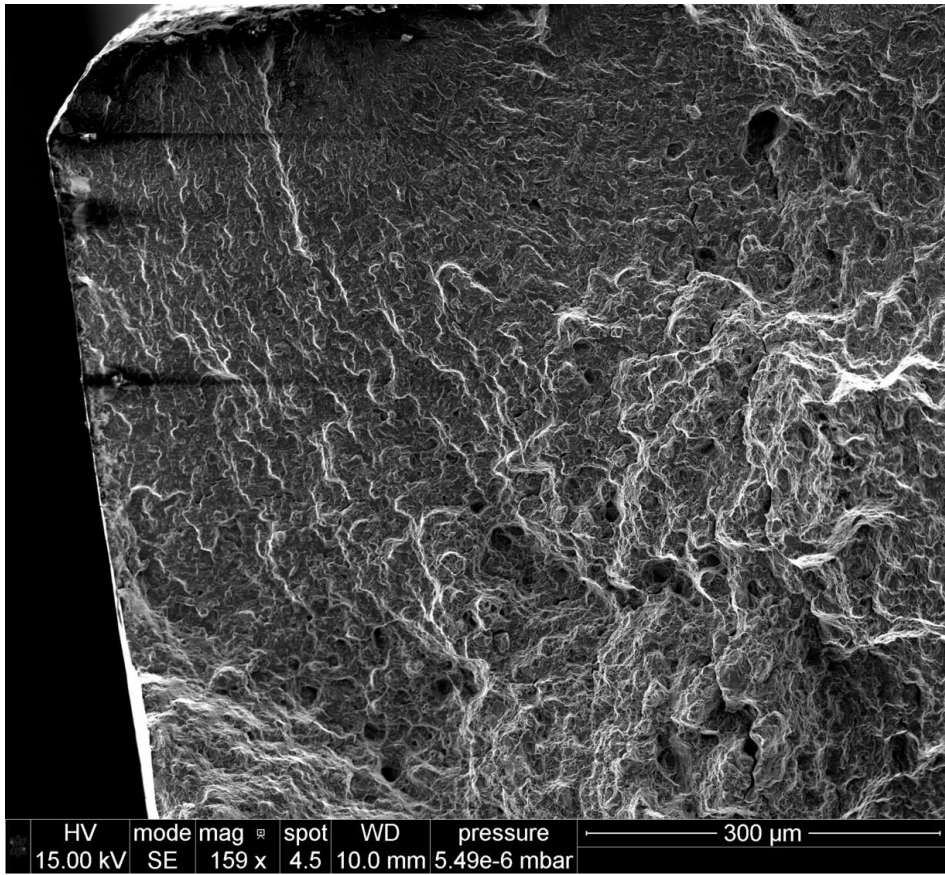


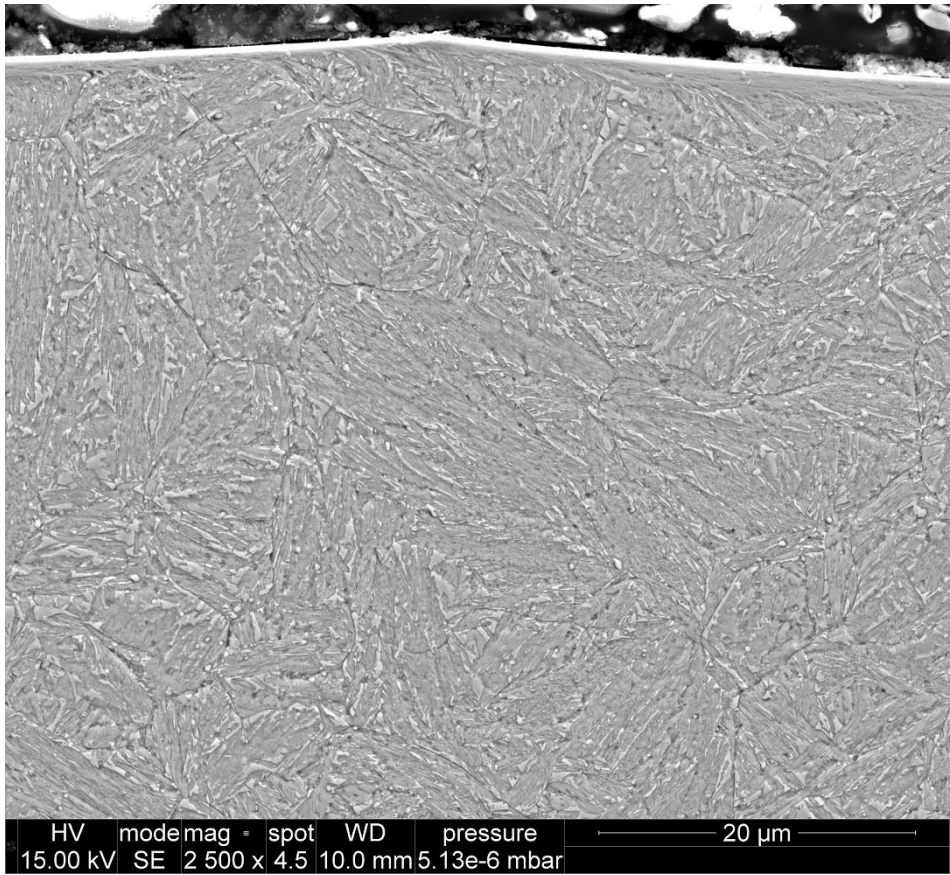












Appendix VII Subroutine

```
subroutine vuhard(
C Read only -
* nblock,
* nElement, nIntPt, nLayer, nSecPt,
* lAnneal, stepTime, totalTime, dt, cmname,
* nstatev, nfieldv, nprops,
* props, tempOld, tempNew, fieldOld, fieldNew,
* stateOld,
* eqps, eqpsRate,
C Write only -
* yield, dyieldDtemp, dyieldDeqps,
* stateNew )
C
include 'vaba_param.inc'
C
dimension nElement(nblock),
* props(nprops),
* tempOld(nblock),
* tempNew(nblock),
* fieldOld(nblock,nfieldv),
* fieldNew(nblock,nfieldv),
* stateOld(nblock,nstatev),
* eqps(nblock),
* eqpsRate(nblock),
* yield(nblock),
* dyieldDtemp(nblock),
* dyieldDeqps(nblock,2),
* stateNew(nblock,nstatev),
* stepTime(nblock),
* totalTime(nblock),
* dt(nblock),
* nIntPt(nblock),
* deleteflag(nblock)
C
character*80 cmname
double precision Trt,Tm,T0,A,B,C,D,E,F,G,U1,U2,U3,U4
double precision
F1,F2,F3,F4,G1,G2,G3,G4,C1,C2,C3,uttemp,uttempmax
double precision small,cT,dHC,HRC,dHRC,SRmin,SRmax
double precision nexpn,mexpn,strain,ut,utprops,Smin,Smax
double precision epR,epR0,lgRatio,HRCr,HRCu,CDV
logical, save :: isFileOpen = .FALSE.
parameter(one=1.0d00,two=2.0d00,three=3.0d00,zero=0.0d00)
Character (LEN=*), Parameter :: wt0='TRUE',wt1='FALSE'
Character*10 datetime(3),date,time,wt
integer date_time(8)
real k
C
C ##### PARAMETER DEFINITION
#####
C
C Element deletion is defined in StateVariable No. 6
C
C Define output textfile location - please create the file before
running subroutine
CHARACTER (LEN=*), PARAMETER :: path='C:\SIMULIA\Temp\0put.txt'
C activate or deactivate textfile output to .true. or .false.
```

```

    logical, save :: output = .true.
c activate or deactivate test mode (simplified JC)
    logical, save :: testmode = .false.
C Static values for ultimate tensile
    logical, save :: SV = .false.
C
C Factor values (absolute only)
    HRC    = 45.0d00
    cT     = 950.0d00
    C1     = 0.0947d00
    C2     = 10.8917d00
    C3     = 360.681d00
    F1     = 0.00283d00
    F2     = 0.49998d00
    F3     = 4.79458d00
    F4     = 570.104d00
    G1     = 0.0001d00
    G2     = 0.1875d00
    G3     = 10.6558d00
    G4     = 120.7277d00
    dHC    = 0.047049d00
C Factor values (not absolute)
    U1     = XXX
    U2     = XXX
    U3     = XXX
    U4     = XXX
    uttempmax = XXX
    small  = 1.0d-07
    SRmin  = 2.0d+04
    SRmax  = 8.0d+05
    Smin   = 0.9d00
    Smax   = 1.5d00
C Testmode variables
c
c Abaqus GUI-Variables
    Trt    = props(1)
    Tm     = props(2)
    A      = props(3)
    B      = props(4)
    C      = props(5)
    D      = props(6)
    E      = props(7)
    mexpn  = props(8)
    nexpn  = props(9)
    epR0   = props(10)
    utprops = props(11)
c
c ##### END OF PARAMETER DEFINITION #####
c
c Starting Calculation
    do 100 k=1, nblock
C
C initialising strain rate e. and e
    if(eqpsRate(k) .lt. SRmin) then
        epR = SRmin
    elseif(eqpsRate(k) .gt. SRmax) then
        epR = SRmax
    else
        epR = eqpsRate(k)

```



```

endif
C
if(eqps(k) .lt. Smin) then
    strain = Smin
elseif(eqps(k) .gt. Smax) then
    strain = Smax
else
    strain = eqps(k)
endif
C
C LOG ratio of strain rate
lgRatio = log(epR/epR0)
C
C Temperature calculation for JC
T0 = tempOld(k)
if(T0 .le. Trt) then
    T0 = Trt
    Tth = small
elseif(T0 .ge. Tm) then
    Tth=one
else
    Tth = (T0-Trt)/(Tm-Trt)
endif
C
C Hardness adjusting model depending on Temperature
HRCr = HRC
If (T0 .gt. cT) then
    dHRC = (dHC)*(T0-cT)
Else
    dHRC = zero
Endif
C
HRCu = HRC + dHRC
C
If (HRCu .gt. HRCr) then
    HRC = HRCu
Else
    HRC = HRCr
Endif
C
C Parameter C, M, F and G
if(.not. testmode) then
    F = -F1*HRC**three+F2*HRC**two-F3*HRC-F4
    G = -G1*HRC**three+G2*HRC**two-G3*HRC+G4
else
    D = one
    E = one
    F = zero
    G = zero
endif
C
C JC calculation
C
yield(k) = A+F+G*strain+B*strain**nexpn
yield(k) = yield(k) * (one+C*lgRatio) * (D-E*Tth**mexpn)
C
C derivation of yield with respect to temperature
C
dyieldDtemp(k) = (A+F+G*strain+B*strain**nexpn)

```

```

dyieldDtemp(k) = dyieldDtemp(k) * (one+C*lgRatio) * (-E*mexpn*Tth**
1      (mexpn-one)/(Tm-Trt))
c
c derivation of yield with respect to strain
c
dyieldDeqps(k,1) = G+nexpn*B*strain**(nexpn-one)
dyieldDeqps(k,1) = dyieldDeqps(k,1) * (one+C*lgRatio) *
1      (D-E*Tth**mexpn)
c
c derivation of yield with respect to strain rate
c
dyieldDeqps(k,2) = (A+F+G*strain+B*strain**nexpn)
dyieldDeqps(k,2) = dyieldDeqps(k,2) * C/epR * (D-E*Tth**mexpn)
c
c additional calculations
c   CDV = C1*HRC**two-C2*HRC+C3
c
c Element Deletion
c UT Tensile calculation depending on the temperature
  if (.not. SV) then
    if (T0 .ge. uttempmax) then
      uttemp = uttempmax
    elseif (T0 .le. Trt) then
      uttemp = Trt
    else
      uttemp = T0
    endif
    ut = (U1*uttemp**three)+(U2*uttemp**two)+(U3*uttemp)+U4
  else
    ut = utprops
  endif
c
  if (yield(k) .ge. ut) then
    deleteflag(k) = zero
  else
    deleteflag(k) = one
  endif
c
c ##### OUTPUT #####
c
stateNew(k,1) = yield(k)
stateNew(k,2) = dyieldDeqps(k,1)
stateNew(k,3) = dyieldDeqps(k,2)
stateNew(k,4) = dyieldDtemp(k)
stateNew(k,5) = HRC
stateNew(k,6) = deleteflag(k)
stateNew(k,7) = ut
c
c Check output file if parameter are given correctly to subroutine
  if((output.eq..true.).and.(.not.isFileOpen).and.((k.eq.one).or.
1  (k.eq.10.0d0))) then
    open(105,file=path,position='append')
    isFileOpen = .TRUE.
    if(.not. testmode) then
      wt = wt1
    else
      wt = wt0
    endif
    call date_and_time(datetime(1),datetime(2),datetime(3),date_time)

```

```

    date=datetime(1)
    time=datetime(2)
write(105,200)date,time,wt,stepTime(k),
* totalTime(k),dt(k),tempOld(k),lgRatio,T0,Tth,
* strain,epR,yield(k),dyieldDtemp(k),dyieldDeqps(k,1),
* dyieldDeqps(k,2),A,B,C,D,E,F,G,nexpn,mexpn,k
200 format('date: ',A,'time: ',A,/, 'Testmode = ',A,/,
& ' Steptime = ',E,/, 'Totaltime = ',E,/, 'dt = ',F8.5,/,
& ' TempOld = ', F8.4,/, 'lgRatio = ', F8.4,/,
& ' T0 = ', F8.4,/, 'Tth = ', E,/,
& ' Eqps = ', E,/, 'EqpsRate = ', E,/,
& ' yield = ', E,/, 'dyieldDtemp = ', E,/,
& ' dyieldDeqps(k,1) = ', E,/, 'dyieldDeqps(k,2) = ', E,/,
& ' A = ', E,/, ' B = ', E,/, ' C = ', E,/, ' D = ', F8.4,/,
& ' E = ', F8.4,/, ' F = ', E,/, ' G = ', E,/,
& ' Exp N = ',F8.5,/, 'Exp M = ',F8.5,/, 'k = ',F5.1,/,
& '#####')
    close(105)
c    isFileOpen = .FALSE.
endif
C
C ##### Closing SUB - do not change! #####
100 end do
return
end
C ##### End of VUHARD #####

```

Appendix VII Script

Main.py

```
## Implementation of the working environment
from part import *
from material import *
from section import *
from assembly import *
from step import *
from interaction import *
from load import *
from mesh import *
from optimization import *
from job import *
from sketch import *
from visualization import *
from connectorBehavior import *
from odbAccess import *
import numpy, math, os
from variablesm import *
from simfunctions import *

# Files and Folder Pre-Check
checkdirs = [workdir, savepath, extractdir]
checkfiles = [tooldir, analysispath, totalan]
if not os.path.isfile(logf):
    with open(logf, 'w+') as f: f.write('\tTime\t\t\tDescription\n')
precheck(checkdirs, checkfiles)
os.chdir(workdir) # Move to workdir

#====Parameter
initialisation=====
=====
if (skipfn != 1): cv = 0
iter = 0
pil = math.pi
wp1 = wp0+ '-1'
tol = to0+ '-1'
wy_backup = wy #will be overwritten - need to restore later

if isinstance(minv, list) == True:
    velo = numpy.array(minv)
    velx = len(velo)
else: velo = numpy.linspace(minv, maxv, velx)
if isinstance(mind, list) == True:
    doci = numpy.array(mind)
    docx = len(doci)
else: doci = numpy.linspace(mind, maxd, docx)
if isinstance(minfr, list) == True:
    FR = numpy.array(minfr)
    frx = len(FR)
else: FR = numpy.linspace(minfr, maxfr, frx)
if isinstance(minl, list) == True:
    lead = numpy.array(minl)
    lax = len(lead)
else: lead = numpy.linspace(minl, maxl, lax)

#====
=====
for i in range(0, velx):
    for j in range(0, docx):
        for k in range(0, frx):
            for l in range(0, lax):
```

```

iter+=1
if ((iter <= skip) and (skipfn == 1)):
    with open(logf, 'a') as f: f.write('{}\tSimulation
No. {} skipped\n'.format(nowdate(),iter))
    continue
try:
    susp = velo[i]
    DOC = docl[j]
    FR1 = FR[k]
    LA = lead[l]

    susp1 = susp*1000          # Converting surface speed
from m/min in MM/MIN
    spin2 =
(susp1)/(2*pi*(TD/2)*math.sin(math.radians(LA+math.degrees(math.acos(((TD/
2)-DOC)/(TD/2)))))) # Spindle speed => results in REV/MIN
    spin1 = spin2/60          # Converting from rev/min
in REV/SEC
    vel2 = FR1*NF*spin2       # Workpiece moving velocity
(MM/MIN) - THIS IS NOT SURFACE SPEED!!!
    vel1 = vel2/60           # Converting from mm/min in
MM/SEC

    if iter < 10: add0 = '0'
    else: add0=''
    with open(logf, 'a') as f: f.write('{}\tSimulation
No. {} started\n'.format(nowdate(),iter))

    Model = str(add0) + str(iter) + '_' + na0 + '-' +
str(i) + '-' + str(j) + '-' + str(k) + '-' + str(l)
    Description = 'Velocity: ' + str(vel1) + 'mm/sec,
\nDoC: ' + str(DOC) + 'mm, \nSpindlespeed: ' + str(spin1) + 'rev/sec,
\nLead Angle: ' + str(LA) + 'deg, \nSimID: ' + str(add0) + str(iter)
    mdb.Model(modelType=STANDARD_EXPLICIT, name=Model,
description=Description)
    mod= mdb.models[Model]

    ## Import Tool ##
    mdb.openAcis(tooldir, scaleFromFile=OFF)
    mod.PartFromGeometryFile(combine=False,
dimensionality=THREE_D, geometryFile=mdb.acis, name=to0,
type=DEFORMABLE_BODY)
    mod.parts[to0].AutoRepair()
    mod.parts[to0].RemoveCells(cellList =
mod.parts[to0].cells[0:1])
    mod.parts[to0].regenerate()

    ## Create Workpiece ##
    if cuttype == 0:
        mod.ConstrainedSketch(name='__profile__',
sheetSize=50.0)

    mod.sketches['__profile__'].rectangle(point1=(0.0, 0.0), point2=(wx, wy))
    mod.Part(dimensionality=THREE_D, name=wp0,
type=DEFORMABLE_BODY)
    mod.parts[wp0].BaseSolidExtrude(depth=wz,
sketch=mod.sketches['__profile__'])
    del mod.sketches['__profile__']
    ## sectioning Workpiece ##
    sh1 = float((wy/2)-sh)
    wx2 = float((wx/2)-wd)

```

```

        wd1 = float(wd/2)
        # Height sectioning
        mod.ConstrainedSketch(gridSpacing=0.65,
name='__profile__', sheetSize=26.3,
transform=mod.parts[wp0].MakeSketchTransform(sketchPlane=mod.parts[wp0].fac
es[4], sketchPlaneSide=SIDE1, sketchUpEdge=mod.parts[wp0].edges[7],
sketchOrientation=RIGHT, origin=(wx/2, wy/2, wz))

mod.parts[wp0].projectReferencesOntoSketch(filter=COPLANAR_EDGES,
sketch=mod.sketches['__profile__'])
        mod.sketches['__profile__'].Line(point1=(-wx2,
sh1), point2=(wx2, sh1))

mod.sketches['__profile__'].HorizontalConstraint(addUndoState=False,
entity=mod.sketches['__profile__'].geometry[6])

mod.sketches['__profile__'].PerpendicularConstraint(addUndoState=False,
entity1=mod.sketches['__profile__'].geometry[2],
entity2=mod.sketches['__profile__'].geometry[6])

mod.sketches['__profile__'].CoincidentConstraint(addUndoState=False,
entity1=mod.sketches['__profile__'].vertices[4],
entity2=mod.sketches['__profile__'].geometry[2])

mod.sketches['__profile__'].CoincidentConstraint(addUndoState=False,
entity1=mod.sketches['__profile__'].vertices[5],
entity2=mod.sketches['__profile__'].geometry[4])

mod.parts[wp0].PartitionFaceBySketch(faces=mod.parts[wp0].faces.getSequence
FromMask(['#10'], ), ), sketch=mod.sketches['__profile__'],
sketchUpEdge=mod.parts[wp0].edges[7])
        del mod.sketches['__profile__']

mod.parts[wp0].PartitionCellBySweepEdge(cells=mod.parts[wp0].cells.getSeque
nceFromMask(['#1'], ), ), edges=(mod.parts[wp0].edges[0], ),
sweepPath=mod.parts[wp0].edges[9])
        # Width sectioning
        mod.ConstrainedSketch(gridSpacing=0.65,
name='__profile__', sheetSize=26.3,
transform=mod.parts[wp0].MakeSketchTransform(sketchPlane=mod.parts[wp0].fac
es[9], sketchPlaneSide=SIDE1, sketchUpEdge=mod.parts[wp0].edges[18],
sketchOrientation=RIGHT, origin=(wx/2, wy, wz/2))

mod.parts[wp0].projectReferencesOntoSketch(filter=COPLANAR_EDGES,
sketch=mod.sketches['__profile__'])
        mod.sketches['__profile__'].Line(point1=(-wx2,
wd1), point2=(-wx2, -wd1))

mod.sketches['__profile__'].VerticalConstraint(addUndoState=False,
entity=mod.sketches['__profile__'].geometry[10])

mod.sketches['__profile__'].PerpendicularConstraint(addUndoState=False,
entity1=mod.sketches['__profile__'].geometry[6],
entity2=mod.sketches['__profile__'].geometry[10])

mod.sketches['__profile__'].CoincidentConstraint(addUndoState=False,
entity1=mod.sketches['__profile__'].vertices[6],
entity2=mod.sketches['__profile__'].geometry[6])

mod.sketches['__profile__'].CoincidentConstraint(addUndoState=False,

```

```

entity1=mod.sketches['__profile__'].vertices[7],
entity2=mod.sketches['__profile__'].geometry[2])
mod.sketches['__profile__'].Line(point1=(wx2,
wd1), point2=(wx2, -wd1))

mod.sketches['__profile__'].VerticalConstraint(addUndoState=False,
entity=mod.sketches['__profile__'].geometry[11])

mod.sketches['__profile__'].PerpendicularConstraint(addUndoState=False,
entity1=mod.sketches['__profile__'].geometry[6],
entity2=mod.sketches['__profile__'].geometry[11])

mod.sketches['__profile__'].CoincidentConstraint(addUndoState=False,
entity1=mod.sketches['__profile__'].vertices[8],
entity2=mod.sketches['__profile__'].geometry[6])

mod.sketches['__profile__'].CoincidentConstraint(addUndoState=False,
entity1=mod.sketches['__profile__'].vertices[9],
entity2=mod.sketches['__profile__'].geometry[2])

mod.parts[wp0].PartitionFaceBySketch(faces=mod.parts[wp0].faces.getSequence
FromMask(['[#200 ]', ), ), sketch=mod.sketches['__profile__'],
sketchUpEdge=mod.parts[wp0].edges[18])
del mod.sketches['__profile__']

mod.parts[wp0].PartitionCellBySweepEdge(cells=mod.parts[wp0].cells.getSeque
nceFromMask(['[#1 ]', ), ), edges=(mod.parts[wp0].edges[0], ),
sweepPath=mod.parts[wp0].edges[24])

mod.parts[wp0].PartitionCellBySweepEdge(cells=mod.parts[wp0].cells.getSeque
nceFromMask(['[#1 ]', ), ), edges=(mod.parts[wp0].edges[12], ),
sweepPath=mod.parts[wp0].edges[24])
elif cuttype == 1:
    cdi= (TD/2)+0.5 #cutter radius distance plus
variance of 0.5
    if LA >=20: wy = wy+0.1
    uch = wy+DOC
    l1 = math.sqrt(math.pow(cdi,2)-math.pow(cdi-
DOC,2))
    sheetSize=50.0
    g, v = s1.geometry, s1.vertices
    s1.setPrimaryObject(option=STANDALONE)
    s1.Line(point1=(0.0, wy), point2=(0.0, 0.0))
    s1.VerticalConstraint(entity=g[2],
addUndoState=False)
    s1.Line(point1=(0.0, 0.0), point2=(-wx, 0.0))
    s1.HorizontalConstraint(entity=g[3],
addUndoState=False)
    s1.PerpendicularConstraint(entity1=g[2],
entity2=g[3], addUndoState=False)
    s1.Line(point1=(-wx, 0.0), point2=(-wx, uch))
    s1.VerticalConstraint(entity=g[4],
addUndoState=False)
    s1.PerpendicularConstraint(entity1=g[3],
entity2=g[4], addUndoState=False)
    s1.Spot(point=(0.0, wy+cdi))
    s1.ConstructionLine(point1=(-5.0, uch),
point2=(5.0, uch))
    s1.HorizontalConstraint(entity=g[5],
addUndoState=False)

```

```

        s1.CoincidentConstraint(entity1=v[3],
entity2=g[5], addUndoState=False)
        s1.ArcByCenterEnds(center=(0.0, wy+cdi),
point1=(0.0, wy), point2=(-l1, uch), direction=CLOCKWISE)
        s1.CoincidentConstraint(entity1=v[5],
entity2=g[5], addUndoState=False)
        s1.Line(point1=(-wx, uch), point2=(-l1, uch))
        s1.HorizontalConstraint(entity=g[7],
addUndoState=False)
        s1.PerpendicularConstraint(entity1=g[4],
entity2=g[7], addUndoState=False)
        mod.Part(dimensionality=THREE_D, name=wp0,
type=DEFORMABLE_BODY)
        mod.parts[wp0].BaseSolidExtrude(depth=wz,
sketch=mod.sketches['__profile__'])
        del mod.sketches['__profile__']

## Part Sets ##

mod.parts[to0].Set(faces=mod.parts[to0].faces.getByBoundingBox(),
name=to0+'-set_geo')

mod.parts[wp0].Set(cells=mod.parts[wp0].cells.getByBoundingBox(),
name=wp0+'-set_geo')

## Material ##
# Workpiece Material
mod.Material(name=wmn)
mod.materials[wmn].setValues(description='')

mod.materials[wmn].InelasticHeatFraction(fraction=0.9)
mod.materials[wmn].Expansion(dependencies=0,
table=(TE), temperatureDependency=ON, type=ISOTROPIC, userSubroutine=OFF,
zero=0.0)

mod.materials[wmn].setValues(materialIdentifier='')

mod.materials[wmn].JohnsonCookDamageInitiation(alpha=0.0, definition=MSFLD,
dependencies=0, direction=NMORI, feq=10.0, fnn=10.0, fnt=10.0, frequency=1,
ks=0.0, numberImperfections=4, omega=1.0, position=CENTROID, table=((d1,
d2, d3, d4, d5, Tm, Trt, epR1), ), temperatureDependency=OFF,
tolerance=0.05)

mod.materials[wmn].Conductivity(dependencies=0,
table=(TC1), temperatureDependency=ON, type=ISOTROPIC)
mod.materials[wmn].Elastic(dependencies=0,
moduli=LONG_TERM, noCompression=OFF, noTension=OFF, table=((wym, wpr), ),
temperatureDependency=OFF, type=ISOTROPIC)
mod.materials[wmn].Density(dependencies=0,
distributionType=UNIFORM, fieldName='', table=((wdens, ), ),
temperatureDependency=OFF)
mod.materials[wmn].Plastic(dataType=HALF_CYCLE,
dependencies=0, hardening=USER, numBackstresses=1, rate=OFF,
strainRangeDependency=OFF, table=((Trt, ), (Tm, ), (pA, ), (pB, ), (pC, ),
(pD, ), (pE, ), (mexpn, ), (nexpn, ), (epR0, ), (utprops, )),
temperatureDependency=OFF)
mod.materials[wmn].SpecificHeat(dependencies=0,
law=CONSTANTPRESSURE, table=(sph), temperatureDependency=ON)
mod.materials[wmn].Depvar(deleteVar=depdel,
n=depno)

# Tool Material
mod.Material(name=tmn)

```



```

        mod.materials[tmn].SpecificHeat(dependencies=0,
law=CONSTANTPRESSURE, table=((sph1, ), ), temperatureDependency=OFF)
        mod.materials[tmn].setValues(materialIdentifier='')
        mod.materials[tmn].setValues(description='')
        mod.materials[tmn].Elastic(dependencies=0,
moduli=LONG_TERM, noCompression=OFF, noTension=OFF, table=((tym, tpr), ),
temperatureDependency=OFF, type=ISOTROPIC)
        mod.materials[tmn].Density(dependencies=0,
distributionType=UNIFORM, fieldName='', table=((tdens, ), ),
temperatureDependency=OFF)

mod.materials[tmn].InelasticHeatFraction(fraction=0.9)
        mod.materials[tmn].Conductivity(dependencies=0,
table=(TC2), temperatureDependency=ON, type=ISOTROPIC)

        ## Create and assigning sections ##
        mod.HomogeneousSolidSection(material=wmn,
name=wmn+'-Section', thickness=None)
        mod.HomogeneousShellSection(name=tmn+'-Section',
preIntegrate=OFF, material=tmn, thicknessType=UNIFORM, thickness=0.01,
thicknessField='', idealization=NO_IDEALIZATION, poissonDefinition=DEFAULT,
thicknessModulus=None, temperature=GRADIENT, useDensity=OFF,
integrationRule=SIMPSON, numIntPts=5)
        mod.parts[wp0].SectionAssignment(offset=0.0,
offsetField='', offsetType=MIDDLE_SURFACE,
region=mod.parts[wp0].sets[wp0+'-set_geo'], sectionName=wmn+'-Section',
thicknessAssignment=FROM_SECTION)
        mod.parts[to0].SectionAssignment(offset=0.0,
offsetField='', offsetType=MIDDLE_SURFACE,
region=mod.parts[to0].sets[to0+'-set_geo'], sectionName=tmn+'-Section',
thicknessAssignment=FROM_SECTION)

        ## Assembly ##
        tooltip = 54
        root = mod.rootAssembly
        root.DatumCsysByDefault(CARTESIAN)
        root.Instance(dependent=OFF, name=tol,
part=mod.parts[to0])
        root.Instance(dependent=OFF, name=wp1,
part=mod.parts[wp0])
        root.translate(instanceList=(wp1, ), vector=(wx,
0.0, 0.0))
        coll =
root.instances[tol].vertices[tooltip].pointOn[0]
        root.rotate(angle=90.0, axisDirection=(1.0, 0.0,
0.0), axisPoint=(wx, wy, coll[2]), instanceList=(tol, ))
        coll =
root.instances[tol].vertices[tooltip].pointOn[0]
        co60= -coll[0]+(wx)
        co61= -coll[1]+wy
        co62 = -coll[2]+(wz)
        root.translate(instanceList=(tol, ), vector=(co60,
co61, co62))
        root.rotate(angle=-LA, axisDirection=(1.0, 0.0,
0.0), axisPoint=(wx, wy, wz), instanceList=(tol, ))
        if isinstance(minl, list) == True: maxl = max(minl)
        la1 = maxl-LA
        la_alpha = (la1/180)*(pi1)
        leaddist = math.cos(la_alpha)
        docadj = ((TD/2)*math.sin(math.radians(LA))) /
((TD/2)*math.cos(math.radians(LA)))

```

```

        if 7 <= LA <= 45: docadj = (docadj) / ((maxl-2)/LA)
        leaddist1 = leaddist * (TD/4) + DOC/1.7
        if LA < 20: leaddist1 = leaddist1 + LA*0.025

#0.035
        if ((DOC >= 0.4) and (LA < 20)): leaddist1 =
leaddist1 + LA*0.042
        if ((DOC >= 0.4) and (LA == 0)): leaddist1 =
leaddist1 + DOC/4
        if LA >= 20: leaddist1 = leaddist1 + LA*0.04 #0.058
        if cuttype == 0: root.translate(instanceList=(tol,
), vector=(0,-DOC,0))
        #if cuttype == 1: root.translate(instanceList=(tol,
), vector=(0,((TD/2)*math.sin(math.radians(SO))),0))
        root.translate(instanceList=(tol, ), vector=(-
SO*3,docadj,leaddist1))
        cool =
root.instances[tol].vertices[598].pointOn[0]
        coo2 =
root.instances[tol].vertices[597].pointOn[0]
        co4 = root.instances[tol].vertices[173].pointOn[0]
        co5 =
root.instances[tol].vertices[tooltip].pointOn[0]
        ave1 = [cool[0],coo2[0]]
        ave11 = round(numpy.mean(ave1),1)
        ave2 = [cool[1],coo2[1]]
        ave21 = numpy.mean(ave2)
        ave3 = [cool[2],coo2[2]]
        ave31 = round(numpy.mean(ave3),1)
        root.DatumPointByCoordinate(coords=(ave11, ave21,
ave31))
        root.DatumPointByCoordinate(coords=(co5[0], co5[1],
co5[2]))
        root.DatumCsysByThreePoints(coordSysType=CARTESIAN,
name='Datum_csys-2', origin=root.datums[6], point1=root.datums[7],
point2=(co4[0],co4[1],co5[2]))
        root.DatumAxisByTwoPoint(point1=root.datums[6],
point2=root.datums[7])

        ## Create Step
        times = wz+leaddist1
        timeper = times/vell

mod.TempDisplacementDynamicsStep(massScaling=((SEMI_AUTOMATIC, MODEL,
AT_BEGINNING, 0.0, mass, BELOW_MIN, 0, 0, 0.0, 0.0, 0, None), ),
name='Milling', previous='Initial', timePeriod=timeper)

        ## Meshing
        # Tool
        root.setMeshControls(elemShape=QUAD,
regions=root.instances[tol].faces.getByBoundingBox(), sizeGrowthRate=1.08

root.setElementType(regions=((root.instances[tol].faces.getByBoundingBox())
), elemTypes=(ElemType(elemCode=S4RT, elemLibrary=EXPLICIT,
secondOrderAccuracy=OFF, hourglassControl=DEFAULT, elemDeletion=OFF),
ElemType(elemCode=S3RT, elemLibrary=EXPLICIT)))
        root.seedPartInstance(minSizeFactor=0.1,
regions=(root.instances[tol], ), deviationFactor=0.1, size=toolmesh)
        root.generateMesh(regions=(root.instances[tol], ))

        # Workpiece
        if cuttype == 0:

```

```

        mwz                = int(wz/wpmesh)
        mwx, mwx2         = int((wx-2*wd)/wpmesh),
int((wd/wpmesh)*0.3)
        msh, msh2, msh3 = int(sh/0.08), int(sh/0.25), 1

root.setMeshControls(regions=root.instances[wp1].cells.findAt(((2*wd),
((sh/2)+sh), wz), ), ((wd/2), ((sh/2)+sh), wz), ), ((wx, ((sh/2)+sh),
(wz/2)), ), ((wx, (sh/2), (wz-wd))), ), elemShape=HEX_DOMINATED,
technique=SWEEP, algorithm=ADVANCING_FRONT)

root.setElementType(elemTypes=(ElemType(elemCode=C3D8RT,
elemLibrary=EXPLICIT, secondOrderAccuracy=OFF,
kinematicSplit=AVERAGE_STRAIN, hourglassControl=DEFAULT,
distortionControl=DEFAULT), ElemType(elemCode=C3D6T,
elemLibrary=EXPLICIT), ElemType(elemCode=C3D4T, elemLibrary=EXPLICIT)),
regions=(root.instances[wp1].cells.findAt(((2*wd), ((sh/2)+sh), wz), ),
(((wd/2), ((sh/2)+sh), wz), ), ((wx, ((sh/2)+sh), (wz/2)), ), ((wx, (sh/2),
(wz-wd))), ), ))
        root.seedEdgeByNumber(constraint=FINER,
number=mwz, edges=root.instances[wp1].edges.findAt(((wd, (wy-sh), (wz/2)),
), ((wd, wy, (wz/2))), ), ((wx-wd), wy, (wz/2))), ((wx-wd), (wy-sh),
(wz/2))), ))
        root.seedEdgeByNumber(constraint=FINER,
number=mwx, edges=root.instances[wp1].edges.findAt(((wx/2), wy, 0.0), ),
(((wx/2), (wy-sh), 0.0), ), ((wx/2), (wy-sh), wz), ), ((wx/2), wy, wz),
)))
        root.seedEdgeByNumber(constraint=FINER,
number=msh2, edges=root.instances[wp1].edges.findAt(((wx-(wd/2)), wy,
0.0), ), ((wx-(wd/2)), (wy-sh), 0.0), ), ((wx-(wd/2)), (wy-sh), wz), ),
(((wx-(wd/2)), wy, wz), ), ((wd/2), wy, wz), ), ((wd/2), (wy-sh), wz), ),
(((wd/2), (wy-sh), 0.0), ), ((wd/2), wy, 0.0), ))
        root.seedEdgeByNumber(constraint=FINER,
number=msh, edges=root.instances[wp1].edges.findAt(((wd, (wy-(sh/2))), 0.0),
), ((wd, (wy-(sh/2))), wz), ), ((wx-wd), (wy-(sh/2))), 0.0), ), ((wx-wd),
(wy-(sh/2))), wz), ))
        root.seedEdgeByNumber(constraint=FINER,
number=mwx2, edges=root.instances[wp1].edges.findAt(((wx, (wy-(sh/2))),
0.0), ), ((wx, (wy-(sh/2))), wz), ), ((0.0, (wy-(sh/2))), wz), ), ((0.0, (wy-
(sh/2))), 0.0), ))
        root.seedEdgeByNumber(constraint=FINER,
number=msh3, edges=root.instances[wp1].edges.findAt(((wx, ((wy-sh)/2), wz),
), ((wx, ((wy-sh)/2), 0.0), ), ((0.0, ((wy-sh)/2), wz), ), ((0.0, ((wy-
sh)/2), 0.0), ))
        root.seedEdgeByNumber(constraint=FINER,
number=mwx2, edges=root.instances[wp1].edges.findAt(((wx/2), 0.0, wz), ),
(((wx/2), 0.0, 0.0), ))
        root.generateMesh(regions=(root.instances[wp1],
))
        if cuttype == 1:

root.setMeshControls(regions=root.instances[wp1].cells.getByBoundingBox(),
elemShape=HEX_DOMINATED, technique=SWEEP, algorithm=ADVANCING_FRONT)

root.setElementType(elemTypes=(ElemType(elemCode=C3D8RT,
elemLibrary=EXPLICIT, secondOrderAccuracy=OFF,
kinematicSplit=AVERAGE_STRAIN, hourglassControl=DEFAULT,
distortionControl=DEFAULT), ElemType(elemCode=C3D6T,
elemLibrary=EXPLICIT), ElemType(elemCode=C3D4T, elemLibrary=EXPLICIT)),
regions=(root.instances[wp1].cells.getByBoundingBox(), ))
        root.seedPartInstance(minSizeFactor=0.1,
regions=(root.instances[wp1], ), deviationFactor=0.1, size=wpmesh)

```

```

        root.generateMesh(regions=(root.instances[wp1],
))

        ##Sets
        root.Surface(name=to0+'-surface_geo',
        sidelFaces=root.instances[tol].faces.getByBoundingBox()
        TNxmin, TNymin, TNzmin, TNxmax, TNymax, TNzmax =
        wx-ll-SO*2, wy/2, 0, wx, uch, wz

        root.Set(nodes=root.instances[wp1].nodes.getByBoundingBox(TNxmin, TNymin,
        TNzmin, TNxmax, TNymax, TNzmax), name=wp0+'-top_nodes')
        root.ReferencePoint(point=root.datums[6])

        root.Set(elements=root.instances[tol].elements.getByBoundingBox(),
        name=to0+'-elements')
        root.Set(name='RefPoint',
        referencePoints=(root.referencePoints[18], )) #original 24

        root.Set(faces=root.instances[wp1].faces.getByBoundingBox(0,0,0,wx,0.1,wz),
        name='wp-bottom')

        root.Set(cells=root.instances[tol].cells.getByBoundingBox(),
        edges=root.instances[tol].edges.getByBoundingBox(),
        faces=root.instances[tol].faces.getByBoundingBox(),
        vertices=root.instances[tol].vertices.getByBoundingBox(), name=to0+'-
        all_geo')

        root.Set(cells=root.instances[wp1].cells.getByBoundingBox(),
        edges=root.instances[wp1].edges.getByBoundingBox(),
        faces=root.instances[wp1].faces.getByBoundingBox(),
        vertices=root.instances[wp1].vertices.getByBoundingBox(), name=wp0+'-
        all_geo')

        ##Output Request
        mod.fieldOutputRequests['F-Output-
        1'].setValues(timeInterval=timeinter, variables=(fieldoutreq))
        mod.HistoryOutputRequest(createStepName='Milling',
        name='H-Output-2', rebar=EXCLUDE, region=root.sets['RefPoint'],
        sectionPoints=DEFAULT, timeInterval=timeinter, variables=(histoutreq))
        # also output history with the analysis sets

        ## Interaction
        mod.ContactProperty('IntProp-1')
        mod.interactionProperties['IntProp-
        1'].TangentialBehavior(dependencies=0, directionality=ISOTROPIC,
        elasticSlipStiffness=None, formulation=PENALTY, fraction=0.005,
        maximumElasticSlip=FRACTION, pressureDependency=OFF, shearStressLimit=None,
        slipRateDependency=OFF, table=((friccoef, ), ), temperatureDependency=OFF)
        mod.interactionProperties['IntProp-
        1'].HeatGeneration(conversionFraction=1.0, slaveFraction=0.9)
        mod.interactionProperties['IntProp-
        1'].ThermalConductance(clearanceDependency=OFF, definition=TABULAR,
        dependenciesP=0, massFlowRateDependencyP=OFF, pressureDepTable=(TC),
        pressureDependency=ON, temperatureDependencyP=OFF)

        mod.SurfaceToSurfaceContactExp(clearanceRegion=None,
        createStepName='Milling', datumAxis=None, initialClearance=OMIT,
        interactionProperty='IntProp-1', master=root-surfaces[to0+'-surface_geo'],
        mechanicalConstraint=PENALTY, name='Interaction', slave=root.sets[wp0+'-
        top_nodes'], sliding=FINITE)

```

```

        ## Constrain
        mod.RigidBody(bodyRegion=root.sets[to0+'-
elements'], name='rigid-'+to0, refPointRegion=root.sets['RefPoint'],
isothermal=ON)

        ## BCC
        mod.VelocityBC(amplitude=UNSET,
createStepName='Milling', distributionType=UNIFORM, fieldName='',
localCsys=root.datums[8], name='spindle-speed',
region=root.sets['RefPoint'], v1=0.0, v2=0.0, v3=0.0, vr1=spin1, vr2=0.0,
vr3=0.0)

        mod.VelocityBC(amplitude=UNSET,
createStepName='Milling', distributionType=UNIFORM, fieldName='',
localCsys=None, name='workpiece-movement', region=root.sets['wp-
bottom'], v1=0.0, v2=0.0, v3=vell, vr1=UNSET, vr2=UNSET, vr3=UNSET)

        ## Predefined fields
        mod.Temperature(createStepName='Initial',
crossSectionDistribution=CONSTANT_THROUGH_THICKNESS,
distributionType=UNIFORM, magnitudes=(Trt, ), name=wp0+'-temp',
region=root.sets[wp0+'-all_geo'])
        mod.Temperature(createStepName='Initial',
crossSectionDistribution=CONSTANT_THROUGH_THICKNESS,
distributionType=UNIFORM, magnitudes=(Trt, ), name=to0+'tool-temp',
region=root.sets[to0+'-all_geo'])

        ## Analyse Sets
        root.regenerate()
        ex1 = ex+1
        d = float((wx-SO*3)/(ex1))
        yb = wy-wpmesh
        xd, yd, zd= (wpmesh*0.5), (wpmesh*0.4), (wz-2*zb)
        for exn in range(1,ex1):
            xb = wx-exn*d
            xmin, ymin, zmin = xb-xd, yb-yd, zb
            xmax, ymax, zmax = xb+xd, yb+yd, zb+zd
            if exn == 2:
                yy = ((uch-wy)/2)+wy
                ymin, ymax = yy-wpmesh-yd, yy-wpmesh+yd
            if exn == 3: ymin, ymax = uch-wpmesh-yd, uch-
wpmesh+yd

        root.Set(nodes=root.instances[wp1].nodes.getByBoundingBox(xmin, ymin, zmin,
xmax, ymax, zmax), name='Analysis-set2-'+str(exn))

        ## JOB
        mdb.Job(activateLoadBalancing=False, atTime=None,
contactPrint=OFF, description='', echoPrint=OFF, explicitPrecision=DOUBLE,
historyPrint=OFF, memory=90, memoryUnits=PERCENTAGE, model=Model,
modelPrint=OFF,

                multiprocessingMode=MPI, name=Model,
nodalOutputPrecision=SINGLE, numCpus=CPUDOM, numDomains=CPUDOM,
parallelizationMethodExplicit=DOMAIN, queue=None, resultsFormat=ODB,
scratch='', type=ANALYSIS, userSubroutine=subpath, waitHours=0,
waitMinutes=0) # _PLUS_PACK DEFAULT
        if jol == 1:
            mdb.jobs[Model].submit(consistencyChecking=OFF)
            mdb.jobs[Model].waitForCompletion()

        with open(logf, 'a') as f: f.write('{}\tSimulation
{} successful\n'.format(nowdate(),iter))

```

```

## Saving MDB
if ((iter % saveinter == 0) or (iter == itermax)):
    del mdb.models['Model-1']
    cv+=1
    mdb.saveAs(savepath+na0+'-'+str(cv)+'.cae')
    Mdb()
    iz=0
    while iz < saveinter:
        iter1 = iter - iz
        if iz == 0:
            wout = str(iter1)
        else:
            wout = wout+" and {} ".format(iter1)
        iz+=1
    with open(logf, 'a') as f: f.write('{}\tCAE-
File {} of simulation {} were successfully saved\n'.format(nowdate(),cv,
wout))

        if email == 1: sendmail('Upadte on Simulation
at {}'.format(nowdate()), '{} Simulations are finished\n Please, check log-
file.'.format(iter), logf)

    #restoring overwritten variables
    wy = wy_backup

except:
    exc_type, exc_obj, exc_tb = sys.exc_info()
    with open(logf, 'a') as f: f.write('{}\tSimulation
No. {} \tUnexpected error during Simulation: {} in line
{}\n'.format(nowdate(),iter,sys.exc_info()[0],exc_tb.tb_lineno))
    continue

#### Writing an E-Mail that all Simulations have been finished
subj = 'Simulation has finished!'
msg = 'All Simulation are finished at {}!\n'.format(nowdate())
with open(logf,'a') as f: f.write(msg)
if email == 1: sendmail(subj, msg, logf)

### Calling Abaqus Analysis ###
if analysis1 == 1: os.system(analysispath)

```

variables.py

```
## Working Paths
subpath = 'C:/SIMULIA/subs/vuhardultimate6.for' # Subroutine path
rootdir = 'C:/SIMULIA/Temp/script/millingexperiment2/' # Root
directory THIS FOLDER MUST EXIST!!! (will contain the pythonfiles)
tooldir = rootdir + 'tool_cut_solid_NEW-cad.sat' # File must
exist!
workdir = rootdir + 'working/' # Working directory
savepath = rootdir + 'CAE//' # CAE - File saving path
extractdir = rootdir + 'extract/' # Extraction directory
analysispath = rootdir + 'abaqanalysis.py' #Path of python
abaqanalysis.py
totalan = rootdir + 'totalan.py' # path of python totalan.py
logf = rootdir + '000-log.log' # log file name including file-
type (.log)

## Handling other scripts
j01 = 1 # Submit jobs 1=yes, 0=no
analysis1 = 1 # Start analysis after finishing all
simulations, 1=yes, 0=no
totalanalysis = 1 # Starting complete analysis of Simulation
1=yes, 0=no
email = 1 # Send status emails; 1=yes, 0=no

## DOE-Approach
velx = 3 # Number of Surface Speeds
docx = 3 # Number of Depth of cuts
frx = 4 # Number of Feed Rates
lax = 4 # Number of Lead Angles
minv, maxv = 250., 350. # Min & Max Surface Speed (m/min) ,
minimum values can be used as an array - automatic range will be
ignored for this instance
mind, maxd = 0.3, 0.5 # Min & Max DoC (mm), minimum values
can be used as an array - automatic range will be ignored for this
instance
minfr, maxfr = 0.08, 0.2 # Min & Max Feed Rate (mm/tooth),
minimum values can be used as an array - automatic range will be
ignored for this instance
minl, maxl = [0,7.5,22.5,45.], 0 # Min & Max Lead Angle (deg),
minimum values can be used as an array - automatic range will be
ignored for this instance

itermax = velx*docx*lax*frx ### DO NOT CHANGE ### Number of max
simulations

## FE Variables
na0 = 'Milling' # Name of the Model
wp0 = 'fatigue_workpiece' # Workpiece name
to0 = 'bn_4_flute' # Tool name
cuttype = 1 # select cut type: 0 - Slotting, 1 -
stepover milling
wx, wy, wz = 3.0,0.3,5.0 # Size Workpiece X, Y, Z-Direction
sh = 1.0 # sectioning height
wd = 0.5 # Width sectioning, it is recommended to
leave enough space for the complete tool
wpmesh = 0.055 # element size in the fine mesh area
toolmesh = 0.45 # seeding size for tool
```

```

mass      = 1.9e-08          # Mass scaling
ex        = 3                # Number of analysis sets
zb        = 0.2              # Distance z-direction for analysis set
frames    = 30               # Number of Frames
timeinter = 0.005           # Recording in x time intervals
CPUDOM    = 24               # Number of CPU and Domains
saveinter = 2                # MDB saving interval - to have all
Models in one database use: itermax
fieldoutreq = ('S', 'PEEQ', 'U', 'UT', 'V', 'VT', 'RF', 'NT',
'TEMP', 'SDV', 'STATUS') # Field output request
histoutreq = ('RF1', 'RF2', 'RF3', 'RM1', 'RM2', 'RM3')
# History output request

# Machining Variables
friccoef  = 0.48            # Friction coefficient
Trt       = 20.0            # Reference Room Temperature
TD        = 8.0             # Tool Diameter (mm)
NF        = 4               # Number of Flutes
SO        = 0.1             # Stepover [mm]

## Material Properties
# WORKPIECE #
wym       = 211000.0        # Youngs Modulus
wpr       = 0.28            # Passions Ratio
wdens     = 7.8e-09        # Density
depdel    = 6               # Depvar delete number
depno     = 7               # Depvar number of variables

# Johnson-Cook Parameter
wmn       = 'H13'          # Material name of the workpiece
Tm        = 1480.0          # Melting Temperature
pA        = 674.88          # JC-Parameter A
pB        = 239.2           # JC-Parameter B
pC        = 0.056           # JC-Parameter C
pD        = 1.16            # JC-Parameter D
pE        = 0.88            # JC-Parameter E
mexpn     = 2.7             # JC-Parameter m
nexpn     = 0.44            # JC-Parameter n
epR0      = 1.0             # Strain Rate reference
utprops   = 1500.0         # Ultimate Tensile

# Johnson-Cook Damage-Parameter
d1        = -0.8            # JC-Damage-Parameter D1
d2        = 2.1             # JC-Damage-Parameter D2
d3        = -0.5            # JC-Damage-Parameter D3
d4        = 0.0002          # JC-Damage-Parameter D4
d5        = 2.7             # JC-Damage-Parameter D5
epR1      = 1.0             # Strain Rate reference

#### Tables ####
# Thermal expansion (Coefficient, Temperature)
TE = ((1.04e-05, 93.0), (1.13e-05, 204.0), (1.24e-05, 316.0), (1.31e-
05, 427.0), (1.35e-05, 538.0))

# Thermal Conductivity (Coefficient, Temperature)
TC1 = ((17.6, 20.0), (24.3, 215.0), (24.4, 350.0), (24.5,
475.0), (24.7, 605.0))

# Specitfic Heat (Coefficient, Temperature)

```



```

sph = ((460000000.0, 20.0), (548000000.0, 500.0), (590000000.0,
600.0))

# TOOL #
tmn      = 'Tungsten'           # Material name of the workpiece
sph1     = 960000000.0         # Specific Heat
tym      = 534000.0           # Youngs Modulus
tpr      = 0.22                # Poissons Ratio
tdens    = 1.93e-08           # Density

# Thermal Conductivity (Coefficient, Temperature)
TC2 = ((163.3, 20.0), (146.0, 200.0), (128.0, 600.0), (117.0,
1000.0))

## Interaction between Tool and Workpiece
# Thermal Conductance (Coefficient, Pressure)
TC = ((0.3, 0.0), (0.8, 10.0), (1.0, 20.0),
(1.03, 23.0), (1.05, 25.0), (1.06, 26.0),
(1.15, 50.0), (1.16, 75.0), (1.165, 100.0),
(1.25, 150.0), (1.5, 200.0), (1.8, 250.0),
(2.045, 300.0), (2.05, 350.0), (2.06, 400.0),
(2.07, 450.0), (2.08, 500.0), (2.09, 600.0),
(2.124, 700.0), (2.13, 800.0), (2.137, 900.0),
(2.2, 1000.0), (2.2, 1100.0), (2.2, 1200.0),
(2.2, 1300.0), (2.2, 1400.0), (2.2, 1500.0))

### IF the script abort at some point, use this funtion to skip
already calculated simulations

skipfn   = 0                   # Switch on (1) or off (0) the skip funtion
skip     = 0                   # Number of the last successful saved ODB
cv       = 0                   # Number of the last successful saved CAE

```

sim_functions.py

```
import smtplib, base64, datetime, os, codecs, time, sys
import numpy as np

#=====
# Generates the actual time and date in ISO-Format
#=====
def nowdate():
    now1 = datetime.datetime.now()
    now2 = now1.isoformat(' ')[:-7]
    return (now2)

#=====
# Sending an E-Mail
# subj = String for stubject
# msg = String for Message
# pwd = byte encoded password - see password generator
# user = email address
# receiver = Receiver email address
# mail contains the SMTP-Server and Port
#=====
def sendmail(subj, msg, logf):
    from email.mime.text import MIMEText
    from email.mime.multipart import MIMEMultipart
    from email.mime.application import MIMEApplication

    pwd= b'cDhwODNxdHNtcDNLJA==' #Encrypted Passwort
    user = 'reimer.andreas@googlemail.com' #Your E-Mail Address
    receiver = "andreas.reimer@strath.ac.uk" #Receiver of this Mail

    msg1 = MIMEMultipart()
    msg1['Subject'] = subj
    msg1.attach(MIMEText(msg))
    with open(logf, "rb") as fil: part =
MIMEApplication(fil.read(),Name=logf)
    part['Content-Disposition'] = 'attachment; filename=logfile.txt'
    msg1.attach(part)

    decodepwd = base64.b64decode(pwd)
    decpwd = decodepwd.decode("utf-8")
    mail = smtplib.SMTP_SSL("smtp.gmail.com",465)
    mail.ehlo()
    mail.login(user,decpwd)
    mail.sendmail(user,receiver,msg1.as_string())
    mail.close()

def encoder(txt_file,encode_format,decode_format):
    #encode_format = "utf-16"
    #decode_format ="utf-8"
    filename = os.path.splitext(txt_file)[0]
    org_file_encoded = filename+'enc.txt'
    sizeinfo = os.stat(txt_file)
    BLOCKSIZE = int(sizeinfo.st_size)
```

```

    with codecs.open(txt_file, "r", encode_format) as sourceFile:
        with codecs.open(org_file_encoded, "w", decode_format) as
targetFile:
            while True:
                contents = sourceFile.read(BLOCKSIZE)
                if not contents: break
                targetFile.write(contents)

#=====
# Checks if neccessay files and folder exists, if folder does not exist it
will be created
# checkdirs = array, folderpaths to check
# checkfiles = array, files(paths) to check
#=====

def precheck(checkdirs, checkfiles):
    from variablesm import logf
    for check in checkdirs:
        if not(os.path.isdir(check)):
            os.makedirs(check)
    for check in checkfiles:
        if not os.path.isfile(check):
            with open(logf, 'a') as f: f.write('{}\t{} does not exists,
please add this file before starting the simulation and
analysis!\n'.format(nowdate(),check))
            sys.exit("Fatal Error - Please check Logfile!")

```

aba_analysis.py

```
import xyPlot, time
import section
import regionToolset
import connectorBehavior
import os,sys,datetime
from odbAccess import *
from visualization import *
import displayGroupOdbToolset as dgo
from variablesm import *
from sketch import *
global ex1
ex1=ex+1
#===FUNCTIONS=====
def nowdate():
    now1 = datetime.datetime.now()
    now2 = now1.isoformat(' ')[:-7]
    return (now2)

def analysis(internalname,outputheader,filename,ansys,noskip):
#=====
#     internalname, outputheader, filename, noskip = must be an array
# [values]
#     ansys must be an boolean (True or False)
#=====
    analysisname2=[]
    for xr1 in range(1,ex1): analysisname2.append(('ANALYSIS-SET-
'+str(xr1)))
    for var in range(0,len(internalname)):
        outxy=[]
        for ansys1 in range(0,ex1-1):
            output = internalname[var]
            outname = filename[var]
            for var1 in range(0, len(outputheader)):
                if len(internalname) != len(outputheader): andesc1 =
outputheader[var1]
                else: andesc1 = outputheader[var]
                if ansys == True: #and (ansys1 in noskip):
                    setname = analysisname2[ansys1]
                    session.xyDataListFromField(odb=odb,
outputPosition=NODAL, variable=(output, ), nodeSets=(setname, ))
                elif ansys == False: #and (ansys1 == 0):
                    setname = 'REFPOINT'
                    session.xyDataListFromField(odb=odb,
outputPosition=NODAL, variable=(output, ), nodeSets=(setname, ))
                else: continue
                ad = odb.rootAssembly.nodeSets[setname].nodes[0]
                for ai in range(0,len(ad)):
                    bx = ad[ai].label
                    data2 = str(andesc1) + str(bx)
                    x = session.xyDataObjects[data2]
                    outxy.append(x)
            session.xyReportOptions.setValues(totals=OFF, minMax=OFF)
            session.writeXYReport(fileName=extractdir+Model+'_'+outname+'.rpt',
appendMode=OFF, xyData=(outxy))
            time.sleep(0.25)
#=====
```

```

#####DEFINING VARIABLES#####
internalset = [('S', INTEGRATION_POINT, ((COMPONENT, 'S11'), )), ('S',
INTEGRATION_POINT, ((INVARIANT, 'Mises'), )), ('TEMP', INTEGRATION_POINT)]
headerset = ['S:S11 (Avg: 75%) PI: WORKPIECE-1 N: ', 'S:Mises (Avg: 75%) PI:
WORKPIECE-1 N: ', 'TEMP (Avg: 75%) PI: WORKPIECE-1 N: ']
filenamest = ['Stress_S11', 'VM', 'temp']

interref = [('RF', NODAL)]
headerref = ['RF:Magnitude PI: ASSEMBLY N: ', 'RF:RF1 PI: ASSEMBLY N:
', 'RF:RF2 PI: ASSEMBLY N: ', 'RF:RF3 PI: ASSEMBLY N: ']
filenameref = ['Force']

#####
with open(logf, 'a') as f: f.write('{} Abaqus analysis
started\n'.format(nowdate()))
checkon, checklist = False, []
for file in os.listdir(workdir):
    if not (file.endswith('.odb')): continue
    if checkon == True:
        for check in checklist:
            if not file.endswith(check): continue
    try:
        odbpath = workdir+str(file)
        Model = str(file)[:4]

# Initialising Viewpot
        session.openOdb(name=odbpath)
        odb = session.odbs[odbpath]
        session.viewports['Viewport: 1'].setValues(displayedObject=odb)

# Analysis work here
        analysis(internalset,headerset,filenameset,True,[1])
        analysis(interref,headerref,filenameref,False,None)

# Saving viewports
        session.viewports['Viewport:
1'].odbDisplay.display.setValues(plotState=(CONTOURS_ON_DEF, ))
        session.viewports['Viewport:
1'].odbDisplay.setPrimaryVariable(variableLabel='S',
outputPosition=INTEGRATION_POINT, refinement=(COMPONENT, 'S11'), )
        session.pngOptions.setValues(imageSize=(2133, 1080))
        session.printOptions.setValues(reduceColors=False,
vpDecorations=OFF)
        session.printToFile(fileName=extractdir+Model, format=PNG,
canvasObjects=(session.viewports['Viewport: 1'], ))

# Clear up the session
        getridkeys=session.xyDataObjects.keys()
        for i in range(0,len(getridkeys)):
            del session.xyDataObjects[getridkeys[i]]

        odb.close()
    except:
        exc_type, exc_obj, exc_tb = sys.exc_info()
        with open(logf, 'a') as f: f.write('{}\tUnexpected error during
analysis with {}: {} in line
{}\n'.format(nowdate(),file,sys.exc_info()[0],exc_tb.tb_lineno))
        with open(workdir+'001failure.txt','a') as f:
f.write("{}{}",".format(file))
        continue
with open(logf, 'a') as f: f.write('{} Abaqus analysis
finished\n'.format(nowdate()))

```

totalanalysis.py

```
from functions import *
import sys, os, csv
import pandas as pd
from variablesm import *

def log_err():
    exc_type, exc_obj, exc_tb = sys.exc_info()
    with open(logf, 'a') as f: f.write('{}\tUnexpected error during the
total analysis with {}: {} in line
{}\n'.format(nowdate(),file,sys.exc_info()[0],exc_tb.tb_lineno))

with open(logf, 'a') as f: f.write('{} Total analysis
started\n'.format(nowdate()))
print('{} Total analysis started\n'.format(nowdate()))

for file in os.listdir(extractdir):
    try:
        filepath = extractdir+file
        if file.endswith('.rpt'):
            if not file.endswith('Force.rpt'):
                alllookups = ["NoValue",":"]
                rmvjunk(alllookups,filepath)
            else: convert2txt(filepath)
    except:
        log_err()
        continue
print("Clean up, Part 1, Done!")
for file in os.listdir(extractdir):
    try:
        filepath = extractdir+file
        if file.endswith("Force.txt"):
            convert2csv(filepath,3,'X,Mag,RF1,RF2,RF3')
            if file.endswith(".txt") and not file.endswith("Force.txt"):
                convert2csv(filepath,2)
    except:
        log_err()
        continue
print("Converting to CSV, Part 2, Done!")

# Listing the average values in the summary
header = str('Filename,Ave S11,Ave S33,Ave Mises,Ave JC, Ave HRC, Ave Temp,
Ave Force, Max Force Mag, Abs Ave Force RF3\n')
with open(extractdir+"summary.csv",'w+') as wf1: wf1.write(header)
for file in os.listdir(extractdir):
    try:
        filepath = extractdir+file
        if file.endswith(".csv"):
            filename = os.path.splitext(file)
            filebase = os.path.basename(file)
            if file.endswith('Force.csv'):
                colnames=['X','Mag','RF1','RF2','RF3']
                sr=1
                cnabsrf3 = "ABS_RF3"
                data = pd.read_csv(filepath, names=colnames, skiprows=sr+1)
                dataRF3 = data.RF3.abs()
                absRF3 = pd.DataFrame(dataRF3).values.tolist()
                addcsvcolumn(filepath,absRF3,sr,cnabsrf3)
                maxi = max(data.Mag.tolist())
                aveRF3 = ifmean(dataRF3,0.001)
                average_column(filepath,True,0.001)
```

```

        ave = pickval(filepath, 'Averages', 1)
    else: ave = average_row(filepath, 'lastrow')
    #Files endings accordingly to the header

lib={'S11_nojunk.csv':1, 'S33_nojunk.csv':2, 'MISES_nojunk.csv':3, 'SDV1_nojun
k.csv':4, 'SDV5_nojunk.csv':5, 'TEMP_nojunk.csv':6, 'Force.csv':7}
    with open(extractdir+"summary.csv", 'a') as wfl:
        keys = lib.keys()
        for key in keys:
            if (key in filebase) == True:
                if key == 'Force.csv':
                    out = (lib[key])*', '
                    out1 = (len(lib)-len(out)+1)*', '
                    wfl.write(str(filebase[:-
4])+out+str(ave)+' '+str(maxi)+' '+str(aveRF3)+'\n')
                else:
                    out = (lib[key])*', '
                    wfl.write(str(filebase[:-4])+out+str(ave)+'\n')

    except:
        log_err()
        continue
print("Average & summarising, Part 3, Done!")
for file in os.listdir(extractdir):
    try:
        filepath = extractdir+file
        if file.endswith("summary.csv"):
            convert2xlsx(filepath)
    except:
        log_err()
        continue
print("Converting summary to XLSX, Part 4, Done!")
with open(logf, 'a') as f: f.write('{} Total analysis
finished\n'.format(nowdate()))

```

Functions.py

```
import smtplib, base64, datetime, os, csv, codecs, time, sys, pandas
from collections import Counter
from xlsxwriter.workbook import Workbook
import numpy as np
import pandas as pd

#=====
# generates the actual time and date in ISO-Format
#=====
def nowdate():
    now1 = datetime.datetime.now()
    now2 = now1.isoformat(' ')[:-7]
    return (now2)

#=====
# Sending an E-Mail
# subj = String for subject
# msg = String for Message
# pwd = byte encoded password - see password generator
# user = email address
# receiver = Receiver email address
# mail contains the SMTP-Server and Port
#=====
def sendmail(subj, msg):
    pwd= b'XXX'          #Encrypted Passwort
    user = 'XXX@gmail.com' #Your E-Mail Address
    receiver = "XXX@gmail.com" #Receiver of this Mail
    msg1 = 'Subject: %s\n\n%s' % (subj, msg)
    decodepwd = base64.b64decode(pwd)
    decpwd = decodepwd.decode("utf-8")
    mail = smtplib.SMTP_SSL("smtp.gmail.com",465)
    mail.ehlo()
    mail.login(user,decpwd)
    mail.sendmail(user,receiver,msg1)
    mail.close()

#=====
# Removes no needed rows form output files
# lookup = array or string find the rows to be removed
# file = file path of the files to be cleared up
#=====
def rmvjunk(alllookups, file):
    filename = os.path.splitext(file)[0]
    if not file.endswith('nojunk.txt'):
        with open(file) as fin, open('temp.txt', 'w') as fout:
            for lookup in alllookups:
                for l in fin:
                    if not (lookup) in l: fout.write(l)
            with open(filename+'_nojunk.txt','w') as fout2,
open('temp.txt','r') as fin1:
                for li in fin1:
                    if li.strip(): fout2.write(li)
    os.remove('temp.txt')
    time.sleep(0.25)

#=====
```



```

# Converts anyfile (possible) file format into a standard text-file
format
# org_file = file path of the to be converted file
#=====
def convert2txt(org_file):
    filename = os.path.splitext(org_file)[0]
    with open(org_file, 'r') as rf, open(filename+'.txt', 'w+') as wf:
        for i in rf: wf.write(i)

#=====
# Converts text files into CSV-files
# txt_file = file path of the to be converted file
# jl = jump lines
# sep = defines the delimiter
#=====
def convert2csv(txt_file, jl, *args):
    filename = os.path.splitext(txt_file)[0]
    sep=', '
    with open(txt_file, 'r') as rtxt, open('temp.txt', 'a') as temp:
        num = rtxt.readlines()[1:1]
        header = None
        for head in args:
            header = head
        if header != None: temp.write('sep='+sep+'\n' + header +'\n')
        else: temp.write('sep='+sep+'\n')
        temp.writelines(num)

    with open(txt_file, 'r') as rtxt, open('temp.txt', 'a') as temp:
        ntxt1 = rtxt.readlines()[jl:]
        for i in ntxt1:
            abc = ' '.join(i.split())
            ntxt = abc.replace(" ", sep)
            ntxt = str(ntxt).strip(':')
            temp.write(ntxt+'\n')
        with open("temp.txt", "r") as temp, open(filename+".csv", 'w+') as
csv_file:
            in_txt = csv.reader(temp, delimiter=sep)
            out_csv = csv.writer(csv_file, delimiter = sep,
lineterminator="\n")
            out_csv.writerows(in_txt)
            os.remove("temp.txt")
            time.sleep(0.25)

#=====
# Converts a CSV into an Excel-File
# The file will have the same name as the original, but in an Excel
format
# csv_filepath = file path of the to be converted file
#=====
def convert2xlsx(csv_filepath):
    filename = os.path.splitext(csv_filepath)[0]
    workbook = Workbook(filename+'.xlsx')
    worksheet = workbook.add_worksheet()
    with open(filename+'.csv', 'r+') as f:
        exr1 = csv.reader(f)
        for r, row in enumerate(exr1, start=0):
            for c, col in enumerate(row):
                worksheet.write(r, c, col)
    workbook.close()

```

```

#=====
# Encodes textfiles from one format to an other - the encoded file
will end with "enc.txt"
# txt_file = file path of the to be converted file
# encode_format = the encoding format (i.e. "utf-16")
# decode_format = the decoding format (i.e. "utf-8")
#=====
def encoder(txt_file,encode_format,decode_format):
    #encode_format = "utf-16"
    #decode_format = "utf-8"
    filename = os.path.splitext(txt_file)[0]
    org_file_encoded = filename+'enc.txt'
    sizeinfo = os.stat(txt_file)
    BLOCKSIZE = int(sizeinfo.st_size)
    with codecs.open(txt_file, "r", encode_format) as sourceFile:
        with codecs.open(org_file_encoded, "w", decode_format) as
targetFile:
            while True:
                contents = sourceFile.read(BLOCKSIZE)
                if not contents: break
                targetFile.write(contents)

#=====
# Calculates an conditional average in a column of a CSV-File and
writes the average value in the bottom of the csv-file
# csv_filepath = CSV file path of the to be converted file
# aveif = activates the conditional average (if "True"==activated,
if "False" == deactivated)
# aveif_val = if conditional average activated the min. value to be
considered in the average, if the deactivated use "0"
#=====

```

```

def average_column(csv_filepath,aveif,aveif_val):
    column_totals = Counter()
    row_count,neg_count,skiprow = 0,0,3
    with open(csv_filepath,"r") as f:
        reader = csv.reader(f)
        for row in reader:
            if not row and isinstance(row, list): neg_count +=1
            for column_idx, column_value in enumerate(row):
                try:
                    if row_count <= skiprow: continue
                    n = float(column_value)
                    if (column_idx > 0) and (n <= aveif_val) and (aveif ==
True):
                        neg_count +=1
                        continue
                    elif (column_idx > 0):
                        if (aveif == True) and (n > aveif_val):
column_totals[column_idx] += n
                        elif (aveif == False): column_totals[column_idx] +=
n
                except ValueError:
                    from variablesm import logf
                    with open(logf, 'a') as f: f.write("{}\tError -- ({}))
Column({}) could not be converted to
float!\n".format(nowdate(),column_value, column_idx))
                    row_count += 1
                    tot_count = row_count - neg_count - skiprow
                    column_indexes = column_totals.keys()
                    averages = [column_totals[idx]/tot_count for idx in column_indexes if
idx >=1]
                    with open(csv_filepath, 'a') as f:
f.write('\nAverages\n'+','+str(averages).strip('[]'))

#=====
# Calculates the average and returns this value of a row.
# "currently" works only with average_column together!
# file = file path of the to be converted file
#=====
def average_row(file,keyword):
    with open(file,'r') as rf:
        reader = csv.reader(rf)
        next(reader, None)
        row_count, ave_row =0,0
        ave_ok = False
        for row in reader:
            for field in row:
                if field == keyword: ave_row = row_count + 1
                elif row_count == ave_row: ave_ok = True
            row_count+=1
        if ave_ok == True:
            times, *values = row
            average = sum([float(value) for value in values]) / len(values)
            return average

#=====
# Checks if necessary files and folder exists, if folder does not exist it
will be created
# checkdirs = array, folderpaths to check
# checkfiles = array, files(paths) to check
#=====

```

```

def precheck(checkdirs, checkfiles):
    from variablesm import logf
    for check in checkdirs:
        os.makedirs(os.path.dirname(check), exist_ok=True)
    for check in checkfiles:
        if not os.path.isfile(check):
            with open(logf, 'a') as f: f.write('{}\t{} does not exists,
please add this file before starting the simulation and
analysis!\n'.format(nowdate(),check))
            sys.exit("Fatal Error - Please check Logfile!")

#=====
# Finds the peak value in a cloumn and writes it on the bottom of the CSV-
File
# csv_filepath = CSV file path of the to be converted file
#=====

def max_column(csv_filepath):
    colnames=['X','Mag','RF1','RF2','RF3']
    data = pandas.read_csv(csv_filepath, names=colnames, skiprows=3)
    maxi = max(data.Mag.tolist()) #change "Mag" to column name which is
required
    return(maxi)
#     i = 0
#     with open(csv_filepath,"r") as f:
#         reader = csv.reader(f)
#         for row in reader:
#             i+=1
#             if (i < skiprow): continue
#             else: maxi = max(float(column[idx].replace(',',' ')) for
column in reader)
#     return(maxi)

#=====
# Find a specific value in a row and column
# csv_filepath = file path to CSV file
# row = integer for csv row (fixed) OR string looking for keyword and to
choose the row (dynamic)
# col = column as integer (fixed)
#=====
def pickval(csv_filepath,row,col):
    try:
        rowa =int(row)
        rowa = rowa-1
        num=True
    except ValueError: num = False
    with open(csv_filepath,"r") as rf:
        reader = csv.reader(rf)
        next(reader, None)
        try:
            if num == False:
                row_count = 0
                reader = list(reader)
                for rowb in reader:
                    for field in rowb:
                        if field == row: rowa = row_count + 1
                    row_count +=1
                ave = reader[rowa][col]
            if num == True:
                reader = list(reader)
                ave = reader[rowa][col]

```

```

    except ValueError:
        from variablesm import logf
        with open(logf, 'a') as f: f.write("{}\tError -- Column({})
could not be converted to float!\n".format(nowdate(), col))
        return ave

#=====#
# Calculates a NDF-Dataset average value, with a certain if value is bigger
# dataset = Numpy dataset / dataframe
# ifval = float for if-value
#=====#
def ifmean(dataset, ifval):
    s = np.array(dataset)
    aveval = s > ifval
    if aveval.any(): return s[aveval].mean()
    else:
        print('Some Problems in ifmean-function!!!')
        return

#=====#
# add column in CSV file
# file = file path
# sr = skip rows (of non-numercial values)
# header = additional Columnname
# values = added values as a list
#=====#
def addcsvcolumn(file, values, sr, header):
    bn = '/TEMP_'+os.path.basename(file)
    dirn = os.path.dirname(file)
    os.rename(file, dirn+bn)
    with open(dirn+bn, 'r') as rf, open(file, 'w+') as wf:
        reader = csv.reader(rf, lineterminator="\n", delimiter=',')
        writer = csv.writer(wf, lineterminator="\n", delimiter=',')
        row_count, i = 0, 0
        for row in reader:
            if (not ''.join(row).strip()) and (row_count <= sr): pass
            elif(''.join(row).strip()):
                if (row_count == 1):
                    row.append(header)
                    writer.writerow([row])
                elif (row_count <= sr) and not (row_count == 1):
writer.writerow([row])
                elif (row_count > sr):
                    row.append(float(str(values[i]).strip('[]')))
                    writer.writerow([row])
                    i+=1
            row_count+=1
    os.remove(dirn+bn)

```

Appendix IIX Matlab Codes

Main.m

```
%% INITIALIZE THE NEURAL NETWORK & GA PROBLEM%
clear all;
savepic = 0;
reg = 0; % running poly regression
RBF = 0; % running RBF
GA = 1; % running GA
single = 1; % running single FFBP
global netGA
% ### NN initialisation ###
inp = 'C:\Users\Andy\Documents\ANN\';
impIN = [inp 'ANN_input.txt'];
impIN2 = [inp 'ANN_input_S11-Sa-HRC.txt'];
impOUT = [inp 'ANN_output_cycle.txt'];
z = load(strcat(impIN));
z2 = load(strcat(impIN2));
t = load(strcat(impOUT));
z = z'; t = t'; z2=z2';
numNN = 200; % number of training neural network system
l11 = 10; l22 = 10; l33 = 10; %layers for single network

% ### GA initialisation ###
fitness = @ga_testfn;
nonlcon = @nonlinconst;
nvar = 4;
lb = [200 0.1 0.02 0];
ub = [400 0.6 0.2 45];

%% ### Running GA ###
if GA == 1
    netGA = NNGA(z,z2,l11,l22,l33);
    options = optimoptions(@gamultiobj,'PlotFcn', @gaplotpareto);
    [x,fval,exitflag] =
gamultiobj(fitness,nvar,[],[],[],[],lb,ub,nonlcon,options);
end

%% ### Running Radial Basis Function ###
if RBF ==1
    net = newrb(z,z2);
    y1 = sim(net,z);
    y3 = sim(net,x');

    net2 = newrb(z2,t);
    y4 = sim(net2,y3);
    y5 = sim(net2,fval');
end

%% ### Polynomial regression ### - cannot be used hence multiple input and
output
if reg == 1
    z = z'; t = t';
    md = fitlm(z,z2,'poly4321');
    y2 = predict(md,z);
    y21 = predict(md,x);

    md1 = fitlm(z2,t,'poly4321');
    y22 = predict(md1,y21);
    y23 = predict(md1,fval);
end
```

```

%% ### Single Network run ###
if single == 1
    t2 = z; %input variable handover
    t3 = t; %output variable handover
    t4 = z2;
    mincorr = 0.85;
    NNb2=[];iz2=[];
    net4 = newff(t4,t3,[111 122
133],{'logsig','tansig','tansig','tansig'],'trainrp','learngd');
    net4.trainParam.showWindow = true;
    net4.divideFcn = 'dividerand';
    net4.trainParam.goal = 1;
    for i = 1:numNN
        fprintf('Training %d/%d\n', i, numNN)
        IW = net4.IW{1,1};
        LW = net4.LW{2,1};
        [net4,tr] = train(net4,t4,t3);
        net4.IW{1,1} = IW;
        net4.LW{2,1} = LW;
        y7 = net4(fval');
        y77 = net4(t4);
        trainTargets = t3 .* tr.trainMask{1};
        valTargets = t3 .* tr.valMask{1};
        testTargets = t3 .* tr.testMask{1};
        NNb2 = corrcoef(t3,y77);
        NNb2 = NNb2(1,2);
        NNb22(i) = NNb2;
        iz2(i)=i;
        plo2 = plot(iz2,NNb22);
    end
    if (NNb2 < mincorr) && (i >= numNN)
        while (NNb2 <= mincorr)
            IW = net4.IW{1,1};
            LW = net4.LW{2,1};
            [net4,tr] = train(net4,t4,t3);
            net4.IW{1,1} = IW;
            net4.LW{2,1} = LW;
            y7 = net4(fval');
            y77 = net4(t4);
            i=i+1;
            NNb2 = corrcoef(t3,y77);
            NNb2 = NNb2(1,2);
            NNb22(i) = NNb2;
            iz2(i)=i;
            plo2 = plot(iz2,NNb22);
        end
    end
end
end
%% output / display
##### RBF #####
if RBF == 1
    disp(y5);
    disp(y4);
end
### Regression ###
if reg == 1
    bz1 = corrcoef(z2,y2);
    bz1 = bz1(1,2);
    bz1 = corrcoef(z2,y2);
    bz2 = corrcoef(t,y21);
    bz2 = bz2(1,2);

```

```

        bz2 = corrcoef(t,y22);
end
#### FFBP ####
if single == 1
    disp(y7);
    disp(['bz = ',num2str(max(NNb2))]);
end
%% Save network picture
if savepic == 1
    jframe = view(net4);
    hFig = figure('Menubar','none', 'Position',[100 100 565 166]);
    jpanel = get(jframe,'ContentPane');
    [~,h] = javacomponent(jpanel);
    set(h, 'units','normalized', 'position',[0 0 1 1])
    jframe.setVisible(false);
    jframe.dispose();
    set(hFig, 'PaperPositionMode', 'auto')
    saveas(hFig, 'RBFnetwork.png')
    close(hFig)
end
%% Handeling comments
if exitflag == 1
    exitflag = '1 - Average change in value of the spread over
options.MaxStallGenerations generations less than
options.FunctionTolerance, and the final spread is less than the average
spread over the past options.MaxStallGenerations generations.';
elseif exitflag == 0
    exitflag = '0 - Maximum number of generations exceeded.';
elseif exitflag == -1
    exitflag = '-1 - Optimization terminated by an output function or plot
function.';
elseif exitflag == -2
    exitflag = '-2 - No feasible point found.';
else
    exitflag = '-5 - Time limit exceeded';
end
disp(exitflag);

```


Ga_testfn.m

```
%% Regression formula
% y(1) = S11 max
% y(2) = Sa min
% y(3) = HRC min
function y = ga_testfn(x)
% Using FFBP network
global netGA
yy1 = netGA([x(:,1) x(:,2) x(:,3) x(:,4)]');

y(1) = yy1(1,:);
y(2) = yy1(2,:);
y(3) = yy1(3,:);

end
```

NNGA.m

```
function netGA2 = NNGA(z,z2,l11,l22,l33)
global netGA
numNN1=200;
netGA = newff(z,z2,[l11 l22
l33],{'logsig','tansig','tansig','tansig'},'trainrp','learnngd');
netGA.trainParam.showWindow = true;
netGA.divideFcn = 'dividerand';
netGA.trainParam.goal = 1;
b2=[];iz=[];
for i = 1:numNN1
    fprintf('Training-1 %d/%d\n', i, numNN1)
    IW = netGA.IW{1,1};
    LW = netGA.LW{2,1};
    [netGA,tr] = train(netGA,z,z2);
    netGA.IW{1,1} = IW;
    netGA.LW{2,1} = LW;
    y1 = netGA(z);
    trainTargets = z2 .* tr.trainMask{1};
    valTargets = z2 .* tr.valMask{1};
    testTargets = z2 .* tr.testMask{1};
    b1 = corrcoef(z2,y1);
    b1 = b1(1,2);
    b2(i) = b1;
    iz(i)=i;
end
disp(['bz = ',num2str(max(b2))]);
netGA2 = netGA;
end
```

nonlinconst.m

```
function [c,ceq]= nonlinconst(x)
```

```
% c(1) = S11  
% c(2) = Sa >= 0  
% c(3) = HRC >= 0
```

```
    c(1) = (-0.13134*x(:,1).^2+158.1*x(:,1)*x(:,2)-69.719*x(:,1)*x(:,3)-  
1.1179*x(:,1)*x(:,4)+0.00055106*x(:,1).^3-  
0.81561*x(:,1).^2*x(:,2)+0.41529*x(:,1).^2*x(:,3)+38.984*x(:,1)*x(:,2)*x(:,  
3)+0.016616*x(:,1).^2*x(:,4)-6.7745*x(:,1)*x(:,2)*x(:,4)-  
1.2565*x(:,1)*x(:,3)*x(:,4)+996.52*x(:,2)*x(:,3)*x(:,4)-1.1582e-  
06*x(:,1).^4+0.0023615*x(:,1).^3*x(:,2)-  
0.74851*x(:,1).^2*x(:,2).^2+97.135*x(:,1)*x(:,2).^3-  
0.00052979*x(:,1).^3*x(:,3)-0.11359*x(:,1).^2*x(:,2)*x(:,3)-  
0.10743*x(:,1).^2*x(:,3).^2-2.8697e-  
05*x(:,1).^3*x(:,4)+0.0017578*x(:,1).^2*x(:,2)*x(:,4)+7.6171*x(:,1)*x(:,2).  
^2*x(:,4)+0.0027643*x(:,1).^2*x(:,3)*x(:,4)-  
2.3892*x(:,1)*x(:,2)*x(:,3)*x(:,4));
```

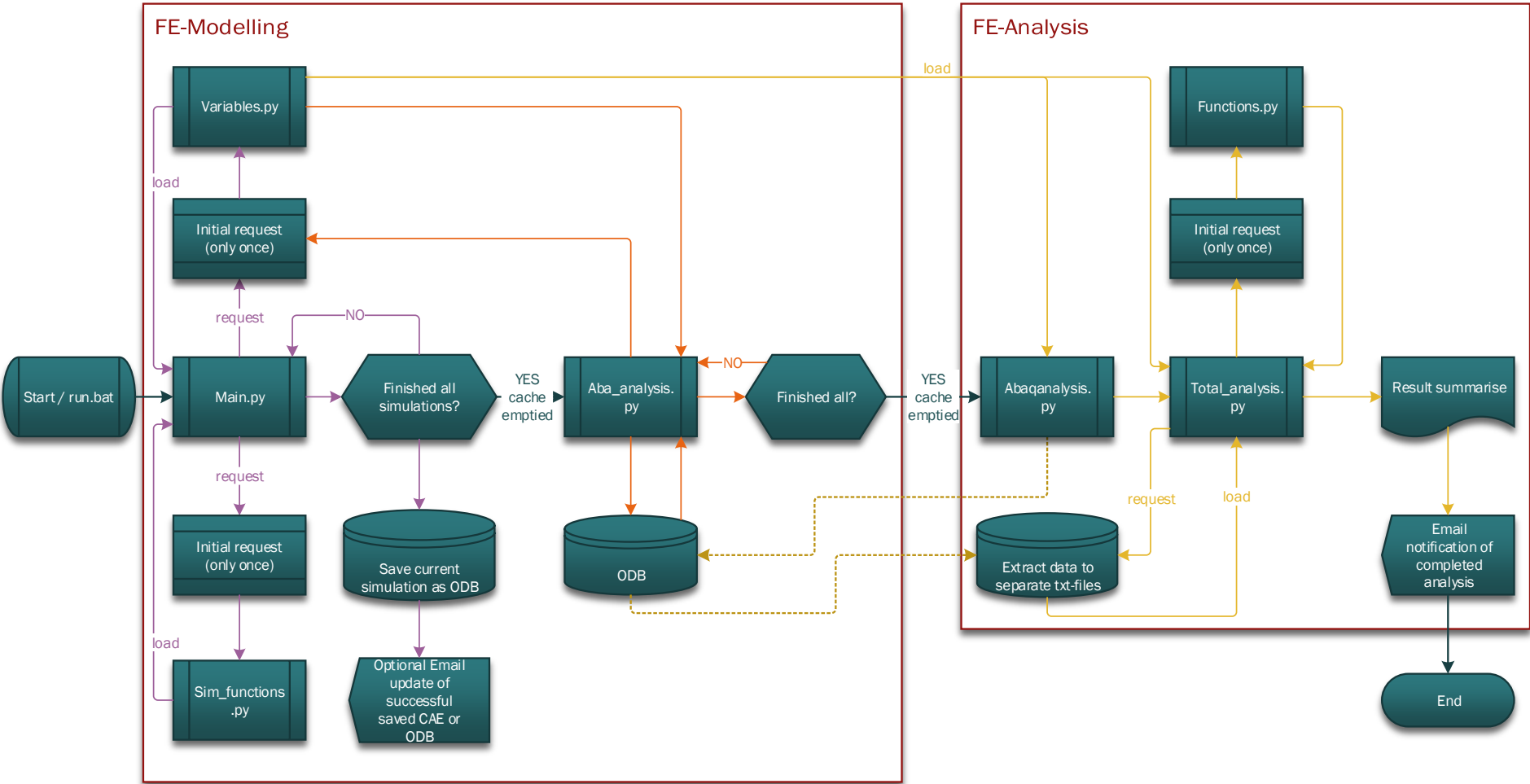
```
    z = (0.00020744*x(:,1).^2-0.20683*x(:,1)*x(:,2)-  
0.0010168*x(:,1)*x(:,3)+0.0022568*x(:,1)*x(:,4)-5.9257e-  
07*x(:,1).^3+0.00076777*x(:,1).^2*x(:,2)+9.5776e-  
08*x(:,1).^2*x(:,3)+0.30607*x(:,1)*x(:,2)*x(:,3)-4.1889e-  
05*x(:,1).^2*x(:,4)+0.021648*x(:,1)*x(:,2)*x(:,4)+0.015042*x(:,1)*x(:,3)*x(  
:,4)-13.914*x(:,2)*x(:,3)*x(:,4)+1.5703e-09*x(:,1).^4-3.9518e-  
06*x(:,1).^3*x(:,2)+0.0023002*x(:,1).^2*x(:,2).^2-  
0.39705*x(:,1)*x(:,2).^3+3.7933e-07*x(:,1).^3*x(:,3)-  
0.0012786*x(:,1).^2*x(:,2)*x(:,3)-1.6367e-05*x(:,1).^2*x(:,3).^2+8.117e-  
08*x(:,1).^3*x(:,4)-2.2718e-05*x(:,1).^2*x(:,2)*x(:,4)-  
0.018644*x(:,1)*x(:,2).^2*x(:,4)-4.8688e-  
05*x(:,1).^2*x(:,3)*x(:,4)+0.046437*x(:,1)*x(:,2)*x(:,3)*x(:,4));  
    c(2) = -1*z;
```

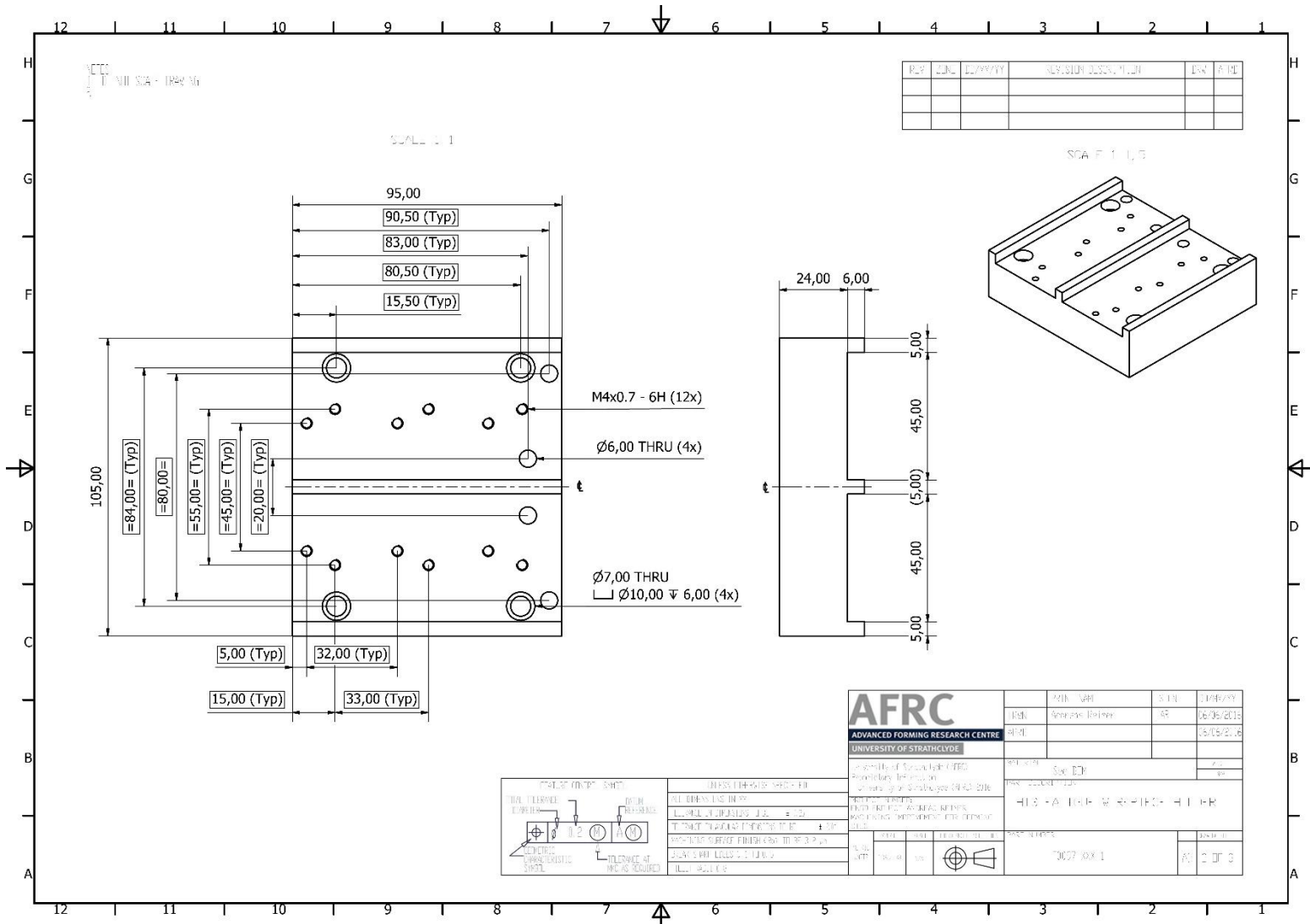
```
    zz = (0.004439*x(:,1).^2-0.42475*x(:,1)*x(:,2)+0.95028*x(:,1)*x(:,3)-  
0.00026253*x(:,1)*x(:,4)-1.351e-05*x(:,1).^3-0.0021216*x(:,1).^2*x(:,2)-  
0.0071018*x(:,1).^2*x(:,3)-1.2593*x(:,1)*x(:,2)*x(:,3)-  
0.00010926*x(:,1).^2*x(:,4)+0.078345*x(:,1)*x(:,2)*x(:,4)-  
0.074636*x(:,1)*x(:,3)*x(:,4)+65.292*x(:,2)*x(:,3)*x(:,4)+1.0837e-  
08*x(:,1).^4-1.0353e-  
07*x(:,1).^3*x(:,2)+0.0036323*x(:,1).^2*x(:,2).^2+0.50644*x(:,1)*x(:,2).^3+  
1.2911e-  
05*x(:,1).^3*x(:,3)+0.0030571*x(:,1).^2*x(:,2)*x(:,3)+0.002371*x(:,1).^2*x(  
:,3).^2+2.0247e-07*x(:,1).^3*x(:,4)+1.3962e-05*x(:,1).^2*x(:,2)*x(:,4)-  
0.10986*x(:,1)*x(:,2).^2*x(:,4)+0.00020148*x(:,1).^2*x(:,3)*x(:,4)-  
0.19583*x(:,1)*x(:,2)*x(:,3)*x(:,4));  
    c(3) = -1*zz;
```

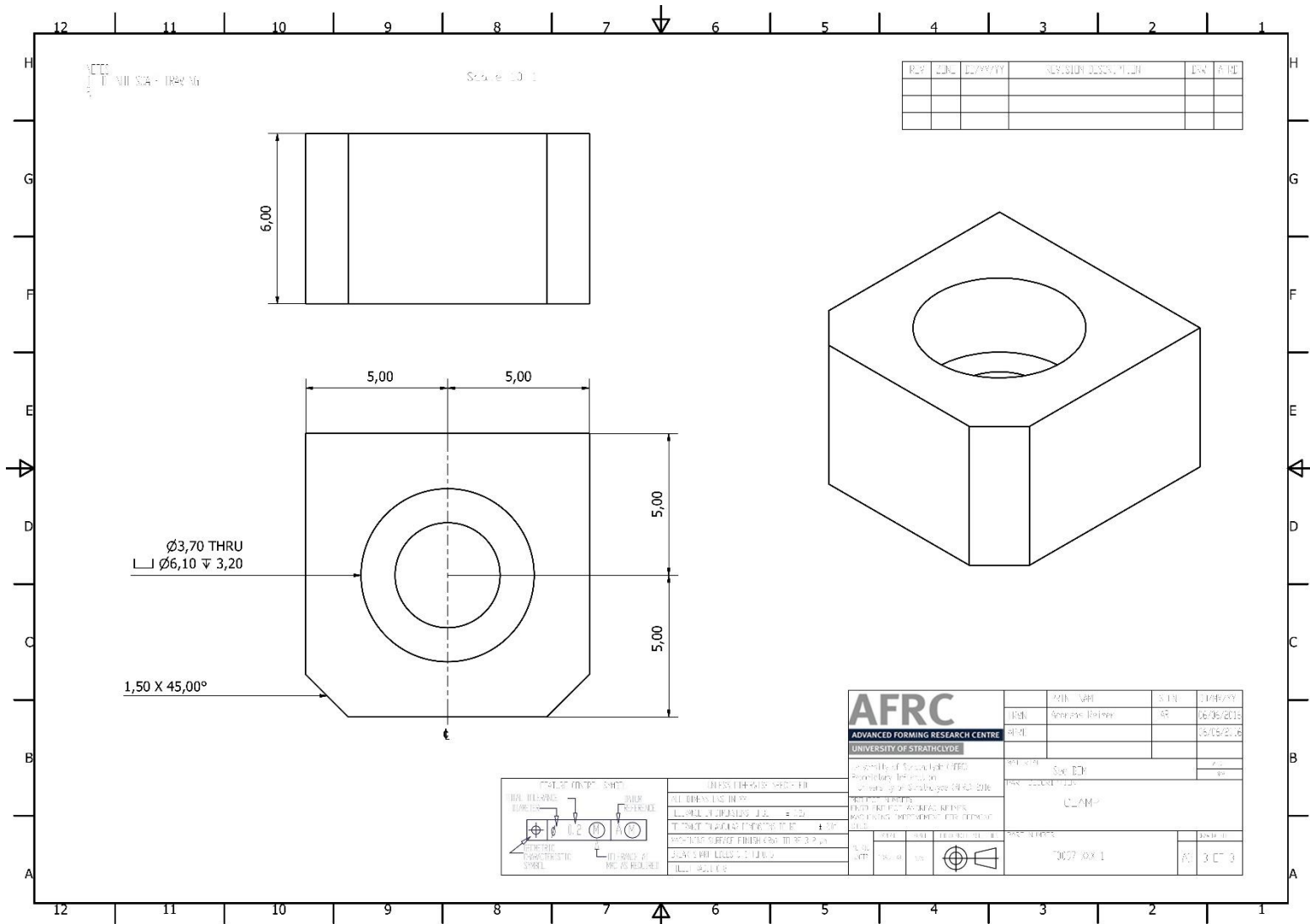
```
    ceq = [] ;
```

```
end
```

Appendix IX Script Framework

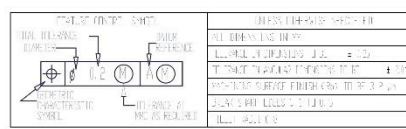






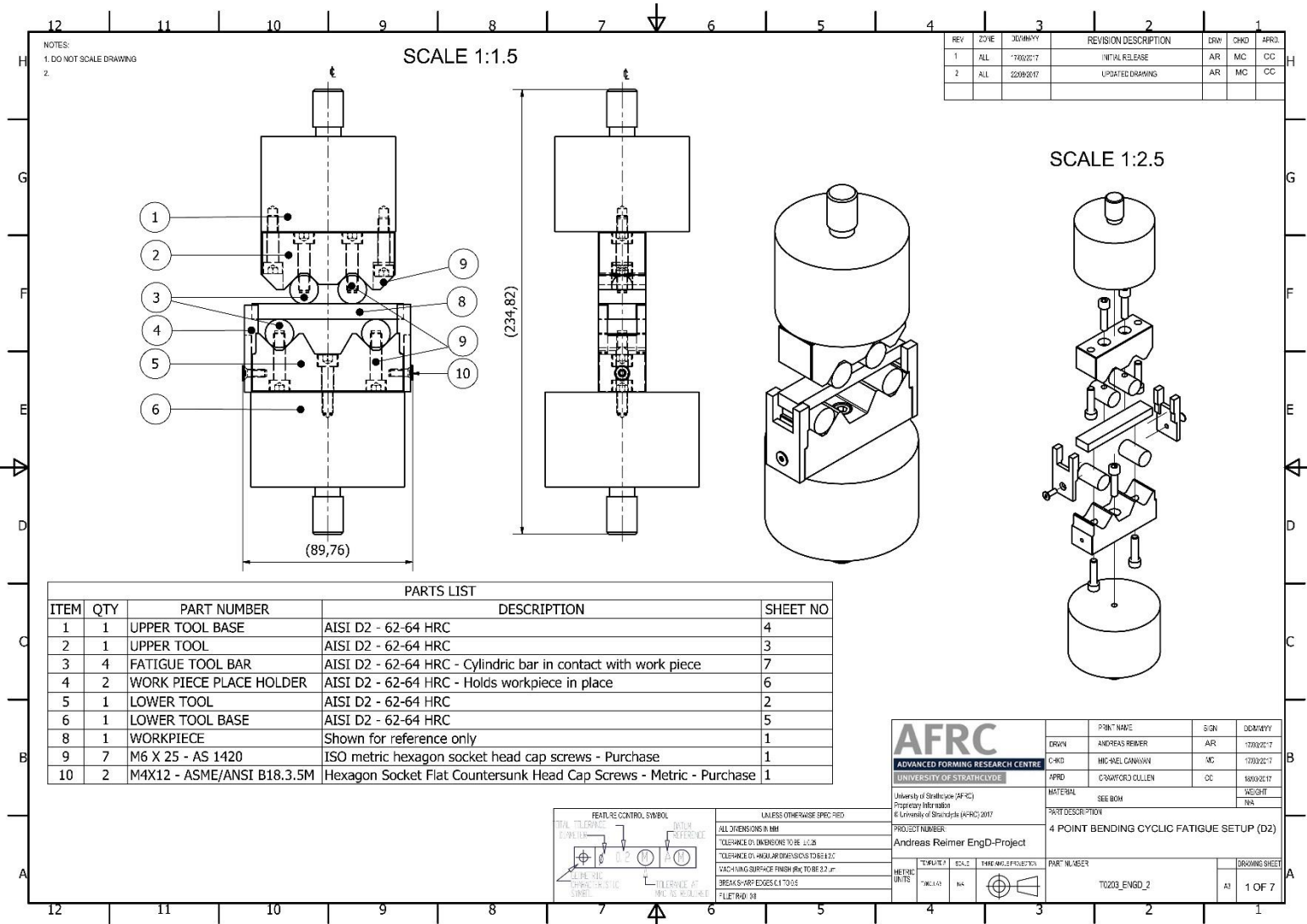
REV	DATE	DESCRIPTION	BY	APP

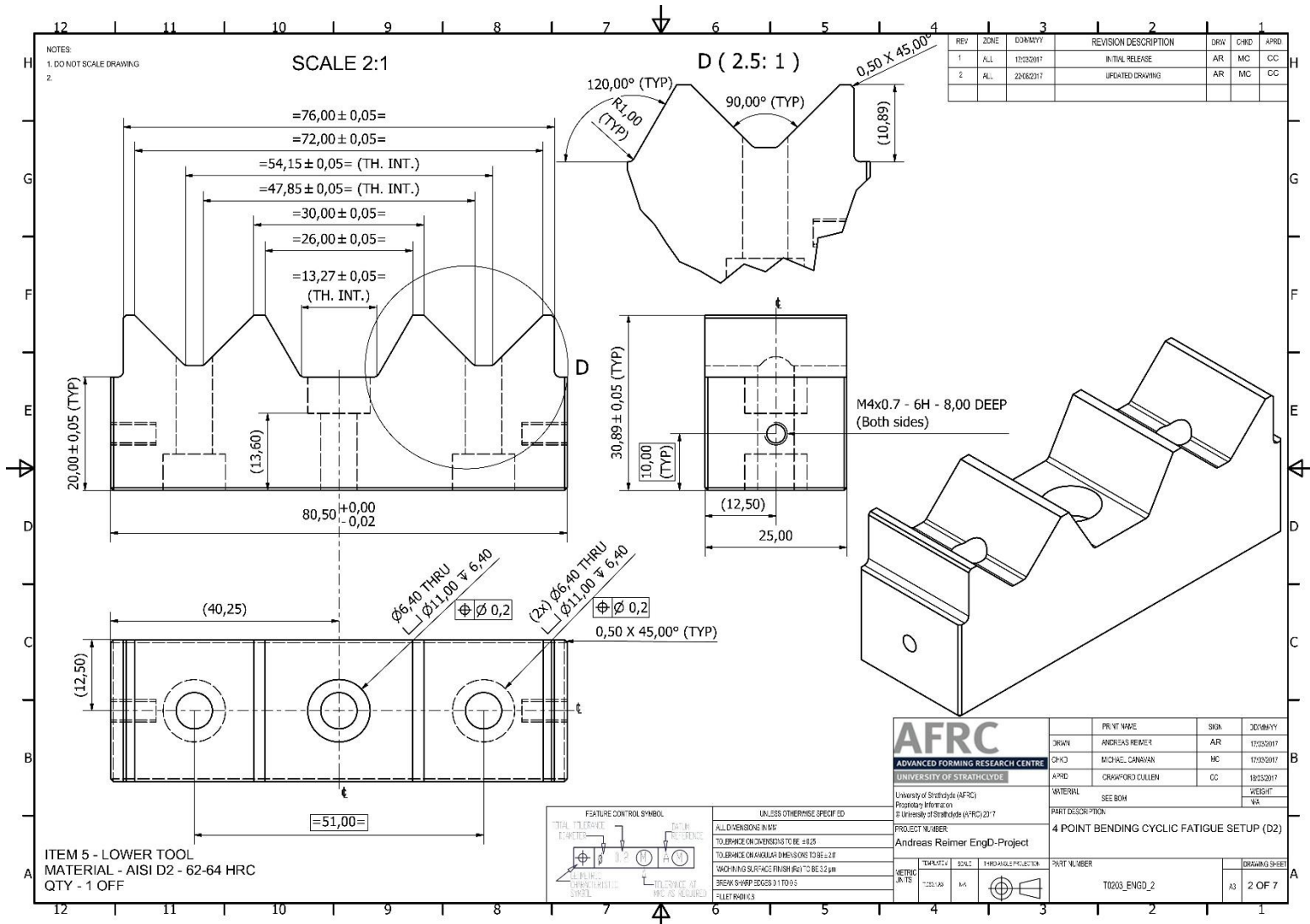
AFRC		REV	APP	DATE	DATE
ADVANCED FORMING RESEARCH CENTRE		1/01	Approved Release	88	06/05/2019
UNIVERSITY OF STRATHCLYDE		8/01			16/05/2016
School of Mechanical Engineering Department of Manufacturing Engineering University of Strathclyde G4 0LN		8/01/19	Doc ID		
PROJECT TITLE		CLAM			
PROJECT NUMBER		7007 001			
PROJECT LOCATION					
PROJECT STATUS					
PROJECT LEADER					
PROJECT CONTACT					

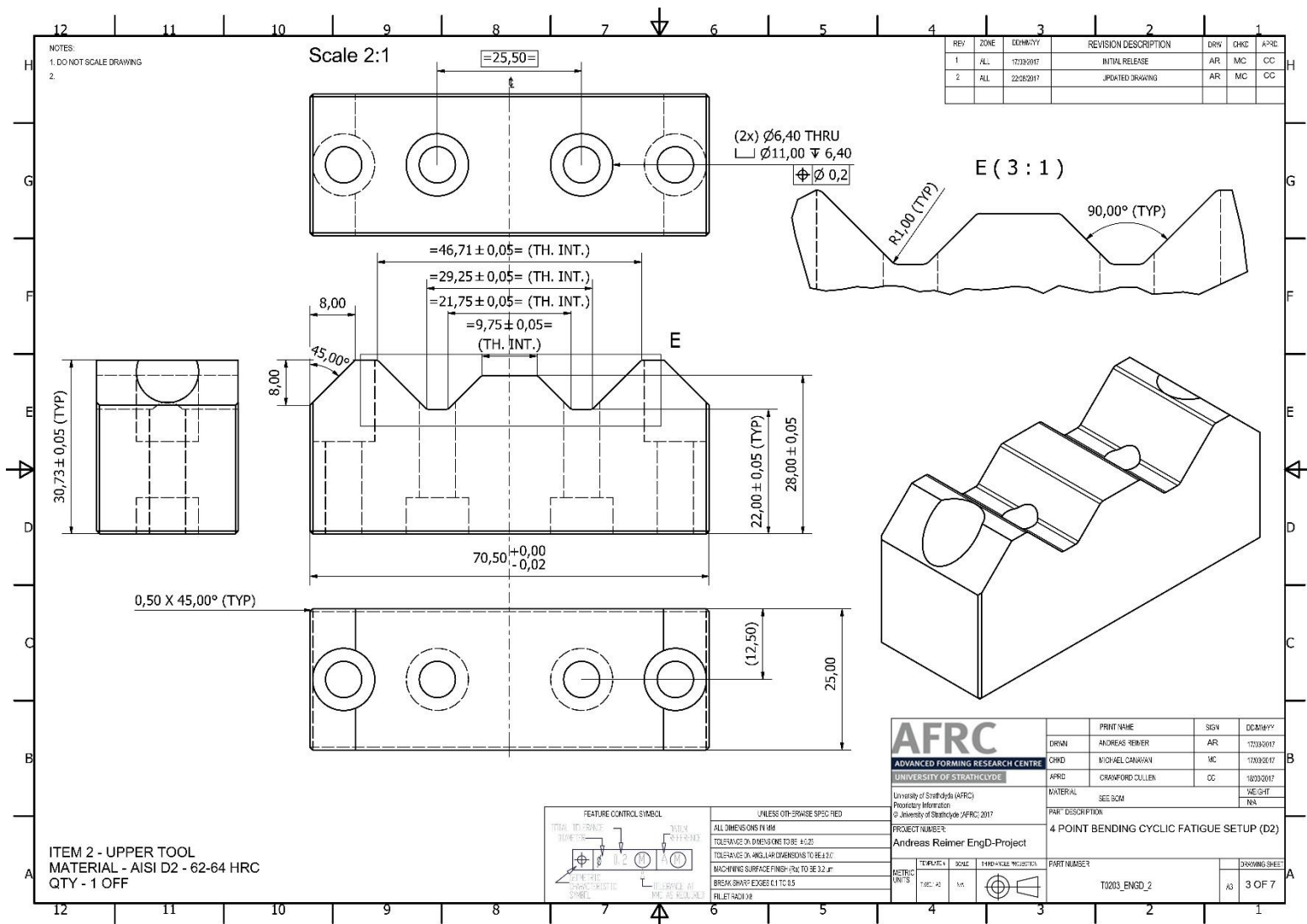


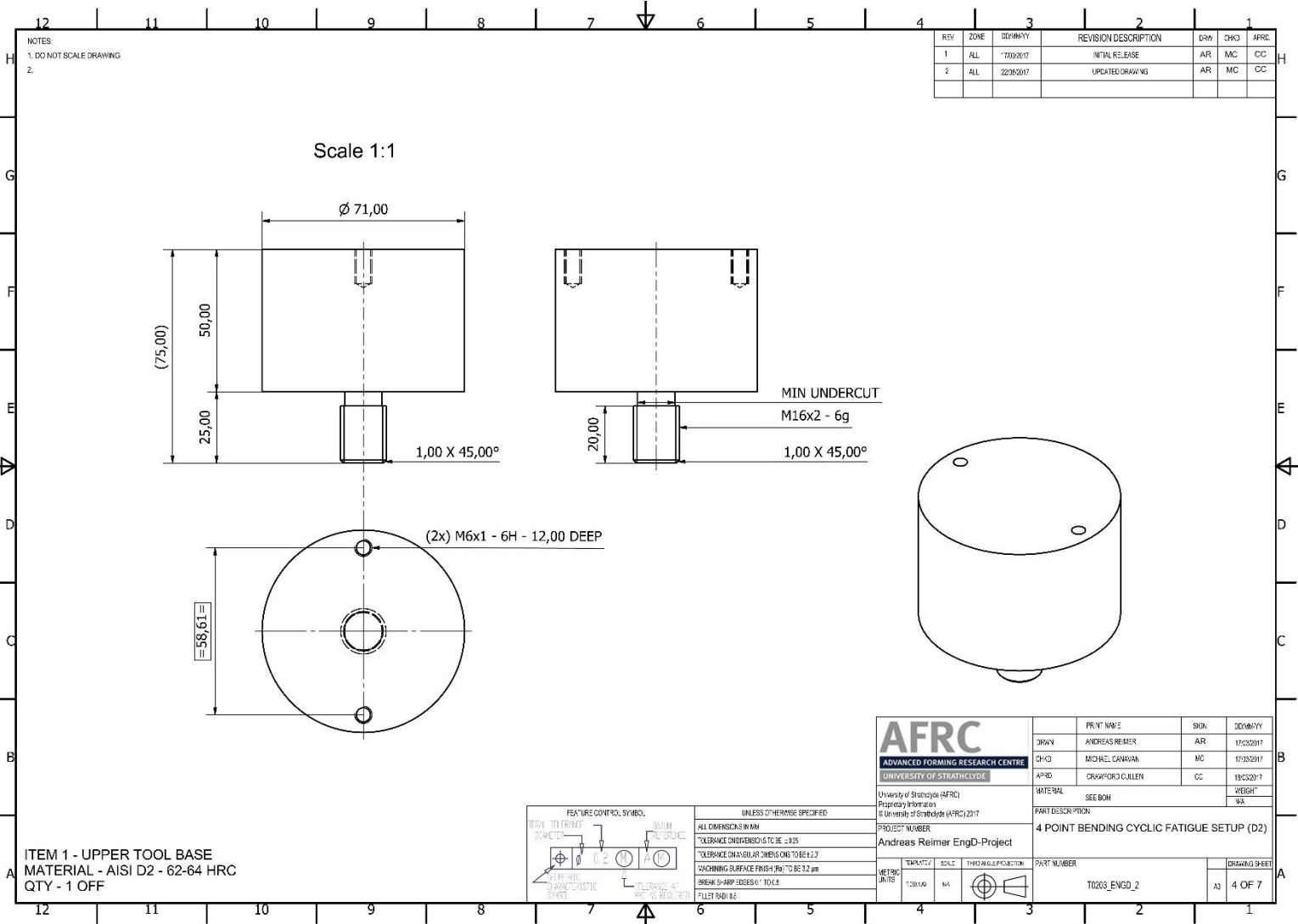
Appendix XI Fatigue Testing Setup Drawings

Initial Design





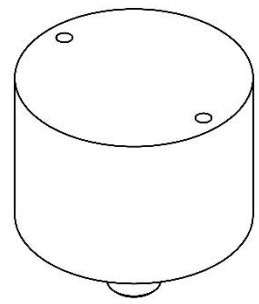
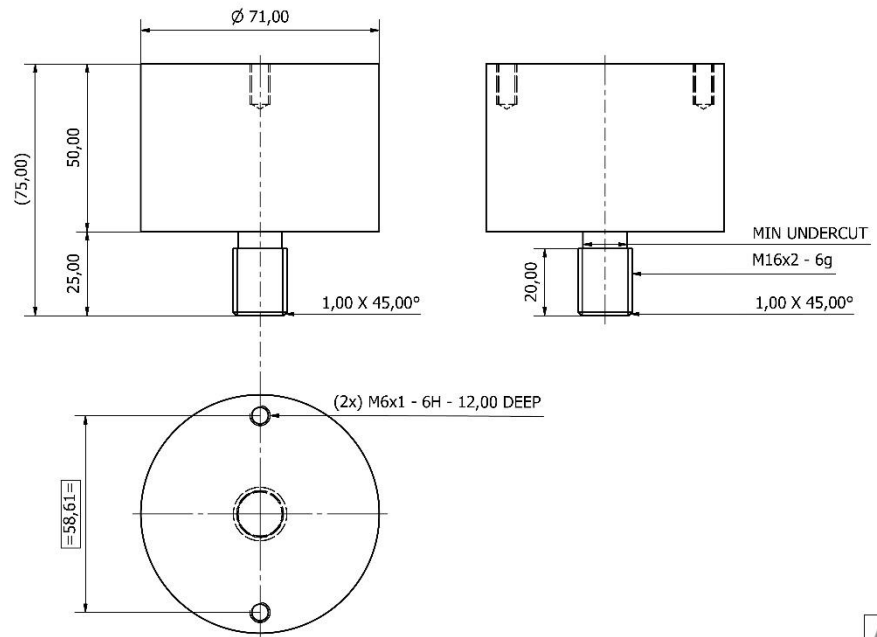




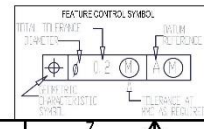
NOTES
 1. DO NOT SCALE DRAWING
 2.

REV	ZONE	DDMMYY	REVISION DESCRIPTION	DRW	CHKD	APRD
1	ALL	17/03/2017	INITIAL RELEASE	AR	MC	CC
2	ALL	22/03/2017	UPDATED DRAWING	AR	MC	CC

Scale 1:1



ITEM 1 - UPPER TOOL BASE
 MATERIAL - AISI D2 - 62-64 HRC
 QTY - 1 OFF



UNLESS OTHERWISE SPECIFIED

ALL DIMENSIONS IN MM

TOLERANCE ON DIMENSIONS TO BE ±0.25

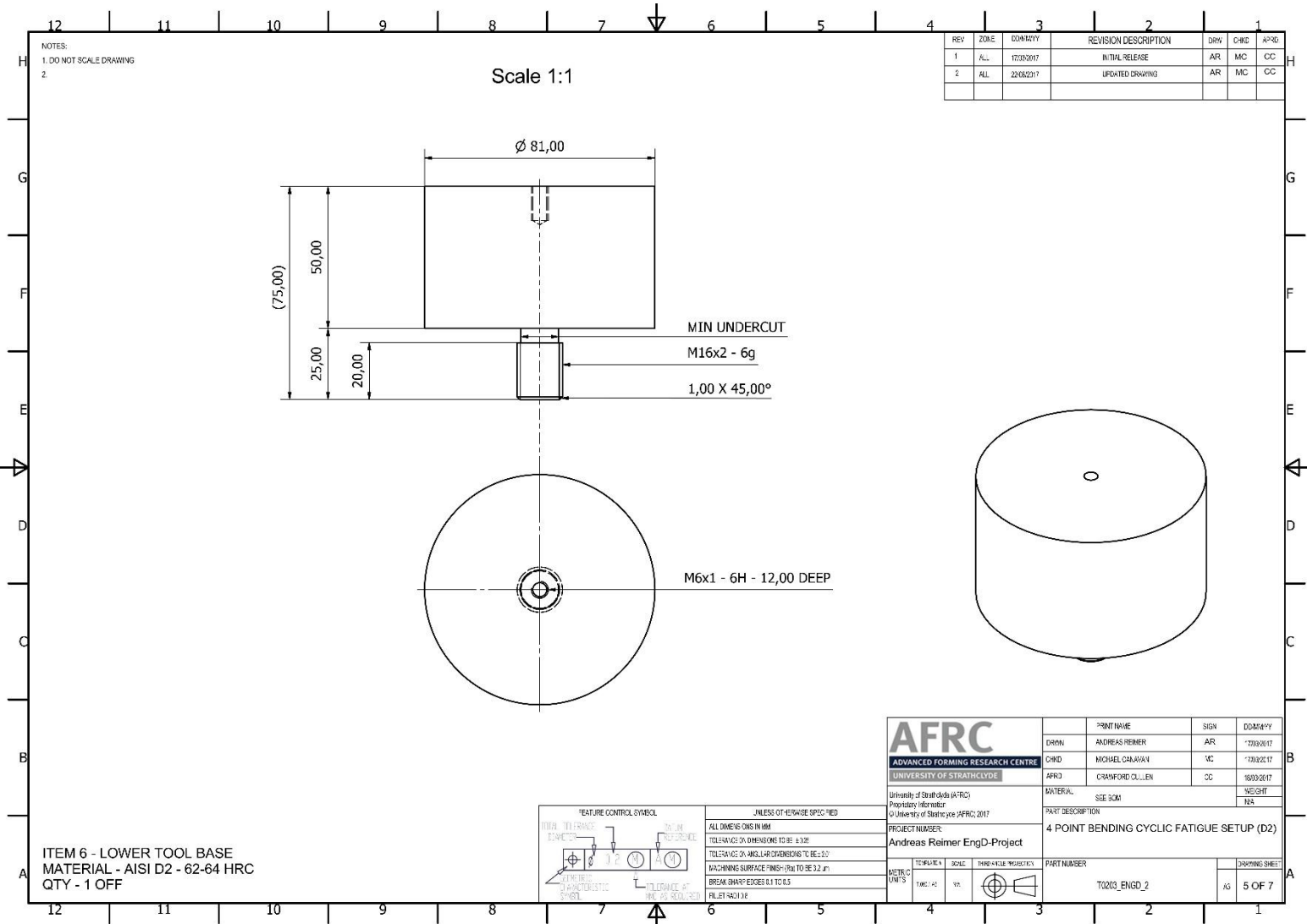
TOLERANCE ON ANGULAR DIMENSIONS TO BE ±2.0

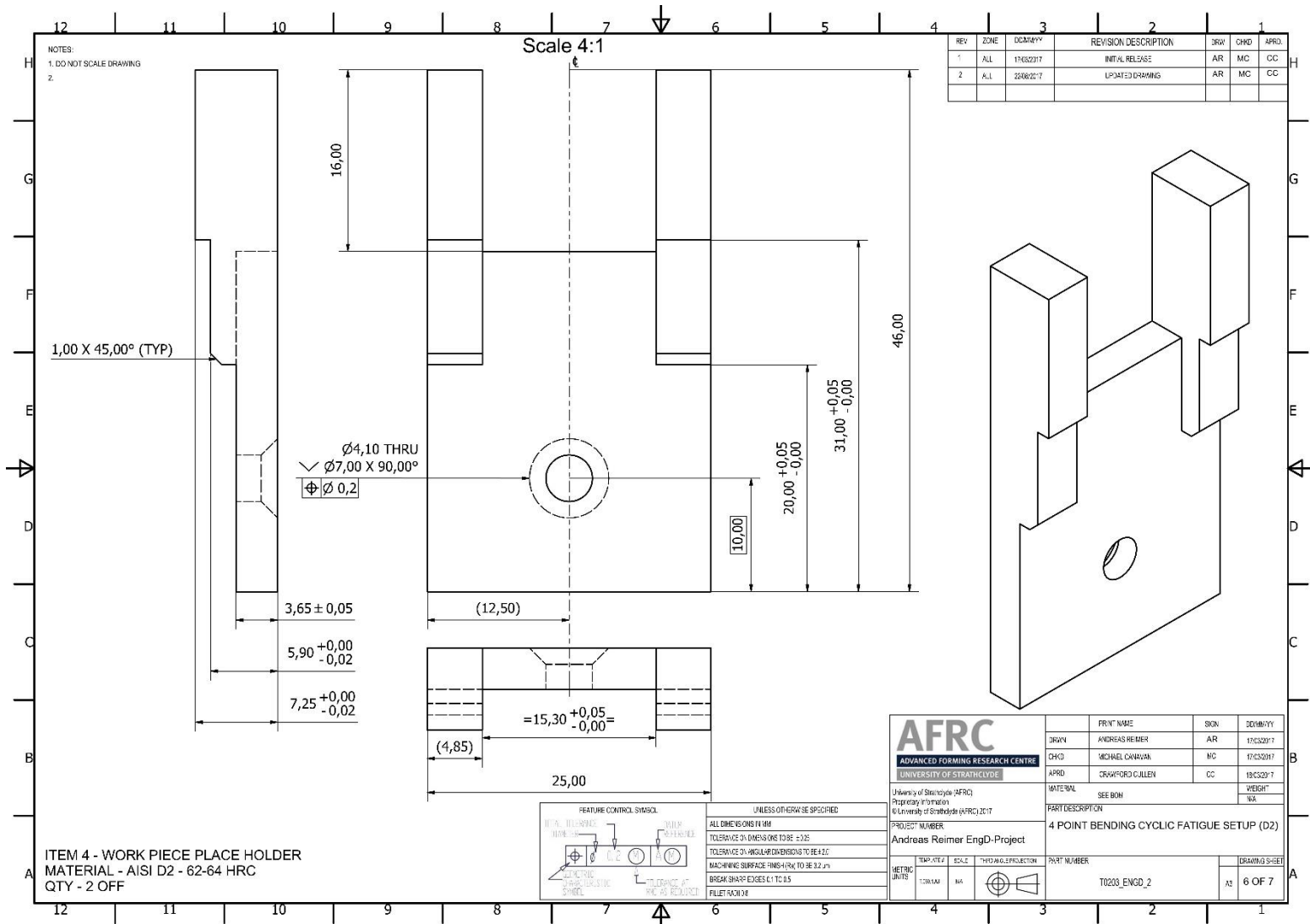
WORKING SURFACE FINISH (Ra) TO BE 3.2 µm

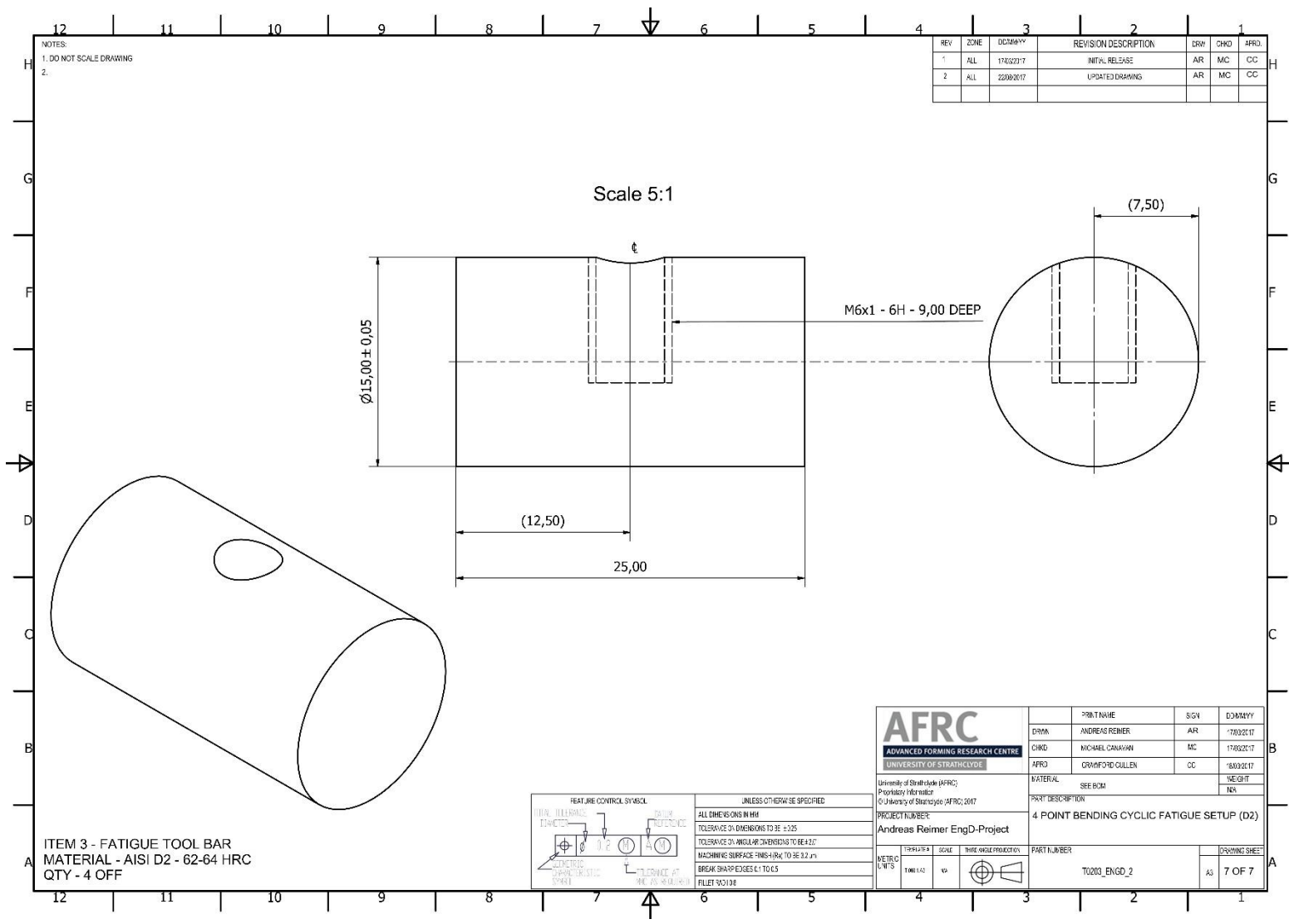
BREAK SHARP EDGES TO 0.25 R

FILLET RADI 0.8

AFRC ADVANCED FORMING RESEARCH CENTRE UNIVERSITY OF STRATHCLYDE University of Strathclyde (AFRC) Property Information © University of Strathclyde (AFRC) 2017	PRINT NAME	SIGN	DDMMYY	
	DRWN	ANDREAS REIMER	AR	17/03/2017
	CHKD	MICHAEL CANNAN	MC	17/03/2017
	APRD	ORWYFORD CULLEN	CC	18/05/2017
MATERIAL	SEE BOM	WEIGHT	N/A	
PROJECT NUMBER	PART DESCRIPTION			
Andreas Reimer EngD-Project	4 POINT BENDING CYCLIC FATIGUE SETUP (D2)			
METRIC UNITS	TYPICALLY SCALE	THIRD ANGLE PROJECTION	PART NUMBER	
1:200 LAB	N/A		T0203_ENGD_2	
			DRAWING SHEET	
			A3 4 OF 7	



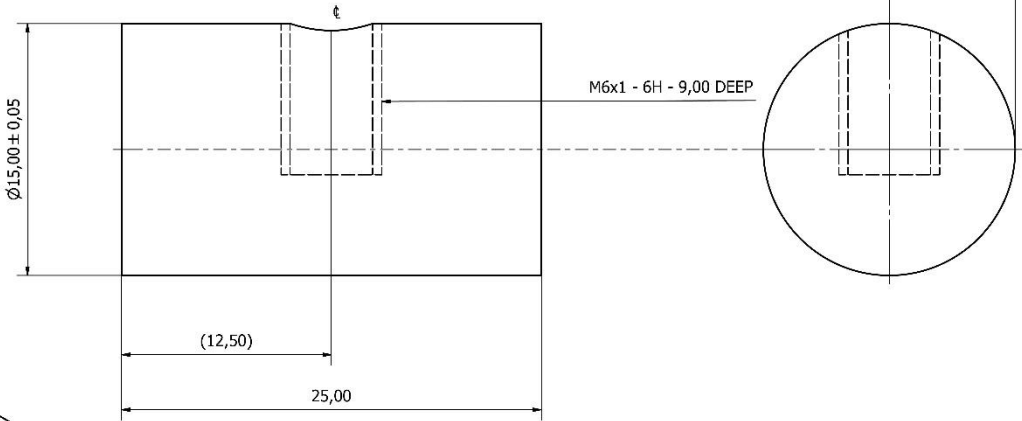




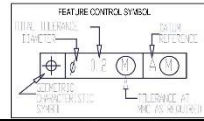
NOTES:
 1. DO NOT SCALE DRAWING
 2.

REV	ZONE	DC/MAY/YY	REVISION DESCRIPTION	DRW	CHKD	APRD.
1	ALL	17/03/2017	INITIAL RELEASE	AR	MC	CC
2	ALL	22/09/2017	UPDATED DRAWING	AR	MC	CC

Scale 5:1



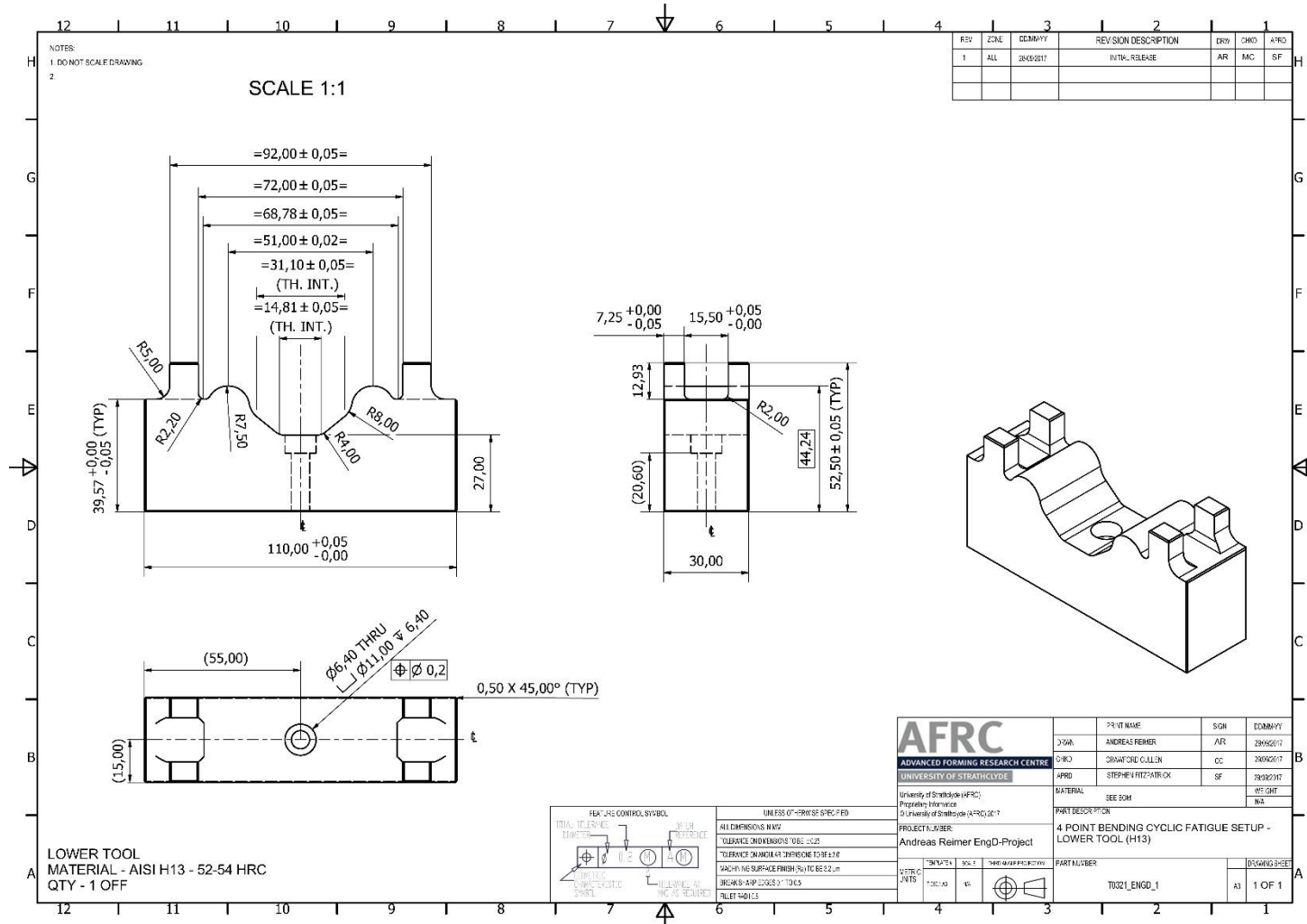
ITEM 3 - FATIGUE TOOL BAR
 MATERIAL - AISI D2 - 62-64 HRC
 QTY - 4 OFF



UNLESS OTHERWISE SPECIFIED:
 ALL DIMENSIONS IN MM
 TOLERANCE ON DIMENSIONS TO BE ±0.25
 TOLERANCE ON ANGULAR DIMENSIONS TO BE ±0.5°
 MACHINING SURFACE FINISH (Ra) TO BE 3.2 µm
 BREAK SHARP EDGES L1 TO L5
 FILET R0.10

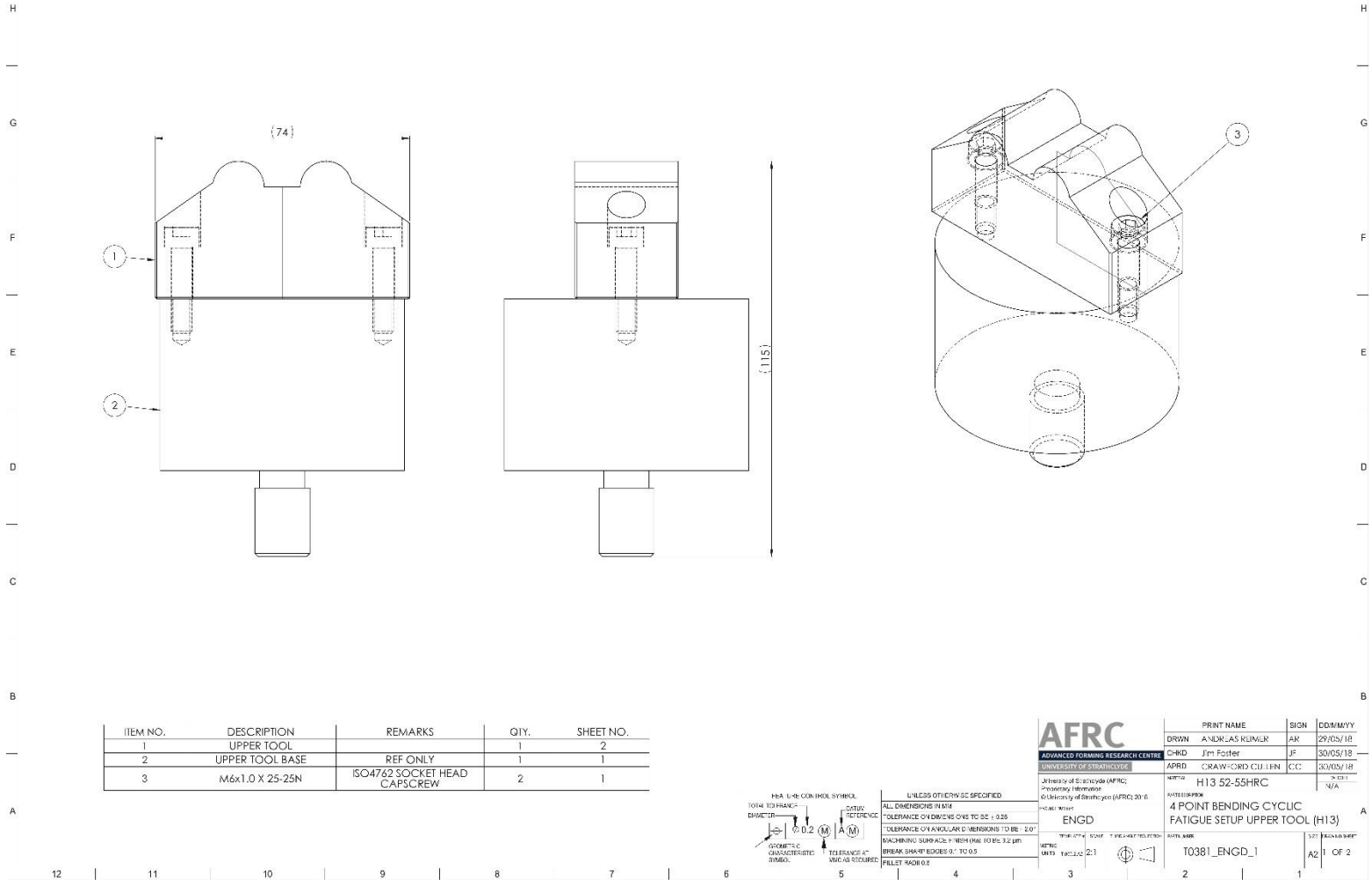
AFRC ADVANCED FORMING RESEARCH CENTRE UNIVERSITY OF STRATHCLYDE		PRINT NAME	SGN	DC/MAY/YY
University of Strathclyde (AFRC) Priority Materials © University of Strathclyde (AFRC) 2017		DRWA	ANDREAS REIMER	AR
PROJECT NUMBER: Andreas Reimer EngD-Project		CHKD	MICHAEL CANNAN	MC
MATERIAL: SEE BOM		AFRC	ORWALD CULLEN	CC
PART DESCRIPTION: 4 POINT BENDING CYCLIC FATIGUE SETUP (D2)		VEGIT		18/03/2017
PART NUMBER: T0203_ENGO_2		WEIGHT		NA
DRAWING SHEET: 7 OF 7				

Revised Parts



GENERAL DWG NOTES:
 1. DO NOT SCALE DRAWING
 2. SIZES STATED TO BE INSPECTED AT 20°C

REV	ZONE	DDMMYY	REVISION DESCRIPTION	DRW	CHKD	APRD
1	ALL	29/05/18	INITIAL RELEASE	AR	JF	CC
2						
3						



ITEM NO.	DESCRIPTION	REMARKS	QTY.	SHEET NO.
1	UPPER TOOL		1	2
2	UPPER TOOL BASE	REF ONLY	1	1
3	M6x1.0 X 25-25N	ISO4762 SOCKET HEAD CAPSCREW	2	1

AFRC
 ADVANCED FORMING RESEARCH CENTRE
 University of Bath, Bath, BA2 9AY, UK
 Tel: +44 (0)1225 309311
 Email: afrc@bath.ac.uk

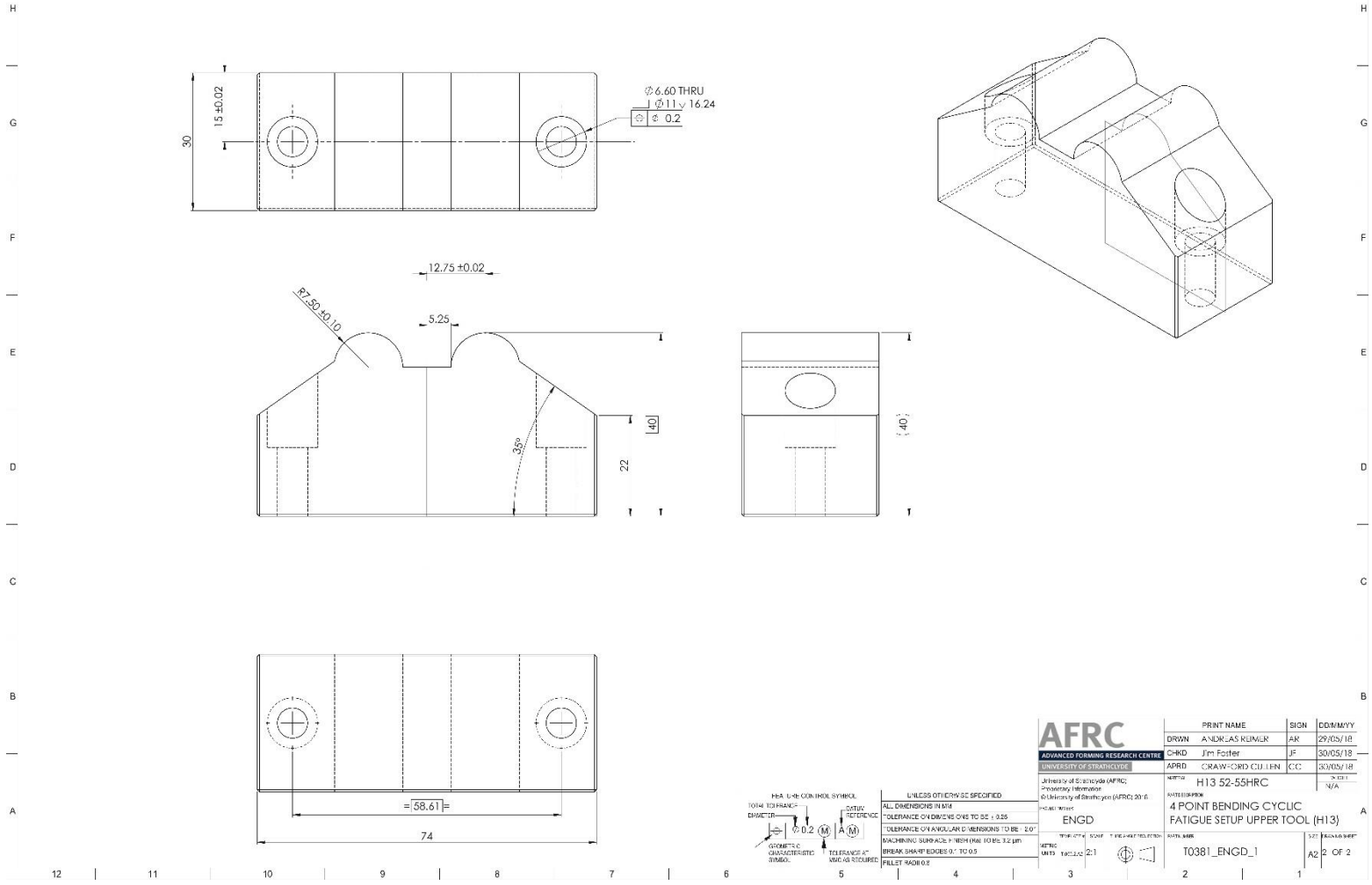
PRINT NAME	SIGN	DDMMYY
DRWN: ANNE-LAS RUMER	AR	29/05/18
CHKD: Jim Foster	JF	30/05/18
APRD: CRAWFORD CULLEN	CC	30/05/18
REF: H13 52-55HRC		N/A

UNLESS OTHERWISE SPECIFIED
 ALL DIMENSIONS IN MM
 TOLERANCE ON DIMENSIONS TO BE ± 0.25
 TOLERANCE ON ANGULAR DIMENSIONS TO BE ± 0.1°
 FINISHING SURFACE FINISH (RA) TO BE 3.2 µm
 BREAK SHARP EDGES TO 0.5
 FILLET RADIUS

ENGD
 TITLES: 4 POINT BENDING CYCLIC FATIGUE SETUP UPPER TOOL (H13)
 FILE NAME: T0381_ENGD_1
 SHEET: 1 OF 2

GENERAL DWG NOTES:
 1. DO NOT SCALE DRAWING
 2. SIZES STATED TO BE INSPECTED AT 20°C

REV	ZONE	DDMMYY	REVISION DESCRIPTION	DRW	CHKD	APRD
1	ALL	29/05/18	INITIAL RELEASE	AR	JF	CC
2						
3						



ISO 15-18 CONTOUR SYMBOL	UNLESS OTHERWISE SPECIFIED
TOUCH TO FINISH	ALL DIMENSIONS IN MM
EMITTER	TOLERANCE ON DIMENSIONS TO BE ± 0.25
GEOMETRIC QUALIFIER/TYPE SYMBOL	TOLERANCE ON ANGULAR DIMENSIONS TO BE ± 0.1°
TELERANCE SYMBOL	FINISHING SURFACE FINISH (RA) TO BE 3.2 µm
	BREAK SHARP EDGES TO 0.5
	FILET RADIUS

AFRC		PRINT NAME	SIGN	DDMMYY	
ADVANCED FORMING RESEARCH CENTRE		DRWN	ALEXAS RUMER	AR	29/05/18
University of Bath		CHKD	Jm Foster	JF	30/05/18
Department of Mechanical Engineering		APRD	CRAWFORD CULLIN	CC	30/05/18
Faculty of Engineering		REFNO	H13 52-55HRC		N/A
Address: 10, Bath Road, Bath, BA2 9BN, UK		4 POINT BENDING CYCLIC FATIGUE SETUP UPPER TOOL (H13)			
Tel: +44 (0)1225 309311		DATE	T0381_ENGD_1	3/2	ISSUED
Fax: +44 (0)1225 309312		UNIT	MKS	A2	2 OF 2

Appendix XII Certificates of Conformance

AISI H13 Material Certificate of Conformance



Cogne UK Ltd

Don Road
Newhall
Sheffield
South Yorkshire
S9 2UD



Telephone
Fax:
Email:

Customer: UNIVERSITY OF STRATHCLYDE		Deliver To: ADVANCED FORMING RESEARCH CENTRE		Despatch Note No. A1-732028.1 Despatch Date: 06/10/2016 Delivery Per: OUTSIDE CARRIER	
Account No.	Original Order No.	DESPATCH NOTE		Customer Reference	Sheet No. 1
Item 1	Product Code TF50X610H13BA	Description & Batch Detail (Q Batches denote Quality Assured source) TOOL STEEL ANNEALED BLACK FLAT 610MM X 50MM Batch No=Q140143 Cast No=881403195 Warehouse=SHEFFIELD C=0.37,Si=1.05,Mn=0.45,S=0.0008,P=0.026,Cr=5.13,Mo=1.28,V=0.95,		Qty Despatched 5 x 105 MM CP	Wgt Despatched 10 KG
1 BOX BAY 3		Loaded by: Date: Run 15689		Received in good condition by: Print: Date:	
COGNE UK Limited VAT No. GB 684 3750 08 Reg. No. 03298004		TITLE OF ALL GOODS REMAINS WITH COGNE UK LIMITED UNTIL PAID FOR IN FULL - SEE REVERSE FOR FULL TERMS AND CONDITIONS			

Stock Control Solutions from InterTalia Business Solutions (0800 056927)

INSPECTION REPORT

Order Number		Quantity	5
--------------	--	----------	---

Drawing Number	
Date	27/09/16

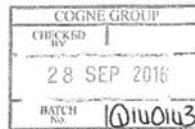
PAIR		L	W	H	SQ
1A	1B	✓	✓	✓	✓
2A	2B	✓	✓	✓	✓
3A		✓	✓	✓	✓
4A	4B				
5A	5B				
6A	6B				
7A	7B				
8A	8B				
9A	9B				
10A	10B				
11A	11B				
12A	12B				
13A	13B				
14A	14B				
15A	15B				
16A	16B				
17A	17B				
18A	18B				
19A	19B				
20A	20B				
21A	21B				
22A	22B				
23A	23B				
24A	24B				
25A	25B				
26A	26B				
27A	27B				
28A	28B				
29A	29B				
30A	30B				
31A	31B				
32A	32B				
33A	33B				
34A	34B				
35A	35B				
36A	36B				

PAIR		L	W	H	SQ
37A	37B				
38A	38B				
39A	39B				
40A	40B				
41A	41B				
42A	42B				
43A	43B				
44A	44B				
45A	45B				
46A	46B				
47A	47B				
48A	48B				
49A	49B				
50A	50B				
51A	51B				
52A	52B				
53A	53B				
54A	54B				

Comments

INSPECTED BY.....

OPERATOR.....





BETA HEAT TREATMENTS LTD

SUMMERTON ROAD, OLDBURY, WARLEY, WEST MIDLANDS, B69 2EL

Tel:0121 511 1190

Fax:0121 270 9605

http://www.claytonholdings.com rw@claytonholdings.com

Customer Name

CERTIFICATE OF CONFORMITY

Approval: C of C
Certificate No: 25781,25782,25783,25784
Date of Test: 20/09/2016
Order No: w01-006609

Part No.	Drg Iss.	Description of Process	Job No.	Qty	Weight	Material Spec	Batch ID / Serial No.
COGNE 52 - 54 HRC HARDEN & TEMPER 52/54 HRC COGNE BLOCKS	0	COGNE BLOCKS	0000026055	5	50	H13	L101-00 6608
100 70 x 45 mm							
COGNE 52 - 54 HRC HARDEN & TEMPER 52/54 HRC COGNE BLOCKS	0	COGNE BLOCKS	0000026054	20	510	H13	
122 x 132 x 202 mm							
COGNE 52 - 54 HRC HARDEN & TEMPER 52/54 HRC COGNE BLOCKS	0	COGNE BLOCKS	0000026053	12	306	H13	
122 x 132 x 202 mm = 12							
COGNE 52 - 54 HRC HARDEN & TEMPER 52/54 HRC COGNE BLOCKS	0	COGNE BLOCKS	0000026052	20	510	H13	
122 x 132 x 202 = 20							

TEST NAME	Lower Limit	Upper Limit
Rockwell HRC	52.0000	54.0000
52 _ _ _ _		
MD.DL		

Inspector(s)

